The Fourier transform interrogator

Grillo Peternella, F.

Important note
To cite this publication, please use the final published version (if applicable).
Please check the document version above.

The Fourier transform interrogator

The Fourier transform interrogator

Proefschrift

ter verkrijging van de graad van doctor
aan de Technische Universiteit Delft,
op gezag van de Rector Magnificus Prof.dr.ir. T.H.J.J. van der Hagen,
voorzitter van het College voor Promoties
in het openbaar te verdedigen op mandag 27 september 2021 om 15:00 uur

door

Fellipe GRILLO PETERNELLA

Master in Electrical Engineering,
University of Campinas, Brazilië,
geboren te Campinas, Brazilië.

Dit proefschrift is goedgekeurd door de

promotor: Prof.dr. H.P. Urbach
copromotor: Dr.ir. A.J.L. Adam

Samenstelling promotiecommissie:

Rector Magnificus,	voorzitter
Prof.dr. H.P. Urbach	Technische Universiteit Delft, promoter
dr.ir. A.J.L. Adam	Technische Universiteit Delft, copromoter

Onafhankelijke leden:

Prof.dr. K. J. Boller	U. Twente
Prof.dr. K. A. Williams	TU Eindhoven
Prof.dr. H. Hernández-Figueroa	U. of Campinas
Prof.dr. P. J. French	TU Delft

Overige lid:

Dr.ir. P. Harmsma	TNO

Keywords:Interrogators, Photonic Sensors, Fourier transform spectroscopy

I dedicate this thesis to my family. To my parents, my brother and, in special, I dedicate this thesis to my wife. She has not only supported during hard times, but also helped me with the technical work: measurements, CNPq reports and in reviewing the chip design.

Contents

Summary

Photonic sensors have recently attracted much attention in both industry and academia. High accuracy, low weight and the possibility of building a large sensor network are key benefits of photonic sensors. Another benefit is installing optical sensors in harsh environments where electronic sensors' usage is not plausible: aerospace applications where ionizing radiation is present or gas and oil pipes are some examples.

Integrated photonics brings new challenges to the interrogation of multiplexed sensors in WDM. Unlike FBG sensors, whose resonance wavelength can be chosen to an accuracy better than 1.0 nm, the resonance wavelength of integrated micro-ring resonators cannot be chosen during the design stage. The main reason is the imperfections of the manufacturing process. The fact that the resonance wavelength is unpredictable is a problem for interrogators based on interferometry. Such interrogators perform the demultiplexing and demodulation in different stages: first, a spectrometer separates the optical channels; subsequently, outputs of the spectrometer are conveyed to interferometers. From the photo-receiver voltages connected to MZI outputs, the signal from the sensors can be demodulated. As the resonance value of sensors cannot be determined during design, two sensors may have their resonances in the same spectrometer's channel. As a result, the demultiplexing step fails, compromising the interrogator's operation.

In Chapter 4 of this thesis, a new interrogation method is proposed. Much of the effort of interferometric interrogators is to separate the spectrum of the sensors correctly. In the Fourier Transform Interrogator, the spectrum of all sensors is sent to an array of Mach-Zehnder interferometers (MZI) with different OPDs. Using the output voltages from the photo-receivers attached to the MZIs, we derive a system of non-linear equations, whose solution provides the signal from each sensor. The demodulation and demultiplexing steps are performed simultaneously for the Fourier interrogator, which guarantees the interrogator's unique flexibility. On the other hand, the computational cost is high since the system of non-linear equations is solved using Newton's method. For each set of voltages sampled over time, a different system of equations is obtained. Chapter 4 leaves some unanswered questions:

1. Does the system of non-linear equations have a unique solution?

2. How many solutions are there?

3. What is the physical meaning of each of the solutions?

4. Is it possible to solve non-linear systems of equations for fast sensors in real-time?

All these questions are answered in Chapter 5. As a consequence of the new algebraic formulation, it is possible to solve about 1 000 000 algebraic systems of equations in 10 ns, i.e., allowing the real-time interrogation of high-speed sensors. The interrogator is a candidate for interrogating arrays of ultrasound ring resonator sensors in the tens of MHz range.

Samenvatting

Fotonische sensoren krijgen de laatste tijd veel aandacht in zowel de industrie als de academische wereld. Hoge nauwkeurigheid, laag gewicht en de mogelijkheid om een groot sensornetwerk te bouwen zijn belangrijke voordelen van fotonische sensoren. Een ander voordeel is het installeren van optische sensoren in onbewerkte omgevingen waar het gebruik van elektronische sensoren niet aannemelijk is: ruimtevaarttoepassingen waar ioniserende straling aanwezig is of gas- en olieleidingen zijn enkele voorbeelden.

Geïntegreerde fotonica brengt nieuwe uitdagingen voor de ondervraging van gemultiplexte sensoren in WDM (wavelength division multiplexing) met zich mee. In tegenstelling tot Fiber Bragg-sensoren (FBG-sensoren), waarvan de resonantiegolflengte kan worden gekozen met een nauwkeurigheid die beter is dan 1,0 nm, kan de resonantiegolflengte van geïntegreerde microring resonators niet worden gekozen tijdens de ontwerpfase. De belangrijkste redenen zijn de onvolkomenheden van het productieproces. Het feit dat de resonantiegolflengte onvoorspelbaar is, is een probleem voor ondervragers op basis van interferometrie. Dergelijke ondervragingen voeren de demultiplexing en demodulatie uit in verschillende fasen: eerst scheidt een spectrometer de optische kanalen; Daarna worden de outputs van de spectrometer getransporteerd naar interferometers. Van de foto-ontvanger spanningen die zijn aangesloten op de MZI-uitgangen, kan het signaal van de sensoren worden gedemoduleerd. Omdat de resonantiewaarde van sensoren tijdens het ontwerp niet kan worden bepaald, kunnen twee sensoren hun resonantie in hetzelfde spectrometerkanaal hebben. Als resultaat mislukt dan de demultiplexingstap, waardoor de werking van de ondervrager in gevaar komt.

In hoofdstuk 4 van dit proefschrift wordt een nieuwe ondervragingsmethode voorgesteld. Een groot deel van de inspanning van interferometrische ondervragers is om het spectrum van de sensoren correct te scheiden. In de Fourier Transform Interrogator wordt het spectrum van alle sensoren naar een reeks Mach-Zehnder-interferometers (MZI) met verschillende OPD's gestuurd. Met behulp van de uitgangsspanningen van de foto-ontvangers die aan de MZI's zijn bevestigd, leiden we

een systeem van niet-lineaire vergelijkingen af, waarvan de oplossing het signaal van elke sensor levert. De demodulatie- en demultiplexingstappen worden gelijktijdig uitgevoerd voor de Fourier-ondervrager, wat de unieke flexibiliteit van de ondervrager garandeert. Aan de andere kant zijn de rekenkosten hoog omdat het stelsel van niet- lineaire vergelijkingen wordt opgelost met behulp van de methode van Newton. Voor elke set spanningen die in de loop der tijd is bemonsterd, wordt een ander systeem van vergelijkingen verkregen. Hoofdstuk 4 laat een aantal onbeantwoorde vragen achter:

1. Heeft het stelsel van niet-lineaire vergelijkingen een unieke oplossing?

2. Hoeveel oplossingen zijn er?

3. Wat is de fysieke betekenis van elk van de oplossingen?

4. Is het mogelijk om niet-lineaire stelsels van vergelijkingen voor snelle sensoren in realtime op te lossen?

Al deze vragen worden beantwoord in Hoofdstuk 5. Als gevolg van de nieuwe algebraïsche formulering is het mogelijk om ongeveer 1 miljoen algebraïsche stelsels van vergelijkingen in 10 ns op te lossen, d.w.z. de real-time ondervragen van hogesnelheidssensoren mogelijk te maken. De ondervrager is een kandidaat voor het ondervragen van arrays van ultrasone ring resonator sensoren.

1

Introduction

This thesis focuses on the interrogation of photonic sensors. The goal of this Chapter is to introduce the principles of photonic sensors and some basic concepts of the different interrogation methods. The key idea is that the sensors work as modulators, encoding the external signal to be sensed into one of the fundamental properties of light such as amplitude, phase or polarization phase. The interrogators, in contrast, work as demodulators and demultiplexers: they separate the information of each sensor and convert the modulated light signal into an understandable value, in general, proportional to the intensity of the external signal. The thesis is divided into three parts: Chapters 1 and 2 introduce the key concepts, Chapter 3 presents the demodulation of a ring resonator sensor using a Mach-Zehnder interferometer, while in Chapters 4 and 5 a new interrogation method based on Fourier transform spectroscopy is proposed.

1.1. Preface

Photonic sensors, sensors based on light technology, have recently attracted much attention in industry and academia. They can offer high accuracy, low weight and the possibility of building an extensive sensor network. Photonic sensors can be employed in various situations and can be used in harsh environments where electronic sensors are not suitable [1]. *Sahota et al.* identify [2] two main types of photonic sensors: distributed sensors in which a certain quantity is continuously sensed along a fiber optic cable; and point sensors at which a quantity is sensed at the specific position where the sensor is located. As an example of the application of distributed sensors, *Schenanto et al.* [3] reviews OTDR and OFDR techniques for geo-hydrological applications. Attention is given in this thesis to point sensors such as on FBG (fiber Bragg gratings) and integrated sensors. The spectrum of the sensors is assumed to be finite and so that it can be multiplexed using wavelength division multiplexing techniques (WDM).

The fiber Bragg gratings (FBGs) have been first fabricated and characterized at the end of the 1970s [4]. As detailed in Section 1.2.2, it consists of a periodic modulation of the refractive index of the fiber's core, resulting in a dip into the transmission spectrum and a peak in the reflection spectrum. The reflection spectrum peak is modulated according to the applied strain or stress or any other signal to be sensed [2]. FBG sensors can be easily multiplexed in a large WDM network, forming quasi-distributed sensors. They are typically employed as strain and temperature sensors in different situations, such as structural health monitoring [5] and the oil industry [6]. Other examples of FBGs sensors application are in acoustic sensing [7, 8], shape sensing [9–11], pH-sensing [1], and for monitoring geohazards, landslides and Debris flows [12, 13].

The idea of fabricating optical components on chips date from the 1960s [14]. Integrated photonics allowed the development of a novel generation of sensors and interrogators. Examples of applications are gas sensing [15, 16], strain sensing [17, 18], biosensing [19–21]. In the health care field, possible applications are ultrasound intravascular imaging [22, 23] and photoacoustic imaging [24]. While most FOS are made of silica, integrated sensors can be manufactured using different waveguide materials. Silicon [25, 26], silicon nitride [27], and indium phosphide [14] are the most common materials used in photonic integrated circuits (PIC). The recent rise in work with PICs can be mainly explained by [14]: (a) the maturity of the fabrication process, both for CMOS platforms (silicon and silicon nitride) and InP; (b) the availability of building blocks, i.e. a list of integrated components usually provided by the foundry (or by a third party) which have been fabricated and tested multiple times and can be easily added to the design. Most foundries provide designs of input/output couplers, beam splitters, and if active components are available, photodetectors, modulators or light amplifiers (for III-V semiconductors); (c) the possibility of fabrication under the multi-project wafer (MPW) regime, in which multiple users share the same wafer, reducing the fabrication costs.

The field of Silicon photonics and silicon photonics sensors is currently under intensive research [28]. The material is transparent at 1550 nm, and PICs based on silicon-on-insulator (SOI) technology feature a high refractive index contrast between the waveguide core and cladding (it can be as high as 2). The larger the refractive index contrast is, the more the light is confined within the waveguide core, allowing an overall reduction of the footprint of the components. Therefore, many integrated sensors can be fabricated in a single die. In contrast, the design of thermally insensitive devices is challenging due to the large thermo-optical coefficients compared to other materials (silicon nitride, for instance). The drift of the sensor's resonance wavelength induced by temperature variations is typically compensated using another integrated temperature sensor as reference [29, 30]. Components such as modulators based on the drift and diffusion of free carriers or germanium photodetectors, which are useful for the design of interrogators, are available and can be integrated into a Si platform. Monolithic light sources in silicon (electrically pumped) is challenging due to silicon indirect bandgap, although much progress has been made in hybrid Si/III-V integrated circuits [31] and in silicon

Raman lasers [32].

One of the key properties of indium phosphide and other III-V semiconductors is its direct bandgap, allowing for the design of active components. High-quality semiconductor optical amplifiers, continuous [33, 34] and pulsed lasers [35, 36] have already been demonstrated in integrated InP chips. Compared to silicon, the footprints of the components are much larger due to a reduced contrast between the core and cladding materials[1]. Since fully passive sensors are often desirable, the platform faces strong competition from silicon and silicon nitride in the design of passive sensors. Nevertheless, InP is quite an attractive platform for the development of interrogators, as will be demonstrated in Chapters 4 and 5. In applications where active sensors are desirable, such as optical gyroscopes [37], InP is a promising platform.

Finally, silicon nitride features reduced thermo-optical coefficients compared to Silicon and InP, allowing for the design of nearly thermally insensitive sensors. The material is transparent from 400 nm – 3700 nm, making the platform flexible. Propagation losses in silicon nitride waveguides as low as 2.25 dB/cm (at $\lambda =$532 nm), 0.04 dB/cm (at $\lambda =$1550 nm), 0.16 dB/ cm (at $\lambda =$2630 nm) and 2.10 dB/cm (at $\lambda =$3700 nm) have been reported [38, 39]. In addition, the refractive index contrast is high compared to other platforms such as InP and silica, enabling the fabrication of devices with a reduced footprint. Although high-speed modulators[2] and photodetectors are not available in the silicon nitride platform (or its development is in an early stage), the material is compatible with the CMOS fabrication process. Thus, silicon nitride can to monolithically integrated with silicon platform [40, 41].

Integrated photonic technology provides large flexibility in designing photonic sensors based on different components. For instance, *Hallynck et. al.* [17] compare the performance of a ring resonator (RR) and Mach-Zehnder photonic sensors, *Rosenthal* [42] demonstrates an ultrasound sensor based on integrated Bragg gratings and *Tadayon* [43] shows the characterization of a polymer high-Q integrated Fabry-Perot cavity, which can be used as a sensor. This work focuses on RRs, especially in Chapter 3, where the interrogation of an ultrasound sensor based on an integrated silicon RR is demonstrated. Similarly to FBGs, the transmission spectrum of the RR is a peak (or a dip depending on the output port) whose resonance is modulated according to the intensity of the external signal.

1.2. Principle of photonic sensors based on ring resonators and on Fiber bragg gratings

Dutta et al [44] classified photonic sensors into three categories according to their external excitation signal type: (a) Physical sensors, which detect physical properties such as temperature, strain, ultrasound or acceleration, (b) chemical sensors,

---

[1]An InP deep etch waveguide fabricated in the COBRA/Smart Photonics foundry (see Fig. 4.1(c) in Chapter 4) features a high lateral refractive index contrast between InP core waveguide(3.367) and a polymer (1.5) and a low vertical refractive index contrast between the InP layers (3.367 and 3.17). As a result, a low loss 90° bend has a radius of about 100 μm, while in silicon, this radius is 5 μm, 20 times smaller.

[2]Thermal based modulators are available in silicon nitride.

which detect the concentration of chemical species or gases and (c) biosensors, used to determine concentrations of biological media such as bacteria, viruses or antibodies [19–21]. Photonic sensors act as modulators, in which the signal to be sensed is encoded in one of the fundamental properties of the input light signal, such as the amplitude, wavelength, phase or polarization phase. For the sensors of interest here, the signal to be sensed does not directly interact with the light signal[3] but with the waveguide materials instead. Fig. 1.1(a) shows a schematic of a situation where a section of a waveguide is exposed to an external signal which induces a modulation of the refractive index of the waveguide materials and of the length L. As shown in the following subsections, this yields a modulation of the resonance wavelengths for RR sensors and FBGs. For instance, *Zhang et al.* [46] reported an ultrasound sensor whose refractive index changes according to the intensity of an ultrasound wave. *Westerveld* and *Leinders* [18, 22] report a strain and ultrasound sensor in which the waveguide is elongated and the refractive index changes according to the pressure. [19, 20] reports several types of label-free biosensors whose waveguide refractive index changes according to the presence of relevant biochemical materials.

1.2.1. Ring Resonators

Ring resonators (RRs) are photonic components widely used as sensors. The structure of a RR is shown in Fig. 1.1: it consists of a waveguide loop connected to itself (usually in a ring shape) where light is coupled via evanescent fields. Fig. 1.1 shows two input ports of the ring (input port and add port, the second one is not used for sensor applications) and two output ports (pass port and drop port). The transmission spectrum of the ring resonator pass ports and drop ports [47] is given by:

$$T_{pass} = \frac{r^2 + r^2 a^2 - 2r^2 a cos\theta}{1 + r^4 a^2 - 2r^2 a cos\theta},$$
$$T_{drop} = \frac{a(1 - r^2)^2}{1 - 2r^2 a cos\theta + r^4 a^2}, \tag{1.1}$$

where r is the coupling coefficient from the waveguide to the ring, a is the single round-trip amplitude transmission and θ is the accumulated phase along the length L, given by:

$$\theta = \frac{2\pi}{\lambda} n_{eff} L, \tag{1.2}$$

where L is the ring length, n_{eff} the waveguide effective index and λ the optical wavelength. The resonance condition is defined as:

$$OP = n_{eff} L = m\lambda_r, \tag{1.3}$$

where OP is the optical path length within the ring, m is an integer and λ_r is the resonance wavelength. If the resonance condition is satisfied, i.e., the optical path

---

[3]In some sensors such as gas sensors [45] the sensing is based on light absorption. Thus, the signal to be sensed interacts directly with the light.

is an integer multiple of the wavelength, the optical field interferes constructively within the ring. Mathematically, this occurs when $\theta = m2\pi$, leading to $\cos(\theta) = 1$ in Eq. (1.1), which results in a peak at the drop port and a dip in the pass port as as shown in the Fig. 1.1(b). The RR spectrum features multiple resonances in the C-band.[4] As explained in Chapter 2, this is an issue when multiplexing an array of RR sensors in the wavelength domain. *Claes et al.* [48] solves this issue using another RR as an optical filter (See Section 2.1 for further details). The spectral distance between two dips (or two peaks) is defined by the free spectral range, given by:

$$P_{RR} = \frac{\lambda_r^2}{n_g L},$$ (1.4)

where λ_r is one of the resonances and n_g the effective group index of the waveguide of the ring. Eq. (1.4) implicitly assumes that the RR waveguides are monomode, which is the case of most RR sensors. A multimode waveguide would introduce undesirable extra resonances.

The external excitation signal x_{ext} (which could be pressure, temperature, the concentration of a chemical substance, or any other signal to be sensed) may change the ring length L or the refractive indices of the waveguide materials, causing the effective index to change. By deriving the resonance condition (Eq. (1.3)) with respect to the external excitation, we obtain[5]:

$$\Delta\lambda_r = \frac{1}{m}\left(L\frac{dn_{eff}}{dx_{ext}} + n_{eff}\frac{dL}{dx_{ext}}\right)\Delta x_{ext}.$$ (1.5)

For strain and ultrasound sensors, according to *Westerveld* [18], the two terms in Eq. (1.5) have opposite signs, but dL/dx_{ext} is dominant. The effective index can be written as:

$$n_{eff} = \sum_j \Gamma_j n_j,$$ (1.6)

where n_j is the refractive index of the ring j-th material and Γ_j is the confinement factor of light in the j-th material, defined as [49]:

$$\Gamma_j = \frac{\int\int_{\partial\Omega} \mathbf{E}(x,y)\cdot\mathbf{E}^*(x,y)dxdy}{\int_{-\infty}^{\infty}\int_{-\infty}^{\infty} \mathbf{E}(x,y)\cdot\mathbf{E}^*(x,y)dxdy},$$ (1.7)

where $\partial\Omega$ s the area of the waveguide cross-section occupied by the j-th material and $\mathbf{E}(x,y)$ is the electric field. Differentiating Eq. (1.6) with respect to the external signal, we obtain:

$$\frac{\partial n_{eff}}{\partial x_{ext}} = \sum_j \left(\frac{\partial\Gamma_j}{\partial x_{ext}}n_j + \Gamma_j\frac{\partial n_j}{\partial x_{ext}}\right)$$ (1.8)

---

[4]The optical conventional band (C-band) ranges from 1530 nm to 1565 nm and corresponds to the gain bandwidth of erbium-doped fiber amplifiers.
[5]In the following derivation, optical dispersion is neglected. For a complete analysis, see [18].

Placing Eq. (1.8) into Eq. (1.5):

$$\Delta\lambda = \frac{1}{m}\left[L\sum_j\left(\frac{\partial\Gamma_j}{\partial x_{ext}}n_j + \Gamma_j\frac{\partial n_j}{\partial x_{ext}}\right) + n_{eff}\frac{dL}{dx_{ext}}\right]\Delta x_{ext}. \tag{1.9}$$

For most chemical and biological sensors, the dL/dx_{ext} term is zero, and the resonance wavelength depends only on the variation of the refractive indices. Typically, the waveguide of the core material remains unchanged, while one of the cladding materials is designed to sense the specific biological or chemical component, as reported in [19, 20]. For strain, acoustic and acceleration sensors, all the terms of Eq. (1.9) are non-zero: the elasto-optical effect induces a modification of the refractive indices while the local strain changes the waveguide length and width. The change of the waveguide width alters the waveguide cross-section and induces changes in the confinement factor, according to the term see the term $d\Gamma/dx_{ext}$, as seen in Eq. (1.9).

1.2.2. Fiber Bragg gratings

Photonic sensors based on FBG components are widely used nowadays and have many applications in industry. The fabrication of the first gratings dates from the late 1970s [4], but a major improvement on the FBG fabrication process is achieved in the end of the 1980s. *Meltz et. al.* [50] reported in 1989 the fabrication of a grating within the fiber using the interference of a monochromatic UV light source. As a result, a periodic modulation of the refractive index of the fiber core was obtained. Here, the refractive index modulation is modelled as a single harmonic function:

$$\delta n(z) = \overline{\Delta n}\left[1 + (v_n/2)\cos\left(\frac{2\pi m}{\Lambda}z\right)\right], \tag{1.10}$$

where δn is the refractive index modulation, z is the coordinate corresponding to the light propagation direction, Λ is the grating period, $\overline{\Delta n}$ is the average refractive index within a grating period, v_n is the visibility of the refractive index modulation and m is the grating diffraction order (typically $m = 1$). The variation in the refractive index is in the order of 10^{-5} to 10^{-3} [51] and causes the input light signal to be continuously reflected along the grating. Thus, two optical beams propagate simultaneously through the FBG: a forward beam, which propagates in the direction of the input signal, and a backward beam, induced by the grating reflections. The fiber is assumed to be monomode. It can be shown using coupled-mode theory that the reflection spectrum for an uniform fiber Bragg grating is given by [52, 53]:

$$R_{FBG}(\lambda) = \frac{|\kappa|^2\sinh^2(\sqrt{|\kappa|^2 - \Delta(\lambda)^2}L)}{|\kappa|^2\cosh^2\left(\sqrt{|\kappa^2| - \Delta(\lambda)^2}\right) - \Delta(\lambda)^2}, \tag{1.11}$$

where

$$\Delta(\lambda) = \frac{2\pi}{\lambda}v_n\overline{\Delta n} + 2\pi n_{eff}\left(\frac{1}{\lambda_r} - \frac{1}{\lambda_B}\right), \tag{1.12}$$

n_{eff} is the effective index of the LP_{01} mode and κ is the coupling coefficient of the forward and backward propagating modes, defined by the overlapping integral:

$$\kappa = \omega n_{eff}\varepsilon_0 \int_{-\infty}^{\infty}\int_{-\infty}^{\infty} \frac{v_n\overline{\Delta n}}{2}\mathbf{E_{LP01}}(x,y)\mathbf{E_{LP01}}^*(x,y)dxdy, \qquad (1.13)$$

where ε_0 is the vacuum permittivity, ω the angular frequency, and $\mathbf{E_{LP01}}(x,y)$ is the normalized transversal component of the LP_{01}. The reflection spectrum $R_{FBG}(\lambda)$ has a peak lineshape as shown in Fig. 1.1(c). λ_r is defined as the wavelength at which the reflection spectrum has a maximum, which occurs for $\Delta = 0$ in Eq. (1.12):

$$\frac{2\pi}{\lambda_r}v_n\overline{\Delta n} + 2\pi n_{eff}\left(\frac{1}{\lambda_r} - \frac{1}{\lambda_B}\right) = 0. \qquad (1.14)$$

Isolating λ_r in Eq. (1.14), we obtain:

$$\lambda_r = \lambda_B\left(1 + \frac{v_n\overline{\Delta n}}{n_{eff}}\right), \qquad (1.15)$$

where $\lambda_B = 2\Lambda n_{eff}$ is the so-called Bragg wavelength[6] In contrast to RRs, FBGs have a single resonance in the whole optical C-band. They can be used as optical filters by extracting the wavelengths close to λ_r from the input spectrum. In contrast, FBGs can be used as sensors by modulating λ_r with an external signal x_{ext}. Repeating the steps performed for the RR, Eq. (1.15) is derived with respect to x_{ext}:

$$\Delta\lambda_r = \frac{\partial\lambda_r}{\partial x_{ext}}\Delta x_{ext} \cong \frac{\partial\lambda_B}{\partial x_{ext}}\Delta x_{ext}. \qquad (1.16)$$

By substituting in the definition of $\lambda_B = 2n_{eff}\Lambda$:

$$\Delta\lambda_r = 2\left[n_{eff}\frac{\partial\Lambda}{\partial x_{ext}} + \Lambda\frac{\partial n_{eff}}{\partial x_{ext}}\right]\Delta x_{ext}. \qquad (1.17)$$

The two terms in Eq. (1.17) have opposite signs, but $\frac{\partial\Lambda}{\partial x_{ext}}$ is dominant for strain sensors [51]. $\frac{\partial n_{eff}}{\partial x_{ext}}$ is dominant for temperature sensors [54] (the thermal expansion causes $\frac{\partial\Lambda}{\partial x_{ext}}$ to be different than zero).

1.3. Thesis outline

In this Chapter, thus far, the basic concepts of photonic sensing have been introduced. Photonic sensors work as modulators, which encode the external excitation into the light signal in the sensor. Interrogators, in contrast, work as demodulators and demultiplexers.

---

[6]SSome authors refer to the Bragg wavelength as the wavelength at which $R_{FBG}(\lambda)$ is maximum. Here, we keep the notation of [52], where $\lambda_B = 2\Lambda n_{eff}$. λ_r reduces to λ_B as $\overline{\Delta n}$ tends to zero.

1
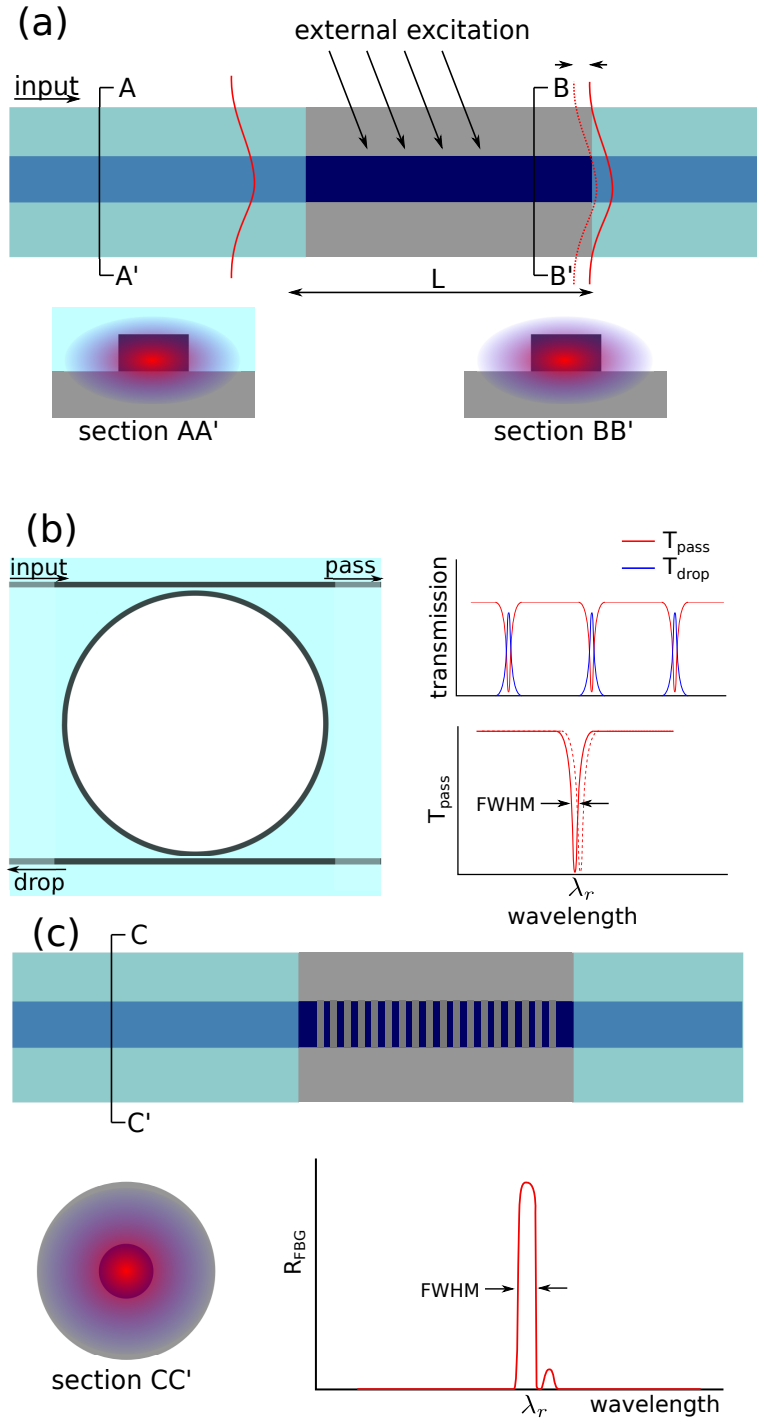
Figure 1.1: (a) Schematic of a waveguide section which is exposed to sense an external signal. (b) Schematic of a RR sensor. On the left, the input, the pass and the drop ports are shown. On the right, the typical spectra of the drop and pass ports are shown. (c) Schematic of an FBG sensor. The illustration on the top shows the cladding and the core of the fiber. The FBG refractive index modulation, which is also exposed to the external excitation, is also shown. On the lower left, the cross-section of the fiber is shown. On the lower right, typical reflection and transmission spectra are shown.

1

Chapter 2 provides an overview of the different interrogation techniques in the wavelength domain. The interrogation methods are classified into three main groups: induced power modulation and edge filter interrogators, interrogators based on spectrometers and interrogators based on interferometry. The basic operation principle for each case is presented. The different interrogators are compared based on five different parameters, all defined in Chapter 2: maximum interrogation resolution, sensitivity, dynamical range/ wavelength operation range, maximum speed, and flexibility. Special attention is given to interferometric techniques in order to introduce the concepts used in Chapters 3-5.

In Chapter 3, the interrogation of an ultrasound sensor based on a RR sensor using a Mach-Zehnder interferometer is detailed. The basic concepts of interferometric interrogation for a single sensor are introduced, and no demultiplexing is performed. In order to calibrate the interrogation method, an induced power modulation interrogator, described in Chapter 2, is used. The appendix of Chapter 3 provides the key ingredients and an inspiration for the Fourier transform interrogator.

In Chapter 4, the method presented in Chapter 3 is generalized, and a novel interrogation method is proposed based on an integrated Fourier transform spectrometer. It is demonstrated that the number of interferometers needed is only as many as the number of sensors, which results in a reduced footprint device. Although the spectrometer features a reduced spectral resolution (about 50 pm) compared to other integrated FT-spectrometers, signal excursions as small as 400 fm could be demodulated, two orders of magnitude lower than other integrated FT-spectrometers.

In Chapter 5, the non-linear equations proposed in Chapter 4 are solved using semi-analytical methods. Under the transformation $z_k = \exp\left[i(\Phi_k - \Phi_{ref})\right]$, where Φ_k is a phase which encodes the external signal detected by the k-th sensor and Φ_{ref} a constant, an algebraic system of polynomials have been obtained. To solve it, we compute the Gröbner basis of the polynomial ideal using a lexicographical order, resulting in an algebraic system which can be easily solved. However, the algebraic system features multiple solution sets per instant of time where, in general, only one of them gives the actual modulation provided by the external signal. The algebraic equations have been solved using a graphical processing unit, resulting in a processing time per equation of about 9 ns. This allows for real-time interrogation of high-speed sensors such as an array of ring based ultrasound sensors. A conclusion is presented in Chapter 6.

References

[1] H. Alemohammad, R. Liang, D. Yilman, A. Azhari, K. Mathers, C. Chang, B. Chan, and M. A. Pope, *Fiber optic sensors for harsh environments: Environmental, hydrogeological, and chemical sensing applications,* in *26th International Conference on Optical Fiber Sensors* (Optical Society of America, 2018) p. TuB4.

[2] J. K. Sahota, N. Gupta, and D. Dhawan, *Fiber Bragg grating sensors for mon-*

itoring of physical parameters: a comprehensive review, Optical Engineering **59**, 1 (2020).

[3] L. Schenato, *A review of distributed fibre optic sensors for geo-hydrological applications,* Applied Sciences **7** (2017), 10.3390/app7090896.

[4] K. O. Hill, Y. Fujii, D. C. Johnson, and B. S. Kawasaki, *Photosensitivity in optical fiber waveguides: Application to reflection filter fabrication,* Applied Physics Letters **32**, 647 (1978), https://doi.org/10.1063/1.89881 .

[5] X.-W. Ye, Y.-H. Su, and P.-S. Xi, *Statistical analysis of stress signals from bridge monitoring by fbg system,* Sensors **18**, 1 (2007).

[6] A. D. Kersey, *Optical fiber sensors for downwell monitoring applications in the oil and gas industry,* IEICE Transactions on Electronics , 400 (2000).

[7] A. Rosenthal, D. Razansky, and V. Ntziachristos, *High-sensitivity compact ultrasonic detector based on a pi-phase-shifted fiber bragg grating,* Opt. Lett. **36**, 1833 (2011).

[8] Q. Wu, Y. Okabe, and F. Yu, *Ultrasonic structural health monitoring using fiber bragg grating,* Sensors **18** (2018), 10.3390/s18103395.

[9] J. P. Moore and M. D. Rogge, *Shape sensing using multi-core fiber optic cable and parametric curve solutions,* Opt. Express **20**, 2967 (2012).

[10] M. Amanzadeh, S. M. Aminossadati, M. S. Kizil, and A. D. Rakić, *Recent developments in fibre optic shape sensing,* Measurement **128**, 119 (2018).

[11] X. Chen, X. Yi, J. Qian, Y. Zhang, L. Shen, and Y. Wei, *Updated shape sensing algorithm for space curves with fbg sensors,* Optics and Lasers in Engineering **129**, 106057 (2020).

[12] H.-H. Zhu, B. Shi, and C.-C. Zhang, *Fbg-based monitoring of geohazards: Current status and trends,* Sensors **17** (2017), 10.3390/s17030452.

[13] C.-J. Huang, C.-R. Chu, T.-M. Tien, H.-Y. Yin, and P.-S. Chen, *Calibration and deployment of a fiber-optic sensing system for monitoring debris flows,* Sensors **12**, 5835 (2012).

[14] M. Smit, X. Leijtens, H. Ambrosius, E. Bente, J. Tol, van der, E. Smalbrugge, T. Vries, de, E. Geluk, J. Bolk, P. Veldhoven, van, L. Augustin, P. Thijs, D. D'Agostino, H. Rabbani Haghighi, K. Lawniczuk, S. Stopinski, M. Tahvili, A. Corradi, E. Kleijn, D. Dzibrou, M. Felicetti, E. Bitincka, V. Moskalenko, J. Zhao, R. Lemos Alvares Dos Santos, G. Gilardi, W. Yao, K. Williams, R. Stabile, P. Kuindersma, J. Pello, S. Bhat, Y. Jiao, D. Heiss, G. Roelkens, M. Wale, P. Firth, F. Soares, N. Grote, M. Schell, H. Debregeas, M. Achouche, J.-L. Gentner, A. Bakker, T. Korthorst, D. Gallagher, A. Dabbs, A. Melloni, F. Morichetti, D. Melati, A. Wonfor, R. Penty, R. Broeke, B. Musk, and D. Robbins, *An introduction to inp-based generic integration technology,* Semiconductor Science and Technology **29**, 083001 (2014).

[15] N. A. Yebo, D. Taillaert, J. Roels, D. Lahem, M. Debliquy, D. Van Thourhout, and R. Baets, *Silicon-on-insulator (SOI) ring resonator-based integrated optical hydrogen sensor,* IEEE Photonics Technology Letters **21**, 960 (2009).

[16] N. A. Yebo, W. Bogaerts, Z. Hens, and R. Baets, *On-chip arrayed waveguide grating interrogated silicon-on-insulator microring resonator-based gas sensor,* IEEE Photonics Technology Letters **23**, 1505 (2011).

[17] E. Hallynck and P. Bienstman, *Integrated optical pressure sensors in silicon-on-insulator,* IEEE Photonics Journal **4**, 443 (2012).

[18] W. J. Westerveld, J. Pozo, P. J. Harmsma, R. Schmits, E. Tabak, T. C. van den Dool, S. M. Leinders, K. W. van Dongen, H. P. Urbach, and M. Yousefi, *Characterization of a photonic strain sensor in silicon-on-insulator technology,* Opt. Lett. **37**, 479 (2012).

[19] K. De Vos, J. Gironès Molera, S. Popelka, E. Schacht, R. Baets, and P. Bienstman, *Soi optical microring resonator with poly(ethylene glycol) polymer brush for label-free biosensor applications,* Biosensors & Bioelectronics **24**, 2528 (2009).

[20] K. de Vos, Girones, J. Girones, T. Claes, Y. D. Koninck, S. Popelka, E. Schacht, R. Baets, and P. Bienstman, *Multiplexed antibody detection with an array of silicon-on-insulator microring resonators,* IEEE Photonics Journal **1**, 225 (2009).

[21] G. G. Daaboul, C. A. Lopez, A. Yurt, S. Member, and B. B. Goldberg, *Label-Free Optical Biosensors for Virus Detection and Characterization,* IEEE Journal of selected topics in quantum electronics **18**, 1422 (2012).

[22] S. M. Leinders, W. J. Westerveld, J. Pozo, P. L. M. J. van Neer, B. Snyder, P. O'Brien, H. P. Urbach, N. de Jong, and M. D. Verweij, *A sensitive optical micro-machined ultrasound sensor (OMUS) based on a silicon photonic ring resonator on an acoustical membrane.* Scientific reports **5**, 14328 (2015).

[23] F. G. Peternella, B. Ouyang, R. Horsten, M. Haverdings, P. Kat, and J. Caro, *Interrogation of a ring-resonator ultrasound sensor using a fiber mach-zehnder interferometer,* Opt. Express **25**, 31622 (2017).

[24] B.-Y. Hsieh, S.-L. Chen, T. Ling, L. J. Guo, and P.-C. Li, *Integrated intravascular ultrasound and photoacoustic imaging scan head,* Opt. Lett. **35**, 2892 (2010).

[25] M. Hochberg and T. Baehr-Jones, *Towards fabless silicon photonics,* Nature Photonics **4**, 492 (2010).

[26] T. Baehr-Jones, T. Pinguet, P. Lo Guo-Qiang, S. Danziger, D. Prather, and M. Hochberg, *Myths and rumours of silicon photonics,* Nature Photonics **6**, 206 (2012).

1

1

[27] C. G. H. Roeloffzen, M. Hoekman, E. J. Klein, L. S. Wevers, R. B. Timens, D. Marchenko, D. Geskus, R. Dekker, A. Alippi, R. Grootjans, A. van Rees, R. M. Oldenbeuving, J. P. Epping, R. G. Heideman, K. Wörhoff, A. Leinse, D. Geuze-broek, E. Schreuder, P. W. L. van Dijk, I. Visscher, C. Taddei, Y. Fan, C. Tabal-lione, Y. Liu, D. Marpaung, L. Zhuang, M. Benelajla, and K.-J. Boller, *Low-loss si3n4 triplex optical waveguides: Technology and applications overview,* IEEE Journal of Selected Topics in Quantum Electronics **24**, 4400321 (2018).

[28] A. Rahim, T. Spuesens, R. Baets, and W. Bogaerts, *Open-access silicon pho-tonics: Current status and emerging initiatives,* Proceedings of the IEEE **106**, 2313 (2018).

[29] S. Abdulla, B. de Boer, J. Pozo, J. van den Berg, A. Abutan, R. Hagen, D. L. Cascio, and P. J. Harmsma, *Sensing platform based on micro-ring resonator and on-chip reference sensors in SOI,* Proceedings of SPIE **8990**, 89900W (2014).

[30] A. L. Moras, V. Silva, M. C. M. M. Souza, G. A. Cirino, A. A. G. Von Zuben, L. A. M. Barea, and N. C. Frateschi, *Integrated photonic platform for robust differential refractive index sensor,* IEEE Photonics Journal **12**, 1 (2020).

[31] T. Komljenovic, M. Davenport, J. Hulme, A. Y. Liu, C. T. Santis, A. Spott, S. Srinivasan, E. J. Stanton, C. Zhang, and J. E. Bowers, *Heterogeneous silicon photonic integrated circuits,* Journal of Lightwave Technology **34**, 20 (2016).

[32] M. A. Ferrara and L. Sirleto, *Integrated raman laser: A review of the last two decades,* Micromachines **11** (2020), 10.3390/mi11030330.

[33] S. Latkowski, A. Hänsel, N. Bhattacharya, T. De Vries, L. Augustin, K. Williams, M. Smit, and E. Bente, *Novel Widely Tunable Monolithically Integrated Laser Source,* IEEE Photonics Journal **7** (2015), 10.1109/JPHOT.2015.2493722.

[34] S. Latkowski, A. Hansel, D. D'Agostino, P. J. Van Veldhoven, H. Rabbani-Haghighi, B. Docter, N. Bhattacharya, P. J. A. Thijs, H. P. M. M. Ambrosius, M. K. Smit, K. A. Williams, and E. A. J. M. Bente, *Long wavelength mono-lithic photonic integration technology for gas sensing applications,* Interna-tional Conference on Transparent Optical Networks **2016-Augus**, 2 (2016).

[35] M.-C. Lo, R. Guzmán, and G. Carpintero, *Femtosecond pulse and terahertz two-tone generation from facet-free multi-segment laser diode in InP-based generic foundry platform,* Optics Express **26**, 18386 (2018).

[36] E. Bente, S. Tahvili, V. Moskalenko, S. Latkowski, M. Wale, J. Javaloyes, P. Landais, and M. Smit, *Integrated InP based modelocked lasers and pulse shapers,* Integrated Optics: Devices, Materials, and Technologies XVII **8627**, 86270E (2013).

[37] C. Ciminelli, D. D'Agostino, G. Carnicella, F. Dell'Olio, D. Conteduca, H. P. M. M. Ambrosius, M. K. Smit, and M. N. Armenise, *A high-Q InP resonant angular velocity sensor for a monolithically integrated optical gyroscope,* IEEE Photonics Journal **8** (2016).

[38] P. Muñoz, G. Micó, L. A. Bru, D. Pastor, D. Pérez, J. D. Doménech, J. Fernández, R. Baños, B. Gargallo, R. Alemany, A. M. Sánchez, J. M. Cirera, R. Mas, and C. Domínguez, *Silicon nitride photonic integration platforms for visible, near-infrared and mid-infrared applications,* Sensors **17** (2017), 10.3390/s17092088.

[39] A. T. Mashayekh, T. Klos, D. Geuzebroek, E. Klein, T. Veenstra, M. Büscher, F. Merget, P. Leisching, and J. Witzens, *Silicon nitride pic-based multi-color laser engines for life science applications,* Opt. Express **29**, 8635 (2021).

[40] P. Dong, X. Liu, S. Chandrasekhar, L. L. Buhl, R. Aroca, and Y.-K. Chen, *Monolithic silicon photonic integrated circuits for compact 100 gb/s coherent optical receivers and transmitters,* IEEE Journal of Selected Topics in Quantum Electronics **20**, 150 (2014).

[41] J. K. S. Poon and W. D. Sacher, *Multilayer silicon nitride-on-silicon photonic platforms for three-dimensional integrated photonic devices and circuits,* in *2017 75th Annual Device Research Conference (DRC)* (2017) pp. 1–2.

[42] A. Rosenthal, M. Omar, H. Estrada, S. Kellnberger, D. Razansky, and V. Ntziachristos, *Embedded ultrasound sensor in a silicon-on-insulator photonic platform,* Applied Physics Letters **104**, 021116 (2014), publisher: American Institute of Physics.

[43] M. A. Tadayon, M.-E. Baylor, and S. Ashkenazi, *High quality factor polymeric fabry-perot resonators utilizing a polymer waveguide,* Opt. Express **22**, 5904 (2014).

[44] A. Dutta, *Brief review on integrated planar waveguide-based optical sensor,* in *Planar Waveguide Optical Sensors From Theory to Applications* (Springer, Cham, 2016) Chap. 2, pp. 9–69.

[45] M. A. Butt, S. A. Degtyarev, S. N. Khonina, and N. L. Kazanskiy, *An evanescent field absorption gas sensor at mid-ir 3.39 μm wavelength,* Journal of Modern Optics **64**, 1892 (2017).

[46] C. Zhang, S.-L. Chen, T. Ling, and L. J. Guo, *Imprinted polymer microrings as high-performance ultrasound detectors in photoacoustic imaging,* J. Lightwave Technol. **33**, 4318 (2015).

[47] W. Bogaerts, P. DeHeyn, T. V. Vaerenbergh, K. D. Vos, S. K. Selvaraja, T. Claes, P. Dumon, P. Bienstman, D. V. Thourhout, and R. Baets, *Silicon microring resonators,* Laser and Photonics Reviews **6**, 47 (2012), arXiv:1208.0765v1 .

1

1

[48] T. Claes, W. Bogaerts, and P. Bienstman, *Vernier-cascade label-free biosensor with integrated arrayed waveguide grating for wavelength interrogation with low-cost broadband source,* Opt. Lett. **36**, 3320 (2011).

[49] A. Yariv and P. Yeh, *Photonics: Optical Electronics in Modern Communications*, 6th ed. (Oxford University Press, 2007).

[50] G. Meltz, W. W. Morey, and W. H. Glenn, *Formation of bragg gratings in optical fibers by a transverse holographic method,* Opt. Lett. **14**, 823 (1989).

[51] D. Krohn, T. MacDougall, and A. Mendez, *Fiber optics sensors fundamentals and applications*, 4th ed. (SPIE Press, 2014).

[52] R. Kashyap, *Fiber Bragg gratings*, 2nd ed. (Academic Press, 2010).

[53] T. Erdogan, *Fiber grating spectra,* Journal of Lightwave Technology **15**, 1277 (1997).

[54] A. D. Kersey, *A review of recent developments in fiber optic sensor technology,* Optical Fiber Technology **2**, 291 (1996).

2

Review of the most common methods for interrogating photonic sensors

In this Chapter, a brief review of the different interrogation techniques is presented. The spectra of the sensors are assumed to be finite, typically with a peak lineshape, so that the photonic sensors can be multiplexed in the wavelength domain. The interrogation methods are classified here into three main groups: induced power modulation and edge filter interrogators, interrogators based on spectrometers and interrogators based on interferometry. Despite the simplicity of induced power modulation and edge filter interrogators, they usually feature a limited dynamic range. Moreover, these interrogators may introduce distortions in the interrogated signal due to non-linear components. Spectrometer based interrogators feature a high interrogation resolution, are pretty flexible but usually limited to reduced speeds. Finally, interferometric interrogators feature high-resolution and can be used to demodulate high-speed sensors. As explained along with this Chapter, the performance of interrogators based on interferometry can be strongly affected by variations of resonance wavelength of the sensors introduced by the fabrication process.

2.1. Review introduction

One of the key benefits of sensors based on photonic technology is the possibility of multiplexing them and building a large sensor network. Many applications require an extensive array of sensors. For instance, for structure-health monitoring applications, which aim to evaluate the degradation of structures such as buildings or bridges, *Xiao Wei et al.*[1] and *Dai et al.* [2] perform the interrogation of 64 and 100 FBG sensors. Larger sensor networks are presented by *Hu et. al* [3] and *Wang*

et. al[4], who report the interrogation of 843 and 1000 FBG sensors. There are different techniques described in the literature to multiplex photonic sensors, and the most common approaches are time-division and wavelength division multiplexing. Refs. [5–7] demonstrated that a combination of these techniques could be used in order to accommodate more sensors in the network.

Fig. 2.1 shows three schemes for interrogating FBG and ring resonator sensors using Wavelength Division Multiplexing (WDM) [5, 8]. The optical source used to illuminate the photonic sensors is typically broadband, but tunable coherent sources can also be used (see Section 2.4.2). The key idea of WDM is to keep the resonance wavelengths of the photonic sensors sufficiently separated so that their combined output spectra do not overlap, as shown in Fig. 2.1 (d). As discussed along with the Chapter, the different interrogators provide a different tolerance to how close the resonance wavelengths can be to each other. A typical scheme for interrogating FBG sensors is shown in Fig. 2.1 (a) [5, 8–10]: the light signal from the source is conveyed, using a circulator, to the FBGs, and their reflection is sent to the interrogator. For ring resonators, the input optical signal is sent to the ring input port, and the signal from the ring pass port (see Fig. 2.1 (b)) [11–13] or by the drop port [14] is collected and conveyed to the interrogator (see Fig. 2.1 (c)). RRs have a finite spectrum, and multiple resonances may occur within the C-band. In Chapter 3, an FBG is employed as an optical filter to select the spectrum from a single resonance. Fig. 2.1(d) shows an example of the combined spectrum $S(\lambda, t)$ for K photonic sensors, which can be written as:

$$S(\lambda, t) = \sum_{k}^{K} s_k(\lambda - \lambda_{r,k}(t)), \tag{2.1}$$

where K is the number of sensors and $s_k(\lambda)$ is the lineshape of the output spectrum [1] of the k-th photonic sensor centred at the resonance wavelength $\lambda_{r,k}(t)$. The resonance wavelength of the sensor is modulated according to the intensity of the external signal to be sensed. $S(\lambda, t)$ is conveyed to the interrogator, which determines the resonances $\lambda_{r,k}(t)$ as a function of time.

A schematic of time-division multiplexing (TDM) is shown in Fig. 2.2. Instead of illuminating the photonic sensors with a continuous light signal, optical pulses are sent to a photonic sensor array, which are typically FBGs. The source can be either coherent [4, 5, 7, 8] or broadband [2, 15, 16]. In order to generate the pulses, an optical intensity modulator (OIM) is coupled to the output of the optical source. The OIM works as an optical switch that blocks or allows the transmission of the optical signal depending on an external voltage applied to it. The OIM is kept in its off state most of the time, except for a short period when it allows the transmission of the light signal, producing a pulse. The fiber couplers, shown in Fig. 2.2, split the input pulse into K pulses, which are subsequently sent to the K photonic sensors. The resonance wavelengths of the photonic sensors (without the excitation of an external signal) are typically the same unless the sensor network

---

[1]For FBGs, the output spectrum refers to the reflected spectrum. The output spectrum for arrays of ring resonator sensors may refer to the drop or the through port, according to the ring array design.
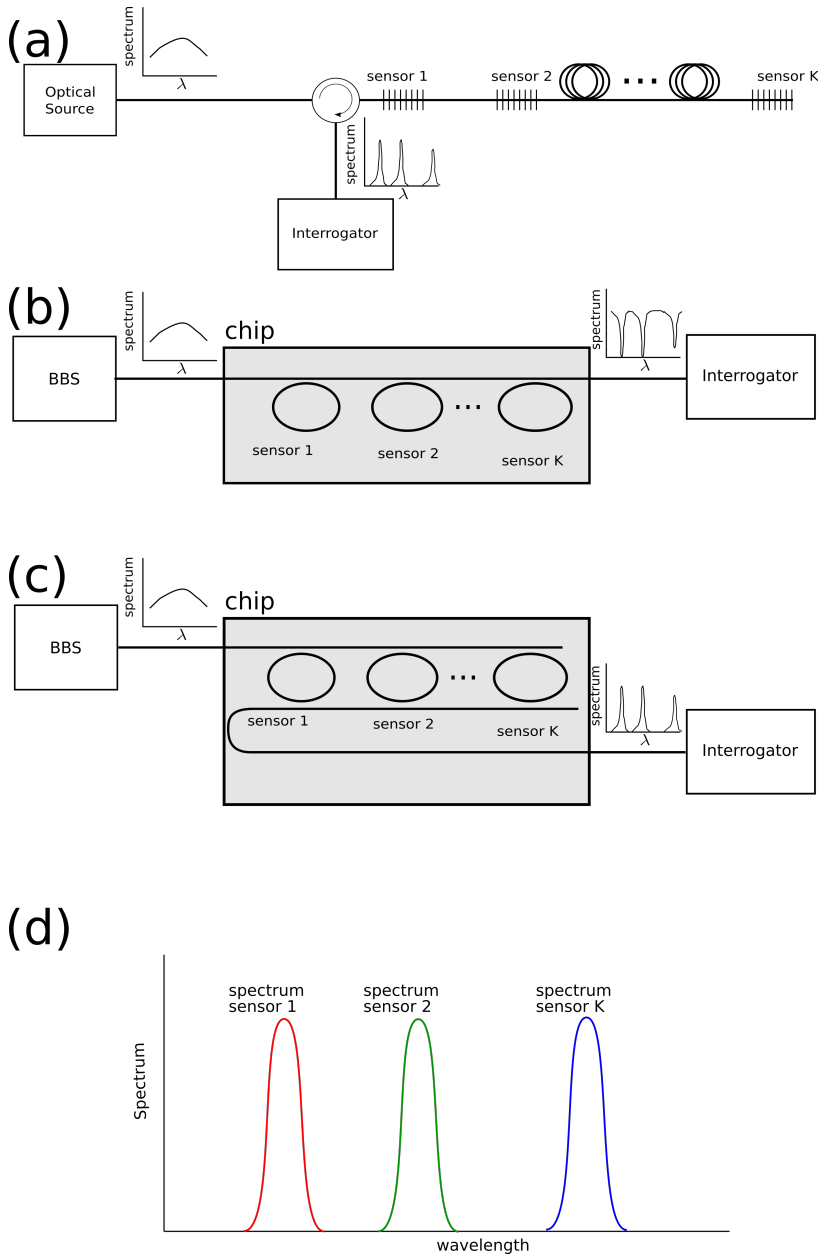
Figure 2.1: Schematic of the wavelength division multiplexing (WDM). The spectrum of each sensor must be limited so that resonances can be accommodated in the wavelength domain without overlap. Different interrogators have different tolerances about how distant the resonances must be kept apart. (a) Interrogation of an FBG array. (b) Interrogation of an array of ring resonators, connected via the through port. In this case, the combined spectrum is an array of dips, as explained in Chapter 1. (c) Interrogation of an array of ring resonators connected via the pass port. The combined spectrum is an array of peaks. (d) Example of the combined spectrum of the sensors.

2
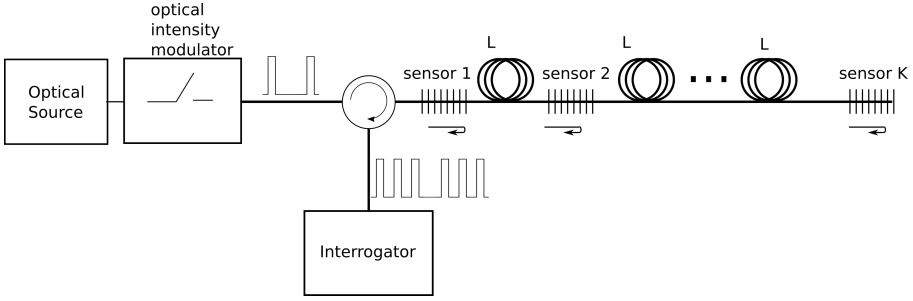
Figure 2.2: Schematic of the time-division multiplexing of the photonic sensors. A pulse coming from the optical source is divided in K pulses using the fiber couplers. The fiber lengths L_k ($k = 1, ..., K$), through which the K pulses travels, must be sufficiently large so that the recombined optical signal does not overlap in the time domain.

is designed in such a way as to combine TDM and WDM methods [6, 7]. The k-th photonic sensor encodes the information of the external signal into the k-th part of the original pulse. The output pulses from the photonic sensors are then conveyed to the interrogator.

For TDM to work correctly, the duration of the pulses must be sufficiently short, and the distance L_k (shown in Fig. 2.2), through which the light pulse travels, is sufficiently large. L_k amounts about a few meters, while the pulse durations are of the order of ns [2, 4, 16]. Thus, the optical pulses travelling back from the photonic sensors can be recombined without overlap, allowing the interrogator to perform the demultiplexing properly. Moreover, ultra-low reflectivities (-35 dB in [3] and -40 dB in [4]) have been reported, reducing multiple reflections in between the FBGs and the cross-talk among the sensors.

In this Chapter, a review of the different interrogation techniques is presented. Although the sensors are assumed to be multiplexed in the WDM scheme, the interrogators presented in Chapters 3, 4 and 5 can be operated using the TDM approach. The choice of the proper interrogation method depends on the properties of the photonic sensors: as discussed in the following sections, sensor speed, dynamic range and sensitivity strongly depend on the interrogation method.

2.2. Criteria of analysis of WDM photonic interrogators

As discussed in Chapter 1, the goal of the interrogator is to determine the resonance wavelength of the photonic sensors as a function of time. The interrogation methods were classified into three main groups: induced power modulation and edge filter interrogators, interrogators based on spectrometers and interrogators based on interferometry. In order to better compare the different interrogation methods, the following parameters are introduced [17]:

- **Interrogator resolution**. Let $s_k(\lambda)$ be defined as the lineshape of the output spectrum of k-th photonic sensor. The external excitation sensed causes

the $s_k(\lambda)$ to be shifted to $s_k(\lambda + \Delta\lambda)$, where $\Delta\lambda$ is the resonance wavelength shift. The resolution is the minimum value of $\Delta\lambda$ which the interrogator can resolve.

2

- **Interrogator sensitivity.**[2] Defined by the derivative $\partial y/\partial x_{ext}$, where y is one of the interrogator output parameters. For edge and induced power modulation interrogators, y is the interrogator output voltage. For interferometric sensors, the signal is encoded in a phase $\Phi(t)$ of the complex voltage: $\hat{V} \sim \exp(i\Phi(t))$; thus $y = \Phi(t)$ and the sensitivity is given by $\partial\Phi/\partial x_{ext}$ (see Section 2.5 for details). For interrogators based on spectrometers, this parameter is defined according to the post-processing algorithm used (see Sections 2.4).

- **Interrogator Dynamic range.** The range of values that the interrogator can resolve. For temperature sensors, the dynamic range is defined by the minimum and maximum temperature, which the interrogator can evaluate. The sensor properties typically determine the dynamic range. However, since interrogators may limit the dynamic sensor range, it is worth defining an overall dynamic range for sensors and interrogators. [3]

- **Wavelength operation range.** The range of resonance wavelength values which the interrogator can retrieve for each sensor. Since the resonance wavelength is assumed to be linearly related to the external excitation, the dynamic range is defined by the sensor sensitivity and the wavelength operation range. [4]

- **Interrogator response time and speed.** It is defined as the response time from which the interrogator takes to react from the external excitation. Specifically, [17] defines this parameter as the time taken by interrogator output to reach a certain level of the stable value (95 %, for instance) when exposed to the signal to be sensed. A high-speed interrogator features a short response time.

- **Flexibility.** The interrogator tolerance concerning variations in the sensor parameter. In some cases, the interrogators expect the resonance wavelengths and the FWHM of the sensor to operate around certain pre-established values. It describes how the interrogator may handle variations in the sensor parameters.

---

[2]Sensor sensitivity is a different parameter. For photonic sensors such as rings and FBGs, the sensitivity is defined as $\partial\lambda_r/\partial x_{ext}$, where λ_r is the resonance wavelength shift.
[3]Some authors [18] define the dynamic range as the ratio of the maximum and minimum value that can be resolved. Here, we use the definition presented by [17].
[4]Some authors (See Fig. 4 of [19]) use this parameter as wavelength dynamic range. Here, dynamic range refers to the range of values the signal to be sensed, according to to [17] .

2

2.3. Induced power modulation and edge filter interrogators

The principle of interrogators based on induced power modulation and edge filter interrogators is to convert the modulation of the resonance wavelength into optical intensity modulation. The voltage obtained by the photoreceivers [5] is assumed to be linear related or can be linearized to the resonance wavelength of the sensors. Fig. 2.3 shows on the top an interrogator based on laser-induced power modulation, while on the bottom, an interrogator based on edge filtering. Induced power modulation and edge filter interrogators do not provide any mechanism to demultiplex photonic sensors. Thus, a WDM filter or a dispersive spectrometer (see Section 2.4) should be used in combination with the interrogators for this purpose.

2.3.1. Interrogation based on laser-induced power modulation

Fig. 2.3(a) shows a schematic of an interrogator based on laser-induced power modulation, in which a tunable laser is used as the optical source. The method is used by Refs [11, 12, 20–22] and also here in Chapter 3 [23]. The laser wavelength is set at the flank of the photonic sensor spectrum, where the sensor lineshape is typically linear. As an external signal modulates the resonance wavelength of the photonic sensor, a power modulation is imprinted onto the light signal as indicated in the scheme of Fig. 2.3(a). The output optical signal is sent to a photoreceiver. The photoreceiver output voltage $v_{PD}(t)$ is given by:

$$v_{PD}(t) = g_{TIA} R_{ph} P_0 s \left(\lambda_0 + \Delta\lambda(t) \right), \tag{2.2}$$

where g_{TIA} is the photoreceiver transimpedance gain, R_{ph} is the photodetector responsivity, P_0 the laser power, λ_0 the laser wavelength and $s(\lambda)$ the spectrum of the sensor. The external signal to be sensed induces the spectrum $s(\lambda)$ to be shifted to $s(\lambda + \Delta\lambda(t))$, where $\Delta\lambda(t)$ is the resonance wavelength modulation. By expanding the function $s(\lambda + \Delta\lambda(t))$ in a Taylor series around $\lambda = \lambda_0$, Eq. (2.2) can be rewritten as:

$$v_{PD}(t) = g_{TIA} R_{ph} P_0 \left[s(\lambda_0) + \Delta\lambda(t) \left. \frac{\partial s(\lambda)}{\partial \lambda} \right|_{\lambda=\lambda_0} + O(\Delta\lambda(t)^2) \right], \tag{2.3}$$

By rearranging Eq. (2.3), we obtain:

$$\Delta v_{PD}(t) \equiv v_{PD}(t) - g_{TIA} R_{ph} P_0 s(\lambda_0) = \Delta\lambda(t) g_{TIA} R_{ph} P_0 \left. \frac{\partial s(\lambda)}{\partial \lambda} \right|_{\lambda=\lambda_0}. \tag{2.4}$$

Thus, the resonance wavelength modulation is proportional to the modulation of the detected voltage $\Delta v_{PD}(t)$. Eq. (2.4) can be simplified by differentiating both sides of Eq. (2.2) with respect to the laser wavelength, in absence of an external excitation ($\Delta\lambda = 0$):

$$\frac{\partial v_{PD}(\lambda)}{\partial \lambda} = g_{TIA} R_{ph} P_0 \frac{\partial s(\lambda)}{\partial \lambda}, \tag{2.5}$$

---

[5]A transimpedance amplifier(TIA) is usually connected to the output of the photodetectors. Here, the photoreceiver is the set photodector+TIA.

Linear interrogators

(a)

| Laser | Photonic Sensor | Photo-detector |

(b)

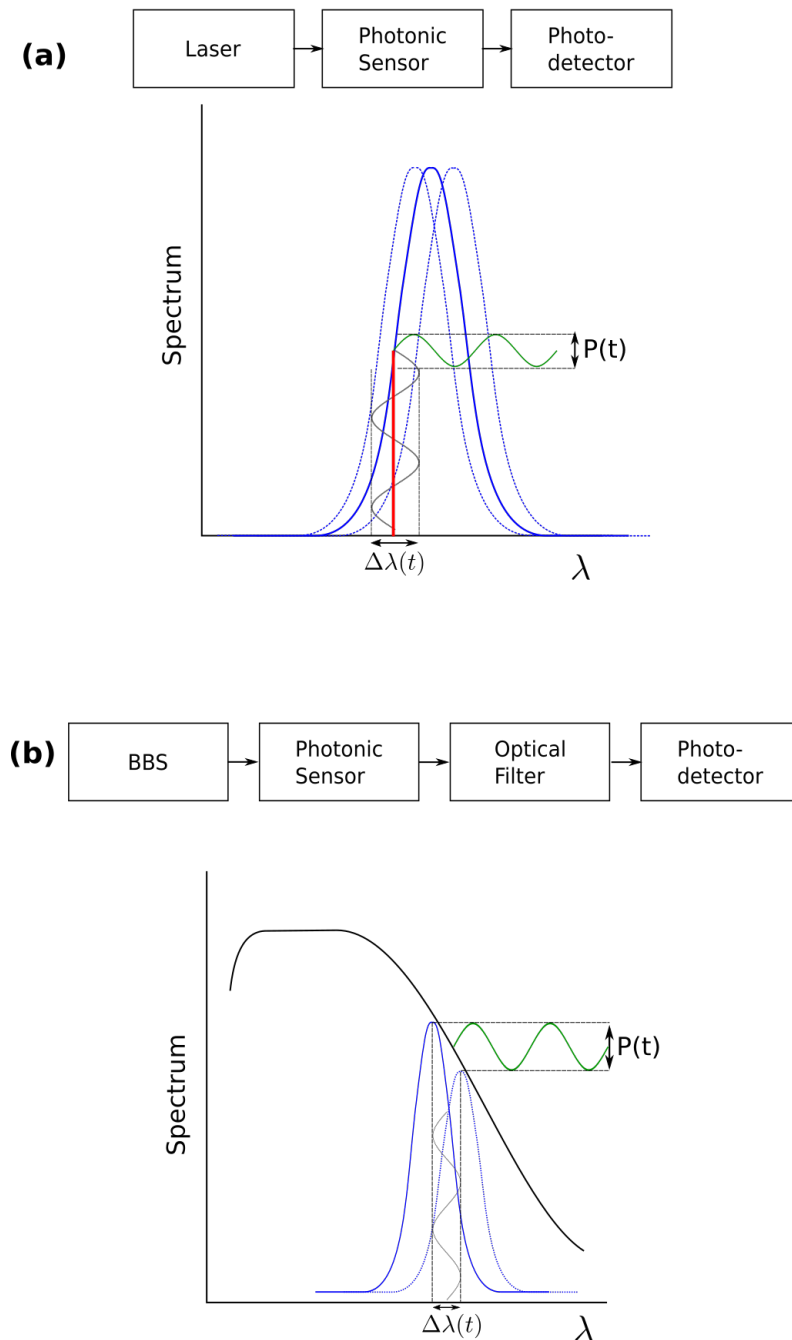| BBS | Photonic Sensor | Optical Filter | Photo-detector |

Figure 2.3: (a) An interrogator based on induced power modulation (b) An interrogator based on edge filtering. In both cases, the spectral power density of the photonic sensor is graphed, and how the resonance wavelength modulation induces an optical power modulation in the output signal is indicated.

where we assumed that $\frac{\partial s(\lambda)}{\partial \lambda} = \frac{\partial s(\lambda + \Delta\lambda(t))}{\partial \lambda}$ around λ_0. The function $v_{PD}(\lambda)$ can be easily obtained by sweeping the laser wavelength along the spectrum of the photonic sensor and by recording the photoreceiver output. Substituting Eq. (2.5)(for $\lambda = \lambda_0$) into Eq. (2.4):

$$\Delta v_{PD}(t) = \frac{\Delta\lambda(t)}{\left.\frac{\partial v(\lambda)}{\partial \lambda}\right|_{\lambda = \lambda_0}}. \tag{2.6}$$

Eq. (2.6) does not depend on the photoreceiver parameters g_{TIA} and R_{ph} or on the applied laser power.

The main advantage of the technique is its simplicity since it only requires a photodetector and a tunable laser. As long as the laser power is sufficiently high, a high interrogation resolution can be achieved. Since the interrogator speed is limited only by the speed of the electronics, high-speed photonic sensors can be demodulated using this technique, such as ultrasound sensors [11, 12, 21, 22]. On the other hand, the main disadvantage of this method is that the technique limits the dynamic range of the sensor. As the modulation of the resonance wavelength increases, the relation between Δv_{PD} and $\Delta\lambda_r(t)$ becomes non-linear, and the non-linear terms can be compensated only up to a certain extent.

2.3.2. Interrogation based on edge filtering

Examples of edge-filter interrogators are provided by [19, 24–28]. A schematic of the edge filtering method is shown in Fig. 2.3(b). Instead of using a monochromatic light source as in the previous case, this method employs a broadband source. The output spectrum of the photonic sensor is sent to an optical filter whose transfer function is linear and known around the region of interest, as shown in the schematic of Fig. 2.3(b). The voltage measured at the photoreceiver is given by:

$$v_{PD}(t) = g_{TIA}R_{ph}\int_0^\infty E_f(\lambda)s(\lambda + \Delta\lambda(t))d\lambda, \tag{2.7}$$

where $E_f(\lambda)$ is the spectrum of the edge filter. Expanding $E_f(\lambda)$ in a Taylor series up to the first order around the resonance wavelength of the sensor λ_r when no excitation is applied gives:

$$v_{PD}(t) = g_{TIA}R_{ph}\int_0^\infty \left[E_f(\lambda_r) + (\lambda - \lambda_r)\left.\frac{\partial E_f(\lambda)}{\partial \lambda}\right|_{\lambda = \lambda_r}\right]s(\lambda + \Delta\lambda)d\lambda. \tag{2.8}$$

By changing the integration variable $\lambda \to u = \lambda + \Delta\lambda$ and rearranging the terms, we obtain:

$$v_{PD}(t) = g_{TIA}R_{ph}\int_0^\infty \left[E_f(\lambda_r) + (u - \lambda_r - \Delta\lambda(t))\left.\frac{\partial E_f(\lambda)}{\partial \lambda}\right|_{\lambda = \lambda_r}\right]s(u)du. \tag{2.9}$$

Eq. (2.9) can be rewritten as:

$$v_{PD}(t) = A\Delta\lambda(t) + B \tag{2.10}$$

where:

$$A = -g_{TIA}R_{ph} \left.\frac{\partial E_f(\lambda)}{\partial \lambda}\right|_{\lambda=\lambda_r} \int_0^\infty s(u)du$$

$$B = g_{TIA}R_{ph} \int_0^\infty \left(E_f(\lambda_r) + (u-\lambda_r)\left.\frac{\partial E_f(\lambda)}{\partial \lambda}\right|_{\lambda=\lambda_r}\right) s(u)du$$

$$= g_{TIA}R_{ph} \left(E_f(\lambda_r) - \lambda_r \left.\frac{\partial E_f(\lambda)}{\partial \lambda}\right|_{\lambda=\lambda_r}\right) \int_0^\infty s(u)du +$$

$$+ g_{TIA}R_{ph} \left.\frac{\partial E_f(\lambda)}{\partial \lambda}\right|_{\lambda=\lambda_r} \int_0^\infty us(u)du. \tag{2.11}$$

The voltage modulation $\Delta v(t) \cong v_{PD}(t) - B$ is proportional to the resonance wavelength modulation, and the coefficients A and B can be experimentally determined [24, 27].

Authors report edge filtering technique as an inexpensive interrogation method [25, 28]. *Tiwari et al.* [26] used an erbium-doped fiber as the edge filter; *Aulakh et al.* uses another FBG [28], while *Diaz et al.* [25] uses the linear region of a Fabry-Perot interferometer produced by a catastrophic fuse effect. The demultiplexing can be performed using WDM filters [19, 24] or the TDM method [16]. The dynamic range and the sensitivity strongly depend on the properties of the edge filter. A highly sensitive interrogator, i.e., with a large value of $|A|$, compromises the wavelength operation range. This can be observed in Fig. 2.3(b): the higher the slope $|A|$ is, the more voltage $v_{PD}(t)$ is attenuated as the resonance wavelength shifts towards to $+\infty$.

2.4. Interrogators based on spectrometers

2.4.1. Interrogators based on dispersive spectrometers

Despite their simplicity, interrogators based on induced power modulation and edge filter interrogators can impose strong limitations on the dynamic range of the sensor. A schematic of interrogators based on spectrometers is shown in Fig. 2.4(a): a broadband light source is used to illuminate an array of photonic sensors, and their combined spectrum is sent to a spectrometer. In this section, we focus on dispersive spectrometers, i.e., spectrometers which detect the spectrum using dispersive optical components such as gratings and prisms [29] (interrogators based on Fourier transform spectrometers are discussed in the next section). *Guo et. al.* [30] demonstrated a spectrometer using an integrated echelle, while others [31–33] employed integrated arrayed waveguide gratings. Interrogacation can be performed using commercial spectrometers [34–36]. For instance, the commercial spectrometer *IBSEN I MON 512 HS* [37] gives an operation range of 90 nm, while the spectral resolution is about 170 pm.

Xiau et al.[33] modelled the lineshape of the AWG channels as a gaussian func-

tion, given by:

$$T_{ch,m}(\lambda) = \exp\left[-4\log(2)\frac{(\lambda - \lambda_{ch,m})^2}{w_{ch,m}^2}\right], \tag{2.12}$$

where $T_{ch,m}(\lambda)$ is the transmission function of the m-th spectrometer channel, $\lambda_{ch,m}$, is its central wavelength and $w_{ch,m}$, its FWHM. Thus, the output voltage obtained by the k-th photodetector, connected to the k-th spectrometer output is given by:

$$v_{ch,m}(t) = g_{TIA}R_{ph}\int_0^\infty S(\lambda, t)\exp\left[-4\log(2)\frac{(\lambda - \lambda_{ch,m})^2}{w_{ch,m}^2}\right]d\lambda \tag{2.13}$$

Assuming that the FWHM of the spectrometer channels is much smaller than the FWHM of the photonic sensors, $T_{ch,m}(\lambda)$ can be approximated to a Dirac delta, and Eq. (2.13) can be written as:

$$v_{ch,m}(t) = g_{TIA}R_{ph}\int_0^\infty S(\lambda, t)\delta(\lambda - \lambda_{ch,m})d\lambda = g_{TIA}R_{ph}S(\lambda_{ch,m}, t), \tag{2.14}$$

where $\delta(\lambda)$ is the Dirac delta function. Thus, the set of voltages $\{v_{ch,1}, v_{ch,2}, ..., v_{ch,M}\}$ is proportional to $S(\lambda_{ch,m}, t)$ sampled at the points $\lambda_{ch,1}, ..., \lambda_{ch,M}$, where M is the number of spectrometer channels.

   After retrieving the spectrum of the combined photonic sensor array, a postprocessing algorithm needs to be applied in order to determine the resonance wavelengths, as described by *Tosi et al.* [34]. In most cases, however, the assumption that the FWHM of the spectrometer channels is much smaller than the FWHM of the photonic sensors does not hold, as illustrated in case 1 of Fig. 2.4(b). The spectrometer resolution plays a key role in the interrogation: FBGs have a typical FWHM of hundreds of picometers, which is comparable, or at the most, one order of magnitude larger than the spectrometer resolution [23, 38]. A high spectrometer resolution, in this case, comes with the disadvantage of having a large device footprint. *Tosi et al.*[34] listed techniques for determining the resonance wavelength using the measured spectrum of the sensors. The most robust techniques are those based on applying transformations (such as the Fourier transform) to the measured spectrum. Although a subwavelength resolution can be achieved [36], the implementation of these algorithms can be computationally expensive.

   Pustakhod and other authors [30–32] use a different approach to obtain the resonance wavelength modulation: the spectrometer is designed in such a way that the FWHMs of its channels are much larger than the FWHMs of the sensors, as indicated as case 2 of Fig. 2.4(c). Thus, the resonance wavelengths are expected to operate close to the border of the AWG channels, where the lineshape of $T_{ch,m}(\lambda)$ can be linearized. The AWG channels work as an edge filter: although the spectrum of the photonic array cannot be obtained, the modulation of each sensor can be determined using Eqs. (2.10,2.11), as defined in the previous section. The spectrometer is designed in such a way that the lineshapes of two adjacent channels overlap, avoiding a strong attenuation in the case that the resonance wavelength

of one of the sensors is exactly in the centre of the two channels. *Pustakhod* [31] reports a minimum modulation amplitude smaller than 1 pm, which is much smaller than the AWG resolution. This comes with the disadvantage of reduced flexibility: using the AWG channels as an edge filter defines regions at which the resonance wavelengths must be placed. As discussed in detail in the following sections, this could be an issue for integrated sensors since the resonance wavelengths cannot be exactly defined during the design. Moreover, the dynamic range increase of the photonic sensors is limited by the regions at which the lineshape of the spectrometer channels can be linearized. Similarly to the edge filter interrogators, non-linearities can be compensated only up to a certain extent.

Another issue for interrogators based on dispersive spectrometers is a large number of outputs. Spectrometers such as [37] feature a resolution of 170 pm with a 90 nm bandwidth, leading to 500 output channels. Having many outputs requires a large number of channels to be sampled, which enhances the complexity of the electronic circuits for high-speed sensors. Some of the commercial spectrometers, such as [37], serializes the sampled data and reducing the maximum sampling speed of the photonic sensor array to the kHz range.

2.4.2. Spectral scanning interrogators
In order to overcome the issues with interrogators based on dispersive spectrometers, the spectral scanning technique can be used. Such an interrogator features a high resolution and large wavelength operation range. A broadband light signal is coupled to photonic sensors, and their output spectrum is conveyed to a high-Q optical cavity such as an RR [39–41] or a Fabry-Perot [42]. Alternatively, instead of a broadband source and a tunable filter, a tunable laser can be employed [43]. The output of the photonic cavity is then sent to a photoreceiver, as shown in Fig. 2.4(b). The operation principle of this method consists of tuning the resonance wavelength of the optical cavity using a known modulation signal. The voltage measured by a photoreceiver is given by:

$$v_{PD}(t) = R_{ph}g_{TIA}\int_0^\infty S(\lambda)T_f(\lambda)d\lambda, \tag{2.15}$$

where $T_f(\lambda)$ is the spectrum of the tunable optical cavity and $S(\lambda)$ is the combined spectrum of the photonic sensors. Assuming that the FWHM of the tunable filter is much smaller than the FWHM of the photonic sensors, the voltage measured by a photoreceiver is given by:

$$v_{PD}(t) \cong R_{ph}g_{TIA}\int_0^\infty S(\lambda)\delta(\lambda - \lambda_0(t))d\lambda = R_{ph}g_{TIA}S(\lambda_0(t)), \tag{2.16}$$

where $\delta(\lambda)$ is the Dirac delta function and $\lambda_0(t)$ is the resonance wavelength of the tunable filter. The voltage measured by the photodetector is proportional to the combined spectrum of the photonic sensors. If the modulation speed of the optical cavity is much faster than the speed of the external signal to be sensed by the photonic sensors, $S(\lambda, t)$ can be accurately obtained. A postprocessing step is

needed; the same algorithms described by *Tosi et al.*[34] can be used in order to retrieve the resonance wavelengths.

In general, the spectral scanning technique gives a much better resolution than interrogators based on dispersive spectrometers. A tunable laser, for instance, may have a FWHM ranging from hundreds of kHz [44] to a few Hz [45], and the wavelength can be set at a sub-picometer accuracy [43, 46]. In contrast, the resolution of dispersive spectrometers is in the order of tens of pm (in the wavelength domain). However, most spectral scanning interrogators are based on thermal tuning [39, 40] or micromechanical systems [41], limiting the speed to the few kHz range. *Kim et al.*[40] presented an optimized design of a thermally modulated RR whose speed could reach 100 kHz. In spite of this improvement, the assumption that the tuning speed of the optical cavity needs to be much higher than the speed of the photonic sensors limits the interrogation to sensors with speeds up to one order of magnitude slower than the maximum tuning speed of the optical cavity. Moreover, this method faces a trade-off between wavelength operation range and tuning speed: a higher tuning speed comes at the cost of a lower wavelength operation range.

2.5. Interrogators based on interferometry

2.5.1. Interrogator based on interferometry in combination with a dispersive spectrometer

Fig. 2.5(a) shows a schematic for an interrogator based on interferometry. Light from a broadband source is sent to a photonic sensor array, whose combined spectrum is conveyed to a dispersive spectrometer in order to demultiplex the sensor spectra. If a single sensor is being interrogated (see Chapter 3), no dispersive spectrometer needs to be used. Following the schematic of the figure, the demultiplexed output spectrum of each sensor is sent to an unbalanced Mach-Zehnder interferometer, through which the modulation of the resonance wavelengths is converted to a phase modulation. By first assuming that the MZI has a single output, its transmission spectrum is given by:

$$T_{MZI}(\lambda) = p + q \cos\left[\frac{2\pi}{\lambda}OPD + \varphi_e\right] \cong p + q \cos\left[\frac{2\pi}{FSR}\lambda + \psi_e\right], \qquad (2.17)$$

where the constants p and q which define the interferometer visibility p/q. FSR is the MZI free spectral range, and ψ_e is a phase whose value changes according to local variations in temperature. The derivation of Eq. (2.17) is presented in Chapters 3 and 4. The relation between the MZI optical path difference (OPD) and its free spectral range is given by:

$$FSR = \frac{\lambda_0^2}{OPD}, \qquad (2.18)$$

where λ_0 is a reference wavelength, typically close to 1550 nm for sensors that operate in the C band. The output voltage of the photoreceiver connected to the

Interrogators based on spectrometers

(a) BBS → Photonic Sensors → Dispersive Spectrometer → PDs

2

input spectrum / wavelength

Spectrometer

PD PD PD PD ... PD

Spectrum / wavelength

(b) case 1:

(c) case 2:

Spectrum / wavelength

(d) BBS → Photonic Sensors → Tunneable Filter → PDs

sensor 1   sensor 2   sensor 3

tunneable filter

Spectrum / wavelength
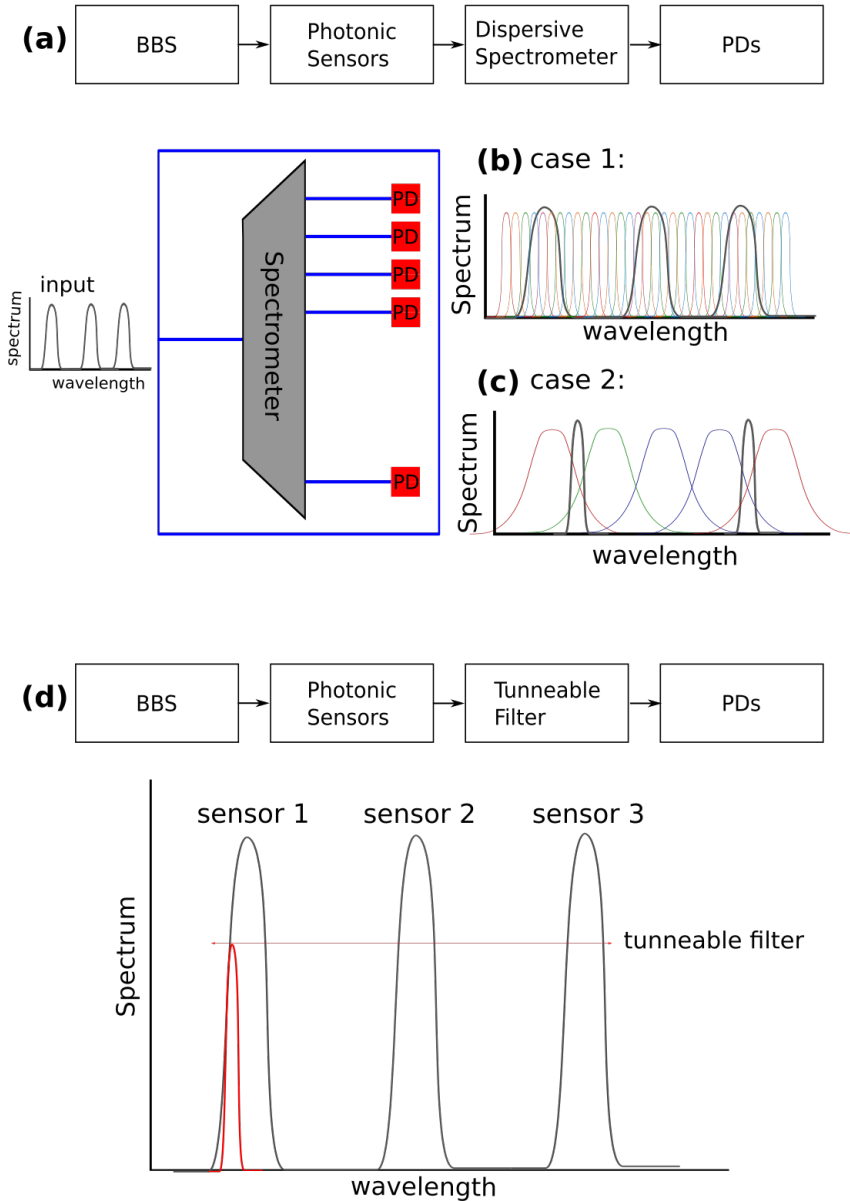
Figure 2.4: Interrogators based on spectrometers: (a) Schematic of an interrogator based on a dispersive spectrometer. The figure illustrates the two situations discussed in the main text. In (b), the FWHM of the photonic sensors (shown in gray) is smaller than the FWHM of the spectrometer channels (shown as different colors); in (c), The FWHM of the photonic sensors is much larger than the FWHM of the spectrometer channels. (d) Interrogator based on tuning filter. The illustration shows the spectra of the photonic sensors and of the tuning filter.

MZI is given by:

$$v_{PD,k}(t) = R_{ph} g_{TIA} \int_0^\infty T_{ch,k}(\lambda) S(\lambda) T_{MZI}(\lambda) d\lambda, \tag{2.19}$$

where $T_{ch,k}(\lambda)$ is the transmission spectrum of the k-th spectrometer channel. For such case, it is desired for the spectrometer lineshape to be flat, so that $T_{ch,k}(\lambda) S(\lambda) = s_k(\lambda)$. Substituting this expression into Eq. (2.19):

$$v_{PD,k}(t) = R_{ph} g_{TIA} \int_0^\infty s_k(\lambda) T_{MZI}(\lambda) d\lambda. \tag{2.20}$$

For a peaked lineshape sensor, the voltage is given by:

$$v_{PD,k}(t) = A \cos \left(\Phi_k(t) + \psi_{e,k} \right), \tag{2.21}$$

where A is a constant, $\psi_{e,k}$ is a phase proportional to $\phi_{e,k}$ and the phase modulation is given by:

$$\Phi_k(t) = \frac{2\pi \lambda_k(t)}{FSR}, \tag{2.22}$$

where $\lambda_k(t)$ is the resonance wavelength of the k-th sensor.

As indicated in Eq. (2.22), the sensitivity of $\Phi_k(t)$ with respect to $\lambda_k(t)$ and the external signal increases as the MZI free spectral range decreases. A larger value for the OPD is accompanied by a smaller value for the FSR, as these two quantities are inversely proportional. It is shown in Chapters 3 and 4 that if the FSR is smaller than or equal to the sensor $FWHM$, the visibility of the interferometric fringes and the voltages $v_{k,j}$ are strongly attenuated. Therefore, the choice of the OPD value needs to consider both the sensitivity and the attenuation of the interferometric fringes.

Retrieving $\Phi_k(t)$ from Eq. (2.21) can be difficult since the phase is wrapped into the cosine. For instance, assuming for $t = t_0$, $\Phi_k(t_0) = 0$ and $m\psi_{e,k} = m\pi$ (where m is an integer), $v_{PD,k}(t)$ gives an ambiguous response [5]: both positive and negative variations of $\Phi_k(t_0 + dt)$ produce the same value of $v_{PD,k}(t)$. This happens because the voltage signal, which is proportional to $\sin(\Phi(t) + \psi_{e,k})$, is unknown. If the MZI has a single output, the best option would be tuning $\psi_{e,k} = \pi/2$ (using a phase modulator, for instance) so that Eq. (2.21) gives an approximately linear response for small modulations of $\Phi_k(t)$. Two other approaches are commonly used instead: (a) active modulation or (b) passive modulation using a 3×3 coupler.

The idea of active modulation [47, 48] is to place a phase modulator into one of the MZI arms. In this case, Eq. (2.21) is rewritten as:

$$v_{PD,k}(t) = A \cos \left(\Phi_k(t) + \phi_V(t) + \psi_{e,k} \right), \tag{2.23}$$

where $\phi_V(t)$ is the induced phase proportional to an external voltage applied to the modulator. Typically, $\phi_V(t) = A\sin(2\pi f_0 t)$, where f_0 is much higher than the speed of the sensor. Let $\tilde{v}_{PD,k}(f) = F\{v_{PD,k}(t)\}$ be the Fourier transform of $v_{PD,k}(t)$. *Marin et. al.* [48] demonstrated that $\tilde{v}_{PD,k}(f_0)$ is proportional to $\sin(\Phi_k(t))$, while

$\tilde{v}_{PD,k}(2f_0)$ is proportional to $\cos(\Phi_k(t))$. Since both the sine and the cosine of the angular deflection are known, $\Phi_k(t)$ can be determined using Eq. (2.27) (presented later).

In most situations, however, the usage of active modulation is undesirable since such interrogators depends on a high-speed phase modulator. An alternative is the interrogation using a 3×3 coupler: the optical signals coming from the arms of the MZIs typically interfere within a 3×3 coupler, producing three 120° phase shifted output signals. It is shown in Chapters 3 and 4 that the output voltage $v_{k,j}$ (j = 1,2,3) of the photoreceiver connected to the j-th MZI output is given by:

$$v_{k,1}(t) = \frac{R_k}{3}\cos(\Phi_k(t) - 2\pi/3 + \psi_{e,k}) + a_k,$$

$$v_{k,2}(t) = \frac{R_k}{3}\cos(\Phi_k(t) + \psi_{e,k}) + b_k,$$

$$v_{k,3}(t) = \frac{R_k}{3}\cos(\Phi_k(t) + 2\pi/3 + \psi_{e,k}) + c_k, \qquad (2.24)$$

where R_k, a_k, b_k and c_k are constants. Linear combinations of the outputs give 90° phase shifted voltage signals. Let's introduce

$$v_{k,x}(t) = 2v_{k,1} - v_{k,2} - v_{k,3}$$
$$v_{k,y}(t) = \sqrt{3}\left(v_{k,2} - v_{k,3}\right), \qquad (2.25)$$

where $v_{k,x}(t)$ and $v_{k,y}(t)$ are 90° phase shifted phase signals. By substituting Eq. (2.24) into Eq. (2.25) and manipulating, one obtains:

$$v_{k,x}(t) = R_k\cos(\Phi_k(t) + \psi_{e,k}) + x_0,$$
$$v_{k,y}(t) = R_k\sin(\Phi_k(t) + \psi_{e,k}) + y_0, \qquad (2.26)$$

where x_0 and y_0 are constants which depend on a_k, b_k and c_k. Eq. (2.26) describes a parametric equation of a circle with radius R_k and centre (x_0, y_0). The angle $\Phi_k(t)$ is given by:

$$\Phi_k(t) = \text{unwrap}(\arctan_2(v_{k,y}(t) - y_0, v_{k,x}(t) - x_0)) - \psi_{e,k}. \qquad (2.27)$$

The phase, however, is still wrapped so unwrap algorithms needs to be employed. Nevertheless, the ambiguous response for small modulations of $\Phi(t)$ no longer occurs. In contrast, the ambiguous response faced for small modulations of $\Phi_k(t)$ no longer occurs. [6]

According to *Orr. et. al.* [49], interrogators based on interferometry give the best resolution of all methods. However, the interferometry method requires for the phase $\psi_{e,k}$, which drifts as the temperature of the MZI locally changes, to be stable. For low-speed sensors, this is an issue, as accurately controlling the temperature

---

[6]For the example given previously, take $m\psi_{e,k} = m\pi$ (where m is an integer). Both positive and negative modulations of $\Phi_k(t)$ lead to positive variations of the value of $v_{k,x}(t)$ but lead to values of $v_{k,y}(t)$ with opposite signs. Nevertheless, the interrogator is still unable to distinguish variations of $\Phi_k(t)$ larger than 2π.

of the MZI is required. For high-speed sensors, the effect can be compensated by applying a high pass filter. This is the approach used in Chapter 3. In spite of the high resolution of this method, attention should be paid in order to properly align the outputs of the spectrometer to the sensor spectrum. In the case of photonic sensors based on FBGs, this is not an issue since the Bragg wavelength can be chosen with an accuracy better than 1 nm. Nevertheless, *Orr.* [49] reports that if one of the FBG sensors in the network shown in Fig. 2.5(a) fails, it needs to be replaced by another sensor with the same resonance wavelength, indicating a lack of flexibility with this method.

For integrated RR sensors, the alignment between the outputs of the spectrometer and the sensor spectra is critical. For most foundries, it is not possible to predict the resonance wavelength of the rings during the design stage [50]. Up to certain extend, this can be solved by tunning the integrated spectrometer using the thermo-optic effect [51]. As a side effect, this could trigger the interferometer thermal drift of the phase $\psi_{e,k}$. *Selvaraja et al.* [52] reports a standard deviation of the resonance wavelengths of silicon micro-rings of about 1.8 nm for devices distant 20 mm apart within the wafer. A flexible interrogator method is key so that sensors fabricated from different parts of the wafer can be interrogated.

2.5.2. Interrogator based on Fourier transform
The main focus of this thesis is on an interrogator based on the Fourier transform. This method comes as an alternative to the passive interferometric interrogator, offering unprecedented flexibility and resolution. Even under large variances of the nominal value of the photonic sensor resonances, the sensor's response can be demodulated. Moreover, this method also provides a meaningful reduction of the interrogator footprint. No dispersive spectrometer is used, and demultiplexing and demodulation steps are performed simultaneously. A schematic of the interrogator design is shown in Fig. (2.5)(b). A broadband source is used to illuminate the photonic sensor array. Its output spectrum is sent to an MZI array integrated on an InP chip. The combined spectra of the sensors is shared among M interferometers with progressively higher optical path differences ($OPD_m = mOPD_1$). The two 90° phase-shifted voltages are given by:

$$v_{x,m}(t) = \sum_{k=1}^{M} R_k \cos(m\Phi_k(t) + \psi_{e,k})$$

$$v_{y,m}(t) = \sum_{k=1}^{M} R_k \sin(m\Phi_k(t) + \psi_{e,k}) \tag{2.28}$$

where the coefficients R_k ($k = 1, ..., K$) are to be determined during a calibration procedure. Eq. (2.28) can be obtained from Eq. (2.26) by superimposing the individual contributions of the photonic sensors. In Chapter 4, it is demonstrated that $v_{x,m}$ and $v_{y,m}$ are coefficients of a Fourier series so the combined spectrum can be retrieved. Instead of calculating the combined spectrum, a system of non-linear
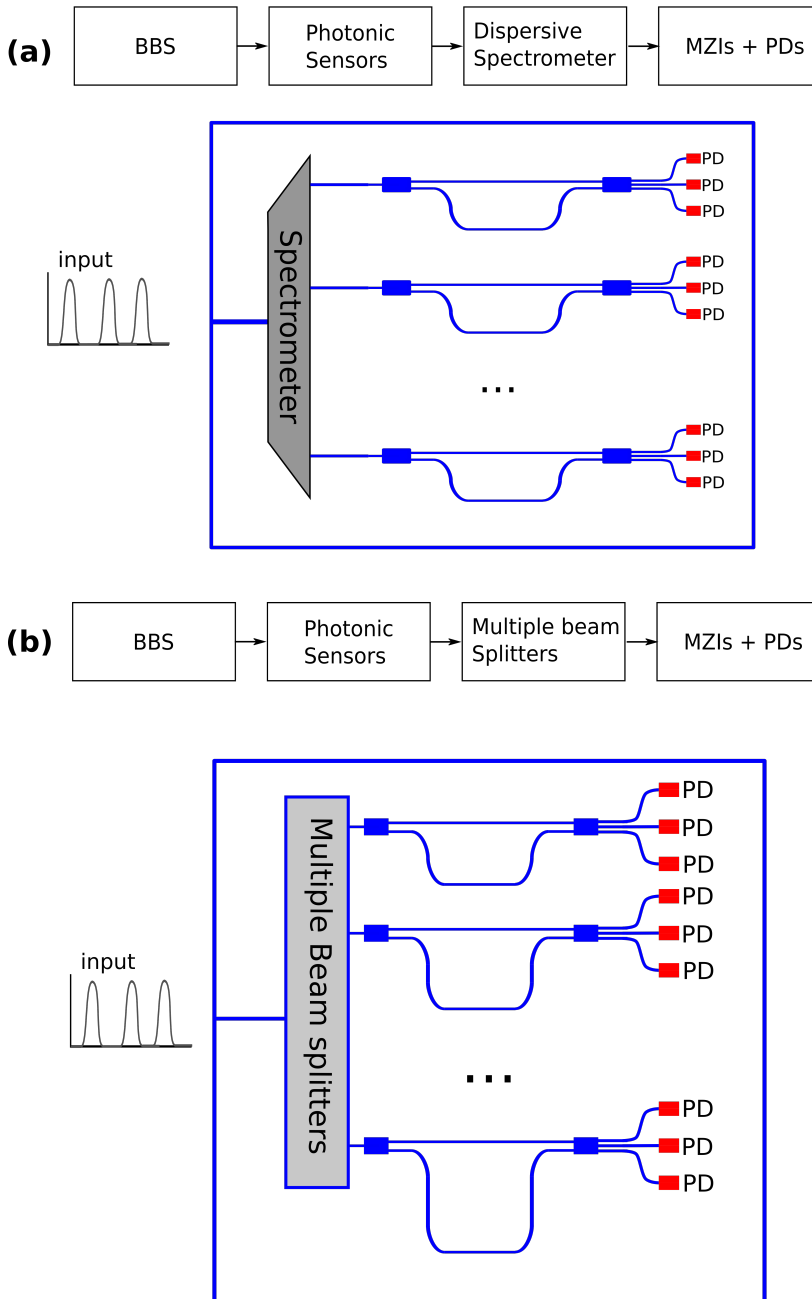
Interrogators based on interferometry

Figure 2.5: Schematic of interrogators based on interferometers (a) Spectrometer + MZI Interferometer (b) Fourier transform Interrogator.

equations is solved. Let

$$\hat{V}_m = v_{x,m}(t) + iv_{y,m}(t),　\quad (2.29)$$

where $\hat{V}_m$ is the complex voltage and i the imaginary unit. Substituting Eq. (2.28) into Eq. (2.29), we obtain:

$$\hat{V}_m(t) = e^{i\psi_{e,k}} \sum_{k=1}^{M} R_k \exp(im\Phi_k(t)).　\quad (2.30)$$

Eq. (2.30) represents a system of non-linear equations. The number of MZIs must be at least as large as the number of sensors so that we have a system of K unknowns and $K \leq M$ independent equations. Using one of the sensors as a reference, one could also compensate for the drift of the phases $\psi_{e,k}$. The flexibility of the method comes with the disadvantage of a high computational cost. The non-linear system of Eq. (2.30) needs to be solved at each time step . In Chapter 5, we propose semi-analytical methods to solve Eq. (2.30), allowing the interrogation of high-speed sensors.

2.6. Review conclusion

In this Chapter, an overview of the different interrogation techniques was given. The choice of the interrogation method depends on the property of the photonic sensor array since the interrogator affects the sensitivity, the dynamic range and the speed of the photonic sensors. Induced power modulation and edge filter interrogators are, in general, among the simplest methods. They work for both low-speed and high-speed sensors, whereas they may impose hard limitations on the sensor dynamic range. Interrogators based on spectrometers have high flexibility and are usually employed in large sensor networks. The minimum modulation depth that can be detected by this method depends on the spectrometer resolution. In order to achieve a higher resolution, a post-process step is required, which may affect the interrogation speed. An alternative is interrogators based on tunable filters that provide a higher resolution but limited speed.

The interrogators based on interferometry feature the highest resolution of all methods. However, highly accurate control of the MZI temperature is needed to avoid the thermal phase drift, which can plague the interrogation of low-speed sensors. This method requires the resonance wavelengths to be known during the design stage in order to properly align the spectrum of the sensors with the spectrum of the channels of the dispersive spectrometer. In order to handle those issues, an interrogator based on the Fourier transform is proposed. This is probably the most flexible method, providing a high resolution while the drift of the phases can be compensated using a reference sensor. A detailed comparison of the FT-interrogator with other common interrogation methods is presented in Chapter 5, section 5.5.3.

References

[1] X.-W. Ye, Y.-H. Su, and P.-S. Xi, *Statistical analysis of stress signals from bridge monitoring by fbg system,* Sensors **18**, 1 (2007).

[2] Y. Dai, Y. Liu, J. Leng, G. Deng, and A. Asundi, *A novel time-division multiplexing fiber Bragg grating sensor interrogator for structural health monitoring,* Optics and Lasers in Engineering **47**, 1028 (2009).

[3] C. Hu, H. Wen, and W. Bai, *A Novel Interrogation System for Large Scale Sensing Network With Identical Ultra-Weak Fiber Bragg Gratings,* Journal of Lightwave Technology **32**, 1406 (2014), publisher: IEEE.

[4] Y. Wang, J. Gong, B. Dong, D. Y. Wang, T. J. Shillig, and A. Wang, *A Large Serial Time-Division Multiplexed Fiber Bragg Grating Sensor Network,* Journal of Lightwave Technology **30**, 2751 (2012), conference Name: Journal of Lightwave Technology.

[5] C. K. Kirkendall and A. Dandridge, *Overview of high performance fibre-optic sensing,* Journal of Physics D: Applied Physics **37**, R197 (2004).

[6] Z. Luo, H. Wen, H. Guo, and M. Yang, *A time- and wavelength-division multiplexing sensor network with ultra-weak fiber bragg gratings,* Opt. Express **21**, 22799 (2013).

[7] B. Dong, S. He, Y. Hushu, W. Tianda, F. Lvjun, T. Guo, and Q. Zhao, *Combined time- and wavelength-division-multiplexing demodulation technique of fiber grating sensor arrays using a tunable pulsed laser,* Appl. Opt. **46**, 1015 (2007).

[8] A. D. Kersey, *A review of recent developments in fiber optic sensor technology,* Optical Fiber Technology **2**, 291 (1996).

[9] Y. Zhao and Y. Liao, *Discrimination methods and demodulation techniques for fiber Bragg grating sensors,* Optics and Lasers in Engineering **41**, 1 (2004).

[10] B. Lee, *Lee, b.: Review of the present status of optical fiber sensors. optical fiber technology 9, 57-79,* Optical Fiber Technology **9**, 57 (2003).

[11] W. J. Westerveld, M. Mahmud-Ul-Hasan, R. Shnaiderman, V. Ntziachristos, X. Rottenberg, S. Severi, and V. Rochus, *Sensitive, small, broadband and scalable optomechanical ultrasound sensor in silicon photonics,* Nature Photonics **15** (2021), 10.1038/s41566-021-00776-0.

[12] A. Maxwell, S.-W. Huang, T. Ling, J.-S. Kim, S. Ashkenazi, and L. Jay Guo, *Polymer Microring Resonators for High-Frequency Ultrasound Detection and Imaging,* IEEE Journal of Selected Topics in Quantum Electronics **14**, 191 (2008), conference Name: IEEE Journal of Selected Topics in Quantum Electronics.

2

[13] H. Wei, A. K. Amrithanath, and S. Krishnaswamy, *High-frequency ultrasonic sensor arrays based on optical micro-ring resonators,* in *Health Monitoring of Structural and Biological Systems XII*, Vol. 10600 (International Society for Optics and Photonics, 2018) p. 1060003.

[14] K. de Vos, Girones, J. Girones, T. Claes, Y. D. Koninck, S. Popelka, E. Schacht, R. Baets, and P. Bienstman, *Multiplexed antibody detection with an array of silicon-on-insulator microring resonators,* IEEE Photonics Journal **1**, 225 (2009).

[15] D. J. F. Cooper, T. Coroy, and P. W. E. Smith, *Time-division multiplexing of large serial fiber-optic bragg grating sensor arrays,* Appl. Opt. **40**, 2643 (2001).

[16] G. D. Lloyd, L. A. Everall, K. Sugden, and I. Bennion, *A high-performance miniaturized time division multiplexed sensor system for remote structural health monitoring,* in *Optical Sensing*, Vol. 5459, edited by B. Culshaw, A. G. Mignani, and R. Riesenberg, International Society for Optics and Photonics (SPIE, 2004) pp. 145 – 156.

[17] K. Kalantar-zadeh, *Sensors Characteristics,* in *Sensors: An Introductory Course* (Springer US, Boston, MA, 2013) pp. 11–28.

[18] *Dynamic range control,* in *Digital Audio Signal Processing* (John Wiley and Sons, Inc, 2008) Chap. 7, pp. 225–239, https://onlinelibrary.wiley.com/doi/pdf/10.1002/9780470680018.ch7 .

[19] G. Kouroussis, D. Kinet, E. Mendoza, J. Dupuy, V. Moeyaert, and C. Caucheteur, *Edge-filter technique and dominant frequency analysis for high-speed railway monitoring with fiber Bragg gratings,* Smart Materials and Structures **25**, 075029 (2016), publisher: IOP Publishing.

[20] W. J. Westerveld, J. Pozo, P. J. Harmsma, R. Schmits, E. Tabak, T. C. van den Dool, S. M. Leinders, K. W. van Dongen, H. P. Urbach, and M. Yousefi, *Characterization of a photonic strain sensor in silicon-on-insulator technology,* Opt. Lett. **37**, 479 (2012).

[21] C. Zhang, S.-L. Chen, T. Ling, and L. J. Guo, *Imprinted polymer microrings as high-performance ultrasound detectors in photoacoustic imaging,* J. Lightwave Technol. **33**, 4318 (2015).

[22] S. M. Leinders, W. J. Westerveld, J. Pozo, P. L. M. J. van Neer, B. Snyder, P. O'Brien, H. P. Urbach, N. de Jong, and M. D. Verweij, *A sensitive optical micro-machined ultrasound sensor (OMUS) based on a silicon photonic ring resonator on an acoustical membrane.* Scientific reports **5**, 14328 (2015).

[23] F. G. Peternella, B. Ouyang, R. Horsten, M. Haverdings, P. Kat, and J. Caro, *Interrogation of a ring-resonator ultrasound sensor using a fiber mach-zehnder interferometer,* Opt. Express **25**, 31622 (2017).

[24] K. Ogawa, S. Koyama, Y. Haseda, K. Fujita, H. Ishizawa, and K. Fujimoto, *Wireless, portable fiber bragg grating interrogation system employing optical edge filter,* Sensors **19** (2019), 10.3390/s19143222.

[25] C. A. Díaz, C. A. Marques, M. F. F. Domingues, M. R. Ribeiro, A. Frizera-Neto, M. J. Pontes, P. S. André, and P. F. Antunes, *A cost-effective edge-filter based fbg interrogator using catastrophic fuse effect micro-cavity interferometers,* Measurement **124**, 486 (2018).

[26] U. Tiwari, K. Thyagarajan, M. R. Shenoy, and S. C. Jain, *EDF-based edge-filter interrogation scheme for FBG sensors,* IEEE Sensors Journal **13**, 1315 (2013).

[27] J. E. Alfonso, L. G. Cárdenas, C. A. Triana, and M. V. Durán, *Design of an optical sensing interrogator using an edge filter scheme,* in *2013 SBMO/IEEE MTT-S International Microwave & Optoelectronics Conference (IMOC) (Rio de Janeiro, Brazil, August 2013)* (IEEE, 2013).

[28] N. S. Aulakh and R. S. Kaler, *Fiber Bragg grating interrogator using edge filtering technique with microbend loss error mitigation,* Optik **122**, 796 (2011).

[29] V. Saptari, *Fourier-Transform Spectroscopy Instrumentation Engineering*, 2nd ed. (SPIE Press, 2003).

[30] H. Guo, G. Xiao, N. Mrad, and J. Yao, *Echelle diffractive grating based wavelength interrogator for potential aerospace applications,* Journal of Lightwave Technology **31**, 2099 (2013).

[31] D. Pustakhod, E. Kleijn, K. Williams, and X. Leijtens, *High-resolution awg-based fiber bragg grating interrogator,* IEEE Sensors Journal **28**, 2203 (2016).

[32] N. A. Yebo, W. Bogaerts, Z. Hens, and R. Baets, *On-chip arrayed waveguide grating interrogated silicon-on-insulator microring resonator-based gas sensor,* IEEE Photonics Technology Letters **23**, 1505 (2011).

[33] G. Z. Xiao, P. Zhao, F. Sun, Z. Lu, , and Z. Zhang, *Arrayed-waveguide-grating-based interrogator for wavelength-modulated multi-fiber-optic sensor applications,* IEEE Photonics Technology Letters **17**, 1710 (2005).

[34] D. Tosi, *Review and analysis of peak tracking techniques for fiber bragg grating sensors,* Sensors (Switzerland) **17** (2017), 10.3390/s17102368.

[35] D. Tosi, *Advanced Interrogation of Fiber-Optic Bragg Grating and Fabry-Perot Sensors with KLT Analysis,* Sensors **15** (2015), doi: 10.3390/s151127470.

[36] D. Tosi, *KLT-Based Algorithm for Sub-Picometer Accurate FBG Tracking With Coarse Wavelength Sampling,* IEEE Photonics Technology Letters **27** (2015), 10.3390/s17102368.

[37] *Ibsen spectrometer,* https://ibsen.com/, accessed: 2019-03.

[38] F. G. Peternella, T. Esselink, B. Dorsman, P. Harmsma, R. C. Horsten, T. Zuidwijk, H. P. Urbach, and A. J. L. Adam, *On-chip interrogator based on Fourier Transform spectroscopy,* Opt. Express **27**, 1 (2019), 1812.00823 .

[39] F. Yang, W. Zhang, S. Zhao, Q. Liu, J. Tao, and Z. He, *Miniature interrogator for multiplexed fbg strain sensors based on a thermally tunable microring resonator array,* Opt. Express **27**, 6037 (2019).

[40] H.-T. Kim and M. Yu, *High-speed optical sensor interrogator with a silicon-ring-resonator-based thermally tunable filter,* Opt. Lett. **42**, 1305 (2017).

[41] W. R. Allan, Z. W. Graham, J. R. Zayas, D. P. Roach, and D. A. Horsley, *Multiplexed fiber bragg grating interrogation system using a microelectromechanical fabryperot tunable filter,* IEEE Sensors Journal **9**, 936 (2009).

[42] V. M. N. Passaro, A. V. Tsarev, and F. De Leonardis, *Wavelength interrogator for optical sensors based on a novel thermo-optic tunable filter in SOI,* Journal of Lightwave Technology **30**, 2143 (2012).

[43] S. K. Ibrahim, M. Farnana, D. M. Karabacakab, and J. M. Singer, *Enabling technologies for fiber optic sensing,* Proceedings of SPIE **9899**, 89900W (2016).

[44] S. Latkowski, A. Hänsel, N. Bhattacharya, T. De Vries, L. Augustin, K. Williams, M. Smit, and E. Bente, *Novel Widely Tunable Monolithically Integrated Laser Source,* IEEE Photonics Journal **7** (2015), 10.1109/JPHOT.2015.2493722.

[45] P. A. Morton and M. J. Morton, *High-Power, Ultra-Low Noise Hybrid Lasers for Microwave Photonics and Optical Sensing,* Journal of Lightwave Technology **36**, 5048 (2018), conference Name: Journal of Lightwave Technology.

[46] S. K. Ibrahim, M. Farnan, and D. M. Karabacak, *Design of a photonic integrated based optical interrogator,* in *Photonic Instrumentation Engineering IV*, Vol. 10110 (International Society for Optics and Photonics, 2017) p. 101100U.

[47] Y. E. Marin, A. Celik, S. Faralli, L. Adelmini, C. Kopp, F. D. Pasquale, and C. J. Oton, *Integrated dynamic wavelength division multiplexed fbg sensor interrogator on a silicon photonic chip,* J. Lightwave Technol. **37**, 4770 (2019).

[48] Y. E. Marin, T. Nannipieri, C. J. Oton, and F. D. Pasquale, *Integrated FBG Sensors Interrogation Using Active Phase Demodulation on a Silicon Photonic Platform,* Journal of Lightwave Technology **35**, 3374 (2017).

[49] P. Orr and P. Niewczas, *High-speed, solid state, interferometric interrogator and multiplexer for fiber Bragg grating sensors,* Journal of Lightwave Technology **29**, 3387 (2011).

[50] Z. Lu, J. Jhoja, J. Klein, X. Wang, A. Liu, J. Flueckiger, J. Pond, and L. Chrostowski, *Performance prediction for silicon photonics integrated circuits with layout-dependent correlated manufacturing variability,* Opt. Express **25**, 9712 (2017).

[51] Y. Yang, X. Hu, J. Song, Q. Fang, M. Yu, X. Tu, G.-Q. Lo, and Rusli, *Thermo-Optically Tunable Silicon AWG with above 600 GHz Channel Tunability,* IEEE Photonics Technology Letters **27**, 2351 (2015).

[52] S. K. Selvaraja, W. Bogaerts, P. Dumon, D. Van Thourhout, and R. Baets, *Sub-nanometer Linewidth Uniformity in Silicon Nanophotonic Waveguide Devices Using CMOS Fabrication Technology,* IEEE Journal of Selected Topics in Quantum Electronics **16**, 316 (2010), conference Name: IEEE Journal of Selected Topics in Quantum Electronics.

2

3

Interrogation of a ring-resonator ultrasound sensor using a fiber Mach-Zehnder interferometer

We experimentally demonstrate an interrogation procedure of a ring-resonator ultrasound sensor using a fiber Mach-Zehnder interferometer (MZI). The sensor comprises a silicon ring resonator (RR) located on a silicon-oxide membrane, designed to have its lowest vibrational mode in the MHz range, which is the range of intravascular ultrasound (IVUS) imaging. Ultrasound incident on the membrane excites its vibrational mode and as a result induces a modulation of the resonance wavelength of the RR, which is a measure of the amplitude of the ultrasound waves. The interrogation procedure developed is based on the mathematical description of interrogator operation presented in Appendix A, where we identify the amplitude of the angular deflection Φ_0 on the circle arc periodically traced in the plane of the two orthogonal interrogator voltages, as the principal sensor signal. Interrogation is demonstrated for two sensors with membrane vibrational modes at 1.3 and 0.77 MHz, by applying continuous wave ultrasound in a wide pressure range. Two optical path differences (OPDs) of the MZI are used. Thus, different interference conditions of the optical signals are defined, leading to a higher apparent sensitivity for the larger OPD, which is accompanied by a weaker signal, however. Ultrasound is detected at a pressure as low as 1.2 Pa.

3.1. Introduction

Integrated photonics is an enabling technology for important application fields, such as telecommunication [1, 2], optical signal processing [3] and various types of photonic sensing [4]. In the field of sensing the main advantages of integrated photonics sensors are small size, mass producibility, low cost and electromagnetic immunity. The lab-on-chip approach to chemical sensing and particle identification also benefits strongly from integrated photonics. This is demonstrated for example by recent advances in excitation and collection of spontaneous Raman scattering near silicon nitride waveguides [5] and in optical trapping and Raman spectroscopy of micro-particles using a dual-beam trap made from composite silicon oxide-nitride waveguides [6].

In the field of sensing for health and medicine, integrated silicon photonics is used in our department for an ultrasound sensor based on a ring resonator (RR) located on a thin membrane [7]. Ultrasound waves make the membrane vibrate and as a result induce a modulation of the optical resonance wavelength of the RR, which characterizes the waves. The sensor is very promising for medical ultrasound imaging, in particular for intravascular ultrasound (IVUS) imaging, which is widely used to diagnose atherosclerosis in humans. For IVUS, important advantages of our RR ultrasound sensor are its high sensitivity [7], the possibility to realize an array of sensors on a single chip, which is spontaneously enabled by the CMOS fabrication technology, and the absence of electrical wiring as needed for piezoelectric IVUS sensors. Wiring has the disadvantages of being rather cumbersome for an array of piezoelectric sensors and susceptible to cross-talk, while making the sensors incompatible with magnetic resonance imaging.

Here, we present an interrogation procedure of a RR ultrasound sensor of the type introduced in [7] using a passive fiber Mach-Zehnder interferometer [8, 9]. The procedure yields a well-defined relation between the sensor signal and the applied ultrasound pressure, thus qualifying a sensor of this type for IVUS. For amplitudes of the ultrasound-induced resonance-wavelength modulation smaller than the bandwidth of the spectrum incident on the RR, the signal is proportional to the applied ultrasound pressure. The MZI employs a 3×3 fiber output coupler, of which at least two of the three outputs are non-zero for any optical phase difference between the MZI arms. This is beneficial for the signal-to-noise ratio of the quadrature signal components defined with the three outputs. We demonstrate detection of ultrasound waves of a pressure amplitude as small as 1.2 Pa. The interrogation method we present for a single sensor is the first step towards interrogation of an array of sensors. A complete mathematical description of the operation of the interrogator, resulting in the interrogation procedure we apply, is given in Appendix A.

3.2. Silicon ring-resonator sensor for ultrasound

The heart of the ultrasound sensor is a silicon RR of the racetrack type, coupled to two bus waveguides, as depicted in Fig. 3.1. Ring and waveguides are located on a thin silicon oxide membrane designed to have its lowest vibrational mode in the MHz

range. Typically, to mimic the situation of IVUS imaging of an artery, the sensor is operated in water. Ultrasound waves of the proper characteristics impinging upon the membrane excite the vibrational mode and thus periodically deform the RR, leading to encoding of the optical signal with information of the ultrasound waves for imaging, in particular modulation of the RR resonance wavelength at the ultrasound frequency. The modulation results from the combined effect [10] of elongation of the racetrack's straight part, change of the ring cross section due to the Poisson effect, change of the refractive indices of silicon and of silicon oxide of the cladding, and finally change of the effective index of the waveguide mode circulating the ring due to the elasto-optic effect. The RRs were fabricated at ePIXfab, Imec [11] on
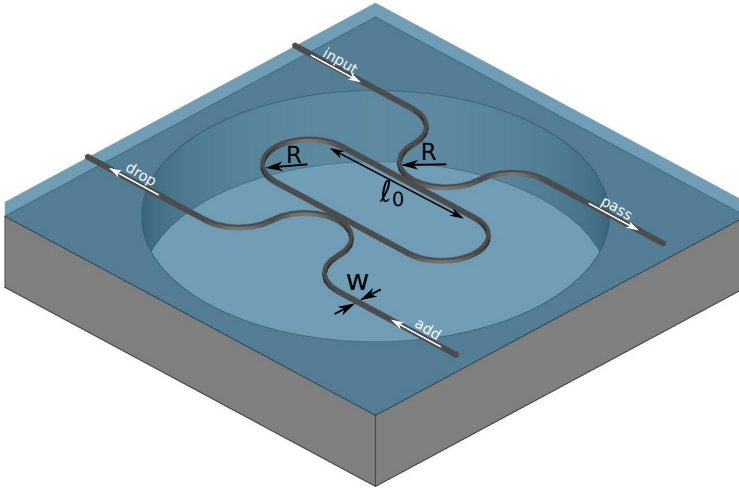
Figure 3.1: Schematic view of the silicon ring-resonator sensor fabricated on a circular silicon oxide membrane. Width of coupling waveguides and racetrack is w=400 nm, while the gap of the directional couplers is 200 nm. Radius of bends is R=5 μm. The length of the straight part of the racetrack ℓ_0 varies among the devices.

silicon-on-insulator wafers thinned to 250 μm. The silicon device layer and the buried oxide (BOX) layer are 220 nm and 2 μm thick, respectively. The width of the ring and the bus waveguides is 400 nm, implying these are single mode around the operational wavelength of 1550 nm. The gap of the two identical directional couplers of the RR is 200 nm. The length ℓ_0 of the straight part of racetracks is in the range 20-100 μm, while the bending radius is 5 μm. For light coupling from and to external fibers we use grating couplers (GCs), to which 10 μm wide waveguides are connected. The GCs are polarization sensitive, implying that the modes coupled into and out of the waveguides and circulating the ring are TE polarized, according to the building block specification [11]. Between GCs and RR, the 10 μm wide waveguides are adiabatically tapered down to 400 nm in two steps. The fibers are permanently connected to the sensor via angled and aluminium coated Pyrex mirror blocks glued to the chip [12]. The mirror blocks reflect the in-plane light leaving the fiber towards the grating coupler. Only the pass port is fiber-connected, implying

that the transmission spectrum shows a series of dips (see Fig. 3.2).

The current sensors result after the fabrication (in Kavli Nanolab Delft) of a membrane, which vibrates in the MHz range, in the backside of the chip. At the position of a RR a membrane is created by deep reactive ion etching (Bosch process) of a circular hole in the handle wafer. This etching from the backside stops selectively at the BOX layer, and thus a membrane is formed spontaneously. In this procedure a 2.5 μm PECVD oxide layer is used as a hard mask and the photonic circuitry on the front side is protected by a 0.5 μm thick PECVD oxide layer, which also serves as upper cladding. The resulting membranes thus have a thickness of 2.5 μm. The cavity under the membrane is closed by gluing a glass platelet to the chip's backside, entrapping air (see Fig. 3.3). The sensor thus effectively operates with a membrane that is water loaded on one side.

The silicon waveguiding platform, owing to its high index contrast, allows for small bending radii, which is advantageous for small footprint sensors. This advantage has been recognized before in [13], which reports pressure sensors using a silicon RR on an oxide membrane. This work, however, is focused on the demonstration of sensing of static pressures, while the reported RR is relatively large. Ultrasound detection with polymer RRs is reported in [14]. These RRs are not located on a membrane and thus only rely on the elasto-optic effect. Further, the polymer waveguides have a relatively low index contrast with respect to the cladding, implying that bending radii are more limited than for silicon RRs.

We concentrate on two sensors: sensor #1 with ℓ_0 = 30 μm located on a 66 μm diameter membrane (vibrational mode at 1.3 MHz) and sensor #2 with ℓ_0 = 40 μm located on a 124 μm diameter membrane (vibrational mode at 0.77 MHz). For sensor #1, the transmission spectra without applied ultrasound are shown in Fig. 3.2. The resonance dips captured in Fig. 3.2(a) give a free spectral range P_{RR} = 6.01 nm. Fig. 3.2(b) is a zoom-in of the central dip at 1550.19 nm, which we use for experiments with the interrogator (Section 3.4). The setup for measuring the dips is addressed in connection to the modulation method (Appendix B).

To analyze a single resonance, we start from the expression for the transmission to the pass port for two identical directional couplers, which is [15]

$$T_{pass}(\theta) = \frac{r^2 + r^2 a^2 - 2r^2 a \cos\theta}{1 + r^4 a^2 - 2r^2 a \cos\theta}. \tag{3.1}$$

Here r is the self-coupling coefficient of the directional coupler, a the single round-trip amplitude transmission, and θ is the accumulated phase of the mode for a single round trip in the ring. When concentrating on a single resonance of the overall spectrum, the phase can be approximated by

$$\theta = \frac{2\pi}{L} n_{eff} L \cong 2\pi m - 2\pi n_g L \frac{\lambda - \lambda_r}{\lambda_r^2}. \tag{3.2}$$

Here λ is the wavelength, λ_r the resonance wavelength, L the round-trip length and m an integer. n_{eff} and n_g are the wavelength dependent effective index and the group index at resonance, respectively. The right-hand side of Eq. (3.2) results from keeping only the first order term of the Taylor expansion of the function $n_{eff}(\lambda)/\lambda$
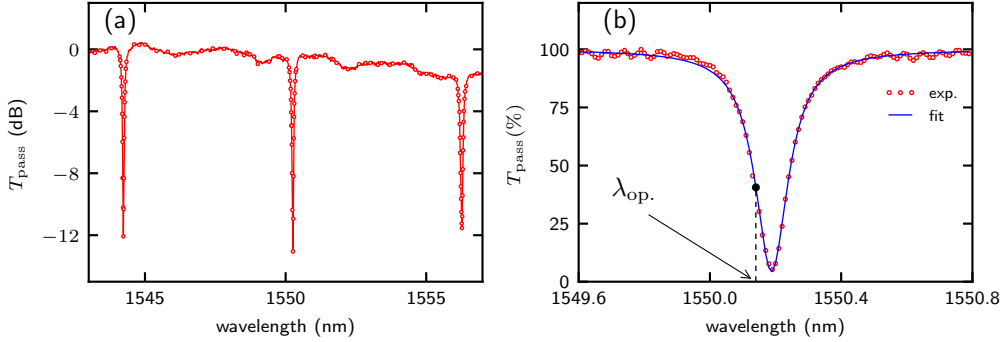
Figure 3.2: (a) Transmission spectrum of a ring resonator on a silicon oxide membrane, showing three resonance dips. (b) Zoom-in of the central dip in (a). The blue curve is a fit of Eq. (3.3) to the data points. On the linear part of the dip's left flank the operation point $\lambda_{\mathrm{op.}}$ is shown, the static wavelength to which the laser is tuned in the modulation method (see Appendix B).

around λ_r and implementing the resonance condition $n_{eff}(\lambda_r)L = m\lambda_r$. Eq. (3.1) simplifies further by using $\cos\theta \cong 1 - \theta^2/2$ near the resonance phase $\theta = 2\pi m$, which for the cosine is equivalent to $\theta = 0$, and by using Eq. (3.2). This yields the single-dip transmission

$$T_{pass}(\lambda) \approx \frac{(\lambda - \lambda_r)^2 + \varepsilon(\gamma_r/2)^2}{(\lambda - \lambda_r)^2 + (\gamma_r/2)^2}. \tag{3.3}$$

Here γ_r and ε are defined by, respectively

$$\gamma_r = \frac{\lambda_r^2(1 - ar^2)}{\pi n_g L r \sqrt{a}} = FWHM \tag{3.4}$$

$$\varepsilon = \frac{r^2(1 - a)^2}{(1 - ar^2)^2}. \tag{3.5}$$

In Eq. (3.4), γ_r=FWHM is the full width at half minimum of the resonance dip. The line shape function of Eq. (3.3) corresponds to $[1 - (1 - \varepsilon)L(\lambda)]$, with $L(\lambda)$ a Lorentzian function of maximum value unity, centred at λ_r. We note that using Eq. (3.3) instead of Eq. (3.1) is not really needed for analysis of a single dip. However, we already introduce Eq. (3.3) in view of later analyses, which are strongly simplified by it.

A fit of Eq. (3.3) to the measured dip of Fig. 3.2(b) yields the blue curve in that figure, giving fit parameters $\varepsilon = 0.043$ and $\gamma_r = 122$ pm. Thus, the quality factor $Q = \lambda_r/\gamma_r$ is 12706. The value of ε being close to zero, the ring operates close to critical coupling, which holds for [15] $a = 1$, i.e. $\varepsilon = 0$. With $n_g = 4.37$ derived from the free spectral range $P_{RR} = \lambda_r^2/(n_g L) = 6.01$ nm, Eqs. (3.4,3.5) give the values $r = 0.975$ and $a = 0.987$.

3.3. Fiber interrogator

3.3.1. Circuitry and signal flow of the interrogator

The interrogator is a fiber optic circuit based on a Mach-Zehnder interferometer (MZI) with a 2×2 input coupler and a 3×3 output coupler. A schematic of the circuit is shown in Fig. 3.3. Light from a broadband source (BBS, EXALOS EXS210069-01 superluminescent diode, maximum output power 14 mW) is guided to the RR sensor, via a circulator, a fiber Bragg grating (FBG, from TeraXion, FWHM 200 pm) and an EDFA set at gain of 24 dB (Amonics, AEDFA-PM-33-B-FA, noise figure approx. 3.5 dB at 1 dBm). The width of the FBG reflection spectrum is such that a single resonance of the sensor can be selected, in particular the one of Fig. 3.2(b). Selection is by tuning the center of the FBG spectrum to the sensor's resonance wavelength in the absence of ultrasound, by applying axial strain with a mechanical stretcher and temperature using a thermo-electric cooler. The light from the sensor is guided to the MZI, of which one arm has a variable length air gap, thus providing a variable optical path difference (OPD). The air gap is realized using two lenses (ThorLabs FiberPort collimators), one of which can be accurately translated. One input of the 3×3 coupler is left open. Each coupler output is connected to a combination of a photodetector (Fermionics, FD100, max dark current = 3 nA) and a transimpedance amplifier (TIA, ADA4899-1 from Analog Devices with gain 2.2 kV/A, noise: $1nV/\sqrt{Hz}$), after which further amplification (gain=196) and high pass filtering (f_c =1.0 kHz) are applied (last two operations not shown in Fig. 3.3). The resulting output voltages V_i are sampled by a data acquisition system (based on National Instruments NI 5734, max. sampling rate 120 MSa/s). The sensor is immersed in a water tank. Glued to a stick, it is mounted on one side of a frame (see Fig. 3.3). On the other side, coaxial with the sensor and at a distance of 135 mm, a transducer is mounted for sending ultrasound waves, which is actuated by an arbitrary waveform generator (AWG, Rigol DG1022). The fibers of the optic circuit are standard connectorized fibers for telecom wavelengths. Prior to ultrasound measurements with the sensor, the amplitude of the ultrasound pressure is calibrated with a hydrophone (Precision Acoustics, SN2082, 1.0 mm) placed in the sensor's position.

The power transmission T_i ($i = 1, 2, 3$) of the MZI, supposed lossless, at the optical outputs is given by [16]

$$T_{MZI,i} = \frac{1}{3}\left[p + q \cos\left(\frac{2\pi}{\lambda}OPD + \varphi_i + \varphi_e\right)\right].$$ (3.6)

The parameters p and q determine the fringe visibility q/p. OPD is the optical path difference between the MZI arms. For an ideal 3×3 coupler $p = 1$ and $\varphi_i = 0°, 120°, -120°$ for $i = 1, 2, 3$. The phase φ_e is a so-called environmental phase [9], that drifts slowly in time. Its origin is temperature instability of the fiber optic circuit. Owing to the three phase shifted cosines in Eq. (3.6), at least two of the voltages V_i are non-zero for any total argument of the cosines, thus avoiding signal fading [9]. For further analyses we rewrite Eq. (3.6) for wavelengths λ close to the
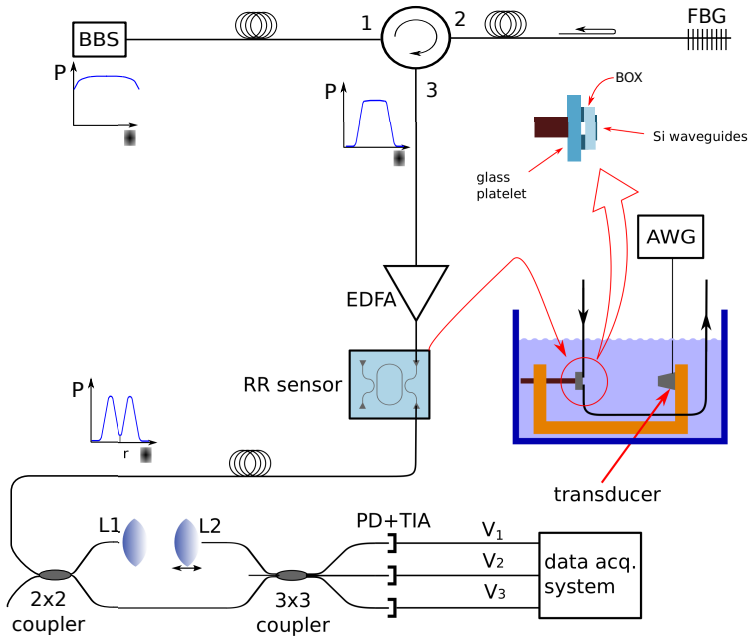
Figure 3.3: Schematic of the fiber interrogator, based on a Mach-Zehnder interferometer with a 2×2 coupler and a 3×3 coupler. BBS is the broad band source, FBG the fiber Bragg grating, EDFA the erbium doped amplifier and AWG the arbitrary waveform generator. The lenses L1 and L2 are part of the variable optical path length of one MZI arm, ranging from 4 to 13.5 mm. PD + TIA denotes combination of photodetector and transimpedance amplifier. V_1, V_2 and V_3 are the three output voltages sampled by the data acquisition system. At the BBS, after the circulator and before the MZI the signal spectrum has been indicated. The water tank with sensor and transducer shows the setup for ultrasound measurements.

resonance wavelength λ_r, using a first order Taylor expansion of $1/\lambda$. This gives

$$T_{MZI,i} \approx \frac{1}{3}\left[p + q\cos\left(2\pi\lambda\frac{OPD}{\lambda_r^2} - \frac{4\pi}{\lambda_r}OPD - \varphi_i - \varphi_e\right)\right]$$

$$= \frac{1}{3}\left[p + q\cos\left(\xi\lambda + \varphi_i + \varphi_e\right)\right]. \tag{3.7}$$

Here we have used $\xi = 2\pi OPD/\lambda_r^2 = 2\pi/FSR$, with FSR the MZI's free spectral range. Further, ψ_e is defined by $\psi_e = -4\pi OPD/\lambda_r - \varphi_e$, which thus shows the same drift as φ_e. Renumbering the outputs has removed the minus sign of φ_e. Retaining only the Taylor expansion's first order term is justified, as the deviation of λ from λ_r is about 100 pm, to be compared with $\lambda_r \cong 1550$ nm.

$T_{MZI,i}$ of Eq. (3.7) is a main ingredient in the mathematical description leading to the output voltages V_i of the overall circuit in Fig. 3.3. For the total description we refer to Appendix A, from which we have extracted the interrogation procedure summarized in Section 3.4.1 and applied in Section 3.4.2.

3.3.2. Characterization of the fiber Bragg grating and Mach-Zehnder interferometer

The FBG was characterized by measuring its reflection spectrum, using an optical spectrum analyzer (OSA, Yokogawa AQ6315A) coupled to port 3 of the circulator (see Fig. 3.3). Fig. 3.4(a) shows the measured spectrum (blue data points), which has a top-hat shape and decays steeply. We have fitted a super-Lorentzian function to the data points. This function, also used to describe the transverse profile of optical beams [17], is given by

$$R_{FBG}(\lambda) = \left[1 + \left(\frac{\lambda - \lambda_0}{\gamma_{FBG}/2} \right)^N \right]^{-1}. \tag{3.8}$$

Here γ_{FBG} is the FWHM of the line shape with central wavelength λ_0, and the integer N is the order of the super-Lorentzian. $N = 8$ gives the best fit result. In Fig. 3.4(a) we also show the fitted function, which yields γ_{FBG} = 207 pm, in agreement with the specification.

The combined spectrum of the FBG and sensor #1 is presented in Fig. 3.4(a) as well (green data points). It was measured in the configuration of Fig. 3.3, but with the difference that the OSA instead of the MZI is coupled to the sensor's pass port. Alignment of the FBG spectrum is close to symmetric with respect to the resonance dip, which here is broader than in Fig. 3.2b. The increase of ring FWHM results from the OSA resolution and the higher power applied to the RR in this measurement configuration, due to non-linear optical absorption [15, 18]. This changes the effective index of the ring waveguide, which explains the dip's shift to longer wavelength as compared to Fig. 3.2b. The normalization of the two curves shown in Fig. 3.4(a) causes an apparent broadening of FBG reflection spectrum. The combined spectrum indicates a latitude of about 100 pm before the dip moves out of the FBG reflection spectrum as a result of applied ultrasound.

The MZI was characterized by directly connecting a tunable laser (Santec TSL-210VF, set at output power 500 μW) to the MZI input, to measure the output voltages V_i as a function of wavelength. The wavelength was swept from 1550 to 1551 nm at a rate of 1.2 nm/min, giving a measurement time of 50 s. This time, unlike the very short measurement times in the actual ultrasound experiments (Section 3.4.2), is comparable to the time scale of the environmental phase drift[1]. Therefore, to exclude the drift, a stabilization time of the setup of several hours was observed before the measurements, with the laser on. The characterization was done for five OPDs, *i.e.* five positions of lens L2 in Fig. 3.3. In agreement with Eq. (3.8), the resulting five sets of $V_i(\lambda)$ traces are cosines, each oscillating around a non-zero average.

Traces for OPD = 12.9 mm are shown in Fig. 3.4(b), together with fits of the function

---

[1]Thermal fluctuations along the MZI are the main cause of the phase drift. This effect can be mitigated by fabricating the MZI on a chip: since the chip dimensions are much reduced, it is easier to control its temperature. However, MZIs can be extremely sensitive to temperature depending on its OPD, and a different strategy is used in Chapter 4.
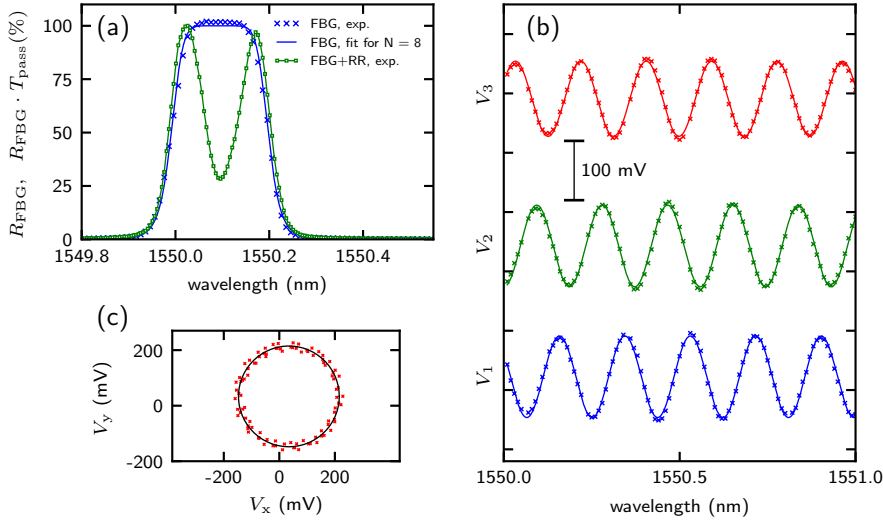
Figure 3.4: (a) FBG reflection spectrum and combined FBG reflection and RR transmission spectrum, both normalized to their maximum value, and a fit of Eq. (3.8) to the FBG spectrum for $N = 8$. (b) Traces of the interrogator outputs V_i as a function of wavelength, with data points shown as crosses. Due to the way of plotting, the DC component of the V_i is not visible. The oscillatory functions are fits of $A_i \cos(\xi\lambda + \varphi_e + \psi_e)$ to the data points. The fits give: $A_i = 63.4, 68.9, 68.7$ mV ($i = 1, 2, 3$) and $\varphi_e + \psi_e = 176°, 59°$ and -67° ($i = 1,2,3$). The traces were used in obtaining the correction factors and in Eqs. (9) and (10). (c) Corrected (V_x, V_y) points, together with the fitted circle. The circle radius is 181 mV.

$V_i = A_i \cos(\xi\lambda + \varphi_i + \psi_e)$ to the traces, from which first the average was subtracted. The fits are performed for the five sets, treating A_i and the sum $\varphi_i + \psi_e$ as fit parameters. The fits indicate that the amplitudes of the three cosines of a set are not equal (see caption), which contradicts Eq. (3.8). This implies that the circle defined by voltages V_x and V_y in Eqs. (3.32) and (3.33), respectively, is deformed to an ellipse. As explained in Appendix A, the circular shape defined by these equations plays a central role in the interrogation procedure. Taking for the traces of Fig. 3.4(b) the fitted phase of output V_1 as a reference ($\varphi_1 + \psi_e = 0$), we obtain $\varphi_2 + \psi_e = -117°$ and $\varphi_3 + \psi_e = 117°$. Thus, the phases deviate somewhat from the nominal values. We note that slight non-ideal behavior of amplitude and phase of 3×3 fiber couplers is not uncommon and has been reported before [8, 19]. The measured traces also yield the relation between the FSR and the setting of the dial for choosing the OPD.

In order to make the amplitudes of the cosines equal, we modified Eqs. (3.32) and (3.33) by including correction factors c_2 and c_3:

$$V_x(t) = 2V_1 - c_2 V_2 - c_3 V_3 \tag{3.9}$$

$$V_y(t) = \sqrt{3}\,(c_3 V_3 - c_2 V_2). \tag{3.10}$$

Initially, we set $c_2 = c_3 = 1$ for the traces in Fig. 3.4(b). Using these start values the equation of the ellipse given by the locus of points (V_x, V_y) defined by Eqs. (3.9) and (3.10) is obtained by least square fitting [20], giving the ellipse semi-axes a and b. Next, using an optimization algorithm [21] the function $f(c_2, c_3) = |1 - a(c_2, c_3)/b(c_2, c_3)|$ is minimized, yielding the circle aimed for. The initial ellipse semi-axes a and b serve as start values. The result is c_2=0.85 and c_3=0.86, for minimum $f(c_2, c_3) = 0.001$. The corrected (V_x, V_y) points have been plotted in Fig. 3.4(c), together with the fitted circle. The correction factors c_2 and c_3 are used in the interrogation procedure of Section 3.4.2.

3.4. Interrogation of the ultrasound sensor

3.4.1. Interrogation procedure

The goal of the interrogation procedure of the sensor is quantitative extraction of the ultrasound-induced optical signal of the sensor from the three output voltages $V_i(t)$ ($i = 1, 2, 3$) of the interrogator. Appendix A is the basis of the procedure. Here, we give the main data-processing steps for the case of continuous ultrasound waves of frequency f_0. We start from slightly modified versions of Eqs. (3.35) and (3.36) for the mutual orthogonal voltages $V_x(t)$ and $V_y(t)$ constructed from the measured $V_i(t)$:

$$V_x(t) = 2V_1 - V_2 - V_3 = 3R_K \cos\left(\Phi(t) + \psi_e\right) + x_0(\psi_e) \tag{3.11}$$

$$V_y(t) = \sqrt{3}\,(V_3 - V_2) = 3R_K \sin\left(\Phi(t) + \psi_e\right) + y_0(\psi_e). \tag{3.12}$$

As compared to Eqs. (3.35) and (3.36) the modifications in Eqs. (3.11) and (3.12) comprise neglect of constant parameters in the argument of the cosine and sine, and in the functions x_0 and y_0. It is understood that these are absorbed in ψ_e. This simplifies the analysis, but has no consequences for the final result. Eqs. (3.11) and (3.12) are parametric equations of a circle of radius $3R_K$ and with center (x_0, y_0). $\Phi(t) = \Phi_0 \sin(2\pi f_0 t)$ is the instantaneous angular deflection of the point (V_x, V_y) on an arc of the circle, which is periodically traced at the frequency f_0 of the ultrasound. R_K is constant for constant total gain of the interrogator circuit, independent of the applied ultrasound pressure, but dependent on the OPD of the MZI. Dependence of $V_x(t)$ and $V_y(t)$ on the environmental phase ψ_e is not an issue for the analysis, since ψ_e is constant on the time scale of a single interrogation of the sensor.

The data-processing steps are as follows. First, for a reference ultrasound pressure of high enough amplitude, implying a long enough arc of the circle, the radius $3R_K$ and the center (x_0, y_0) are determined using the fit procedure already described for an ellipse in Section 3.3.2. The fitted value of $3R_K$ then holds for all other pressures of a measurement series. We typically use a rather high reference pressure of a series of pressures (in Section 3.4.2 we use 2280 Pa for sensor #1 and 312 Pa for sensor #2), since a high pressure gives a long arc and thus an accurate fit result for $3R_K$.

Next, the fitted $3R_K$ is used to retrieve the circle center (x_0, y_0) for each amplitude pressure p_0 of the series by minimizing [20, 21] the average squared deviations of

the locus of points (V_x, V_y) from a circle of radius $3R_K$.

Subsequently, for each pressure of the series we determine the instantaneous deflection. In more detail, we obtain the wrapped deflection from Eqs. (3.11) and (3.12) according to

$$\Phi(t)_{wr.} = \mathsf{atan2}\left(V_y - y_0, V_x - x_0\right) - \psi_e. \tag{3.13}$$

Here atan2 is the four-quadrant arctangent function. Upon input of the coordinates of a point in the plane, atan2 returns the angle of the point in the range $(-\pi, \pi\,]$. $\Phi(t)_{wr.}$ in principle oscillates regularly in time around $-\psi_e$, but may be discontinuous in view of the limited range of atan2, even for small resonance-wavelength modulation. Therefore, we unwrap $\Phi(t)_{wr.}$ using the unwrap function of MATLAB [22], which returns the smooth unwrapped deflection. After subtracting from the unwrapped deflection its average $-\psi_e$, we arrive at the proper instantaneous deflection $\Phi(t)$, which describes the periodic tracing of the circle arc in the right way. Fourier transformation of $\Phi(t)$ then yields the amplitude Φ_0, the quantity sought for.

As a last step, again following Appendix A, the amplitude δ_0 of the resonance-wavelength modulation is obtained from

$$\delta_0 = \kappa \frac{\Phi_0}{\xi} = \kappa \frac{\lambda_r^2 \Phi_0}{2\pi OPD}. \tag{3.14}$$

Here κ is the correction factor introduced in Appendix A, where its values are derived. In the next section we will follow an experimental approach for obtaining κ.

The data-processing just described is performed offline, which is adequate for the present purpose. Various scenarios can be conceived for real-time data processing, which is required for later application to IVUS imaging.

3.4.2. Interrogation experiments

We interrogated sensors #1 and #2 according to the above procedure, using OPD values of 6.9 and 12.9 mm, which almost span the available range. We applied two series of pressures amplitudes, which become apparent in Fig. 3.6 below. For each pressure we acquired time traces of the three voltages $V_i(t)$ during 300 ms, sampled at 30 MSa/s.

In Fig. 3.5(a), as an example, we show for sensor #1 part of the $V_i(t)$ traces and of the $V_x(t)$ and $V_y(t)$ traces deduced from these, for OPD=12.9 mm and a pressure of 2280 Pa, the reference pressure for determining radius $3R_K$ for this sensor. Similar traces (not shown) were obtained for sensor #2 for reference pressure 312 Pa. The traces results after noise reduction, applying a Gaussian bandpass filter of FWHM=80 Hz centred at the fundamental frequency and its harmonics. The ultrasound period of 0.77 μs is clearly present in the traces, while the second harmonic can be seen as well. In Fig. 3.5(b) the points (V_x, V_y) are plotted, together with the fitted circle of radius $3R_K = (191\pm 6)$ mV. The spectral content of the $V_i(t)$ of sensor #1 is more apparent in the Fourier transforms in Fig. 3.5(c), in which the

3
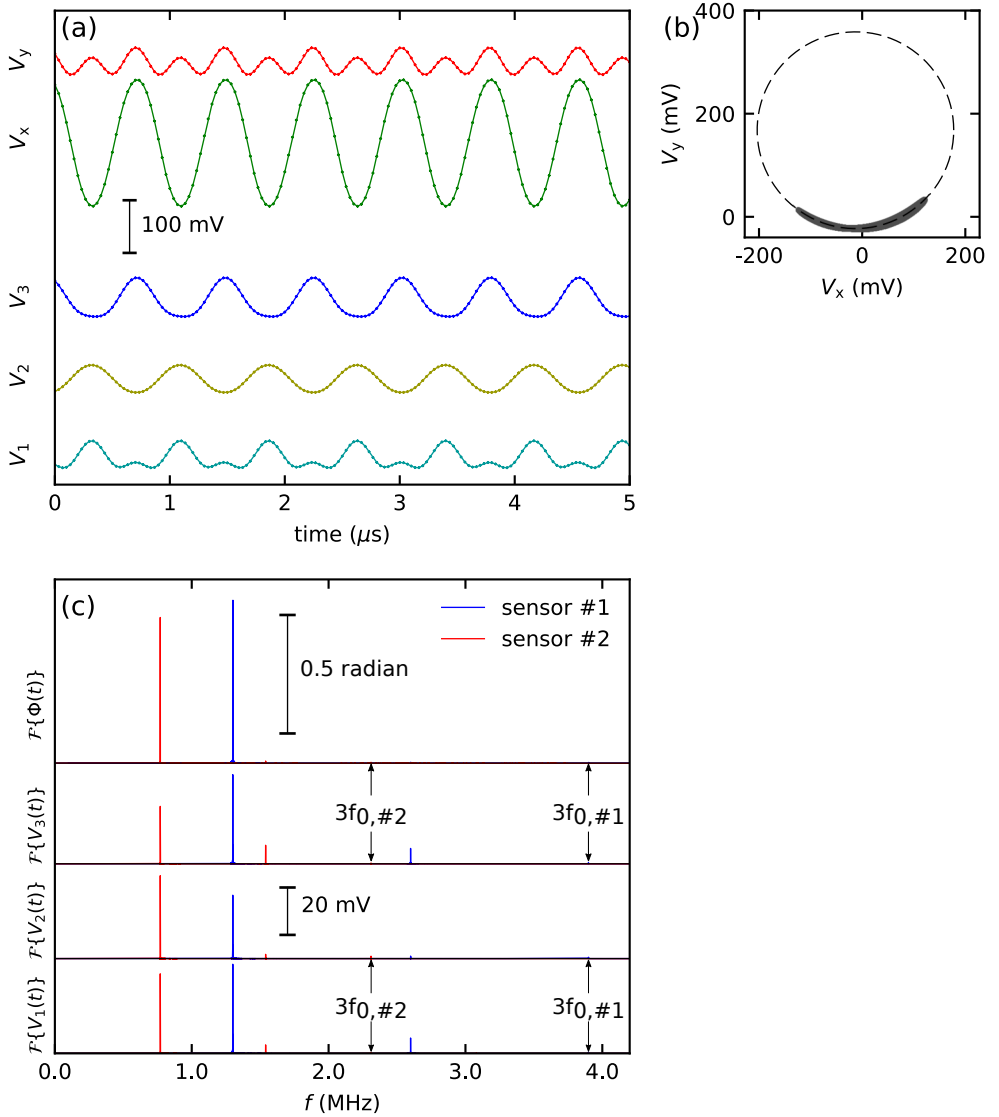
Figure 3.5: (a) Part of traces of $V_i(t)$ ($i = 1, 2, 3$) for sensor #1, sampled while interrogating the sensor, and of the mutual orthogonal voltages V_x and V_y, for OPD = 12.9 mm and p_0 = 2280 Pa. (b) Plot of the points (V_x, V_y), which trace a circle arc, together with the fitted circle. (c) Fourier transforms of the $V_i(t)$ and of the angular deflection $\Phi(t)$ for OPD = 12.9 mm and p_0 = 2280 Pa (sensor #1) and p_0 = 312 Pa (sensor #2). The weak signals at the third harmonic are indicated as $3f_{0,\#1}$ and $3f_{0,\#2}$ for sensor #1 and #2, respectively.

transforms for sensor #2 are included as well for reference pressure 312 Pa. Apart from the fundamental frequency (1.3 and 0.77 MHz for sensor #1 and #2, respectively), the transforms also show peaks for the second and third harmonic, albeit a very small peak for the third harmonic. Peaks at the harmonics agree with the Bessel function expansion referred to in Appendix A. To obtain the angular deflection $\Phi(t)$ we follow Section 3.4.1, leading to the Fourier transforms in Fig. 3.5(c), upper panel. At the fundamental frequency the transforms show a sharp peak. Its height is the angular deflection's amplitude and amounts to $\Phi_0 = (0.69 \pm 0.04)$ radian and $\Phi_0 = (0.62 \pm 0.05)$ radian for sensor #1 and #2, respectively. This is the main interrogation result for these experimental conditions.

For all other pressures we determined the $\Phi(t)$ traces and the corresponding amplitudes Φ_0 for both sensors. For sensor #1, Fig. 3.6(a) shows the main plot of Φ_0 versus p_0. The pressure range is 2.3 - 5750 Pa. Fig. 3.6(b) zooms in on the lower pressures. The straight lines through the origin are fits to those data points showing the linear behavior discussed in Appendix A. The slopes $\partial\Phi_0/\partial p_0$ of the fitted lines, which are the sensitivities of sensor #1 for these OPDs, are given in Table 1, along with the sensitivities of sensor #2 and other parameters of the two sensors. For sensor #2, a comparable data set is shown in Fig. 3.6(c,d) for the pressure range 1.2 - 775 Pa. The plots indicate that sensor #2 is more sensitive than sensor #1. This arises from the larger membrane diameter of sensor #1, which results in a
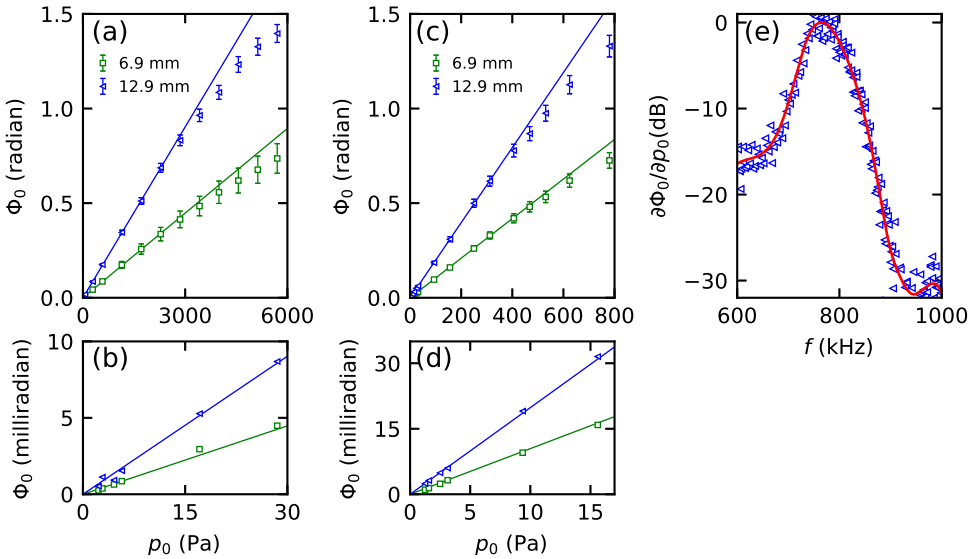
Figure 3.6: Main results of the interrogation of the sensors: (a) amplitude of the angular deflection Φ_0 for sensor #1 as a function of the pressure amplitude p_0 of 1.3 MHz ultrasound. (b) Zoom-in of (a) for the pressure range 0-30 Pa. (c) Amplitude of the angular deflection Φ_0 for sensor #2 as a function of the pressure amplitude p_0 of 0.77 MHz ultrasound. (d) Zoom-in of (c) for the pressure range 0-15 Pa. In (a)-(d) OPDs of the MZI are as stated and the lines are fitted straight lines through the origin. (e) Sensitivity as a function of frequency of sensor #2 for OPD = 12.9 mm.

Table 3.1: Parameters obtained for sensors #1 and #2: $\partial\Phi_0/\partial p_0$ is the sensor sensitivity, $\partial\delta_0/\partial p_0$ is the amplitude of the resonance-wavelength modulation of the sensor per unit of pressure, while $\kappa_{exp.}$ and $\kappa_{theo.}$ are the experimental and theoretical correction factors, respectively, which relate to Eq.(3.14). The uncertainty in $\partial\delta_0/\partial p_0$ was omitted, since its contribution to the uncertainty of $\kappa_{exp.}$ is negligible.

OPD (mm)	Parameter	Sensor #1	Sensor #2
6.9	$\partial\Phi_0/\partial p_0$	0.15 ± 0.02	1.04 ± 0.06
12.9	(milliradian/Pa)	0.30 ± 0.01	1.98 ± 0.08
-	$\partial\delta_0/\partial p_0$ (fm/Pa)	5.4	25.9
6.9	$\kappa_{exp.}$	0.65 ± 0.3	0.45 ± 0.03
12.9		0.60 ± 0.02	0.44 ± 0.02
6.9	$\kappa_{theo.}$	1.07	1.03
12.9		1.26	1.16

larger membrane deflection per unit of pressure. Further, the sensitivity is higher for the larger OPD for both devices. This agrees with Eq. (3.14), which indicates that the ratio Φ_0/OPD is constant for a constant δ_0. The sub-linear behavior in the plots above a certain pressure indicates that in that range the amplitude of the resonance-wavelength modulation is such that the bandwidth of the FBG becomes limiting. The minimum pressures we succeed to detect in these measurements are 2.3 and 1.2 Pa for sensor #1 and #2, respectively, detection limits comparable to the one reported in [7]. The present detection limit is determined noise, both electronic and shot-noise. We also observed sources of disturbing signals external to the interrogator. The order of magnitude of the spurious signals is a few mV, comparable to the voltage values for small pressure amplitudes.

The data shown in Fig. 3.6(a)-(d) were obtained using monochromatic continuous wave ultrasound, chosen at the frequency of the membrane's maximum deflection. The sensors, however, are broadband owing to the membrane's intrinsic loss. This property is apparent from the sensitivity as a function of frequency, which for sensor #2 is shown in Fig. 3.6(e). The function plotted is $\partial\Phi_0/\partial p_0$, normalized to unity at its maximum. It was measured using continuous waves and a frequency sweep. The function has the typical shape for a damped resonator. The peak occurs at 0.77 MHz, while the -6 dB bandwidth is 14.5%. This sensitivity curve and the one in [7] for the same sensor are very close to each other. We note that the bandwidth of the sensor enables application of tailored ultrasound pulses, as may be more appropriate for later imaging. If for certain applications a larger bandwidth is needed, it can for example be increased by adding a lossy layer to the membrane.

We now discuss the correction factor κ occurring in Eq. (3.14) and finally, in relation to κ, make further comments on the sensitivities $\partial\Phi_0/\partial p_0$ listed in Table 3.1.

From Eq. (3.14), the correction factor can be rewritten as:

$$\kappa = 2\pi OPD \frac{\partial \delta_0}{\partial p_0}\left[\lambda_r^2 \frac{\partial \Phi_0}{\partial p_0}\right]^{-1},\tag{3.15}$$

where the missing ingredient is $\partial \delta_0/\partial p_0$. The pressure dependence of δ_0 is derived using the modulation method detailed in Appendix B, for low pressures leading to linear behavior and the derivatives $\partial \Phi_0/\partial p_0$ listed in Table 1. For the two sensors and for either OPD we thus obtain the experimental values $\kappa_{exp.}$ listed in Table 1, to be compared with the listed values $\kappa_{theo.}$ taken from Appendix A (discussed there in relation to Fig. 3.7). The $\kappa_{exp.}$ values for sensor #1 exceed those of sensor #2, in agreement with the behaviour of $\kappa_{theo.}$. Further, on average the ratio of the values is 0.47 for sensor #1 and 0.61 for sensor #2. In our opinion, the agreement to much better than one order of magnitude validates the mathematical description of Appendix A in presenting the proper physics picture.

The ratio of the experimental sensitivities in Table 3.1 for the two OPDs equals 0.50 and 0.53 for sensor #1 and sensor #2, respectively. The ratio of the theoretical sensitivities can be obtained using the above relation between κ and $\partial \Phi_0/\partial p_0$ (where we use $\kappa_{theo.}$). This yields for the theoretical ratio 0.63 and 0.60 for sensor #1 and sensor #2, respectively. The relative difference between the theoretical and experimental sensitivity ratios is 18% on average. This indicates a high degree of consistency of our description of the operation of the interrogator and the actual interrogation experiments.

Conclusion

We interrogated two silicon ring-resonator sensors for ultrasound in the MHz range using an interrogator based on a fiber Mach-Zehnder interferometer (MZI), by applying the procedure based on our mathematical description of the interrogator operation in Appendix A. According to the geometrical interpretation of the operation, the amplitude of the angular deflection Φ_0 on the circle arc periodically traced in the plane of the two orthogonal interrogator voltages, is the principal sensor signal. Φ_0 is proportional to the amplitude of the resonance-wavelength modulation of the sensor in response to the ultrasound. The main interrogation results are the linear relations between Φ_0 and the pressure amplitude of continuous wave ultrasound, in a broad pressure range and for optical path differences (OPDs) of the MZI of 6.9 and 12.9 mm. The minimum detected pressures is 1.2 Pa. For sensor #1, the sensitivity amounts to 0.15 and 0.30 milliradian/Pa, for OPDs of 6.9 and 12.9 mm, respectively. For sensor #2, the sensitivity is 1.04 and 1.98 milliradian/Pa for these OPDs. This higher sensitivity for the larger OPD is accompanied by a lower output voltages of the MZI, in agreement with the prediction in Appendix A. This suggests a trade-off between sensitivity and signal strength, for which in future a brighter broadband source will be helpful, also for avoiding the EDFA we use now.

This work on the fiber interrogator is an important step towards an integrated photonics interrogator. The architecture of an integrated photonics version can be similar to the fiber version but should be much smaller so that the environmental

phase drift we have encountered here will be much less severe. The ultrasound sensors should then be equipped with a drop port, which gives a peak in the transmission. Interrogating a dip is a major issue. The optical background around the minimum is also amplified by the EDFA and has no information about ring resonance. As a result, a high-optical gain applied can quickly saturate the analogue-to-digital converters of the acquisition system. To overcome this issue, we used a high-pass electric filter (cut frequency at 1kHz) at the input of the data acquisition system. The FBG filter has a very limited FHMW (200 nm) compared to the ring FHMW (120 pm), limiting the sensor's dynamic range. Furthermore, as the spectra of the ring and the FBG filter feature similar FWHM, their coherence lengths are similar, distorting the function $\hat{F}(\widetilde{\delta\lambda_r})$, as described in Appendix A. It can be shown that such distortion is the cause of the circle centres to be dependent on the thermal phase drift. These effects have been handled by fitting a circle to the Lissajous $(V_x(t), V_y(t))$ in order to retrieve the radius and the circle centre; and by introducing a correction factor, accounting for the deformation of the circle arc. The disturbance of the optical background could be avoided by using an FBG with a wider FWHM, which reduces the coherence length of the optical background and increasing the sensor's dynamic range.

Appendix A : Mathematical description of the operation of the fiber interrogator

In this Appendix we present a mathematical description of the operation of the fiber interrogator when interrogating a ring-resonator sensor in the pass-port configuration. Based on the overall signal flow we arrive at the three outputs of the MZI, of which specific linear combinations yield the signal that is a measure of the amplitude of the applied ultrasound waves. The interrogation procedure we follow in the main text is based on this Appendix. Reproducing Eqs. (3.3), (3.7) and (3.8) of the main text, the latter for $N = 8$ and $\lambda_0 = \lambda_r$, gives

$$T_{\text{pass}}(\lambda, \widetilde{\delta\lambda_r}) = \frac{\left(\lambda - \lambda_r - \widetilde{\delta\lambda_r}(t)\right)^2 + \varepsilon(\gamma_r/2)^2}{\left(\lambda - \lambda_r - \widetilde{\delta\lambda_r}(t)\right)^2 + (\gamma_r/2)^2} \tag{3.16}$$

$$T_{MZI,i}(\lambda) = \frac{1}{3}\left[p + q\cos\left(\xi\lambda + \varphi_i + \varphi_e\right)\right] \tag{3.17}$$

with $\phi_i = 0°, 120°, -120°$ for $i = 1, 2, 3$.

$$R_{\text{FBG}} = \frac{1}{1 + \left(\frac{\lambda - \lambda_r}{\gamma_{FBG}/2}\right)^8}. \tag{3.18}$$

Eq. (3.16) includes the resonance-wavelength modulation $\widetilde{\delta\lambda_r} \equiv \widetilde{\delta\lambda_r}(t) = \delta_0\sin(2\pi f_0 t)$ resulting from application of ultrasound waves of frequency f_0 . Following the signal path in Fig. 3.3 and using the integrating property of the photodetectors, we can write the time-dependent output voltage of the TIAs as

$$V_i(\widetilde{\delta\lambda_r}) = \alpha P_{BBS} R_{ph} G \int_0^\infty R_{FBG}(\lambda) T_{pass}(\lambda, \widetilde{\delta\lambda_r}) T_{MZI,i}(\lambda) d\lambda. \tag{3.19}$$

Here P_{BBS} is the power density of the broadband source, supposed constant in the range the FBG spectrum. R_{ph} is the responsivity of the photodetectors, G the combined gain of the EDFA and TIA, while α is a transmission coefficient of the overall fiber optic circuit. In the following we drop the prefactors of the integral, since later these cancel when extracting Φ_0, which is the principal sensor signal defined below. Cancellation of prefactors becomes clear in Section 3.4.1 of the main text. Also dropping the factor 1/3 of $T_{MZI,i}$ and the subscripts FBG and pass, this leads to $I_i(\widetilde{\delta\lambda_r})$, the ith component of the integral proportional to the voltage $V_i(\widetilde{\delta\lambda_r})$

$$
\begin{aligned}
I_i &= \int_0^\infty R(\lambda) T(\lambda, \widetilde{\delta\lambda_r}) \left[p + q \cos(\xi\lambda + \varphi_i + \psi_e) \right] d\lambda \\
&= p \int_0^\infty R(\lambda) T(\lambda, \widetilde{\delta\lambda_r}) d\lambda + q \int_0^\infty R(\lambda) T(\lambda, \widetilde{\delta\lambda_r}) \cos(\xi\lambda + \varphi_i + \psi_e) d\lambda \\
&= p\, I_\alpha(\widetilde{\delta\lambda_r}) + q\, I_{\beta,i}(\widetilde{\delta\lambda_r}).
\end{aligned}
\tag{3.20}
$$

Here we have used

$$I_\alpha(\widetilde{\delta\lambda_r}) = \int_0^\infty R(\lambda) T(\lambda, \widetilde{\delta\lambda_r}) d\lambda \tag{3.21}$$

$$
\begin{aligned}
I_{\beta,i}(\widetilde{\delta\lambda_r}) &= \int_0^\infty R(\lambda) T(\lambda, \widetilde{\delta\lambda_r}) \cos(\xi\lambda + \varphi_i + \psi_e) d\lambda \\
&= Re\left\{ e^{i(\varphi_e + \psi_e)} \int_0^{+\infty} R(\lambda) T(\lambda, \widetilde{\delta\lambda_r}) e^{i\xi\lambda} d\lambda \right\}.
\end{aligned}
\tag{3.22}
$$

By substituting the expressions for $T(\lambda, \widetilde{\delta\lambda_r})$ and $R(\lambda)$ from Eqs. (3.16) and (3.18) into Eqs. (3.21) and (3.22), we obtain

$$\hat{J} \equiv \int_0^\infty R(\lambda) T(\lambda, \widetilde{\delta\lambda_r}) e^{i\xi\lambda} d\lambda =$$

$$\int_0^\infty \frac{\left(\lambda - \lambda_r - \widetilde{\delta\lambda_r}\right)^2 + \varepsilon(\gamma_r/2)^2}{\left(\lambda - \lambda_r - \widetilde{\delta\lambda_r}\right)^2 + (\gamma_r/2)^2} \frac{e^{i\xi\lambda}}{1 + \left(\frac{\lambda - \lambda_r}{\gamma_{FBG}/2}\right)^8} d\lambda. \tag{3.23}$$

The integrals $I_\alpha(t)$ and $I_{\beta,i}(t)$ can then be written as

$$I_\alpha(t) = \hat{J}\big|_{\xi=0} \tag{3.24}$$

$$I_{\beta,i}(t) = Re\left\{ e^{i(\varphi_e + \psi_e)} \hat{J} \right\}. \tag{3.25}$$

Using the fact that the integrand in Eq. (3.23) is vanishingly small for $\lambda \leq 0$, we can integrate $\hat{J}$ from $(-\infty, \infty)$[2]. Making the substitution $\lambda - \lambda_r \to z$ in Eq. (3.23) and using contour integration we obtain

$$\hat{J}/e^{i\xi\lambda_r} \equiv \hat{K} = \oint_C \frac{\left(z - \widetilde{\delta\lambda}_r\right)^2 + \varepsilon(\gamma_r/2)^2}{\left(z - \widetilde{\delta\lambda}_r\right)^2 + (\gamma_r/2)^2} \frac{e^{i\xi z}}{1 + \left(\frac{z}{\gamma_{FBG}/2}\right)^8} dz = \oint_C f(z)dz. \quad (3.26)$$

The contour C is the upper half circle of radius R in the complex plane, including the interval $[-R, R]$ of the real axis, taken in the limit $R \to \infty$. The poles of $f(z)$ arise from the RR transmission function and FBG reflection function, respectively, and for the contour C occur for $z_{RR} = \widetilde{\delta\lambda}_r + i\gamma_r/2$ (RR pole) and $z_{FBG,k} = (\gamma_{FBG}/2) \exp\left[i\pi\left(k + 1/2\right)/4\right]$, $k = 0, 1, 2, 3$ (FBG poles). Using Cauchy's residue theorem, the integral is evaluated to obtain

$$\oint_C f(z)dz = \hat{F}(\widetilde{\delta\lambda}_r) + \hat{G}(\widetilde{\delta\lambda}_r). \quad (3.27)$$

Here $\hat{F}(\widetilde{\delta\lambda}_r)$ and $\hat{G}(\widetilde{\delta\lambda}_r)$ are given by:

$$\hat{F}(\widetilde{\delta\lambda}_r) = -\frac{\pi\gamma_r}{2} \frac{(1 - \varepsilon) e^{-\xi\gamma_r/2}}{1 + \left(\frac{\widetilde{\delta\lambda}_r + i\gamma_r/2}{\gamma_{FBG}/2}\right)^8} e^{i\xi\widetilde{\delta\lambda}_r} \equiv \hat{E}(\widetilde{\delta\lambda}_r)e^{i\xi\widetilde{\delta\lambda}_r} \quad (3.28)$$

$$\hat{G}(\widetilde{\delta\lambda}_r) = -i\frac{\pi}{4} \sum_{k=0}^{3} \frac{z_{FBG,k}\left[\left(z_{FBG,k} - \widetilde{\delta\lambda}_r\right)^2 + \varepsilon(\gamma_r/2)^2\right]}{\left(z_{FBG,k} - \widetilde{\delta\lambda}_r\right)^2 + (\gamma_r/2)^2} e^{i\xi Re\left(z_{FBG,k}\right)} e^{-\xi Im\left(z_{FBG,k}\right)}. \quad (3.29)$$

The complex functions $\hat{F}(\widetilde{\delta\lambda}_r)$ and $\hat{G}(\widetilde{\delta\lambda}_r)$ are time-domain (oscillatory) signals resulting from light interference in the 3×3 coupler, the time dependence being expressed by $\widetilde{\delta\lambda}_r(t)$.

The oscillatory behavior of $\hat{F}(\widetilde{\delta\lambda}_r)$ is recognized to the full extent from the Bessel function expansions [23] of $\exp(i\xi\widetilde{\delta\lambda}_r) = \cos\left[\xi\lambda\delta_0 \sin(2\pi f_0 t)\right] + i \sin\left[\xi\lambda\delta_0 \sin(2\pi f_0 t)\right]$, which apart from terms at the fundamental frequency also give harmonics. The factor $\exp(i\xi\widetilde{\delta\lambda}_r)$ is multiplied by the envelope $\hat{E}(\widetilde{\delta\lambda}_r)$, implicitly defined in Eq. (3.28). The envelope includes both RR and FBG parameters and attenuates the oscillations with increasing δ_0 and increasing OPD. This OPD-dependence follows from the damping factor $\exp(-\xi\gamma_r/2) = \exp(-OPD/L_{c,r})$. Here $L_{c,r}$ is the coherence length related to the wavelength and spectral width of the ring's resonance dip. $L_{c,r}$ limits the OPD of the MZI for which fringes in traces $V_i(t)$ can be resolved experimentally. For the resonance we are using for the sensing (Fig. 3.2(b) we have $L_{c,r} \approx 6$ mm.

$\hat{G}(\widetilde{\delta\lambda}_r)$ arises from interference of waves within the bandwidth of the FBG, each FBG pole giving rise its own interference signal, damped by the factor $\exp\left[-\xi Im\left(z_{FBG,k}\right)\right]$

---

[2]The same approximation is applied to all integrals from $(-\infty, \infty)$ in Chapters 4 and 5.

$= \exp\left(-OPD/L_{c,\text{FBG}}^{k}\right)$. Here $L_{c,\text{FBG}}^{k}$ is the coherence length related to the width of the FBG spectrum and due to the kth FBG pole. It is given by

$$L_{c,FBG}^{k} = \frac{\lambda_r^2}{2\pi Im(z_{FBG,k})} = \frac{\lambda_r^2}{\pi\gamma_{FBG}\sin\left[\frac{\pi}{4}(k+1/2)\right]}. \tag{3.30}$$

For $k = 0$, we obtain $L_{c,FBG}^{k} \approx 10$ mm.

We have studied the complex functions $\hat{F}(\widetilde{\delta\lambda}_r)$, $\hat{G}(\widetilde{\delta\lambda}_r)$ and their sum $\hat{K}(\widetilde{\delta\lambda}_r)$. The behavior of these functions in the complex plane is exemplified in Fig. 3.7 by plots for OPDs of 6.9 and 12.9 mm, the values used in the experiments (Section 3.4.2 of the main text). The values of the other parameters used in obtaining the data points of the functions are given in the figure caption. It can be seen that $\hat{F}(\widetilde{\delta\lambda}_r)$ and $\hat{K}(\widetilde{\delta\lambda}_r)$ resemble a circle arc, whereas $\hat{G}(\widetilde{\delta\lambda}_r)$ is like a short line segment given by $Re\{\hat{G}(\widetilde{\delta\lambda}_r)\} \approx constant$. Resulting from a single period of $\widetilde{\delta\lambda}_r(t) = \delta_0\sin(2\pi f_0 t)$, where $\delta_0 = 40$ pm is approximately the maximum amplitude in the experiment, the arcs and line segments are symmetric with respect to the real axis.

$\hat{F}(\widetilde{\delta\lambda}_r)$ would be a circle arc if it were given by solely the factor $\exp(i\xi\widetilde{\delta\lambda}_r)$, implying that deviation from an arc is due to the envelope $\hat{E}(\widetilde{\delta\lambda}_r)$. To visualize the deviation, Fig. 3.7 also shows the circle $\hat{F}_0(\widetilde{\delta\lambda}_r) = R_{F0}\exp\{i\xi\widetilde{\delta\lambda}_r\}$, defined by the radius $R_{F0} = \hat{E}(0)$. Deviation form a circle is present for either OPD, albeit most clearly for OPD=6.9 mm.

The rather close resemblance of the sum $\hat{K}(\widetilde{\delta\lambda}_r) = \hat{F}(\widetilde{\delta\lambda}_r) + \hat{G}(\widetilde{\delta\lambda}_r)$ to a circle arc for either OPD suggests as a first approximation

$$\hat{K}(\widetilde{\delta\lambda}_r) = \hat{E}(\widetilde{\delta\lambda}_r)e^{i\xi\widetilde{\delta\lambda}_r} + \hat{G}(\widetilde{\delta\lambda}_r) \cong \hat{F}_0(\widetilde{\delta\lambda}_r) + z_0 = R_{F0}e^{i\xi\widetilde{\delta\lambda}_r} + z_0. \tag{3.31}$$

Here $z_0 = |z_0|\exp(i\varphi_{z0})$ is the circle center's coordinate, which in this approximation can be taken constant and real. Eq. (3.31) for the function $\hat{K}(\widetilde{\delta\lambda}_r)$ has a simple geometrical interpretation: the product $\xi\widetilde{\delta\lambda}_r$ is as the instantaneous angular deflection of the periodic motion of the point $\hat{K}(\widetilde{\delta\lambda}_r)$ on the circle arc, induced by the ultrasound. In Fig. 3.7 the dashed circles through the data points of $\hat{K}(\widetilde{\delta\lambda}_r)$ are fits of a circle to these points, where the circle is given by the right hand side of Eq. (3.31) but R_{F0} is now treated as a fit parameter. Very close similarity to a circle is quantified by the average deviation of 0.1% from the points from the circle.

Although the approximation given by Eq. (3.31) and the periodic motion on the circle arc already present the physics picture, refinement is needed, since the functions $\hat{E}(\widetilde{\delta\lambda}_r)$ and $\hat{G}(\widetilde{\delta\lambda}_r)$ are not constant and thus distort $\hat{K}(\widetilde{\delta\lambda}_r)$. Further, $\hat{E}(\widetilde{\delta\lambda}_r)$ and $\hat{G}(\widetilde{\delta\lambda}_r)$ contribute to the angular deflection of $\hat{K}(\widetilde{\delta\lambda}_r)$, modifying the total bi-directional deflection angle $2\xi\delta_0$ of $\hat{F}_0(\widetilde{\delta\lambda}_r)$ to the value $2\Phi_0$ of $\hat{K}(\widetilde{\delta\lambda}_r)$. In Fig. 3.7 the deflection angles have been indicated. Φ_0 is the amplitude of the periodic deflection $\Phi(t) = \Phi_0\sin(2\pi f_0 t)$ for $\hat{K}(\widetilde{\delta\lambda}_r)$. Assuming that the sensor operates in the linear response regime, characterized by small membrane deflections and small resonance-wavelength modulation compared to the width of the FBG spectrum, the instantaneous deflection $\Phi(t)$ is expected to be proportional to
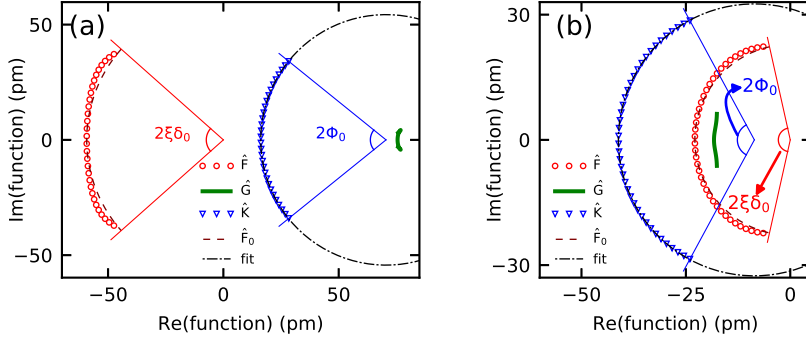
Figure 3.7: Plots of the functions $\hat{F}$, $\hat{G}$, $\hat{K}$ and $\hat{F}_0$ in the complex plane for (a) OPD=6.9 mm and (b) OPD=12.9 mm. Zero angular deflection of the functions occurs for the point where Im(function)=0. The black dash-dotted curve is a fit of a circle to the data points of $\hat{K}$, giving radii of 54.3 and 32.6 pm for the OPDs of 6.9 and 12.9 mm, respectively. For $\hat{F}_0$ the radii are 60.1 and 23.2 pm, for these OPDs. In the plot the total bi-directional angular deflections $2\xi\delta_0$ and Φ_0 for the functions $\hat{F}_0$ and $\hat{K}$, respectively, are indicated. In calculating the functions, the following parameters were used: $\gamma_r = 122$ pm, $\gamma_{FBG} = 207$ pm, $\varepsilon = 0.043$ (the three values in section 3.2) and $\delta_0 = 40$ pm.

$\widetilde{\delta\lambda}_r(t) = \delta_0 \sin(2\pi f_0 t)$. δ_0 in turn, is expected to be proportional to the amplitude p_0 of the ultrasound pressure. Fig. 3.7 shows that $2\Phi_0 < 2\xi\delta_0$, the inequality being marginally observable for OPD=6.9 mm. The modification of the total deflection angle suggests to introduce the correction factor $\kappa = \xi\delta_0/\Phi_0$. The angles in Fig. 3.7 give $\kappa = 1.07$ and $\kappa = 1.26$ for the OPDs of 6.9 and 12.9 mm, respectively. Similarly, for sensor #2, we obtain $\kappa = 1.03$ and $\kappa = 1.16$ for these OPDs, which are some smaller than for sensor #1. This decrease of κ arises from the smaller γ_r of sensor #2 ($\gamma_r = 96$ pm).

In the experiment, the sensor is interrogated by measuring the voltages V_i. Based on the considerations leading to Eq. (3.27), the V_i are described by the function $\hat{J} = \exp(i\xi\lambda_r)\hat{K}(\widetilde{\delta\lambda}_r) = \exp(i\xi\lambda_r)\left[\hat{F}(\widetilde{\delta\lambda}_r) + \hat{G}(\widetilde{\delta\lambda}_r)\right]$. The function $\hat{J}$, via its dependence on $\exp(i\xi\widetilde{\delta\lambda}_r)$ or equivalently on $\exp(i\Phi(t))$, in principle contains all information on the ultrasound sensed by the sensor. From the V_i the following functions are constructed:

$$V_x(t) = 2V_1 - V_2 - V_3, \tag{3.32}$$

$$V_y(t) = \sqrt{3}\,(V_3 - V_2). \tag{3.33}$$

In $V_x(t)$ and $V_x(t)$ the contributions from $I_\alpha(t)$ cancel, as these are independent of φ_i (see Eq. (3.24)). Actually, $I_\alpha(t)$ *does* give an appreciable contribution to the *total* integral $I_i(t)$, while $I_\alpha(t)$ carries no useful information on $\widetilde{\delta\lambda}_r$ and thus limits the smallest measurable $\widetilde{\delta\lambda}_r$.

We now rewrite $I_{\beta,i}$ of Eq.(3.25) in the approximation given by (3.31), using

Eqs. (3.26)-(3.28):

$$\begin{aligned}
I_{\beta,i} &= Re\left\{e^{i(\varphi_i+\psi_e)}\hat{J}\right\} \\
&= Re\left\{e^{i(\varphi_i+\psi_e+\xi\lambda_r)}\left[\hat{E}(\delta\widetilde{\lambda}_r)e^{i\xi\delta\widetilde{\lambda}_r} + \hat{G}(\delta\widetilde{\lambda}_r)\right]\right\} \\
&\cong Re\left\{e^{i(\varphi_i+\psi_e+\xi\lambda_r)}\left[R_K e^{i\Phi(t)} + z_0\right]\right\}.
\end{aligned}$$ (3.34)

Here R_K is used now instead of R_{F0} to emphasize that we are dealing with $\hat{K}(\delta\widetilde{\lambda}_r)$. Based on the definition of κ we have $\Phi(t) = \xi\delta\widetilde{\lambda}_r(t)/\kappa$. Using Eq. (3.34) and omitting the prefactor q of Eq. (3.20), $V_x(t)$ and $V_y(t)$ can be written as:

$$\begin{aligned}
V_x(t) &= 3R_K \cos\left(\Phi(t) + \psi_e + \xi\lambda_r\right) + 3|z_0|\cos\left(\varphi_{z_0} + \psi_e + \xi\lambda_r\right) \\
&= 3Re\left\{e^{i(\xi\lambda_r+\psi_e)}\hat{K}(\Phi(t))\right\},
\end{aligned}$$ (3.35)

$$\begin{aligned}
V_y(t) &= 3R_K \sin\left(\Phi(t) + \psi_e + \xi\lambda_r\right) + 3|z_0|\sin\left(\varphi_{z_0} + \psi_e + \xi\lambda_r\right) \\
&= 3Im\left\{e^{i(\xi\lambda_r+\psi_e)}\hat{K}(\Phi(t))\right\}.
\end{aligned}$$ (3.36)

$V_x(t)$ and $V_y(t)$ oscillate around levels x_0 and y_0, respectively, given by

$$x_0 = 3|z_0|\cos\left(\varphi_{z_0} + \psi_e + \xi\lambda_r\right),$$ (3.37)

$$y_0 = 3|z_0|\sin\left(\varphi_{z_0} + \psi_e + \xi\lambda_r\right).$$ (3.38)

Eqs. (3.35) and (3.36) show that $V_x(t)$ and $V_y(t)$ are orthogonal, a known property [16] for the combinations of outputs of a 3×3 coupler defined by Eq. (3.32) and (3.33). Further, in time, the point $\left(V_x(t), V_y(t)\right)$ traces a circle arc in the $V_x - V_y$ plane, of radius $3R_K$ and with center (x_0, y_0). Equivalently, the circle arc according to these equations is a partial plot of the function $3\exp\left(i\xi\lambda_r + i\psi_e\right)\hat{K}(\Phi(t))$ in the complex plane. Experimentally, measuring $V_x(t)$ and $V_y(t)$ leads to $\Phi(t)$, which yields Φ_0 by Fourier transformation. Details about the interrogation procedure in practice are given in Section 3.4.1 of the main text.

As described in Section 3.3.1, a high pass filter is applied after the TIAs. The signal components x_0 and y_0, which are close to DC in view of the slow drift of the environmental phase ψ_e, will thus be removed. However, by rewriting the terms with $\sin\left(\Phi(t) + \xi\lambda_r + \psi_e\right)$ and $\cos\left(\Phi(t) + \xi\lambda_r + \psi_e\right)$ in Eqs. (3.35) and (3.36) towards linear combinations of $\sin\left(\Phi(t)\right)$ and $\cos\left(\Phi(t)\right)$, and by using Bessel function expansions [23], it can be shown that signal components at the ultrasound frequency f_0 and its harmonics result. These components, which survive the high pass filtering, are modulated by $\sin\left(\xi\lambda_r + \psi_e\right)$ or $\cos\left(\xi\lambda_r + \psi_e\right)$ and thus still depend on the environmental phase. This is not an issue, since the time scale for interrogation of the sensor is much shorter than the time scale of the drift. Thus, the angular deflection amplitude Φ_0, which is the principal sensor signal, can be obtained for IVUS imaging.

Appendix B : Modulation method for measuring the amplitude of the resonance-wavelength modulation

The modulation method is based on laser induced power modulation, described in Chapter 2, operated in a point on the steep and linear flank of the transmission dip (see Fig. 3.2b). The laser also used for characterizing the MZI (Section 3.3.2) actuates the sensor and is tuned to operation point $\lambda_{\text{op.}} = 1550.14$ nm. We measure the modulated power transmitted through the sensor using a photodetector (New Focus, 1811-FC-AC). The resonance-wavelength modulation according to this method is

$$\widetilde{\delta\lambda}_r(t) \approx \frac{T_{\text{pass}}^0(\lambda_{\text{op.}}) - T_{\text{pass}}(\lambda_{\text{op.}}, t)}{\partial T_{\text{pass}}^0/\partial\lambda\big|_{\lambda_{\text{op.}}}} \tag{3.39}$$

Eq. (3.39) implies that $\widetilde{\delta\lambda}_r$ can be obtained from a time trace $T_{\text{pass}}(\lambda_{\text{op.}}, t)$, and from the static transmission value $T_{\text{pass}}^0(\lambda_{\text{op.}})$ and its derivative $\partial T_{\text{pass}}^0/\partial\lambda\big|_{\lambda_{\text{op.}}}$. The latter two quantities follow from the static transmission curve in Fig. 3.2b, which is also measured using the laser setup just described, albeit that the laser wavelength is swept and the DC mode of the detector is used. The modulation amplitude δ_0 is obtained as the peak value of the Fourier transform of $\widetilde{\delta\lambda}_r(t)$ at 1.3 and 0.77 MHz for sensors #1 and #2, respectively.

References

[1] T. Tsuchizawa, K. Yamada, T. Watanabe, S. Park, H. Nishi, R. Kou, H. Shinojima, and S.-i. Itabashi, *Monolithic Integration of Silicon-, Germanium-, and Silica-Based Optical Devices for Telecommunications Applications,* IEEE Journal of Selected Topics in Quantum Electronics **17**, 516 (2011), conference Name: IEEE Journal of Selected Topics in Quantum Electronics.

[2] A. P. Freitas, G. B. Farias, F. G. Peternella, Y. R. R. Bustamante, D. A. Motta, and J. C. R. F. d. Oliveira, *112 Gb/s compact silicon-on-insulator coherent receiver,* in *Next-Generation Optical Networks for Data Centers and Short-Reach Links II*, Vol. 9390 (International Society for Optics and Photonics, 2015) p. 93900D.

[3] C. Koos, P. Vorreau, T. Vallaitis, P. Dumon, W. Bogaerts, R. Baets, B. Esembeson, I. Biaggio, T. Michinobu, F. Diederich, W. Freude, and J. Leuthold, *All-optical high-speed signal processing with silicon–organic hybrid slot waveguides,* Nature Photonics **3**, 216 (2009), bandiera_abtest: a Cg_type: Nature Research Journals Number: 4 Primary_atype: Research Publisher: Nature Publishing Group.

[4] V. M. N. Passaro, C. D. Tullio, B. Troia, M. L. Notte, G. Giannoccaro, and F. D. Leonardis, *Recent Advances in Integrated Photonic Sensors,* Sensors **12**, 15558 (2012), number: 11 Publisher: Multidisciplinary Digital Publishing Institute.

[5] A. Dhakal, A. Raza, F. Peyskens, A. Z. Subramanian, S. Clemmen, N. L. Thomas, and R. Baets, *Efficiency of evanescent excitation and collection of spontaneous Raman scattering near high index contrast channel waveguides,* Optics Express **23**, 27391 (2015), publisher: Optical Society of America.

[6] M. Boerkamp, T. v. Leest, J. Heldens, A. Leinse, M. Hoekman, R. Heideman, and J. Caro, *On-chip optical trapping and Raman spectroscopy using a TripleX dual-waveguide trap,* Optics Express **22**, 30528 (2014), publisher: Optical Society of America.

[7] S. M. Leinders, W. J. Westerveld, J. Pozo, P. L. M. J. van Neer, B. Snyder, P. O'Brien, H. P. Urbach, N. de Jong, and M. D. Verweij, *A sensitive optical micro-machined ultrasound sensor (OMUS) based on a silicon photonic ring resonator on an acoustical membrane,* Scientific Reports **5** (2015), 10.1038/srep14328.

[8] M. Perry, P. Orr, P. Niewczas, and M. Johnston, *High-Speed Interferometric FBG Interrogator With Dynamic and Absolute Wavelength Measurement Capability,* Journal of Lightwave Technology **31**, 2897 (2013), publisher: IEEE.

[9] A. Dandridge, *Fiber optic sensors based on the mach-zehnder and michelson interferometers,* in *Fiber Optic Sensors: An Introduction for engineers and scientists*, edited by E. Udd. (Wiley, 1991).

[10] W. J. Westerveld, S. M. Leinders, P. M. Muilwijk, J. Pozo, T. C. van den Dool, M. D. Verweij, M. Yousefi, and H. P. Urbach, *Characterization of Integrated Optical Strain Sensors Based on Silicon Waveguides,* IEEE Journal of Selected Topics in Quantum Electronics **20**, 101 (2014), conference Name: IEEE Journal of Selected Topics in Quantum Electronics.

[11] ePIXfab, *epixfab website,* (2017).

[12] N. Pavarelli, J. S. Lee, M. Rensing, C. Eason, and P. A. O'Brien, *Optical and electronic packaging process for silicon photonic systems,* in *2014 The European Conference on Optical Communication (ECOC)* (2014) pp. 1–4, iSSN: 1550-381X.

[13] E. Hallynck and P. Bienstman, *Integrated Optical Pressure Sensors in Silicon-on-Insulator,* IEEE Photonics Journal **4**, 443 (2012), conference Name: IEEE Photonics Journal.

[14] C. Zhang, S.-L. Chen, T. Ling, and L. J. Guo, *Imprinted Polymer Microrings as High-Performance Ultrasound Detectors in Photoacoustic Imaging,* Journal of Lightwave Technology **33**, 4318 (2015), conference Name: Journal of Lightwave Technology.

[15] W. Bogaerts, P. DeHeyn, T. V. Vaerenbergh, K. D. Vos, S. K. Selvaraja, T. Claes, P. Dumon, P. Bienstman, D. V. Thourhout, and R. Baets, *Silicon microring resonators,* Laser and Photonics Reviews **6**, 47 (2012), arXiv:1208.0765v1 .

3

[16] R. Priest, *Analysis of fiber interferometer utilizing 3 × 3 fiber coupler,* IEEE Journal of Quantum Electronics **18**, 1601 (1982), conference Name: IEEE Journal of Quantum Electronics.

[17] Y. Li, *Light beams with flat-topped profiles,* Optics Letters **27**, 1007 (2002), publisher: Optical Society of America.

[18] A. Arbabi and L. L. Goddard, *Dynamics of Self-Heating in Microring Resonators,* IEEE Photonics Journal **4**, 1702 (2012), conference Name: IEEE Photonics Journal.

[19] A. D. Dandridge, C. C. Wang, A. B. Tveten, and A. M. Yurek, *Performance of 3 X 3 couplers in fiber optic sensor systems,* in *Tenth International Conference on Optical Fibre Sensors*, Vol. 2360 (International Society for Optics and Photonics, 1994) pp. 549–552.

[20] W. Gander, G. H. Golub, and R. Strebel, *Least-squares fitting of circles and ellipses,* BIT Numerical Mathematics **34**, 558 (1994).

[21] J. C. Lagarias, J. A. Reeds, M. H. Wright, and P. E. Wright, *Convergence Properties of the Nelder–Mead Simplex Method in Low Dimensions,* SIAM Journal on Optimization **9**, 112 (1998), publisher: Society for Industrial and Applied Mathematics.

[22] T. M. Inc., *Matlab 2014a,* (2014).

[23] F. W. J. Olver, *Bessel functions of integer order,* in *Handbook of Mathematical functions with formulas, graphs and mathematical tables*, edited by M. Abramowitz and I. Stegun (Dover Publications, 1965) pp. 266–290.

4

On-chip interrogator based on Fourier transform spectroscopy

In this paper, the design and the characterization of a novel interrogator based on integrated Fourier transform (FT) spectroscopy is presented. To the best of our knowledge, this is the first integrated FT spectrometer used for the interrogation of photonic sensors. It consists of a planar spatial hetero-dyne spectrometer, which is implemented using an array of Mach-Zehnder interferometers (MZIs) with different optical path differences. Each MZI employs a 3×3 multi-mode interferometer, allowing the retrieval of the complex Fourier coefficients. We derive a system of non-linear equations whose solution, which is obtained numerically from Newton's method, gives the modulation of the sensor's resonances as a function of time. By taking one of the sensors as a reference, to which no external excitation is applied and its temperature is kept constant, about 92% of the thermal induced phase drift of the integrated MZIs has been compensated. The minimum modulation amplitude that is obtained experimentally is 400 fm, which is more than two orders of magnitude smaller than the FT spectrometer resolution.

4.1. Introduction

Photonic based sensors find nowadays a wide range of applications. Acoustic and ultrasound sensors [1, 2], pressure sensors [3], biochemical and gas sensors [4, 5] are examples of sensors based on optical technology. They are low cost, immune to

electromagnetic radiation, and operate under a wide range of temperatures. In this paper, we focus our attention on photonic sensors whose transmission or reflection spectra have a peak (or dip) in their lineshape. Examples are sensors based on fiber Bragg gratings (FBGs)[5, 6] or on integrated ring resonators [1, 2, 4]. For these sensors, it is possible to build large and multi-purpose sensor arrays by wavelength multiplexing the spectrum of the sensors [6, 7].

The photonic sensors mentioned above are designed in such a way that the signal to be sensed modulates the sensor's resonance wavelength. Interrogation is the technique of demodulating and demultiplexing the response of an array of photonic sensors. Different methods have been proposed in the past. A common approach is to measure the spectrum of the sensor array using a dispersive spectrometer such as an arrayed waveguide grating (AWG)[8–10] or an echelle grating[11]. Their sensitivity to the external excitation depends on the spectral resolution of the spectrometer; higher resolution comes at the price of a larger footprint. Another approach is edge filtering, where the output spectra of the photonic sensors is conveyed to an optical filter whose transfer function is linear within certain range. As the spectrum of the sensor shifts due to the sensing signal, the filter converts the resonance wavelength modulation into power modulation which can be obtained by a photodetector. The main drawback is that a high sensitivity may compromise the wavelength operation range[12]. *Passaro et al* [13] reports the spectral scanning as a possible solution, which features a high sensitivity and a large wavelength operation range. On the other hand, most of these interrogators are based on thermal tuning which limits their interrogation speed to a few kHz. Another approach for interrogation is to use passive interferometers such as Mach-Zehnder interferometers. In combination with a demultiplexing element, such as an AWG, it is possible to interrogate the photonic sensors as demonstrated in [14, 15]. Despite the high sensitivity of this interrogator, special care should be taken to match the spectra of the AWG outputs to the sensors spectra. This might be an issue for integrated sensors such as ring resonators [1] since the resonance wavelength, in most of the cases, cannot be predicted during the design due to variations of the fabrication process.

The interrogation method here proposed may be applied to any sensor whose spectrum is finite and is modulated by an external signal. We demonstrate its performance using FBG sensors, but the method is equally suitable to other types of sensors such as ring resonators. To the best of our knowledge, this is the first interrogator based on integrated Fourier Transform (FT) spectroscopy. The technique is promising since it benefits from high flexibility, high sensitivity, and offers a high tolerance to variations of the fabrication process. In the past, FT spectroscopy was applied to demultiplexing FBG sensors [16, 17], but at that time, the speed of the method was limited by the mechanical speed of the mirror. Integrated photonics enables the design of new FT spectrometer implementations. The most common one consists of an array of MZIs with different optical path lengths (OPDs) [18–22]. Alternatively, [23] uses a single MZI whose OPD can be dynamically increased by using optical switches. The spectrum can be retrieved by calculating the coefficients of the Fourier cosine series from the interferogram [18, 19] or by solving a system

of linear equations [20–23]. However, since the number of MZIs is finite, the retrieved spectrum is an approximation to the actual one and a large the number of MZIs is required in order to achieve a high spectral resolution.

The design of our integrated FT spectrometer is similar to the one proposed by [24, 25], where the complex Fourier coefficients of the system are obtained by using 3×3 multi-mode interferometers (MMIs). In our case, however, instead of retrieving the spectrum, we demonstrate that the complex Fourier coefficients can be written as a sum of the individual contributions of the sensors. We obtain a coupled system of non-linear equations, whose solution gives the modulation of the sensor's resonance wavelength. The minimum modulation amplitude we experimentally retrieved is 400 fm, more than two orders of magnitude smaller than the spectral resolution of our own FT spectrometer. While the spectrometer's resolution depends on the number of MZIs and their OPDs, the system of non-linear equations is limited by the signal-to-noise ratio of the input signal and the accuracy of the coefficients experimentally obtained (see Section 4.3.2). Moreover, we demonstrate that the number of interferometers can be as small as the number of sensors, which strongly reduces the device footprint without compromising the interrogator sensitivity. Finally, we propose a novel technique for compensating the slow drift with time of the phases of the MZIs due to temperature fluctuations[1, 26].

4.2. Design and characterization of the FT spectrometer

Fig. 4.1(a) shows a picture of the FT spectrometer. The chip was fabricated in a multi-project wafer run at the Smart Photonics foundry using InP technology. Its dimensions are 4.0 mm by 4.5 mm. The chip has a total of 7 inputs, but inputs #5 and #7 are not used, as indicated in the Fig. 4.1(a). The cross-section of the waveguide at the facet of the chip is shown in Fig. 4.1(b) (the mode field diameters are 2.8 μm in the horizontal direction and 0.96 μm in the vertical direction). This waveguide makes an angle of 7 degrees with respect to a normal line perpendicular to edge of the chip, as shown in Fig. 4.1(d). The optical fiber guiding the light signal to be coupled to the chip is placed at an angle of 23 degrees with respect to the normal, avoiding that the reflections from the chip facet to be coupled back to the fiber (the angle of 23 degrees can be obtained using Snell's law, giving the fact that the effective index of the waveguide is 3.26 at 1550 nm). The waveguide at input #4 is the only waveguide which makes an angle of 90 degrees with respect to the chip edge.

By using a taper, the width of the shallow etch waveguide shown in Fig. 4.1(b) is slowly reduced to 2.0 μm, where a proprietary component, provided by Smart Photonics, couples the optical field into the deep etch waveguide shown in Fig. 4.1(c). Compared to the shallow etch waveguide, the deep etch waveguide has a higher mode confinement and it is used everywhere else in the chip. Following the optical path of the main input port (input #1) the light signal is split into nine beams using 1×2 and 2×2 MMIs (the 2×2 MMIs are indicated in the Fig. 4.1(a); all other power splitters are 1×2 MMIs) and guided to nine different Mach-Zehnder interferometers.

The chip has multiple inputs, each providing access to a specific set of MZIs (see Fig. 4.1(a) and Fig. 4.2). The main idea is to optimize the optical power budget: in Section 4.3 it is shown that the number of photonic sensors must be as large as the number of the MZIs. The multiple inputs allow the choice of the number of MZIs to be used during the interrogation. For instance, in order to interrogate up to 5 sensors, it is preferred to use input #6, through which the optical power is shared among MZIs 1-5, instead of input #1. Interrogating the photonic sensors using more MZIs than needed is possible and the extra MZIs may provide some additional information which can be used to increase slightly the signal-to-noise ratio. However, the fringe visibility of the MZIs with larger OPDs are strongly reduced (see the discussion in the end of Section 4.3.1) and better interrogation results have been obtained by using a small number of MZIs. The optical connections shown in the diagram of Fig. 4.2 indicate a non-uniform distribution of optical power for MZIs 1-5. Following the path from input #6, Fig. 4.2 shows that MZIs 4 and 5 receive as much power as MZIs 1,2 and 3; MZI 3 gets the same amount of optical power as MZIs 1 and 2. Using such distribution, MZIs with larger OPDs receive more power, mitigating the reduced visibility of the MZIs with larger OPDs.

One of the key benefits of the FT spectrometers is the large optical throughput (etendue) compared to other types of spectrometers [18, 20, 22]. The design of our FT spectrometer allows the light signal to be coupled from both sides of the chip simultaneously. In this case, it would be needed to split the signal containing the combined spectra of the sensors externally (by using a 1×2 fiber coupler, for instance). This feature has not been explored in this paper, but it could increase the interrogator performance if an additional optical gain is given for the signal to be coupled to the left side of chip, where inputs #2 - #4 provide access to MZIs with larger OPDs (input #1 must not be used, otherwise some of the MZIs would receive the light signal coming from both of chip sides). Optical power is uniformly distributed (see Fig. 4.2) for MZIs 6-9 so that a larger gain is expected for compensating the reduced visibility.

MZIs represent the heart of the on-chip FT spectroscope. The length difference between the arms range from 0.710 mm to 6.39 mm in steps of 0.710 mm. At the end of the MZI, the light signals from the two arms interfere within a 3×3 MMI (360 μm length, 11.4 μm width). The chip is glued to a printed circuit board (PCB), to which the chip pads were wire bonded. Outputs per MZI of this PCB were connected to an other PCB which contain three transimpedance amplifiers (TIAs) for the photodetectors and a pre-processing module. This module gives a linear combination of the outputs, as indicated in the schematic shown Fig. 4.1(e).

In this Section we characterize the MZIs of the FT spectrometer by considering its response to one particular wavelength λ. The transmittance for the given wavelength of l-th output of the m-th MZI is given by:

$$T_{ml}(\lambda) = \frac{1}{3}\left[1 + v_{ml}\cos\left(2\pi\frac{n_{eff,m}(\lambda)\Delta L_m}{\lambda} + \phi_l\right)\right], \qquad (4.1)$$

where v_{ml} is the visibility, $n_{eff,m}(\lambda)$ is the effective index of waveguides of the m-th MZI, ΔL_m the arms length difference of the m-th MZI, and ϕ_l is the MZI phase shift
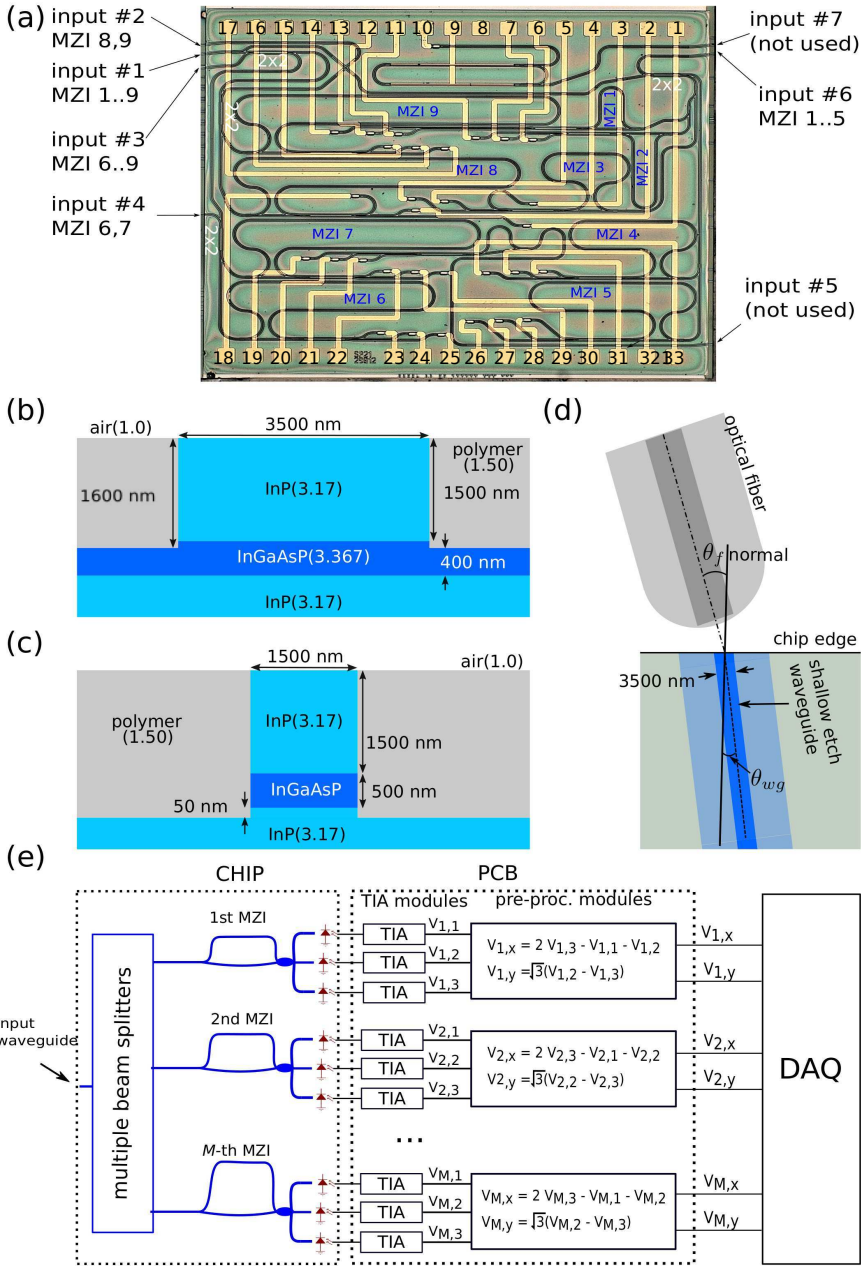
Figure 4.1: (a) Picture of the FT spectrometer chip. ΔL_m is given by $\Delta L_m = m\Delta L_1$ with $\Delta L_1 = 0.710$ mm, leading to $F_m = F_1/m$, where m is an integer number ranging from 1 to 9. The different MZIs are identified with the index m. The 2×2 MMIs are indicated in white. All other power splitters are 1×2 MMIs. (b) Cross-section of the shallow etch waveguide. The refractive indexes at the wavelength of 1550 nm are also indicated. (c) Cross-section of the deep etch waveguide. (d) Schematic of an optical fiber aligned to one of the inputs of the chip. For input #4, $\theta_{wg} = \theta_f = 0°$. For all other inputs, $\theta_{wg} = 7°$ and $\theta_f = 23°$. (e) Schematic of the FT spectrometer and the PCB that implements the TIAs and a pre-processing module. The outputs are sampled by the DAQ.

4

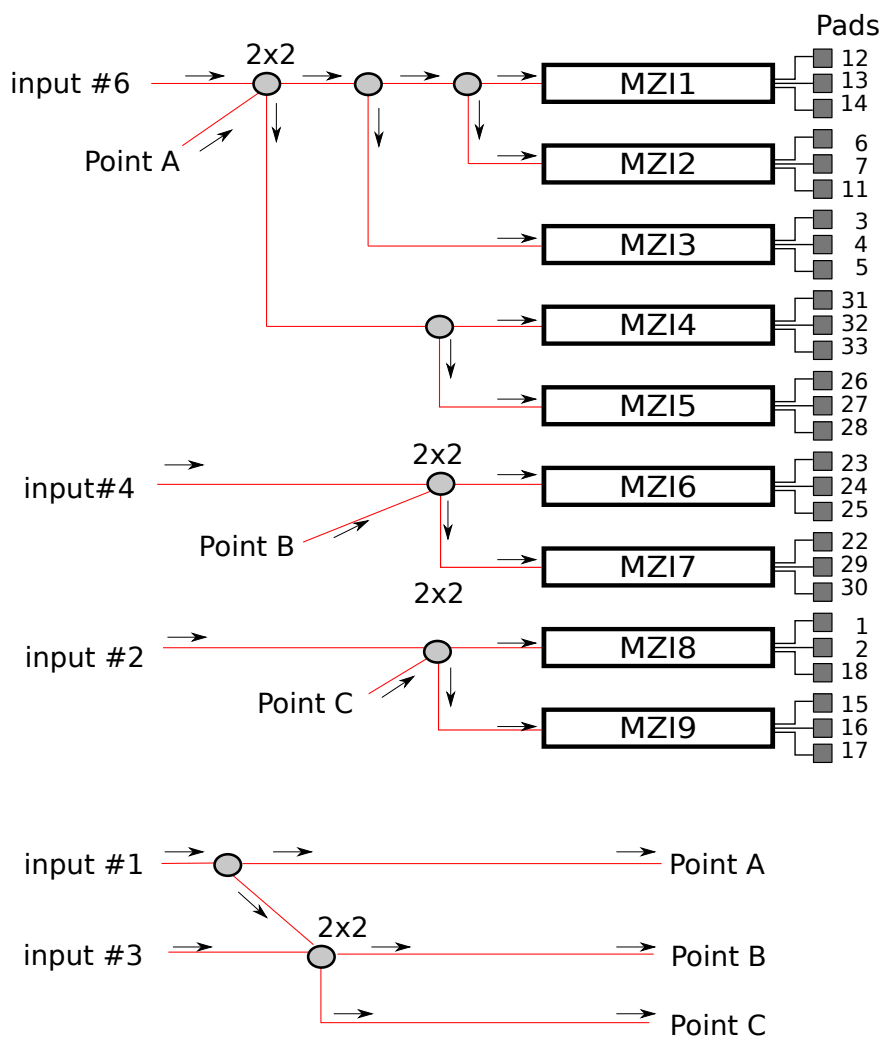Figure 4.2: Optical and electrical connections of the InP chip. Arrows indicate the flow of the optical signal. Optical power is non-uniformly distributed among MZIs 1-5. This mitigates the reduced visibility of MZIs with larger OPDs. Pads are identified in Fig. 4.1.

given by (120°, 0°, -120°) for $l = 1,2,3$ in case the 3×3 coupler is balanced. In our design, the waveguide effective indexes are all the same except by small deviations caused by variations of the fabrication process. Expanding the term $n_{eff,m}(\lambda)/\lambda$ in Taylor series around λ_0, we obtain:

$$\frac{n_{eff,m}(\lambda)}{\lambda} \cong \frac{n_{eff}(\lambda_0) + n_g + \delta n_{eff,m}}{\lambda_0} - \frac{n_g}{\lambda_0^2}\lambda, \tag{4.2}$$

where $\delta n_{eff,m}$ are deviations of the nominal value of the effective index at the m-th MZI and λ_0 a wavelength close to 1550.0 nm. The approximation holds as long as the effect group index (n_g) can be considered constant over the spectrum of interest. Replacing Eq. (4.2) in Eq. (4.1) we obtain [1]:

$$T_{ml}(\lambda) = \frac{1}{3}\left[1 + v_{ml}\cos\left[2\pi\frac{\lambda}{F_m} - \phi_l - \psi_{e,m}\right]\right], \tag{4.3}$$

where $F_m = \lambda_0^2/(n_g \Delta L_m)$ is the free spectral range[2] of the m-th interferometer and

$$\psi_{e,m} = \frac{2\pi\Delta L_m}{\lambda_0}\left(n_g + n_{eff}(\lambda_0) + \delta n_{eff,m}\right). \tag{4.4}$$

In our design, ΔL_m is given by $\Delta L_m = m\Delta L_1$ with $\Delta L_1 = 0.710$ mm, leading to $F_m = F_1/m$, where m is an integer ranging from 1 to 9 and $F_1 = 921.7 \pm 0.5$ pm. $\psi_{e,m}$ depends on $n_{eff}(\lambda_0)$, which might change in case of temperature fluctuations, inducing a phase drift in $T_{ml}(\lambda)$.

The schematic of Fig. 4.1(e) shows that the outputs of the MZIs are connected to integrated photodetectors (PD). The PD current I_{ml} is given by $I_{ml}(\lambda) = P_m R_{ph}T_{ml}(\lambda)$, where P_m is the optical power delivered at the m-th MZI and R_{ph} is the photodetector responsivity. The outputs of the photodetectors are send to TIAs, whose outputs voltage are given by:

$$V_{ml}(\lambda) = g_{TIA,ml}P_m R_{pm}T_{mk}(\lambda)$$
$$= \frac{g_{TIA,ml}P_m R_{pm}}{3}\left[1 + v_{ml}\cos\left(2\pi m\frac{\lambda}{F_1} - \phi_l - \psi_{e,m}\right)\right], \tag{4.5}$$

where $g_{TIA,ml}$ is the transimpedance gain. The 3×3 MMIs were designed to produce interference fringes with similar amplitude and a 120° shift between each other. Aiming for the interrogation of the photonic sensors, the pre-processing module of the PCB combines the TIA output voltages according to [1]:

$$V_{m,x}(\lambda) = 2V_{m,3} - V_{m,1} - V_{m,2} = A_{m,x}\cos\left(2\pi m\frac{\lambda}{F_1} - \psi_{e,m}\right) + x_{off,m},$$
$$\tag{4.6}$$
$$V_{m,y}(\lambda) = \sqrt{3}\left(V_{m,2} - V_{m,3}\right) = A_{m,y}\sin\left(2\pi m\frac{\lambda}{F_1} - \psi_{e,m} - \delta\phi_m\right) + y_{off,m},$$

---

[1]Eq. (4.3) reduces to Eq. (3.7) by neglecting the dispersion of the effective index.
[2]In order to simplify the notation, in this chapter we represent the free spectral range of the m-th MZI as F_m instead of FSR_m.
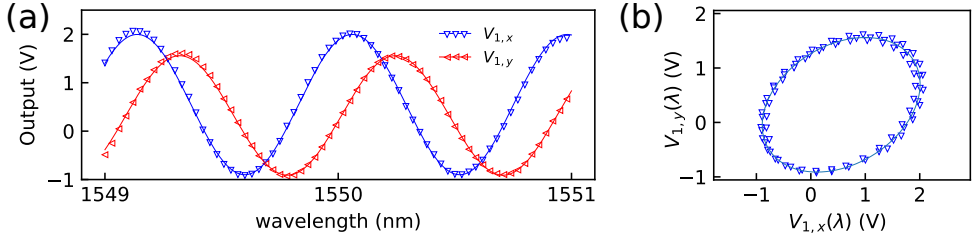
Figure 4.3: (a) Traces of $V_{1,x}$ and $V_{1,y}$ as a function of the laser wavelength. We fitted Eq. (4.6) against the data points and we obtained $F_1 = 921.7 \pm 0.5$ pm, $\delta\phi_1 = 17.9 \pm 0.3°$, $A_{1,x} = 1.449 \pm 0.003$V and $A_{1,y} = 1.234 \pm 0.004$V. (b) Lissajous plot of the data points $[V_{1,x}(\lambda), V_{1,y}(\lambda)]$ shown in Fig. 4.3(a). By fitting an ellipse to the data points we got 1.56 V and 1.09 V for the semi-axis values and 31.2° for the tilt angle with respect to the x-axis.

where $V_{m,x}$ and $V_{m,y}$ are 90° phase shift voltages, $A_{m,x}$ and $A_{m,y}$ are the voltage amplitudes, $x_{off,m}$ and $y_{off,m}$ are voltage offsets, and $\delta\phi_m$ is a phase error. If the 3×3 MMI and the electronic components of the PCB are ideal (ideal operational amplifiers and no variance with respect to the nominal value of the resistors and capacitors), the voltage offsets are zero ($x_{off,m} = y_{off,m} = 0$), $\delta\phi_m = 0$, and $A_{m,x} = A_{m,y} = P_m R_{ph} g v$, where the visibility is $v = v_{m1} = v_{m2} = v_{m3}$ and the TIA gain is $g_{TIA} = g_{TIA,m1} = g_{TIA,m2} = g_{TIA,m3}$. In this case, the Lissajous curve $[V_{m,x}(\lambda), V_{m,y}(\lambda)]$ gives a circle with radius $v P_m R_{ph} g$ centred at the origin.

The transmission spectrum of each MZI has been measured using a tunable laser (Agilent, 81960A). The laser power is set to 6.0 mW and we performed the laser wavelength sweep ranging from 1550 nm to 1551 nm in steps of 1 pm, while the outputs of the pre-processing module are recorded by the digital acquisition module (DAQ, National Instruments, NI 9220). Fig. 4.3(a) shows the measured voltages of the outputs of MZI 1 ($\Delta L_1 = 0.710$ mm), as well as a fit of the measured data against to Eq. (4.6). Since $V_{1,x}$ and $V_{1,y}$ have slightly different amplitudes and $\delta\phi_1 = 17.9°$, the circle is deformed into a tilted ellipse centred outside of the origin, as shown in Fig. 4.3(b).

4.3. Interrogation method and experimental setup
4.3.1. The interrogation method
Here we derive the expressions for determining the resonance wavelengths of the photonic sensors as a function of time. Typically, the spectrum of each sensor has a peaked lineshape, which is modulated by an external signal such as temperature, strain or any other physical or chemical quantity. The photonic sensors are assumed to be wavelength multiplexed. Let there be K sensors with resonance wavelengths $\lambda_k(t)$ at time t, where $k = 1, ..., K$. The combined spectrum $S(\lambda, \lambda_1(t), ..., \lambda_K(t))$ received by the interrogator is given by:

$$S(\lambda, \lambda_1(t), ..., \lambda_K(t)) = \sum_{k=1}^{K} s_k(\lambda, \lambda_k(t)) = \sum_{k=1}^{K} s_k(\lambda - \lambda_k(t)), \qquad (4.7)$$

where $s_k(\lambda, \lambda_k(t))$ is the spectrum of the k-th sensor. The signals that are to be sensed induce time dependent modulations of the resonance wavelengths. The resonances $\lambda_k(t)$ must be separated so that the curves $s_k(\lambda, \lambda_k(t))$ do not overlap. In this paper $s_k(\lambda, \lambda_k(t))$ correspond to the reflection spectra of FBGs sensors. However, the method applies also to integrated photonic sensors as the ones described in [1].

$S(\lambda)$ is assumed to be a poly-chromatic signal and the values of the TIA output voltages are given by:

$$V_{ml}(t) = G \int_{-\infty}^{\infty} S(\lambda, \lambda_1(t), ..., \lambda_K(t)) T_{ml}(\lambda) d\lambda, \qquad (4.8)$$

where the constant G is given by $G = (1 - \alpha_c) g_{TIA}, R_{ph}$ with α_c the coupling losses. The electronic pre-processing module combines the signals from the three outputs of the interferometers according to Eq. (4.6), resulting in the two 90° phase shifted voltages $V_{m,x}(t)$ and $V_{m,x}(t)$:

$$V_{m,x}(t) = 3G \int_{-\infty}^{\infty} S(\lambda, \lambda_1(t), ..., \lambda_K(t)) \cos\left(2\pi m \frac{\lambda}{F_1} - \psi_{e,m}\right) d\lambda + x_{off,m}, \qquad (4.9)$$

$$V_{m,y}(t) = 3G \int_{-\infty}^{\infty} S(\lambda, \lambda_1(t), ..., \lambda_K(t)) \sin\left(2\pi m \frac{\lambda}{F_1} - \psi_{e,m}\right) d\lambda + y_{off,m}. \qquad (4.10)$$

The voltage offsets $x_{off,m}$ and $y_{off,m}$ are mainly caused due to imperfections in the 3×3 MMIs. At the end of a calibration process (see Section 4.3.2), the offsets are removed by averaging and, at this point, they are neglected.

By defining a complex voltage $\hat{V}_m(t) = V_{m,x}(t) + iV_{m,y}(t)$ we obtain:

$$\hat{V}_m(t) = 3G e^{-i\psi_{e,m}} \int_{-\infty}^{\infty} S(\lambda, \lambda_1(t), ..., \lambda_K(t)) \exp\left(i2\pi \frac{m}{F_1} \lambda\right) d\lambda. \qquad (4.11)$$

The chip is characterized after the MZI phase drift has been stabilized, so $\psi_{e,m}$ is constant in time and taken out of the integral in Eq. (4.11). In Section 4.3.3, however, a novel method is presented for compensating the environmental phase drift by using one of the sensors as a reference. We assume that $S(\lambda, \lambda_1(t), ..., \lambda_K(t))$ vanishes outside the interval $[\lambda_0 - F_1/2, \lambda_0 + F_1/2]$ for all times t, where λ_0 is a wavelength close to 1550.0 nm. Then we have:

$$\frac{\hat{V}_m(t) e^{i\psi_{e,m}}}{3G} = \int_{\lambda_0 - F_1/2}^{\lambda_0 + F_1/2} S(\lambda, \lambda_1(t), ..., \lambda_K(t)) \exp\left(i2\pi \frac{m}{F_1} \lambda\right) d\lambda. \qquad (4.12)$$

Eq. (4.12) are the Fourier coefficients of the function $\lambda \to S(\lambda, \lambda_1(t), ..., \lambda_K(t))$ when

considered as periodic function with period F_1. This implies that:

$$S(\lambda, \lambda_1(t), ..., \lambda_K(t)) = \frac{1}{3G} \sum_{m=-\infty}^{\infty} \hat{V}_m(t) e^{i\psi_{e,m}} \exp\left(-i2\pi \frac{m}{F_1}\lambda\right)$$

$$= \frac{2}{3G} \sum_{m=0}^{\infty} \left[V_{m,x}(t) \cos\left(2\pi \frac{m}{F_1}\lambda - \psi_{e,m}\right) - V_{m,y}(t) \sin\left(2\pi \frac{m}{F_1}\lambda - \psi_{e,m}\right) \right],$$

$$(4.13)$$

where $\hat{V}_{-m}(t) = \hat{V}_{-m}^*(t)$ since $S(\lambda, \lambda_1(t), ..., \lambda_K(t))$ is real. The chip contains a finite number of $M = 9$ interferometers. The retrieved spectrum $S_M(\lambda, \lambda_1(t), ..., \lambda_K(t))$ is given by:

$$S_M(\lambda, \lambda_1(t), ..., \lambda_K(t)) = \frac{2}{3G} \sum_{m=0}^{M} \left[V_{m,x}(t) \cos\left(2\pi \frac{m}{F_1}\lambda - \psi_{e,m}\right) - V_{m,y}(t) \sin\left(2\pi \frac{m}{F_1}\lambda - \psi_{e,m}\right) \right].$$

$$(4.14)$$

Function $S(\lambda, \lambda_1(t), ..., \lambda_K(t))$ differs from $S_M(\lambda, \lambda_1(t), ..., \lambda_K(t))$ by the fact that the last one features a finite spectral resolution $\delta\lambda_{res}$ given by:

$$\delta\lambda_{res} = \frac{F_1}{2M}. \tag{4.15}$$

For $M = 9$, $\delta\lambda_{res} = 50$ pm. Moreover, $S_M(\lambda, \lambda_1(t), ..., \lambda_K(t))$ is periodic with period F_1. For a large number of interferometers ($M >> K$), $S_M(\lambda, \lambda_1(t), ..., \lambda_K(t))$ gives a good approximation to $S(\lambda, \lambda_1(t), ..., \lambda_K(t))$ and it is possible to obtain the resonance wavelengths by tracking the peaks of $S_M(\lambda, \lambda_1(t), ..., \lambda_K(t))$. However, $\delta\lambda_{res}$ represents a limitation to the minimum resonance wavelength that can be experimentally obtained.

In order to determine $\lambda_k(t)$ with higher accuracy and using a reduced number of MZIs we derive a non-linear system of equations. We assume in this Section that $\lambda(t)$ is known at $t = 0$. Let

$$\lambda_k(t) = \lambda_k(0) + \delta_k(t), \tag{4.16}$$

where $\delta_k(t)$ is the modulation of the resonance wavelength of the k-th sensor that we aim to determine. By substituting Eq . (4.7) and Eq. (4.16) into Eq. (4.11), we obtain:

$$\hat{V}_m(t) = 3G e^{-i\psi_{e,m}} \sum_{k=1}^{K} \int_{-\infty}^{\infty} s_k(\lambda - \lambda_k(0) - \delta_k(t)) \exp\left(i2\pi \frac{m}{F_1}\lambda\right) d\lambda. \tag{4.17}$$

The right-hand side of Eq. (4.17) represents the Fourier transform of $s_k(\lambda - \lambda_k(0) - \delta_k(t))$ evaluated at m/F_1. Using the shift property of the Fourier transformation, Eq. (4.17) is rewritten as:

$$\hat{V}_m(t) = 3G \sum_{k=1}^{K} \hat{s}_k(m/F_1) \exp\left[i\left(-\psi_{e,m} + 2\pi \frac{m}{F_1}\lambda_k(0)\right)\right] \exp\left(i2\pi \frac{m}{F_1}\delta_k(t)\right), \tag{4.18}$$

where $\hat{s}_k(m/F_1)$ is the Fourier transform of $s_k(\lambda)$. Let

$$a_{mk} = 3G\hat{s}_k(m/F_1) \exp\left[i\left(-\psi_{e,m} + 2\pi\frac{m}{F_1}\lambda_k(0)\right)\right]. \tag{4.19}$$

We rewrite Eq. (4.18) as:

$$\hat{V}_m(t) = \sum_{k=1}^{K} a_{mk} \exp\left[i\frac{2\pi m}{F_1}\delta_k(t)\right], \tag{4.20}$$

for $m = 1, ..., M$. The coefficients a_{mk} are experimentally determined as explained in Section 4.3.2. Eq. (4.20) represents an M×K system of non-linear equations to be solved using Newton's method, where M is the number of interferometers and K is the number of sensors. Hence, the number of interferometers must only be at least as large as the number of sensors (i.e. $M >= K$), which means that the footprint of the device can be relatively small. In our chip $M = 9$. The system is explicitly written in the in Eq. (4.21):

$$\hat{V}_1(t) = a_{11} \exp\left[i\frac{2\pi\delta_1(t)}{F_1}\right] + a_{12} \exp\left[i\frac{2\pi\delta_2(t)}{F_1}\right] + ... + a_{1K} \exp\left[i\frac{2\pi\delta_K(t)}{F_1}\right],$$

$$\hat{V}_2(t) = a_{21} \exp\left[2i\frac{2\pi\delta_1(t)}{F_1}\right] + a_{22} \exp\left[2i\frac{2\pi\delta_2(t)}{F_1}\right] + ... + a_{2K} \exp\left[2i\frac{2\pi\delta_K(t)}{F_1}\right],$$

...

$$\hat{V}_M(t) = a_{M1} \exp\left[Mi\frac{2\pi\delta_1(t)}{F_1}\right] + a_{M2} \exp\left[Mi\frac{2\pi\delta_2(t)}{F_1}\right] + ... + a_{MK} \exp\left[Mi\frac{2\pi\delta_K(t)}{F_1}\right].$$
$$\tag{4.21}$$

It can be show that as long as the phases $2\pi\lambda_k(t)/F_1$ (for $k = 1, ..., K$) are different and the initial guess for $\{\delta_1(t), ..., \delta_K(t)\}$ is close to the actual solution, the Jacobian $\partial\hat{V}_m/\partial\delta_k$ is not singular and the Eqs. (4.21) are independent. From Eq. (4.16), at $t = 0$, $\{\delta_1(0), ..., \delta_K(0)\} = \{0, ..., 0\}$. The solution at time t is taken as an initial guess at $t + 1/f_s$, where f_s is the sampling frequency. This reduces the computational time and assures that the initial guess and the solution are close to each other. The method is also flexible in the sense that the ratio between the arms length difference of the MZIs ($\Delta L_m/\Delta L_1$) does not need to be an integer number, which would cause the m value in Eq. (4.20) to a fractional number. The equations remain independent as long as the ΔL_m values are different.

Assuming that the FBG sensors spectra have a Lorenzian lineshape, we replace the Fourier transform of $s_k(\lambda)$ into Eq. (4.19):

$$a_{mk} = \frac{3Gs_k^{max}}{2} \exp\left(\frac{-mOPD_1}{L_{c,k}}\right) \exp\left[i\left(-\psi_{e,m} + 2\pi\frac{m}{F_1}\lambda_k(0)\right)\right], \tag{4.22}$$

where s_k^{max} is the maximum value of the Lorenzian of the k-th sensor, $OPD_1 = n_g\Delta L_1$ is the optical path difference of MZI 1, and $L_{c,k}$ is the cohenrece length given by:

$$L_{c,k} = \frac{\lambda_0^2}{\pi w_k}, \tag{4.23}$$

where w_k is the full width half maxima (FWHM) of the Lorenzian. The coherence length limits the maximum OPD value which allows interferometric fringes to be experimentally resolved. Eq. (4.22) shows that a_{mk} becomes very small when the MZI free spectral range is comparable or smaller than the FWHM of k-th sensor. As discussed in Section 4.3.1, the MZIs with larger OPDs are not used due to the strong attenuation and the reduced signal-to-noise ratio (SNR).

4.3.2. Calibration and experimental determination of the coefficients

The coefficients a_{mk} are experimentally determined via the following calibration procedure:

1. Apply an excitation to all the sensors individually. During the time interval $t_k^{start} < t < t_k^{end}$, where the k-th sensor is being excited, all other sensors must receive no excitation. As a result, the Lissajous curves $(V_{1,x}V_{1,y})$, ..., $(V_{M,x}, V_{M,y})$ are ellipses. Excitation must be applied for all K sensors. In total, $M \times K$ ellipses are obtained, where M is the number of voltage pairs and K the number of sensors.

2. Fit an ellipse to the voltage pairs $(V_{1,x}, V_{1,y})$, ... $(V_{M,x}, V_{M,y})$ during the interval $t_k^{start} < t < t_k^{end}$. Repeat this procedure for all sensors.

3. Apply the linear transformation that maps the ellipses to circles.

4. Using the radius R_{mk} and the angles of the circular arcs at $t = t_k^{end}$, determine the module and argument of coefficients a_{mk}.

5. Compute the voltage offsets using Eq. (4.32).

Step 1 Let t_k^{start} be the instant of time when the calibration of k-th sensor starts and t_k^{end} be the instant of time when the calibration ends for the same sensor. During the time interval $t_k^{start} < t < t_k^{end}$, all sensors are kept at rest, while sensor k is excited. In case sensor k is a temperature sensor, heat is applied (as much as possible) during the calibration. If sensor k is a strain sensor, a large stress is applied (as much as possible). For an ideal 3×3 couplers, according to Eq. (4.20), the m-th complex voltage $\hat{V}_m(t)$ during the time interval $t_k^{start} < t < t_k^{end}$ is given by:

$$\hat{V}_m(t) = |a_{mk}|e^{i2\pi\frac{m}{F_1}\delta_k(t)} + \sum_{l \neq k}^{K} a_{ml} = |a_{mk}|e^{i\theta_{mk}(t)} + c_{mk}, \qquad (4.24)$$

where $\delta_l(t) = 0$ if $l \neq k$ since no excitation is applied to the other sensors. $c_{mk} = \sum_{l \neq k}^{K} a_{ml}$ and $\theta_{mk}(t)$ is the complex argument of the term $|a_{mk}|e^{im2\pi\delta_k(t)/F_1}$, given by:

$$\theta_{mk}(t) = m2\pi\frac{\delta_k(t)}{F_1} + \arg(a_{mk}). \qquad (4.25)$$

The Lissajous curve $\left(\Re\{\hat{V}_m(t)\}, \Im\{\hat{V}_m(t)\}\right)$ for $t_k^{start} < t < t_k^{end}$ is given by a circular arc:

$$\left(V_{m,x}(t), V_{m,y}(t)\right)\big|_{t_k^{start}<t<t_k^{end}} = \left(\Re\{\hat{V}_m(t)\}, \Im\{\hat{V}_m(t)\}\right)\big|_{t_k^{start}<t<t_k^{end}}$$

$$= [|a_{mk}|\cos\left(\theta_{mk}(t)\right) + \Re\{c_{mk}\}, |a_{mk}|\sin\left((\theta_{mk}(t)) + \Im\{c_{mk}\}\right]\big|_{t_k^{start}<t<t_k^{end}},$$

$$(4.26)$$

where $(\Re\{c_{mk}\}, \Im\{c_{mk}\})$ defines the arc centre, $|a_{mk}|$ the radius, and $\theta_{mk}(t)$ the instantaneous angle with the real axis.

Fig. 4.4 shows a simulation of the calibration for two sensors. The calibration starts at $t = t_0 < 0$ and ends at $t = 0$, when the interrogation procedure starts. During $t_1^{start} < t < t_1^{end}$, sensor 2 is kept at rest, while sensor 1 is excited by moving its resonance wavelength from 1550.50 nm to 1550.16 nm, as shown in Fig. 4.4(a). This induces the oscillations of $V_{1,x}(t)$ and $V_{1,y}(t)$ during $t_1^{start} < t < t_1^{end}$ as shown in Fig. 4.4(b), which are traced as a circular arc in red shown in Fig. 4.4(c). The procedure is repeated for sensor 2: during $t_2^{start} < t < t_2^{end}$, while sensor 1 is not excited, sensor 2 changes its resonance from 1550.75 nm to 1550.33 nm. This causes the oscillations from $t_2^{start} < t < t_2^{end}$ in Fig. 4.4(b) which are traced as the circular arc in green shown in Fig. 4.4(c).

Step 2 As explained in Chapter 3, a slight non-ideal behavior of amplitude and phase of 3×3 couplers are not uncommon and result into a deformation of the circle in an ellipse. An ellipse is fitted to the data points $\left(V_{m,x}(t)', V_{y,m}(t)'\right)$ during the interval $t_k^{start} < t < t_k^{end}$, where $V_{m,x}(t)'$ and $V_{m,y}(t)'$ are the m-th MZI voltages measured during the calibration. A larger excitation of the k-th sensor results in a larger angular deflection, leading to a more accurate retrieval of geometrical parameters of the ellipse.

Step 3 The fitting gives the ellipse semi-axis $r_{1,mk}$ and $r_{2,mk}$ (where $r_{1,mk} > r_{2,mk}$), the angle α that represents the rotation of the ellipse with respect to the x-axis, and the ellipse centre $(x_{mk}^{el}, y_{mk}^{el})$. In order to map the ellipse to an circle, the following transformation is applied:

$$\begin{pmatrix} V_{m,x}(t) \\ V_{m,y}(t) \end{pmatrix} = \begin{pmatrix} r_{1,mk}/r_{2,mk} & 0 \\ 0 & 1 \end{pmatrix} \begin{pmatrix} \cos\alpha & \sin\alpha \\ -\sin\alpha & \cos\alpha \end{pmatrix} \begin{pmatrix} V_{m,x}(t)' \\ V_{m,y}(t)' \end{pmatrix}, \qquad (4.27)$$

where $V_{m,x}$ and $V_{m,y}$ are the corrected values of the 90° phase shifted voltages so that the Lissajous curve $\left(V_{m,x}(t), V_{m,y}(t)\right)$ for $t_k^{start} < t < t_k^{end}$ gives a circle arc with radius $r_{1,mk}$. The correction of Eq. (4.27) needs to be performed for all interferometers ($m = 1, ..., M$). Although the ellipse semi-axis $r_{1,mk}$ and $r_{2,mk}$, as well as the corrected radius $r_{1,mk}$ may change according to the sensor (since it depends on its total transmitted or reflected power spectrum) and according to the interferometer (due to the different MZI's coherence lengths), the ellipse eccentricity depends only on the 3×3 MMI, as discussed in Section 4.2. Thus, for a given interferometer m the ratio $r_{1,mk}/r_{2,mk}$ is constant for $k = 1, ..., K$. The design of the 3×3 MMI is the same for all interferometers, hence the ratio $r_{1,m}/r_{2,m}$ is constant for $m = 1, ..., M$ as long as the variations of the fabrication process are negligible.

Step 4 After calculating the 90° phase shifted voltages, the modulus of the coefficients a_{mk} can be obtained. Since the radius of the circle arc obtained for the m-th interferometer and the k-th sensor is $r_{1,mk}$, the modulus of the coefficients a_{mk}, according to Eq. (4.26), is given by:

$$|a_{mk}| = r_{1,mk}. \tag{4.28}$$

Next, the linear transformation of Eq. (4.27) is applied to the point $(x_{mk}^{el}, y_{mk}^{el})$, which gives the centre $(\Re\{c_{m,k}\}, \Im\{c_{m,k}\})$. The angles $\theta_{mk}(t)$ (for $m = 1, ..., M$ and $k = 1, ..., K$) are given by:

$$\theta_{mk}(t) = \arctan_2(V_{y,m}(t) - \Im\{c_{m,k}\}, V_{x,m}(t) - \Re\{c_{m,k}\}), \tag{4.29}$$

where $\arctan_2(x, y)$ is the four quadrant arc tangent. During the final stage of the calibration of sensor k, the angle $\theta_{mk}(t)$ remains constant because then no excitation is anymore applied to it. By substituting $t = t_k^{end}$ in Eq. (4.25), we obtain:

$$\theta_{mk}(t_k^{end}) = m2\pi \frac{\delta_k(t_k^{end})}{F_1} + \arg(a_{mk}) = m2\pi \frac{\delta_k(0)}{F_1} + \arg(a_{mk}), \tag{4.30}$$

where the calibration procedure ends at $t = 0$. According to Eq. (4.16), $\delta_k(0) = 0$. Therefore, the argument of a_{mk} is given by:

$$\arg(a_{mk}) = \theta_{mk}(t_k^{end}) = \theta_{mk}(0). \tag{4.31}$$

The values of $\lambda_k(t)$ (for $k = 1, ..., K$) are in general unknown at the end of the calibration ($t = 0$), which contradicts the assumption made in Eq. (4.16). Here, we refine our previous statement by assuming that the values of $\lambda_k(t)$ are known at $t = t_0$, before the calibration procedure starts. In most of cases, however, the sensors can be calibrated in such a way that their resonance wavelengths return to their initial value at the end of the calibration ($\lambda_k(t_0) = \lambda_k(0)$). In situations where this is not possible (due to a sensor hysteresis, for instance), the values of $\lambda_k(0)$ can be obtained by following the procedure: (a) determine the value of $\delta(t_k^{start})$ from Eq. (4.25) evaluated at $t = t_k^{start}$; (b) substitute the value of $\delta(t_k^{start})$ in Eq. (4.16) (also evaluated at $t = t_k^{start}$).

Step 5 After finishing the calibration of all sensors in this way, the offsets are determined by averaging:

$$x_{off,m} = \frac{1}{|t_0|} \int_{t_0}^{0} \left\{ V_{m,y}(t) - \sum_k |a_{mk}| \cos[\theta_{mk}(t)] \right\} dt,$$

$$y_{off,m} = \frac{1}{|t_0|} \int_{t_0}^{0} \left\{ V_{m,y}(t) - \sum_k |a_{mk}| \sin[\theta_{mk}(t)] \right\} dt. \tag{4.32}$$

Finally, the complex voltages are computed as function of time to be used in Eqs. (4.20) and (4.21):

$$\hat{V}_m(t) = [V_{x,m}(t) - x_{off,m}] + i[V_{y,m}(t) - y_{off,m}]. \tag{4.33}$$
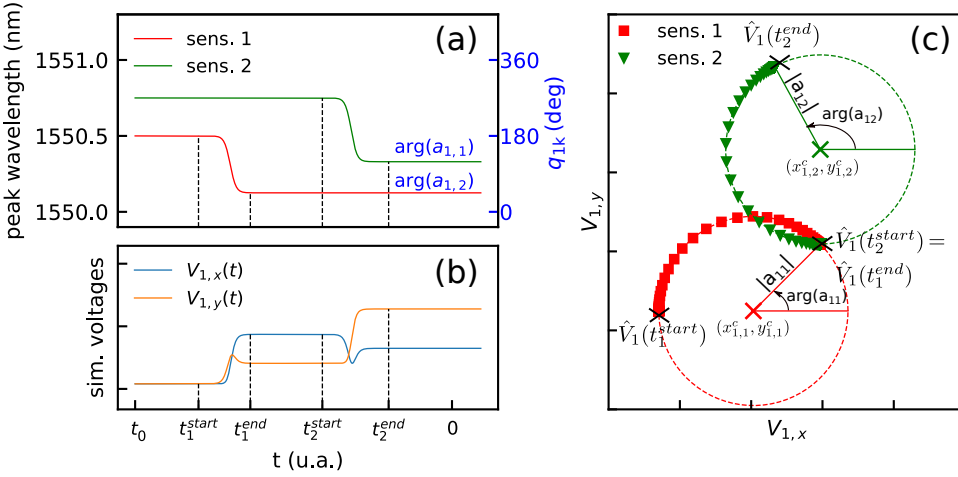
Figure 4.4: Illustration of the calibration procedure for two sensors. (a) Independent excitation of sensor 1 and sensor 2. (b) Simulated values of $V_{1,x}(t)$ and $V_{1,y}(t)$ for MZI 1. The changes in time of the functions $V_{1,x}(t)$ and $V_{1,y}(t)$ are caused by the modulation of the peak wavelengths shown in Fig. 4.4(a). The voltages $V_{m,x}(t)'$ and $V_{m,y}(t)'$ (m = 1,...,M) are measured by our acquisition system. $V_{m,x}(t)$ and $V_{m,y}(t)$ are obtained from Eq. (4.27). For this simulation, $V_{m,x}(t) = V_{m,x}(t)'$ and $V_{m,y}(t) = V_{m,y}(t)'$. (c) Lissajous curve $(V_{1,x}(t), V_{1,y}(t))$ for MZI 1. The modulation of the peak wavelength of the sensors induces an angular deflection in the plane of the voltages $V_{1,x}$ and $V_{1,y}$. From the Lissajous curve, the complex modulus and the phase of the coefficients a_{mk} were extracted. For this simulation, $F_1 = 1.0$ nm.

4.3.3. Compensation of the phase drift

Since the effective index in Eq. (4.4) is temperature dependent, local variations of temperature induces the phase $\psi_{e,m}$ to drift. [22] presents two different methods for compensating the phase drift: by using temperature dependent calibration matrices or by correcting the phases errors of the interferogram in case of narrowband signals. In our case, however, the system of equations is non-linear and a different approach is used. Eq. (4.4) is rewritten according to:

$$\psi_{e,m}(t) = m \frac{2\pi\Delta L}{\lambda_0} \left(n_g + n_{eff}(\lambda_0)(T_0) + \frac{\partial n_{eff}}{\partial T}\Delta T(t) + \delta n_{eff,m} \right) = \psi_{e,m}(0) + m\Delta\psi_e(t),$$

(4.34)

where

$$\Delta\psi_e(t) = \frac{2\pi\Delta L}{\lambda_0}\frac{\partial n_{eff}}{\partial T}\Delta T(t).$$

(4.35)

The temperature dependence of the group index n_g and to δn_{neff} have been neglected. Eq. (4.35) indicates that the phases $\psi_{e,m}$ in Eq. (4.18), (4.20), and (4.21)

are no longer constant. Eq. (4.18) can be rewritten as:

$$\hat{V}_m(t) = 3G \sum_{k=1}^{K} \hat{s}_k(m/F_1) \exp\left[i\left(-\psi_{e,m}(0) + 2\pi\frac{\lambda_k(0)}{F_1}\right)\right] \exp\left[i2\pi\frac{m}{F_1}\left(\delta_k(t) - \Delta\psi_e(t)\frac{F_1}{2\pi}\right)\right]$$

$$= \sum_{m=1}^{M} a'_{mk} \exp\left[i2\pi\frac{m}{F_1}\delta_k(t)'\right],$$

(4.36)

where

$$\delta_k(t)' = \delta_k(t) - \Delta\psi_e(t)F_1/(2\pi). \tag{4.37}$$

The right side of Eq. (4.36) is identical to Eq. (4.20) demonstrating that fluctuations of the environmental phase impacts on the solutions of Eq. (4.20) or Eq. (4.36). This effect can be corrected by using another sensor as a reference, to which no excitation is applied and its temperature is kept constant.

Let $\delta_{ref}(t)$ be the solution of Eq. (4.36) for the reference sensor. The calibration procedure assures that when the interrogation procedure starts ($t = 0$), the values $\delta_k(0)$ are zero for all sensors ($k = 1, ..., K$). Since no excitation is applied to the reference sensor, the function $\delta_{ref}(t)$ remains at zero for $t > 0$. Hence, according to Eq. (4.37):

$$\delta_{ref}(t)' = -\Delta\psi_e(t)F_1/(2\pi). \tag{4.38}$$

Thus, the phase drift can be compensated by subtracting the term $\Delta\psi_e(t)F_1/(2\pi)$ in Eq. (4.37), obtained from Eq. (4.38):

$$\delta_k(t) = \delta_k(t)' - \delta_{ref}(t)'. \tag{4.39}$$

4.3.4. Experimental setup

The schematics of the experiment is depicted in Fig. 4.5. Light from a broadband amplified spontaneous emission source (ASE, Optolink, OLS15CGB-20-FA) is sent, through a circulator (OZ Optics, FOC-12N-111-9), to the FBG sensor array (Technicasa, T10). The broadband source has an approximately flat spectrum, ranging from 1525 nm to 1565 nm. The FBG sensors reflect back to the circulator their combined spectrum, which is amplified by an optical booster amplifier (Thorlabs, S9FC1004P) according to Fig. 4.5(a). The gain is 12 dB and the light is coupled to the chip using lensed fibers (Oz Optics, TSMJ-3A-1550-9). The lensed fiber is placed at an angle of 23° with respect a normal line perpendicular to the edge of the chip (see Fig. 4.1(d)). Outputs of the chip are conveyed to a PCB which implements the transimpedance amplifiers for the photodetectors and a pre-processing module in order to implement Eq. (4.6) electronically (see Fig. 4.1(e)). The PCB outputs are sampled by the DAQ (National instruments, NI9220), which the maximum sampling speed is 100 kSa/s/channel.

The performance of our interrogator is evaluated using four FBG sensors: three as strain sensors one as a reference sensor, used to compensate the environmental phase drift. The reflection spectrum of the FBGs have a peak lineshape.
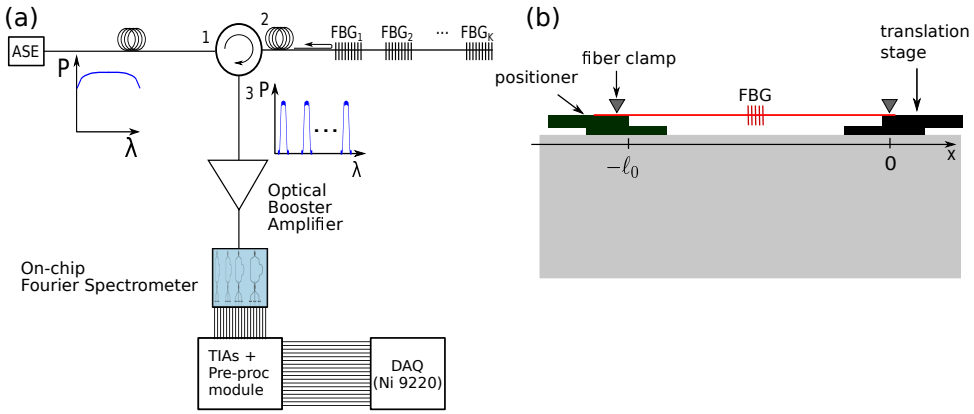
Figure 4.5: (a) Schematic of the setup. Light from an ASE source is sent, through a circulator, to the FBG sensor array. The FBG sensors reflect back to the circulator their combined spectrum, which is amplified by an optical booster amplifier (gain = 12dB). Light is coupled to the chip using lensed fibers. (b) Schematic of the temperature / strain sensors. ℓ_0 = 1.74 m, which is the fiber length between the clamps.

The FWHM is 103 pm and their resonance wavelengths without applied stress is 1550.0 ± 0.5 nm. The calibration is performed in a such way that $\lambda_k(t_0) = \lambda_k(0)$. The ends of the fibers containing the FBGs are clamped to the translation stages as shown in Fig. 4.5(b). In order to tune the resonance wavelengths $\lambda_k(0)$, stress is applied using the manual positioners, avoiding the angles $2\pi (\lambda_k(t)) / F_1$ to overlap during the experiment. FBG #1 represents the main strain sensor and the translation stage (referred as translation stage 1) to which FBG #1 is attached is controlled by a stepper motor. FBGs #2 and #3 are the secondary strain sensors and they are both attached to translation stage 2 controlled by another stepper motor. FBG #4 is the reference sensor and it is attached only to manual positioners. We programmed the stepper motors to operate in cycles of three steps: (a) the translation stage travels at a constant speed from the position $x = 0$ to $x = \Delta\ell$; (b) The stage rests at $x = \Delta\ell$; (c) The stage returns to the original position.

Since FBGs #2 and #3 are secondary strain sensors, we programmed the translation stage to move periodically from the distances $x = 0$ to $x = \Delta\ell^{(2)} = 30\mu$m. In contrast, the translation stage to which FBG #1 is attached, travels to different values of $\Delta\ell^{(1)}$ ranging from 0.5 μm to 200 μm (these values are shown later in Fig. 4.7). Since the stress to be applied to FBG #1 is much larger compared to FBGs #2 and #3, the translation stage 1 is programmed to move towards $-x$. Thus, a negative stress applied to FBG #1, avoiding to damage it. Translation stage 1 repeats three times its motion from $x = 0$ to $x = \Delta\ell^{(1)}$ and from $x = \Delta\ell^{(1)}$ to $x = 0$. Thus, the travelling distances $\Delta\ell^{(1)}_{3j+1}$, $\Delta\ell^{(1)}_{3j+2}$ and $\Delta\ell^{(1)}_{3j+3}$ are the same for $j = 0, ..., J - 1$, where J is the number of different values of $\Delta\ell^{(1)}$.

4.4. Experimental results

As explained in Section 4.3.4, the performance of our interrogator is evaluated using four FBG sensors: three as strain sensors one as a reference sensor, used to compensate the environmental phase drift. Using manual positioners, a constant stress is applied to all FBGs in such a way that the resonance wavelengths of the sensors are set to $\lambda_1(0) = 1550.9$ nm, $\lambda_2(0) = 1550.3$ nm, $\lambda_3(0) = 1551.4$ nm and $\lambda_4(0) = 1549.7$ nm. The differences of $\lambda_k(t) - \lambda_l(t)$ for $l \neq k$ can be larger than F_1 (F_1 is the free spectral range of MZI 1) provided that the angles $2\pi\lambda_k(t)/F_1 \neq 2\pi\lambda_l(t)/F_1$ for all $l, k = 1...K$. The light signal is coupled to the chip using input #6 (see Fig. 4.1(a)), where the input power is shared among MZIs 1 to 5. Better interrogation results are obtained by sharing the optical power among a reduced number of interferometers since the outputs of the MZIs with larger OPDs are strongly attenuated, according to the discussion in the end of Section 4.3.1.

In order to retrieve the coefficients a_{mk}, we individually excited the FBG sensors. Following the procedure described in Section 4.3.2, the complex voltages $\hat{V}_m(t)$ have been obtained by mapping the ellipse arcs to circle arcs according to Eq. (4.27), and by removing the voltage offsets according to Eq. (4.32). Fig. 4.6(a) shows the real and imaginary parts of $\hat{V}_1(t)$, to which a low pass filter (cut-off at 45 Hz) has been applied in order to suppress noise. The real and the imaginary parts of $\hat{V}_1(t)$, shown in Fig. 4.6(a), are plotted in Fig. 4.6(b) as a Lissajous curve. Fig. 4.6(b) shows four circular arcs, which correspond to the individual excitation of the sensors, obtained from the outputs of MZI $m = 1$ during the calibration. The radii and the angles of the arcs at the end of the calibration procedure give the modulus and argument of the coefficients a_{mk}, as described in Section 4.3.2.

Fig. 4.6(b) shows, however, that some regions of the Lissajous curve deviate from the expected circular path. This occurs when the resonance wavelengths of two FBGs are about to cross and the spectra of two FBG sensors overlap. This causes that a part of the input optical signal is reflected multiple times in between the FBGs, creating an Fabry-Perot cavity. The interference of the electric field which is reflected multiple times between the FBGs leads to the deviations of the circular arcs. To overcome this issue, we followed the calibration described in Section 4.3.2 using only the parts of the Lissajous curves that are close to circular. For $t > 0$ s, the interrogation starts and the three strain sensors are simultaneously excited. As a result, an arbitrary Lissajous curve is obtained.

Figs. 4.6(c)-4.6(f) show the solution of Eq. (4.20) obtained using the Newton's method. As explained in Section 4.3.1, the solution obtained at the instant t is used as an initial guess for the Newton's method at the instant $t + 1/f_s$, where f_s is the sampling frequency. As a result, the method converges at any t with a maximum of four iterations. For a sampling rate of 10 kSa/s, about one million of systems of equations needs be solved from $t = 0$ s to $t = 100$ s. Using an Intel i5-3470 processor, the solution is roughly calculated at a rate of a hundred equations per second and the total computational time is about 2h and 45 min.

FBGs #2 and #3 are attached to translation stage 2 which periodically travels from $x = 0$ to $x = \Delta\ell^{(2)} = 30\mu$m. As a result, the functions $\delta_2(t)$ and $\delta_3(t)$ are time periodic, as shown in Figs. 4.6(c) and 4.6(d). On the other hand, Fig. 4.6(f) shows
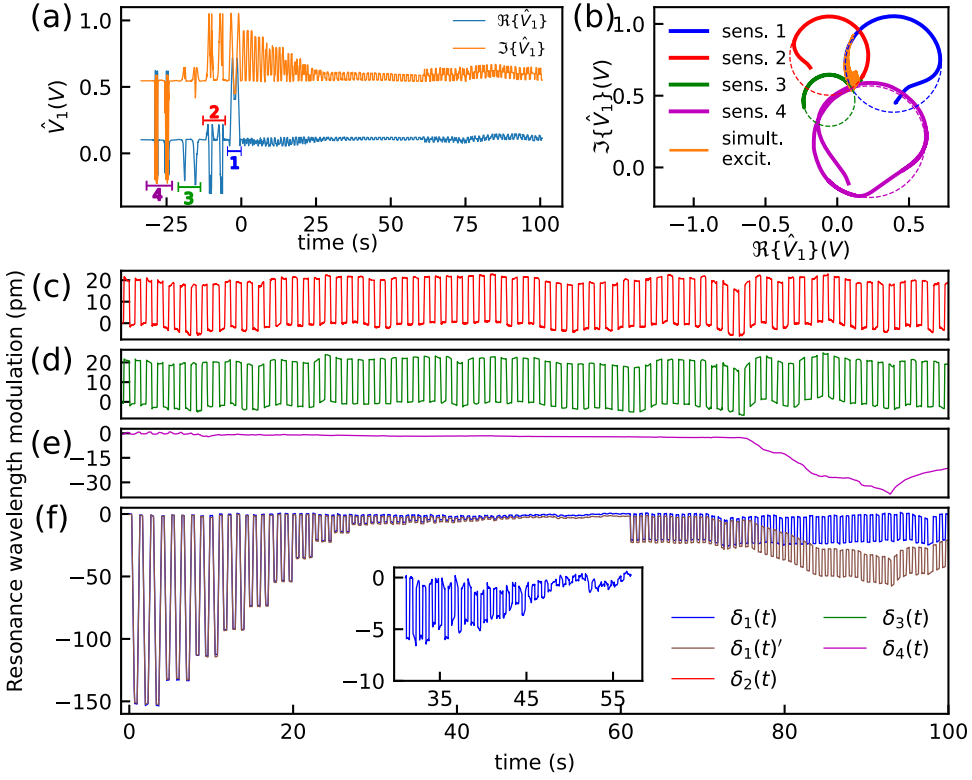
Figure 4.6: Main results of the interrogation. (a) Time traces of the real and imaginary parts of $\hat{V}_1(t)$. A low pass filter (cut-off at 45 Hz) has been applied to the measured voltages $V_{m,x}(t)$ and $V_{m,y}(t)$. The numbers 1,2,3 and 4 indicate the calibration interval ($t_k^{start} < t < t_k^{end}$) for sensors k =1,...,4. (b) Lissajous plot obtained by plotting the real and imaginary parts of $\hat{V}_1(t)$. During the calibration, the Lissajous curve is a circular arc. During the interrogation, all sensors are simultaneously excited, and an arbitrary Lissajous curve is obtained as shown in orange. (c)-(e) Solutions $\delta_2(t)$, $\delta_3(t)$ and $\delta_4(t)'$ of Eq. (4.36) for $t > 0$. FBG #4 is the reference sensor. The phase drift was compensated using Eq. (4.39). (f) Comparison between the solutions $\delta_1(t)$ and $\delta_1(t)'$. The inset shows a zoom of the solution $\delta_1(t)$.

the solution $\delta_1(t)$, which consists of a succession of dips. The dips are obtained because the stepper motor applies a negative stress to FBG #1, as explained in Section 4.3.3. Since the translation stage repeats its motion three times to a given distance $\Delta\ell^{(1)}$, Fig. 4.6(f) shows a series of dips grouped by 3 successive ones with approximately the same depth.

Fig. 4.7 shows the modulation amplitude $\Delta\lambda^{(1)}$ for sensor 1 as a function of the strain applied to FBG #1. The strain is assumed to be constant along the fiber and it is defined as:

$$\varepsilon_j^{(1)} = \frac{\Delta\ell_{3j}^{(1)}}{\ell_0}, \tag{4.40}$$

where $\varepsilon_j^{(1)}$ is the strain at FBG #1 and ℓ_0 the fiber length defined in Fig. 4.5(b). The

index $3j$ in Eq. (4.40) appears since the distances $\Delta\ell_{3j}^{(1)}$, $\Delta\ell_{3j+1}^{(1)}$ and $\Delta\ell_{3j+2}^{(1)}$ are the same, as explained in Section 4.3.3. On the other hand, the modulation amplitude is defined as:

$$\Delta\lambda_j^{(1)} = \left| \overline{\delta_{1,3j}^{dip}} - \overline{\delta_{1,3j}^{max}} \right|, \tag{4.41}$$

where $\overline{\delta_{1,3j}^{dip}}$ is the time average of function $\delta_1(t)$ at the three adjacent dips $(3j+1)$, $(3j+2)$ and $(3j+3)$, as indicated in the upper inset of Fig. 4.7. Similarly, $\overline{\delta_{1,3j}^{max}}$ is the time average of function $\delta_1(t)$ at its $(3j+1)$-th, $(3j+2)$-th and $(3j+3)$-th maxima, which occur when the translation stage rests around the original position $x = 0$. The ratio between the amplitude modulation and the strain gives the sensitivity $S^{(1)}$ of FBG #1:

$$S^{(1)} = \frac{\partial \Delta\lambda^{(1)}}{\partial \varepsilon^{(1)}}. \tag{4.42}$$

By fitting a straight line to the data points $(\Delta\lambda_j^{(1)}, \varepsilon_j^{(1)})$, we retrieved $S^{(1)} = 1.217 \pm 0.006$ pm/μstrain, which agrees with the nominal sensitivity of 1.2 pm/μstrain provided by the manufacturer (Technicasa, T10). The minimum retrieved strain is 365 nanostrain and the corresponding minimum modulation amplitude obtained is $\Delta\lambda_{min}$ = 400$\pm$200 fm. This value is more than two orders of magnitude smaller than the resolution of the FT spectrometer (50 pm). The free spectral range of MZI with the larger OPD limits the resolution of the spectrometer in the chip (see Eqs. 4.14 and 4.15). However, such limitation does not affect the system of non-linear equations derived in Section 4.3.1. The value of $\Delta\lambda_{min}$, experimentally retrieved, is limited by the SNR of the input signal and by the accuracy of the coefficients a_{mk} (where $m, k = 1...K$), obtained by the calibration procedure.

FBG #4 has been taken as a reference sensor and no external excitation is applied to it after the end of the calibration. However, for $t < 10$ s, Fig. 4.6(e) shows small fluctuations of function $\delta_4(t)'$ (of the order of a few pm), caused by the cross-talk among sensors. Since the modulation amplitude of FBG #1 is the larger for $t < 10$ s, its cross-talk with FBG #4 is dominant. The maximum cross talk between FBGs #4 and FBGs #1 is about 1% of the $\delta_1(t)$ value, which is acceptable in most applications. For smaller modulations of the FBG #1 (below 50 pm), resonance wavelength pertubation due to cross-talk is in sub-picometer level.[3]

In order to demonstrate the compensation of the thermal drift of the phases $\psi_{e,m}$ ($m = 1, ..., M$), the chip is heated up using a Peltier element (MCPE1-03108NC-S 18.8W, Multicomp) placed a few centimeters above it. The Peltier hot surface reaches a temperature of 45 °C causing a shift of 35 pm to the solutions $\delta_1(t)'$, $\delta_2(t)'$, $\delta_3(t)'$ and $\delta_4(t)'$. The drift of $\delta_4(t)'$ can be observed in Fig. 4.6(e) for $t > 73$ s. Using Eq. (4.39) we calculated $\delta_1(t)$, $\delta_2(t)$ and $\delta_3(t)'$, where 92.0% of the phase drift has been compensated. Fig. 4.6(f) shows a comparison between $\delta_1(t)'$ and $\delta_1(t)$ while Figs. 4.6(c) and 4.6(d) show only the compensated solutions

---

[3]The resonance wavelength pertubation due to cross-talk is about 1.5 pm. According to *Tosi* [27], most of the applications require an interrogation resolution of 1 pm, in the same order of magnitude of the maximum cross-talk.
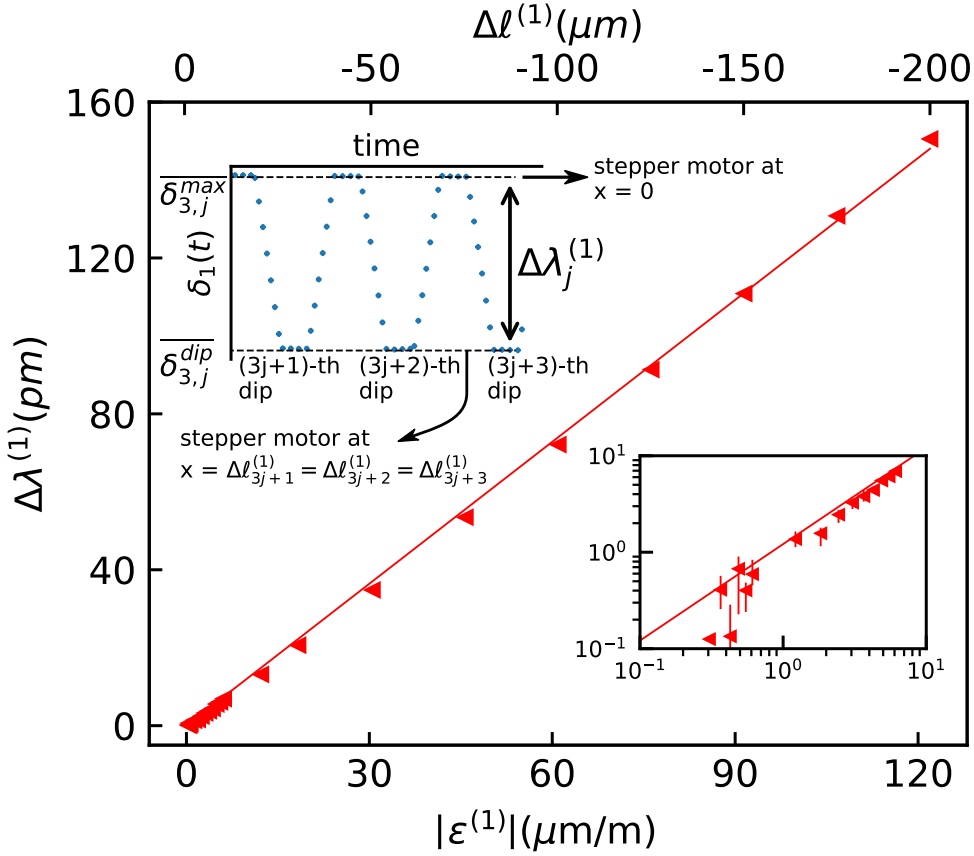
Figure 4.7: Modulation amplitude $\Delta\lambda^{(1)}$ of sensor 1 as a function of the strain applied. $\Delta\lambda^{(1)}$ is calculated from as $\Delta\lambda^{(1)} = \left| \delta^{dip}_{1,3j} - \overline{\delta^{max}_{1,3j}} \right|$, where $\overline{\delta^{dip}_{1,3j}}$ and $\overline{\delta^{max}_{1,3j}}$ are defined in upper inset of the fig. A straight line has been fitted to the data points ($|\varepsilon^{(1)}_j|, \Delta\lambda^{(1)}_j$). The slope, whose value is 1.217±0.006 pm/microstrain, gives the sensitivity of FBG #1. The inset in the bottom of the fig. shows the data points ($\varepsilon^{(1)}_j, \Delta\hat{\lambda}^{(1)}_j$) and the straight line fitted in a Loglog plot. The minimum amplitude modulation retrieved is 400±200 pm.

$\delta_2(t)$ and $\delta_3(t)$. For the sensors presented here, the phase drift could have been removed by applying a high pass filter to $\delta_1(t)'$, $\delta_2(t)'$ and $\delta_3(t)'$. However, for low speed sensors such as biochemical sensors [4], filtering is not possible since the speed of the sensor is comparable to the phase drift speed.

Although the method can be applied to high speed sensors, its real time implementation is challenging. On one hand, the speed of the FT spectrometer is limited only by the electronics and the integrated photodetectors may respond at frequencies of hundreds of MHz. On the other hand, a system of non-linear equations need to be solved at each instant of time. The computational costs, however, can be reduced by calculating the inverse of the Jacobian $\partial\hat{V}_m/\partial\delta_k$ analytically. Using

the transformation $z_k(t) = 2\pi(\lambda_k(0) + \delta_k(t))/F_1$, it can be shown that the Jacobian is given by a product of a diagonal matrix and the Vandermond matrix $V(z_k)$. Since analytic expressions do exist [28] for the inverse of $V(z_k)$, the computational time is mainly governed by the time of calculating product of matrices. Moreover, the reduced number of interactions of Newton's method also contributes in reducing the computational time. In Chapter 5, the non-linear system of equations is solved using semi-analytic methods.

4.5. Conclusion

A novel interrogation method based on FT spectroscopy is presented. The technique is promising due to its high flexibility, high sensitivity and reduced interrogator footprint. It can be applied in different situations, in particular, for arrays of integrated sensors where the resonance wavelengths cannot be predicted during the design stage. Three conditions have been identified for the proper interrogation of the sensors: (a) the number of interferometers must only be at least as large as the number of sensors, allowing the interrogator footprint to be relatively small; (b) the MZIs must have different OPDs; (c) the phases $2\pi\lambda_k(t)/F_1$ (for $k = 1, ..., K$) needs to be different at any time. If the maximum amplitude modulation of the sensors is known, condition (c) is usually not an issue for FBG sensors, since the Bragg wavelengths could be chosen with an accuracy better than 1.0 nm. In case of integrated ring resonators, it is possible in most situations to design rings with a slightly different lengths, assuring a similar free spectral range, but different resonances. Since the phases depend on F_1, the proper design of the FT spectrometer gives an extra flexibility to avoid the phases $2\pi\lambda_k(t)/F_1$ to overlap.

It has been shown that the minimum modulation amplitude experimentally retrieved is not limited by resolution of the FT spectrometer, but limited only by the signal-to-noise ratio of the input signal. The minimum modulation amplitude obtained is 400 ± 200 fm and the cross-talk is about 1%. Moreover, the phase drift of the interrogator, caused by temperature fluctuations, can be compensated by using one of the sensors as reference sensor to which no external excitation is applied. This is important for low speed sensors where the thermal induced drift of MZI phases is comparable to the speed of the sensors. Our method can also be applied for high-speed sensors as the photonic components integrated within the chip can respond at high speed. The implementation of real time interrogators, however, it requires the analytic calculation of the inverse of the Jacobian matrix used in Newton's method. This issue is addressed in Chapter 5, where the non-linear system of equations is solved using semi-analytic methods.

References

[1] F. G. Peternella, B. Ouyang, R. Horsten, M. Haverdings, P. Kat, and J. Caro, *Interrogation of a ring-resonator ultrasound sensor using a fiber mach-zehnder interferometer,* Optics Express **25**, 31622 (2017).

[2] C. Zhang, S. L. Chen, T. L. Ling, and L. J. Guo, *Imprinted polymer microrings*

as high performance ultrasound detectors in photoacoustic imaging, Journal of Lightwave Technology **33**, 4318 (2015).

[3] E. Hallynck and P. Bienstman, *Integrated optical pressure sensors in silicon-on-insulator,* IEEE Photonics Journal **4**, 443 (2012).

[4] K. de Vos, J. Girones, S. Popelka, E. Schacht, R. Baets, and P. Bienstman, *SOI optical microring resonator with poly (ethylene glycol) polymer brush for label-free biosensor applications,* Biosensors and Bioelectronics **24**, 2528 (2009).

[5] X. Zhou, Y. Dai, J. M. Karanja, F. Liu, and M. Yang, *Microstructured FBG hydrogen sensor based on pt-loaded wo 3,* Optics Express **25**, 8777 (2017).

[6] Q. Liang, K. Zou, J. Long, J. Jin, D. Zhang, G. Coppola, W. Sun, Y. Wang, and Y. Ge, *Multi-component FBG-based force sensing systems by comparison with other sensing technologies : A review,* IEEE Sensors Journal **18**, 7345 (2018).

[7] A. D. Kersey, *A review of recent developments in fiber optic sensor technology,* Optical Fiber Technology **2**, 291 (1996).

[8] H. Li, X. Ma, B. Cui, Y. Wang, C. Zhang, J. Zhao, Z. Zhang, C. Tang, and E. Li, *Chip-scale demonstration of hybrid III - V / silicon photonic integration for an FBG interrogator,* Optica **4**, 692 (2017).

[9] D. Pustakhod, E. Kleijn, K. Williams, and X. Leijtens, *High-resolution awg-based fiber,* IEEE Sensors Journal **28**, 2203 (2016).

[10] N. A. Yebo, W. Bogaerts, Z. Hens, and R. Baets, *On-chip arrayed waveguide grating interrogated silicon-on-insulator microring resonator-based gas sensor,* IEEE Photonics Technology Letters **23**, 1505 (2011).

[11] H. Guo, G. Xiao, N. Mrad, and J. Yao, *Echelle diffractive grating based wavelength interrogator for potential aerospace applications,* Journal of Lightwave Technology **31**, 2099 (2013).

[12] U. Tiwari, K. Thyagarajan, M. R. Shenoy, and S. C. Jain, *EDF-based edge-filter interrogation scheme for FBG sensors,* IEEE Sensors Journal **13**, 1315 (2013).

[13] V. M. N. Passaro, A. V. Tsarev, and F. De Leonardis, *Wavelength interrogator for optical sensors based on a novel thermo-optic tunable filter in SOI,* Journal of Lightwave Technology **30**, 2143 (2012).

[14] P. Orr and P. Niewczas, *High-speed, solid state, interferometric interrogator and multiplexer for fiber Bragg grating sensors,* Journal of Lightwave Technology **29**, 3387 (2011).

[15] M. Perry, P. Orr, P. Niewczas, and M. Johnston, *High-speed interferometric fbg interrogator with dynamic and absolute wavelength measurement capability,* Journal of Lightwave Technology **31**, 2897 (2013).

4

[16] M. A. Davis and A. D. Kersey, *Application of a fiber fourier transform spectrometer to the detection of wavelength-encoded signals from bragg grating sensors,* Journal of Lightwave Technology **13**, 1289 (1995).

[17] K. B. Rochford and S. D. Dyer, *Demultiplexing of interferometrically interrogated fiber Bragg grating sensors using Hilbert transform processing,* Journal of Lightwave Technology **17**, 831 (1999).

[18] M. Florjańczyk, P. Cheben, S. Janz, A. Scott, B. Solheim, and D. X. Xu, *Multiaperture planar waveguide spectrometer formed by arrayed Mach-zehnder interferometers,* Optics express **15**, 18176 (2007).

[19] K. Okamoto, H. Aoyagi, and K. Takada, *Fabrication of Fourier-transform, integrated-optic spatial heterodyne spectrometer on silica-based planar waveguide.* Optics letters **35**, 2103 (2010).

[20] A. V. Velasco, P. Cheben, P. J. Bock, A. Delâge, J. H. Schmid, J. Lapointe, S. Janz, M. L. Calvo, D. X. Xu, M. Florjańczyk, and M. Vachon, *High-resolution fourier-transform spectrometer chip with microphotonic silicon spiral waveguides,* Optics letters **38**, 706 (2013).

[21] H. Podmore, A. Scott, P. Cheben, A. V. Velasco, J. H. Schmid, M. Vachon, and R. Lee, *Demonstration of a compressive-sensing fourier-transform on-chip spectrometer,* Optics letters **42**, 1440 (2017).

[22] A. Herrero-Bermello, A. V. Velasco, H. Podmore, P. Cheben, J. H. Schmid, S. Jans, M. L. Calvo, D.-X. Xu, A. Scott, and P. Corredera, *Temperature dependence mitigation in stationary Fourier-transform on-chip spectrometers,* Optics letters **42**, 2239 (2017).

[23] D. M. Kita, B. Miranda, D. Favela, D. Bono, J. Michon, H. Lin, T. Gu, and J. Hu, *High-performance and scalable on-chip digital fourier transform spectroscopy,* Nature Communications **9**, 4405 (2018).

[24] R. Uda, K. Yamaguchi, K. Takada, and K. Okamoto, *Fabrication of a silica-based complex fourier- transform integrated-optic spatial heterodyne spectrometer incorporating 120o optical hybrid couplers,* Applied Optics **57**, 3781 (2018).

[25] K. Okamoto, *Fourier-transform, integrated-optic spatial heterodyne (fish) spectrometers on planar lightwave circuits,* in *International Conference on Fibre Optics and Photonics* (Optical Society of America, 2012) p. M2A.1.

[26] A. Dandridge, *Fiber optic sensors based on the Mach-zehnder and michelson interferometers,* in *Fiber Optic Sensors: an Introduction for engineers and scientists,* edited by E. Udd and W. B. S. Jr. (John Wiley and Sons, Inc., 1991) pp. 231–275.

[27] D. Tosi, *Improved KLT Algorithm for High-Precision Wavelength Tracking of Optical Fiber Bragg Grating Sensors,* Journal of Sensors **2017**, e5412825 (2017), publisher: Hindawi.

[28] F. Soto-Eguibar and H. Moya-Cessa, *Inverse of the Vandermonde and Vandermonde confluent matrices,* Applied Mathematics and Information Sciences **5**, 361 (2011).

4

5

Algebraic solutions for the Fourier transform interrogator

A new method for fast, high resolution interrogation of an array of photonic sensors is proposed. The technique is based on the integrated Fourier transform (FT) interrogator previously introduced by the authors. Compared to other interferometric interrogators, the FT-interrogator is very compact and has an unprecedented tolerance to variations in the nominal values of the sensors' resonance wavelength. In this Chapter, the output voltages of the interrogator are written as a polynomial function of complex variables whose modulus is unitary and whose argument encodes the resonance wavelength modulation of the photonic sensors. Two different methods are proposed to solve the system of polynomial equations. In both cases, the Gröbner basis of the polynomial ideal is computed using lexicographical monomial ordering, resulting in a system of polynomials whose complex variable contributions can be decoupled. Using an NVidia graphics processing card, the processing time for 1 026 000 systems of algebraic equations takes around 9 ms, which is more than two orders of magnitude faster than the interrogation method previously introduced by the authors. Such a performance allows for real time interrogation of high-speed sensors. Multiple solutions satisfy the algebraic system of equations, but, in general, only one of the solutions gives the actual resonance wavelength modulation of the sensors. Other solutions have been used for optimization, leading to a reduction in the cross-talk among the sensors. The dynamic strain resolution is 1.66 $n\varepsilon/\sqrt{Hz}$.

5.1. Introduction

Photonic sensors have recently attracted much attention in both industry and academia. They can offer high accuracy, low weight and the possibility of building a large sensor network. Photonic sensors can be employed in a wide range of situations and can be used in harsh environments where electronic sensors are not suitable. Examples of applications are gas sensing [1, 2], biosensing [3–5], monitoring pressure and temperatures in oil industry [6] and finally, in structure health monitoring [7]. In the health care field, possible applications are ultrasound intravascular imaging [8, 9] and photoacoustic imaging [10]. Attention is given in this Chapter to sensors whose spectrum is finite and can be multiplexed using wide division multiplexing techniques (WDM). Ring resonator sensors and fiber Bragg gratings (FBG)s are examples of this type of photonic sensor.

Interrogators can have a deep impact on sensor performance; they can limit their dynamic range, measurement resolution, and speed. Interrogators based on interferometry are usually implemented using two main stages [11, 12]: a demultiplexer (such as an arrayed waveguide grating (AWG) or an echelle), which separates the spectra of the photonic sensors and then an array of interferometers, which retrieve the information encoded in the resonance wavelength of each photonic sensor. This approach gives a limited tolerance to variations in the resonance wavelength of the sensors. If one of the FBG sensors in the sensor network needs to be replaced, another FBG with the same resonance wavelength must be used [11]. The reason is that the resonance wavelength of the photonic sensors should coincide with a wavelength close to the center of the spectrum of one of the spectrometer's output channels. A flexible interrogator is particularly important for demodulating integrated photonic sensors, since the fabrication stage may introduce large variations in the nominal values of their resonance wavelengths.

The interrogator previously presented by our group [13] is based on a Fourier transform (FT) spectrometer and implements the steps of demultiplexing and demodulation simultaneously. The resonance wavelength modulation of the sensors was obtained by numerically solving (at each instant of time) a system of non-linear equations. The minimum retrieved resonance wavelength modulation was 400 fm, about 130 times smaller than the FT-spectrometer's resolution. Despite the high interrogation resolution, the processing time per non-linear system is around 10 ms[13], limiting the maximum speed of the photonic sensors.

In this work, the non-linear system of equations has been rewritten as a system of polynomial equations. This algebraic system is solved by computing the Gröbner basis of the polynomial ideal. Under a lexicographical monomial ordering, it is possible to decouple the response of the photonic sensors. The algebraic system admits multiple solutions and it is demonstrated in the appendix that, in general, there is only one solution from which the resonance wavelength modulation of the sensors can be obtained. One of the non-physical solutions, however, has been used to adjust the coefficients of the algebraic equations, reducing the cross-talk among the sensors. As will be discussed in Section 5.3, the algebraic formulation enables one to solve the polynomial system of equations using parallel computation. Using an NVidia graphical processing unit (GPU), the overall processing time for 1 026 000

algebraic systems of equations is about 9 ms. The novel formulation allows two orders of magnitude faster than our previous Chapter's approach, which allows real-time interrogation of high-speed sensors. The Fourier transform interrogator is a candidate for interrogating arrays of ultrasound ring resonator sensors [8, 9, 35, 36].

5.2. The Fourier transform interrogator

Different integrated FT spectrometer designs have been presented in the literature [14–19]. While conventional Fourier transform spectrometers use a Michelson interferometer with a moving mirror, in 2007 *Florjanczyk et al.* [14] proposed a spectrometer featuring a set of integrated Mach-Zehnder interferometers (MZI) with different arm lengths. As a result, the interferogram becomes discrete and the retrieved spectrum periodic. The spectral reconstruction takes the Littrow wavelength (defined as the wavelength at which the interferences are completely constructive for all MZIs) as a reference. Given the fact that the spectrum is real and symmetric with respect to the frequency $f = 0$, the sine terms of the complex Fourier series vanish. Moreover, the Fourier coefficients (which are calculated from the outputs of each Mach-Zehnder interferometer) become real.

FT spectrometers can be designed to achieve a resolution as hundreds of MHz [20]. The free spectral range (FSR) of the MZI with the larger optical path difference (OPD) defines the spectral resolution limit of the system, while the periodicity of the spectrum is defined by the FSR of the MZI with the smaller OPD. One of the critical limitations of the spectral reconstruction method presented by [14] are the phase errors: if the interference is not completely constructive at the Littrow wavelength, distortions are introduced into the reconstructed spectrum. *Herrero-Bermello et al.* [21] identify two main sources of phase errors: (a) errors caused by imperfections in the fabrication process, and (b) errors introduced by thermal instabilities during measurement.

The fabrication process introduces variations in the waveguide parameters such as local variations of its width, leading the constructive interference maximum to deviate from the Littrow wavelength. *Takada et al.* [22] solved this issue by using micro-heaters and actively controlling the wavelengths at which the constructive interference maximum occurs. Alternatively, Refs. [15–18] handle the phase errors by including them in the transmission function of each MZI and subsequently solving a linear system of equations. *Uda* [19] and *Okmamoto et. al* [23] simplified the calculation of the spectrum input by employing a 3×3 and a 4×4 MMIs (multimode interference couplers) at the MZI outputs. In this case, both real and imaginary parts of the Fourier coefficients are evaluated, and the phase errors are compensated by multiplying the voltages of the interferogram by a phase factor (see Eq. (5.5)). In contrast, phase errors introduced by thermal instabilities can be mitigated by performing the measurements in a well-controlled environment. One of the methods presented in [24] consists of computing several calibration matrices as a function of temperature. The input spectrum is obtained by multiplying the spectrogram by the inverse (or pseudo-inverse) of a matrix whose elements, previously obtained by calibration, depend on the temperature of the device. Alter-

natively, [21] applies a novel technique based on machine learning, which gives an 80 % success rate. Thermal instabilities also impact the interrogation of photonic sensors. Such instabilities have been compensated for in our previous article using one of the photonic sensors as a reference [13].

The design of the FT interrogator differs from the FT spectrometer in that (a) it contains a reduced number of interferometers and (b) the MZIs contain 3×3 MMI couplers at their outputs, which is unusual for a FT spectrometer. As detailed later in Section 5.3, according to the algebraic formulation, the number of MZIs employed in the interrogation is equal to the number of the sensors. This drastically reduces the number of MZIs which need be integrated on the chip. Fig. 5.1 shows the design of our chip, fabricated by Smart Photonics in Eindhoven using InP technology. Its size is 4.5 mm × 4.0 mm, and it has nine integrated MZIs. The arm-length difference of MZI1, shown in the upper-right corner of Fig. 5.1, is $\Delta L_1 = 710$ μm and its free spectral range is $F_1 = 921pm$. The arm-length differences of the other MZIs are progressively larger and given by $m\Delta L_1$, where m is an integer which identifies the MZI in Fig. 5.1 and ranges from 1 to 9. The MZI free spectral ranges are given by $F_m = F_1/m$. Input 1 is the main entrance, from which all MZIs can be accessed. The other inputs guide the light signal to a smaller group of MZIs, allowing some optical power to be saved if fewer sensors are being interrogated. The MZI outputs are connected to integrated photodetectors (PDs). The PD electrical outputs are conveyed (through a wire-bond connection) to a printed circuit board (PCB), which has the chip on top. This PCB is attached to another PCB which contains an array of trans-impedance amplifiers (TIA) (one per photodetector) and also to an additional electronic circuit designed to calculate the complex Fourier coefficients.

Instead of retrieving the spectrum and thereby computing the resonance wavelength modulation of the sensors, in this work, a system of algebraic equations is derived. The argument of the complex variables of the solution encodes the resonance wavelength modulation of the photonic sensors. By solving the algebraic system, it has been possible to experimentally obtain resonance wavelength modulation amplitudes 140 times smaller than the FT spectrometer's resolution. In standard integrated FT spectroscopy applications, the spectrum is obtained using a finite number of harmonic terms of the Fourier series because a finite number of interferometers are on the chip. This limits the resolution of the retrieved spectrum. An exception to this has been described by *Podmode* [16], in which the spectrum is known to be sparse and was obtained using l1-normalization. In contrast, the algebraic system of equations derived in this work gives an accurate physical description of the modulation of the sensors. The interrogation resolution is limited by the noise and the inaccuracies of the coefficients retrieved in the calibration procedure.

5.3. Theoretical analysis of the FT interrogator

5.3.1. Derivation of the system of polynomial equations

Photonic sensors can be multiplexed in large sensor networks. In this thesis, the focus is on the interrogation of sensors which are multiplexed in the wave-
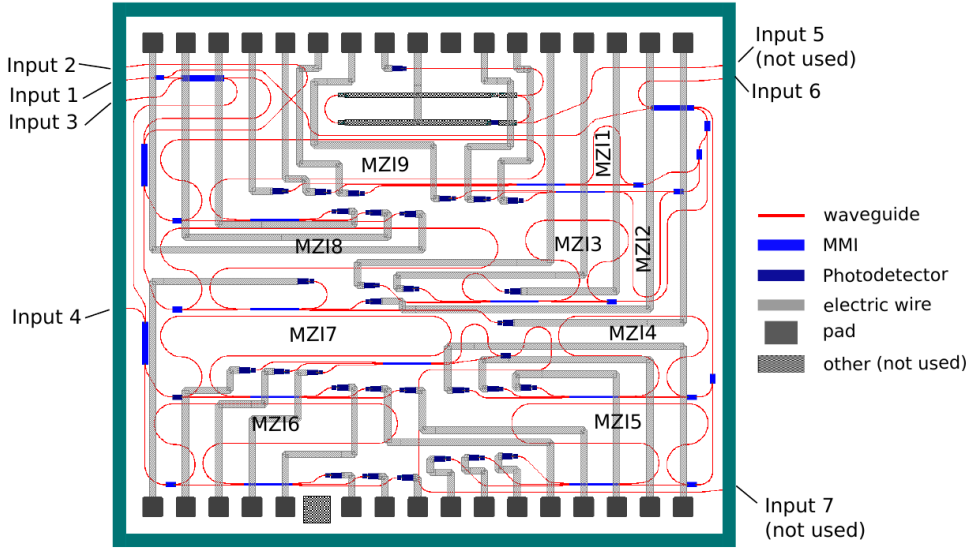
Figure 5.1: Schematic of the FT-Interrogator. The device contains nine MZIs, all with different OPDs. Input 1 is the main entrance, from which all MZIs can be accessed; Input 2 guides the light signal to MZIs 8 and 9; Input 3, to MZIs 6 and 9; Input 4, to MZIs 6 and 7; and Input 6, to MZIs 1 - 5. The other inputs are not used.

length domain (WDM). The spectrum of the sensors is assumed to be finite and shaped as a peak (as with ring resonators or fiber Bragg gratings) and their resonances, i.e., the wavelength at which the spectrum is maximum, are sufficiently separated so that their combined spectra do not overlap. The combined spectrum $S(\delta_1(t), ..., \delta_M(t), \lambda, t)$ as a function of time is given by:

$$S(\delta_1(t), ..., \delta_M(t), \lambda, t) = \sum_{n=1}^{K} s_k(\lambda - \lambda_{0k} - \delta_k(t)), \tag{5.1}$$

where K is the number of photonic sensors, $s_k(\lambda)$ is the spectrum of the k-th sensor, λ_{0k} is the resonance wavelength of the k-th sensor, in the absence of an external signal to be sensed and $\delta_k(t)$ is the resonance modulation of the k-th sensor, encoded by the signal to be sensed. Ring resonators may present multiple resonances along the C-band, and the interrogator expects single resonance. To isolate a single resonance, an optical filter, such as an FBG, can be used [9]. The goal of the interrogator is to determine the function $\delta_k(t)$ as a function of time.

Here we derive the coupled polynomial system of equations for the FT Interrogator. A similar derivation has been presented in our former article [13], here it is partially repeated for the reader's convenience. The PCBs, which are connected

to the TIAs, combine the voltages according to:

$$V_{m,x}(t) = 2V_{m,3}(t) - V_{m,1}(t) - V_{m,2}(t)$$
$$V_{m,y}(t) = \sqrt{3}\left(V_{m,1}(t) - V_{m,2}(t)\right), \tag{5.2}$$

where m is the MZI index, $V_{m,x}(t)$ and $V_{m,y}(t)$ are voltages phase shifted by 90 degrees. Thus, 2 voltages (instead of 3) are sampled per MZI. In our former article, it was shown that the expression for the voltages $V_{m,x}$ and $V_{m,y}$ is given by:

$$V_{m,x}(t) = 3G \int_{-\infty}^{\infty} S(\delta_1(t), ..., \delta_M(t), \lambda, t) \cos\left(2\pi \frac{m}{F_1}\lambda + \psi_{e,m}\right) d\lambda$$

$$V_{m,y}(t) = 3G \int_{-\infty}^{\infty} S(\delta_1(t), ..., \delta_M(t), \lambda, t) \sin\left(2\pi \frac{m}{F_1}\lambda + \psi_{e,m}\right) d\lambda, \tag{5.3}$$

where $\psi_{e,m}$ is an angle which accounts for the phase errors and $F_1 = 921\ pm$ the free spectral range of MZI 1. G is a parameter which depends on the photodetector responsivities, on the TIA gains and on the attenuation of the optical signal within the chip. For further details about this derivation, please refer to our previous paper [13]. The m-th complex voltage is defined according to:

$$\hat{V}_m(t) = V_{m,x}(t) + iV_{m,y}(t) = 3Ge^{-i\psi_m} \int_{-\infty}^{\infty} S(\delta_1(t), ..., \delta_M(t), \lambda, t) \exp\left(i2\pi \frac{m}{F_1}\lambda\right) d\lambda. \tag{5.4}$$

As shown in our previous Chapter, the input spectrum can be reconstructed according to the following expression:

$$S_{rec}(\delta_1(t), ..., \delta_M(t), \lambda, t) = \sum_{m=-M}^{M} \frac{\hat{V}_m(t)e^{i\psi_m}}{G} \exp\left(-i2\pi \frac{m}{F_1}\lambda\right), \tag{5.5}$$

where $S_{rec}(\delta_1(t), ..., \delta_M(t), \lambda, t)$ is the reconstructed spectrum. $S_{rec}(\delta_1(t), ..., \delta_M(t), \lambda, t)$ differs from $S(\delta_1(t), ..., \delta_M(t), \lambda, t)$ in that $S_{rec}(\delta_1(t), ..., \delta_M(t), \lambda, t) = S_{rec}(\delta_1(t), ..., \delta_M(t), \lambda + F_1, t)$ is periodic and that it features a limited resolution, as the number of interferometers is finite. Phase errors that may have been introduced by the fabrication process are compensated by the factor $\exp(i\psi_m)$ in Eq. (5.5).

The spectrometer resolution is given by $F_1/(2M)$. To resolve sensor modulation amplitudes much smaller than the spectrometer's resolution, we derive a system of polynomials equations. Substituting Eq. (5.1) into Eq. (5.4) and changing the integration variable $\lambda \to \lambda' + \lambda_{0k} + \delta_k(t)$, we obtain:

$$\hat{V}_m(t) = \sum_{k=0}^{K} a_{mk} \exp\left[i2\pi \frac{m}{F_1}\delta_k(t)\right], \tag{5.6}$$

where

$$a_{mk} = 3G \exp\left[i\left(-\psi_{e,m} + 2\pi \frac{m}{F_1}\lambda_{0k}\right)\right] \int_{-\infty}^{\infty} s_k(\lambda') \exp\left(i2\pi \frac{m}{F_1}\lambda'\right) d\lambda'. \tag{5.7}$$

Eq. (5.6) represents a system of M non-linear equations (each MZI has one corresponding equation) and K variables. The coefficients a_{mk} are determined via a calibration (see Section 5.4.2). Eq. (5.6) was solved numerically via Newton's method in our former article. The only restriction imposed is for the argument of the complex exponentials in Eq. (5.6) to be all different from each other, otherwise the Jacobian of Eq. (5.6) is singular.

In order to solve Eq. (5.6) analytically, one the sensors is chosen as a reference and both sides of Eq. (5.6) are divided by its coefficient $a_{m,ref}$:

$$
\frac{\hat{V}_m(t)}{a_{m,ref}} = \sum_{k=1}^{K} \frac{a_{m,k}}{a_{m,ref}} \exp\left[i2\pi\frac{m}{F_1}\delta_k(t)\right]
$$

$$
= \sum_{k=1}^{K} \frac{\int_{-\infty}^{\infty} s_k(\lambda') \exp\left(i2\pi\frac{m}{F_1}\lambda'\right) d\lambda'}{\int_{-\infty}^{\infty} s_{ref}(\lambda') \exp\left(i2\pi\frac{m}{F_1}\lambda'\right) d\lambda'} \exp\left[i2\pi\frac{m}{F_1}\left(\lambda_{0k} - \lambda_{0ref} + \delta_k(t)\right)\right].
$$

$$(5.8)$$

We assume that the lineshapes of the photonic sensors $s_k(\lambda)$ are proportional or, in the best case, equal. The coefficients b_k (for $k = 1...K$), defined as:

$$
b_k = \frac{\int_{-\infty}^{\infty} s_k(\lambda') \exp\left(i2\pi\frac{m}{F_1}\lambda'\right) d\lambda'}{\int_{-\infty}^{\infty} s_{ref}(\lambda') \exp\left(i2\pi\frac{m}{F_1}\lambda'\right) d\lambda'} = \left|\frac{a_{mk}}{a_{m,ref}}\right| \cong 1
$$

$$(5.9)$$

are real and given by the ratio of the moduli of the coefficients a_{mk} and a_{mref}. The unity on the right-hand side of Eq. (5.9) occurs if only the spectrum lineshapes $s_k(\lambda)$ (for $k = 1,...,K$) are equal. Let

$$
z_k(t) = \exp\left[i\frac{2\pi}{F_1}\left(\lambda_{0k} - \lambda_{0ref} + \delta_k(t)\right)\right].
$$

$$(5.10)$$

By substituting the definitions of z_k (Eq. (5.10)) and b_k (Eq. (5.9)) into Eq. (5.8), we obtain a system of algebraic equations:

$$
p_m(z_1, ..., z_M) = \sum_{k=1}^{K} b_m z_k(t)^m - \frac{\hat{V}_m(t)}{a_{ref,m}} = 0,
$$

$$(5.11)$$

where $p_1,...,p_M$ are polynomials in the variables $z_1(t),...,z_M(t)$. The methods for solving Eq. (5.11) are discussed in details in Section 5.3.2. According to Eq. (5.10), the resonance wavelength modulation of the k-th photonic sensor is proportional to the argument of z_k, where in theory $|z_k| = 1$. After computing the solution, the resonance wavelength modulation of the sensors is retrieved from the following expression:

$$
\delta_k(t) = F_1 \frac{\text{unwrap}(\arg(z_k(t))) - \arg(z_k(0))}{2\pi},
$$

$$(5.12)$$

where it is assumed that at $t = 0$ no external excitation is applied, thus $\delta_k(0) = 0$.

5.3.2. Algorithm to retrieve the resonance wavelength modulation

This paper aims to solve Eq. (5.11) using analytical and semi-analytical methods. In order to retrieve the modulation for K photonic sensors, at least K complex voltages are needed. In this paper, $K = M$, i. e., the number of sensors is equal to the number of interferometers and complex voltages. The main reason is that the voltages $\hat{V}_m$ (for $m > K$) are attenuated more compared to the voltages for $m \leq K$, and the additional information provided for these equations has a reduced signal-to-noise ratio. The larger the value of m is, the larger the MZI OPD size is, resulting in a stronger attenuation due to the photonic sensors' finite coherence length.

Solutions of Eq. (5.11) are obtained using the computation of Gröbner basis. For a basic introduction of the Gröbner basis, we refer the reader to [25–28]. Let $I = <p_1, ..., p_M>$ be an ideal in the polynomial ring $K_r[z_1, z_2, ..., z_M]$ [1], where the polynomials $p_1, ..., p_M$ are defined by Eq. (5.11). The set $G = \{g_1, ..., g_J\} \subset I$ is a Gröbner basis of I as long as:

$$< LT(g_1), ..., LT(g_J) >=< LT(I) >, \tag{5.13}$$

where LT is the leading term using some monomial ordering. As later discussed, the Eqs. (5.11) intersect in a finite number of points. In this case, and using a lexicographical monomial ordering, the polynomials of the basis G are given by [28]:

$$g_{1,1} \in K_r[z_1, z_2, ..., z_M]$$
$$g_{1,2} \in K_r[z_1, z_2, ..., z_M]$$
$$...$$
$$g_{1,n_1} \in K_r[z_1, z_2, ..., z_M]$$
$$g_{2,1} \in K_r[z_2, ..., z_M]$$
$$...$$
$$g_{2,n_2} \in K_r[z_2, ..., z_M]$$
$$...$$
$$g_{M,n_M} \in K_r[z_M], \tag{5.14}$$

where $n_1, ..., n_M$ are integers. Hence, there exists at least one subset $G_{sub} = \{g_{sub,1}, ..., g_{sub,M}\}$ of G in which the polynomials satisfy a triangular form. Thus

$$g_{sub,1}(z_1, z_2, ..., z_M) = 0$$
$$g_{sub,2}(z_2, ..., z_M) = 0$$
$$...$$
$$g_{sub,M}(z_M) = 0, \tag{5.15}$$

---

[1]Although the coefficients $b_1,...,b_M$ are real, the voltages are complex numbers. Thus the field is $K_r = Q(i)$, as coefficients are represented in fixed-point precision. Solutions are found in the extension field of the complex numbers.

where we dropped the time dependency of $z_m = z_m(t)$ and $V_m = V_m(t)$ (for $m = 1, ..., M$) for simplifying the notation. Eqs. (5.15) can be analytically solved if the degrees of the polynomials are equal or smaller than four. Otherwise, the polynomial roots of Eqs. (5.15) are numerically obtained.

Proposition. Let $(\delta_1(t), ..., \delta_M(t))$ be the resonance wavelength modulation of M sensors, encoded in the argument of the complex variables $z_1(t), z_2(t), ..., z_M(t)$ defined by Eq. (5.10). The spectrum of the sensors is finite and their lineshapes are all equal, except each having a slightly different peak height, so that Eq. (5.11) can be written as:

$$\sum_{k=1}^{M} b_k z_k(t)^m = \hat{V}_m(t)/a_{m,ref},$$
(5.16)

where $b_1 \cong ... \cong b_m \cong 1$. For any value of t, it is assumed that $\arg z_1(t) \neq \arg z_2(t) \neq ... \neq \arg z_M(t)$ and that the arguments of complex variables are sufficiently distant from each other so that Matrix $\mathbf{Q}_H$, defined in Eq. (5.57), is definite positive and the jacobian of Eq. (5.16) is well-conditioned. For this proposition, we assume a noiseless interrogator. The combined spectrum of the sensors interfere in M interferometers according to the FT interrogator description presented in Section 5.2. Eq. (5.16) satisfy the following properties:

1. The polynomials in Eq. (5.16) intersect in $M!$ points;

2. If $Z_{sol} = (z_1, ..., z_M)$ is a solution of Eq. (5.16) and the coefficients $b_1, ..., b_M$ are all equal, the other solutions are given by all possible permutations of the coordinates of Z_{sol}. Moreover, $|z_m| = 1$, for $m = 1, ..., M$;

3. If the coefficients $b_1 \neq b_2 \neq ... \neq b_M$ are all different, there is only one solution whose complex variables satisfy $|z_1| = ... = |z_M| = 1$. For all the other solutions, there is at least one complex variable whose modulus is different from one.

Lemma. If a subgroup of $J < M$ of coefficients of the monomials $z_1^m, z_2^m, ..., z_J^m$ (for $m = 1...M$) in Eq. (12) are all equal ($b_1 = ... = b_J$), there will be $J!$ solutions in which the moduli of all complex variables is one.

Mathematical details of the proposition are presented in the appendix. Item (1) guarantee the existence of the and the amount of intersection points. Items (2) and (3) provide a physical interpretation of the solutions. If the lineshapes $s_k(\lambda)$ (for $k = 1...M$) of the photonic sensors are equal, $b_1 = ... = b_M = 1$ and the polynomials on the left-hand side of Eq. (5.16) become symmetric (see the Appendix for details). Given a solution $Z_{sol} = (z_1, ..., z_M)$, other solutions are given by permutations of Z_{sol} coordinates. In this case all solutions are equally valid as $|z_1| = ... = |z_M| = 1$. If the spectra $s_k(\lambda)$ for k = 1...M) are different, there is only one solution in which the modulus of all the complex variables is equal to the unity. Since the other solutions violate the assumption made in Eq. (5.10), the other solutions are spurious. The lemma can be derived using the same arguments presented in the appendix. Given these properties, the following algorithm has been proposed in order to demodulate the sensor signals:

1. Determine the coefficients a_{mk} (for $m = 1...M$ and $k = 1...M$ and) from the calibration procedure, described in Section 5.4.2.

2. Compute the Gröbner basis of the polynomial ideal using the lexicographic monomial ordering. The complex voltages $\hat{V}_m(t)$ (for $m = 1, ..., M$) are kept as parameters so that the computation of the Gröbner basis needs only to be done once. The computation of the basis uses the SymPY Python module and the F5b [29] algorithm. Similar results can be obtained using Mapple [30].

3. For each instant of time, substitute the values of $\hat{V}_m(t)$ (for $m = 1, ..., M$) into the polynomials obtained from the Gröbner basis analysis and solve the system of equations.

4. Compute the absolute values of variables $z_1, ..., z_M$. Solutions whose absolute value of the complex variables are different than one are discarded. Let:

$$\Delta(t) = \frac{1}{M} \sum_{m=1}^{M} \left| |z_m(t)| - 1 \right|. \tag{5.17}$$

Function $\Delta(t)$ indicates on average how much the modulus of the complex variables deviates from the unity. The valid solution is the one which minimizes $\Delta(t)$.

5. Compute the argument of the complex variables. The arguments of the complex variables may swap with time: if at a certain instant of time the signal of one of the photonic sensors is encoded in the argument of the m-th complex variable $z_m(t)$, at a different time instant, this signal may be encoded into a different complex variable. This phenomenon is explained in detail in Section 5. The identification of the sensor is possible by observing the DC component of the complex variable argument. From the calibration procedure described in Section 5.4.2, we obtain the arguments of all complex variables at $t = 0$ and which photonic sensor the argument corresponds to. Let $\delta_{m,min}$ and $\delta_{m,max}$ be the minimum and maximum modulation amplitudes for the m-th sensor. The complex variable $z_j(t)$ can be associated with the m-th sensor if:

$$\arg(z_j(0)) - \frac{|\delta_{m,min}|F_1}{2\pi} < \text{unwrap}(\arg(z_j(t))) < \arg(z_j(0)) + \frac{\delta_{m,max}}{2\pi}, \tag{5.18}$$

where $\delta_{m,min} \leq 0$ and $\delta_{m,max} > 0$.

6. Finally, the sensor modulation is obtained according to Eq. (5.12).

This first method has been implemented in Python only. It features the disadvantage that the subset G_{sub} of the Gröbner basis, shown in Eq. (5.15), may not be unique. For a given basis Gröbner basis, polynomials might be arranged in different subsets, all of them obeying the triangular form described by Eq. (5.15). Thus, *Lazard* [31] proposed an algorithm which calculates a finite array of triangular systems of polynomials from the Gröbner basis G, obtained using lex monomial

ordering. However,for the case of three sensors studied in the Experimental Section, this is not needed. For $b_1 \neq b_2 \neq b_3$, the Gröbner basis obtained using both Python and Maple has only three equations: the univariate equation in z_3 has the degree of six, while the other two polynomials are linear for z_1 and z_2, respectively. Another issue of the current method is that the computation cost of obtaining the Gröbner basis for non-symmetrical polynomial equations can be extremely high for a larger number of sensors. Other algorithms for algebraic solving the system of equations could also be employed [32]. However, the computation cost stills quite high for a large number of sensors.

We propose a second method for solving the polynomial system described by Eq. (5.11): in step 2 of the algorithm described above, we first approximate $b_1 = ... = b_M = 1$, making the system of equations symmetric. This meaningfully reduces the computational cost of obtaining the Gröbner basis. Next, the symmetric system solution is taken as a starting point in Newton's method. In order to ensure a fast convergence, the coefficients $b_1, ..., b_M$ are expected to be close to unity. As explained in Section 5.3.1, this is obtained if the sensors' spectra lineshapes are all similar. As an alternative to the computation of the Gröbner basis, the symmetric system of polynomial equations can be solved using the approach described by[33], also presented Appendix B. Let $(Z_1, ..., Z_M)$ be one of the solutions of Eq. (5.16) for the case $b_1 = ... = b_M = 1$. We construct an univariate polynomial in variable Z, given by:

$$\prod_{m=1}^{M} (Z - Z_m) = \sum_{m=0}^{M} (-1)^m e_m(\hat{V}_1, ..., \hat{V}_M) Z^{M-m} = 0, \tag{5.19}$$

where $e_0, ..., e_M$ are elementary symmetric polynomials in M variables, which can always be written as a function of the complex voltages $\hat{V}_1, ..., \hat{V}_M$ if $b_1 = ... = b_M = 1$. The relation between the $e_0,...,e_M$ and $\hat{V}_1,...,\hat{V}_M$ is given by [34]:

$$m e_m = \sum_{j=1}^{m} (-1)^{j-1} \hat{v}_j e_{m-j}. \tag{5.20}$$

where $\hat{v}_j = \hat{V}_j/a_{j,ref}$ and $e_0 = 1$. Solving Eq. (5.20) for $e_1,...,e_M$ gives $e_m = e_m(\hat{V}_1, ..., \hat{V}_M)$ (where $m = 1, ..., M$). Therefore, solutions of the symmetric system of the system is given by $Z_{sol} = (Z_1, ..., Z_M)$, where $Z_1, ..., Z_M$ are the roots of Eq. (5.19). Other solutions are given by permutation of Z_{sol} coordinates: $(Z_1, Z_2, ..., Z_M), (Z_2, Z_1, ..., Z_M),$ $(Z_M, Z_2, ..., Z_1),...$ If two or more resonance wavelengths coincide, the polynomial in Eq. (5.19) has multiple roots. In this case, although not explored in the experimental Section, the Newton method's corrections are no longer possible to be obtained as the Jacobian of the left-hand side of Eq. (5.16) becomes singular. As a result, the accuracy of $\delta_1(t), ..., \delta_M(t)$ to obtained from Eq. (5.19) decreases. However, Eq. (5.19) can be solved, indicating the interrogator's high flexibility concerning $\lambda_{01}, ..., \lambda_{0M}$ and $\delta_1(t), ..., \delta_M(t)$ values.

The main difference between the second approach and the method proposed in our previous article [13] is the initial guess of Newton's method: in our last paper,

	Buffer 1	Buffer 2		Buffer M
0	$\hat{V}_1(t_0)$	$\hat{V}_2(t_0)$	...	$\hat{V}_M(t_0)$
1	$\hat{V}_1(t_1)$	$\hat{V}_2(t_1)$	...	$\hat{V}_M(t_1)$
	...	...	...	...
N-1	$\hat{V}_1(t_{N-1})$	$\hat{V}_2(t_{N-1})$	...	$\hat{V}_M(t_{N-1})$

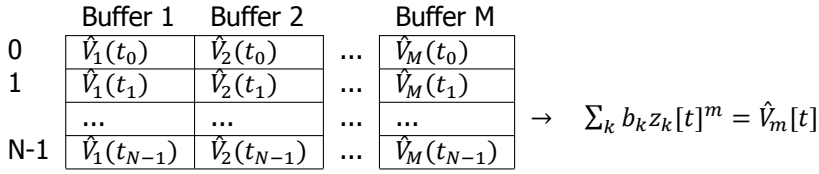$$\rightarrow \quad \sum_k b_k z_k[t]^m = \hat{V}_m[t]$$

Figure 5.2: Buffers copied to CUDA device memory. Each buffers' row represents a different algebraic system of equations, according to Eq. (5.11), displayed on right side of the figure.

the starting point is given by the solution obtained in the previous time step, while in this novel method, the starting point is given by the solution of the symmetric algebraic system. The second approach has been implemented in CUDA. Solving the non-linear equations using a GPU is only possible due to novel algebraic formulation: in the previous article, since the initial guess depends on Newton's method solution of a past time instance, the equations had to be solved sequentially. On the other hand, in the novel algebraic formulation, the complex voltages are stored in M buffers of with N elements each, as shown in Fig. 5.2. Each buffers' row represents a different algebraic system of equations to be solved, as also shown in the figure. All N equations are solved in parallel as earlier described: first, the solution of N symmetric equations is obtained (for $t = 0...t_{N-1}$) by computing the roots of Eq. (5.19); next, the solution is corrected using Newton's method, also evaluated in the GPU.

5.4. Experimental procedure

5.4.1. Experimental setup

The experimental setup is shown in Fig. 5.3. The FT-interrogator has been characterized using three FBG strain sensors. Fig. 5.3(a) shows that the ends of the fibers, which contain the fabricated FBGs, are mechanically attached to a manual positioner and a stepper motor. The manual positioners are used to apply an initial stress to the FBGs so that the resonance wavelengths of the sensors can be controlled at $t = 0$. In our experiment $\lambda_{0,1} = 1550.52$ nm, $\lambda_{0,2} = 1551.7$ nm and $\lambda_{0,3} = 1551.08$ nm. Their full width half maximum (FWHM) are 100, 125 and 112 pm, respectively. As the stepper motor (Standa, 8Mt_167-100) travels along the x-axis, it stresses the fiber, causing the resonance wavelength of the FBGs to be modulated according to the position of the stepper motor. Two stepper motors have been used. FBG 3 is chosen as the reference sensor and is attached to stepper motor (1), and the other two FBG sensors are attached to stepper motor (2). While stepper motor (2) travels back and forth along the x-axis over a fixed distance Δx = - 20 μm, stepper motor (1) moves along different distances on the x-axis (Δx), as shown in Fig. 5.3(b). Thus, different stresses can be applied to the reference sensor. The Δx values are later used to retrieve the curve strain versus resonance wavelength modulation. The stepper motors are defined as always first travelling towards negative x-axis values and afterwards returning in the positive direction to the original position. As a result, the fiber elongation is always negative with

respect to its length at $t = 0$, when the stepper motor is in its original position. Thus, the strain in the FBGs is always negative, preventing the FBGs from being damaged if the stepper motor is accidentally configured to move to a high value of Δx.
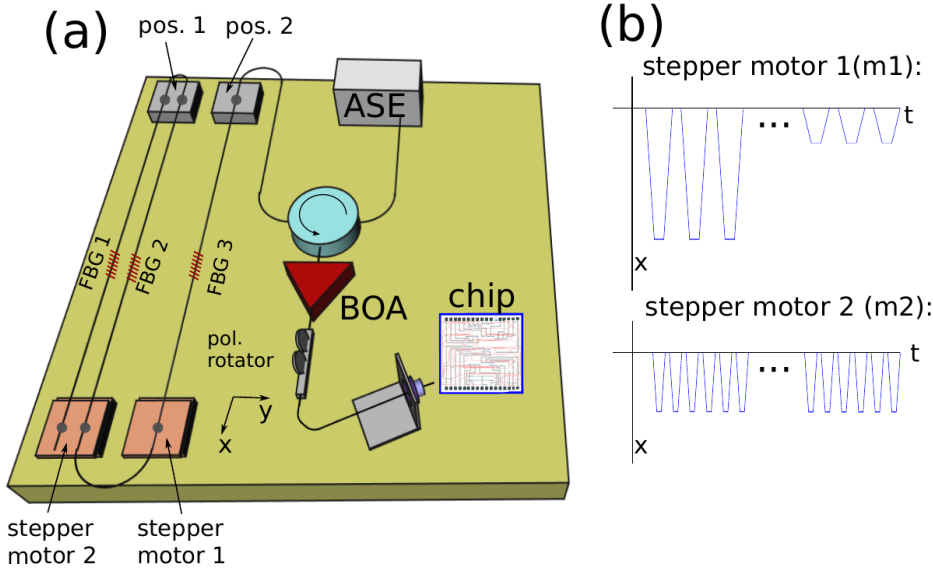

Figure 5.3: (a) Schematic of the experimental setup. The circulator is represented as a blue circle and the booster optical amplifier (BOA) as a red triangle. Three FBGs have been used to characterize the interrogator. The stepper motors and their moving plate are represented in orange. (b) Position of stepper motors 1 and 2 as a function of time.

The amplified spontaneous emission (ASE) light source (Optolink, OLS15CGB-20-FA), shown in 5.3 (a), emits a broadband spectrum, which can be assumed to be flat in the region of operation of the photonic sensors and to be unpolarized. The circulator couples the signal from the ASE source to the FBG sensor array. Next, each FBG reflects a gaussian shaped-peak (whose resonance wavelength is modulated according to the external excitation) to the circulator. The circulator then guides the optical signal to the BOA (Thorlabs, S9FC1004P), which amplifies it and provides a gain of 20.5 dB. It should be noted that the BOA gain is applied only to one of the polarization states of the input light signal. This is an important issue because the integrated photo-detectors on the chip feature a high polarization dependency, being nearly insensitive to quasi-TM modes. Hence, the polarization rotator (shown in Fig 5.3(a)) is used to maximize the power coupled to the quasi-TE modes in the chip waveguides. Subsequently, by using a lensed fiber (Oz Optics, TSMJ-3A-1550_9), the light signal is brought to chip input 6 and guided to MZIs 1 - 5 (see Fig. 5.1). The output voltages of the electronic board are recorded by analog to digital convertors (ADC) at a sampling frequency $f = 10$ kHz. The algorithm described in Section 5.3.2 has been implemented in Python and in C++, using an

™NVidia Tesla K40®graphics processing unit.

5.4.2. Calibration

The goal of the calibration procedure is to determine the coefficients b_k (for $k = 1, ..., M$) in Eq. (5.11), as well as the complex values of $a_{m,ref}$ (for $m = 1, ..., M$). The procedure presented here is similar to the one in our previous paper. The coefficients a_{mk} (for $m = 1, ..., M$) are obtained by exciting the k-th sensor individually. During the calibration time interval t_{cal}^k, when k-th sensor is excited, Eq. (5.6) can be written as:

$$\hat{V}_m(t_{k,cal}) = a_k \exp(im\delta_k(t_{k,cal})) + \underbrace{\sum_{j,j\neq k} a_{mj}}_{\text{other sensors}}, \qquad (5.21)$$

where the other sensors receive no excitation and they contribute only as a constant in Eq. (5.21). Regardless of the excitation applied, Eq. (5.21) describes a circle arc in the complex plane. Hence, we fit a circle to the Lissajous curve $\left(\Re\{\hat{V}_m(t_{cal})\}, \Im\{\hat{V}_m(t_{cal})\}\right)$. The radius and angle of this arc at the beginning of the k-th photonic sensor calibration ($t = t_{start}^k$) give the modulus and argument of a_{mk}:

$$R_{mk} = |a_{mk}|,$$
$$\Phi_{mk}(t_{start}^k) = arg(a_{mk}), \qquad (5.22)$$

where $\Phi_k(t_{start}^k)$ is the angle of the circle arc at $t = t_{start}^k$. Both positive and negative stress is applied to the FBG strain sensors shown in Fig. 5.3(a) so that the excitation applied to the k-th sensor is zero at the end of its calibration ($t = t_{end}^k$), which gives:

$$\delta(t_{start}^k) = \delta(t_{end}^k) = 0. \qquad (5.23)$$

Hence, the resonance wavelengths λ_{0k} (for $k = 1, ..., K$) are unchanged by the calibration procedure. From Eq. (5.10), it can be shown that the argument of z_k (for $k = 1...K$) is given by

$$\arg\left(z_k(t_{start}^k)\right) = \arg\left(z_k(t_{end}^k)\right) = \arg(z_k(0)) = \Phi_{1,k} - \Phi_{1,ref}. \qquad (5.24)$$

According to the convention adopted here, the calibration procedure occurs for $t < 0$, while the experimental simultaneous excitation of the sensors starts at $t = 0$. No excitation is applied during the period $t_{end}^k < t < 0$, and thus, the argument of $z_k(t)$ is constant during this period. Since the arguments of the complex variables at $t = 0$ are known and given by Eq. (5.24), they are used to identify the sensors, as explained in Section 5.3.2. Imperfections in the 3×3 couplers distort the arc of the circle in Eq. (5.21) into an arc of an ellipse. The variation of the parameters in the electronic circuit responsible for computing Eq. (5.2) also contributes to the increasing of the ellipse eccentricity and furthermore introduces voltage offsets. Hence, instead of a circle, we fit an arc of an ellipse to $V_{m,x}(t_{k,cal})$ and $V_{m,y}(t_{cal})$. A linear transformation is applied to map the ellipse arcs to the circle arcs. For further details, please refer to [13].

Table 5.1: Parameters extracted during the calibration

Parameter	Value	Unit
b_1	0.94	1
b_2	1.04	1
$a_{3,1}$	-110.8 + 235.1 i	mV
$a_{3,2}$	-247.7 + 174.8 i	mV
$a_{3,3}$	261.7 - 107.4 i	mV

5.5. Experimental results

5.5.1. Solutions of the algebraic system of equations

The algebraic system of equations is explicitly written for three sensors:

$$p_1(z_1, z_2, z_3) = b_1 z_1 + b_2 z_2 + z_3 - \hat{V}_1/a_{1,3} = 0$$
$$p_2(z_1, z_2, z_3) = b_1 z_1^2 + b_2 z_2^2 + z_3^2 - \hat{V}_2/a_{2,3} = 0 \qquad (5.25)$$
$$p_3(z_1, z_2, z_3) = b_1 z_1^3 + b_2 z_2^3 + z_3^3 - \hat{V}_3/a_{3,3} = 0,$$

where the third sensor is chosen as a reference so that $b_3 = 1$. We dropped the time dependency of $z_m = z_m(t)$ and $V_m = V_m(t)$(for $m = k, ..., M$) for simplifying the notation.

Fig. 5.4(a) shows the measured voltages $V_{1,x}(t)$ and $V_{1,y}(t)$. In order to reduce the noise, a 45 Hz digital low pass filter has been applied to all measured voltage signals. During the calibration procedure, the sensors were excited separately, resulting in three ellipse arcs in the Lissajous curves $(V_{m,x}(t), V_{m,y}(t))$. As explained in Section 5.4.2, the ellipse arcs are obtained instead of circle arcs mainly due to imperfections when using the 3×3 couplers. The linear transformation described in our previous Chapter (see Section 3.2 of [13]), maps the ellipse arcs to circle arcs and removes the voltage offsets. The corrected values of $V_{1,x}(t)$ and $V_{1,y}(t)$ are plotted as a Lissajous curve, seen in Fig. 5.4(b). The figure also shows circles fitted to the data points $(V_{1,x}(t_k^{cal}), V_{1,y}(t_k^{cal}))$, where t_k^{cal} is the calibration interval of the k-th sensor. In some areas of Fig. 5.4(b) the data points deviate from the arc, following a path closer to the center. This phenomenon has already been reported in our previous Chapter, and it occurs when the resonance wavelength between two FBG sensors overlap, creating an undesirable Fabry-Perot effect. Thus, some optical energy is stored in the Fabry-Perot cavity and the radius of the circle to be shortened. During the circle fittings, the points that highly deviate from the circle arc have been neglected. From the radii of the arcs and their angles phases at $t = t_k^{start}$, the parameters of Eqs. (5.25) are retrieved and are shown in Table 5.1.

The system of Eqs. (5.25) have been solved using two different approaches, as described in Section 5.3. *Method 1* consists of computing the Gröbner basis of the ideal $I = < p_1, p_2, p_3 >$, where the polynomials p_1, p_2 and p_3 are defined in Eqs. (5.25). The computation cost of retrieving the Gröbner basis in terms of time and memory is high and the number of monomials of the basis is extremely large. For that reason, the polynomials of the basis are not presented in this paper but can
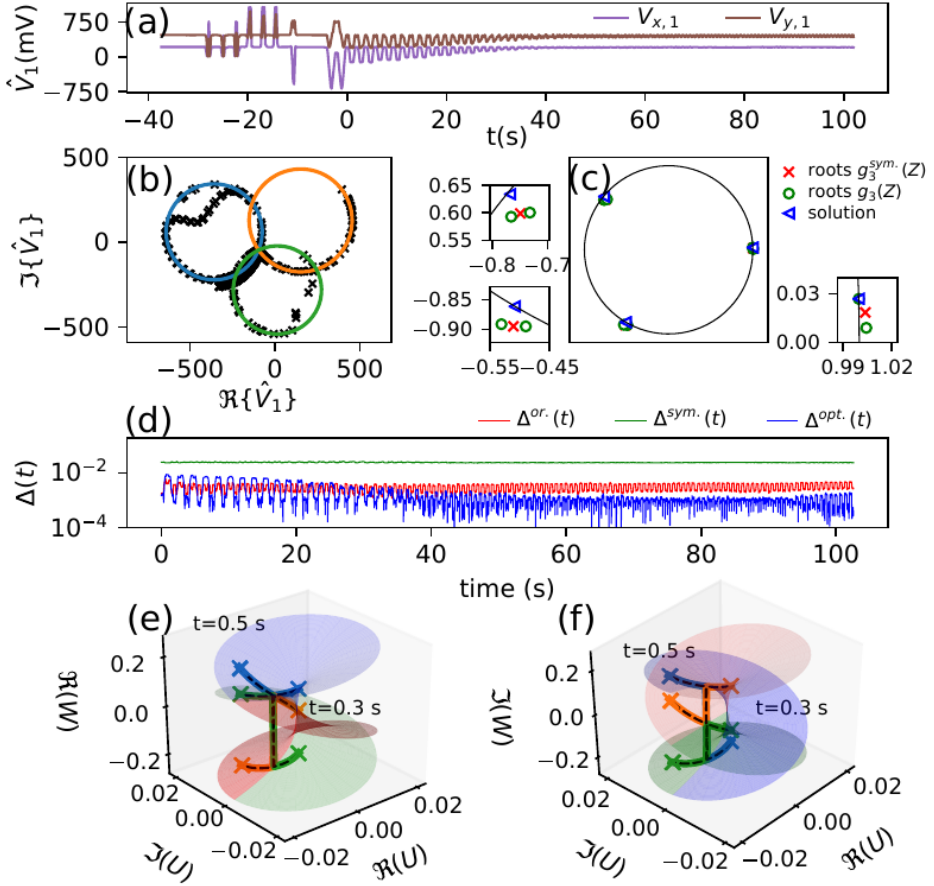
Figure 5.4: (a) Output voltages $V_{1,x}(t)$ and $V_{1,y}(t)$ recorded by the ADCs. The calibration is for $t < 0$. (b) Lissajous plot for $(\Re\{\hat{V}_1(t)\}, \Im\{\hat{V}_1(t)\})$. The circles fitted to the individual excitation of sensors 1,2 and 3 are shown in blue, orange and green, respectively. (c) Root loci of polynomials $g_3(Z)$ and $g_3^{sym.}(Z)$ at $t = 0$. The solution of the algebraic system of Eq. (5.25) from which the resonance wavelength modulation is obtained is also shown in the figure (blue triangle) as is the unit circle. The figure shows the effect of the symmetry breaking: each of the roots of $g_3^{sym.}(Z)$ (red crosses) are split into two roots of $g_3(Z)$ (green circles). Only one of the roots of $g_3(Z)$ lies on the unit circle. (d) Function $U(t)$ evaluated for the solutions of the symmetric system (in green), the original system of equations (in red) and the optimized system (in blue), obtained in Section 5.5.2. (e) Real and (f) imaginary parts of the paths $W_1(t)$, $W_2(t)$ and $W_3(t)$ as a function of $\Re\{U\}$ and $\Im\{U\}$. Branches of the cubic root function are represented by the sheets shown in blue, red and green.

be obtained using the *groebner* command in the SymPY Python module. The computation of the Gröbner basis can be unfeasible for higher order non-symmetrical algebraic systems and the number of solutions follows a factorial growth: for 6 sensors, the algebraic system gives 720 solutions, of which 719 are spurious if the coefficients b_k (in this case for $k = 1...6$) are all different. *Method 1* has been implemented in Python only.

The second method (hereby referred as Method 2) for solving Eqs. (5.25) has two steps: (1) compute the solutions of the symmetric system of equations, obtained under the approximation $b_1 = b_2 = b_3 = 1$; (2) improve the solution using Newton's method. The symmetric system of equations can either be solved by using the Gröbner basis calculation or by calculating the roots of Eq. (5.19), as described in Section 5.3.2. The elements of the Gröbner basis $G^{sym} = \{g_1^{sym}, g_2^{sym}, g_3^{sym}\}$ are:

$$g_1^{sym}(z_1, z_2, z_3) = -\hat{V}_1 + z_1 + z_2 + z_3 = 0,$$
$$g_2^{sym}(z_2, z_3) = \hat{V}_1^2 - 2v_1 z_2 - 2\hat{V}_1 z_3 - \hat{V}_2 + 2z_2^2 + 2z_2 z_3 + 2z_3^2 = 0,$$
$$g_3^{sym}(z_3) = -\hat{V}_1^3 + 3\hat{V}_1 \hat{V}_2 - 6\hat{V}_1 z_3^2 - 2\hat{V}_3 + 6z_3^3 + z_3\left(3\hat{V}_1^2 - 3\hat{V}_2\right) = 0. \quad (5.26)$$

The computational cost for obtaining the G^{sym} is much reduced for the symmetric system of equations. Convergence is achieved with only three Newton's method iterations. This method has been implemented in C++/CUDA, taking approx. 8.6 ms (using a Tesla K40 GPU) and 12.6 ms (using a Ge Force GTX 1050 Ti) to solve approx. 1000 000 systems of equations. The transfer time from CPU to GPU memory is included in the numbers presented in table 5.2. Compared to the formulation we presented in [13], implemented in a CPU, the processing time improves in more than two orders of magnitude, allowing for real-time interrogation of high-speed sensors in tens of MHz range. The previous approach is limited for sensors that operate at maximum in tens of kHz range (eventually 100 kHz for three sensors only). In particular, the current interrogator a candidate for interrogate arrays of ultrasound ring resonator sensors [8, 9, 35, 36]. Ref. [35] uses four ultrasound ring resonators sensors for photoacoustic imaging, allowing to solve the equations using *Method 2*.

Table 5.2: Time comparison of different systems. Time data transfer for CPU and GPU is included in the times below

System	Compiler	Time
i7, Ubuntu 19, GPU (Tesla)	nvcc	8.6 ± 1 ms
i7, Ubuntu 19, CPU	g++	6 s
i7, Ubuntu 19, GPU (GeForce)	nvcc	12.6 ± 0.5 ms
i5, Windows 10, CPU	MinGw, g++	8.3s

For a larger number of sensors, it is no longer possible to compute the roots of polynomials analytically. Thus, the performance is as fast as the GPU can compute roots of polynomials. An estimative of the total computational time has been made for a symmetric system with eight sensors. Using Tesla K40 GPU, it was possible to

solve one million symmetric algebraic systems in 86 ms, of which 26 ms concern the data transfer from CPU+GPU and 60 ms of processing. As a result, real-time inter-rogation is feasible for sensors' that operate up to a few MHz range. For simplicity, Newton's method has been used to find the roots of a univariate polynomial. For a fixed number of iterations (in this case, six iterations), processing time increases linearly with the number of sensors. Other efficient polynomial root algorithms can be used to improve the processing time [37].

A third method, described in [38], has also been implemented. In this case, a larger number of equations and complex voltages are needed: for M sensors, $2M - 1$ equations are needed. For three sensors, five equations are needed. This method generalizes the algebraic approach for solving the symmetric system of equations described in Section 5.3.2 for non-symmetrical polynomials and returns a unique solution. The spurious solutions, which satisfy the three equations in Eq. (5.25), do not satisfy the other two equations. However, due to the coherence length of the photonic sensors, the complex voltages of $\hat{V}_4(t)$ and $\hat{V}_5(t)$ feature a reduced visibility and the resonance wavelength obtained is extremely noisy. For this reason, the results are not shown. In terms of complexity, the method requires solving an M×M linear system + computing the roots of an M order polynomial. For the estimative of processing time with eight sensors, the linear system of equations has been solved using LU decomposition and *cublas* library. The processing time obtained is about 90 ms. In total, we estimate about 200 ms for solving a 1 000 000 non-symmetric algebraic systems with eight sensors. The processing time of LU decomposition features a third-order dependence with respect to the number of sensors.

Fig. 5.4(c) compares the root locus (at t=0) of the univariate polynomials of the Gröbner bases $g_3^{sym}(z_3)$ and $g_3(z_3)$, obtained from both the symmetric and the original system of equations. $g_3^{sym}(z_3)$ has a degree of three, as can be observed in Eq. (5.26), while $g_3(z_3)$ has a degree of six. This symmetry breaking causes each of the roots of $g_3^{sym}(z_3)$ to split into two roots, as shown in Fig. 5.4(c). The univariate polynomial g_3^{sym} can be written as a function of a generic variable Z:

$$g_3^{sym}(Z) = 6Z^3 - 6\hat{V}_1 Z^2 + \left(3\hat{V}_1^2 - 3\hat{V}_2\right)Z - \hat{V}_1^3 + 3\hat{V}_1\hat{V}_2 - 2\hat{V}_3 =$$
$$c_1 Z^3 + c_1 Z^2 + c_3 Z + c_4 = 0, \qquad (5.27)$$

where c_1, c_2, c_3 and c_4 are coefficients of the cubic. By solving Eq. (5.20) in terms of the elementary symmetric polynomials in three variables and substituting into Eq. (5.19), the obtained equation is identical to Eq. (5.27). Therefore, as explained in Section 5.3.2, the solutions of the symmetric system are given by all possible permutations of the coordinates of $Z_{sol} = (Z_1, ..., Z_M)$, where Z_1, Z_2 and Z_3 are the roots of $g_3^{sym}(Z)$. In contrast, the six solutions that satisfy Eqs. (5.25) are obtained by substituting the roots of $g_3(z_3)$ into the other order polynomials of the bases $g_1(z_1, z_3)$ and $g_2(z_2, z_3)$, which are linear with respect to z_2 and z_3, respectively. As a result, six solutions are obtained.

According to the proposition in Section 5.3.2, in general, there is only one so-lution in which the moduli of complex variables are all equal to one. This is the case since matrix $\mathbf{Q}_H$, defined in Eq. (5.57) in the appendix, is definite positive

for any instance of time. The noise causes the moduli of complex variables to be slightly different from one. Thus, *Method 1* chooses the solution which minimizes function $\Delta(t)$, defined by Eq. (5.17), i.e. it chooses the solution whose moduli of complex variables are closer to the unity. The solution obtained from *Method 1* at $t = 0$ is also shown in Fig. 5.4(c). The complex variables lie closer to the unit circle, compared to the complex variables of the symmetric solution, which are given by the roots of $g_3^{sym.}(Z(t))$. This occurs because no approximation has been made for coefficients b_1 and b_2, allowing the complex variable moduli to be closer to the theoretical value. Fig. 5.4(c) shows the value of function $\Delta(t)$ for the solutions of the original and the symmetric system. $\Delta(t)$ is about one order of magnitude lower for the solution of the original system one order of magnitude lower compared to the other spurious solutions obtained by *Method 1* (not shown). After three Newton's method iterations, the solution of the symmetric system converges to the solution obtained from *Method 1* so that the maximum difference of the resonance wavelength of the sensors obtained from the two methods is about 10^{-11} pm.

Figs. 5.5 (a), (b) and (c) show the resonance wavelength modulation obtained from *Method 2*. This method is taken as the reference due to its simplicity and because roots of third order polynomials can be analytically evaluated. The colors in Figs. 5.5 (a), (b) and (c) indicate the root of the cubic equation from which the resonance wavelength has been computed and then later corrected using Newton's method. For $t > 40$, there is a one-to-one correspondence between the j-th root of $g_3^{sym}(Z)$ and the signal of the j-th sensor. However, for $t < 40$, the complex variables swap, as described in Section 5.3.2. This swap occurs when the argument of function $U(t)$, which satisfies Eq. (5.28), reaches 180°. Function $U(t)$ is obtained after applying a series of variable transformations in Eq. (5.27), reducing the degree of the polynomial to two. For details, we refer to Appendix B. $U(t)$ obeys the second order equation:

$$U(t)^2 + Q(t)U(t) - \frac{P(t)^3}{27} = 0, \tag{5.28}$$

where $P(t)$ and $Q(t)$ are the depressed cubic coefficients, also defined in [33]. Eq. (5.28) has two solutions: $U_+(t)$ and $U_-(t)$, given by:

$$U_\pm(t) = \frac{-Q(t)}{2} \pm \sqrt{\frac{P(t)^3}{27} + \frac{Q(t)^2}{4}}. \tag{5.29}$$

The roots of Eq. (5.27) have been obtained using $U_-(t)$, according to:

$$Z_j(t) = W_j(t) - \frac{P(t)}{3W_j(t)} - \frac{c_2}{3c_1}, \tag{5.30}$$

where $W_j(t) = \xi_j U_-(t)^{1/3}$ and $\xi_j = \exp(i(j-1)2\pi/3)$ (for $j = 1, 2, 3$) are cubic roots of unity. Although both values of $U_+(t)$ and $U_-(t)$ are valid and could be used into Eq. (5.30), the choice of $U_+(t)$ or $U_-(t)$ impacts on the swapping of the complex variables: the argument of $U_+(t)$ never reaches 180° and, hence, no swapping occurs. Aiming to understand the swapping of the complex variables, the roots of

Eq. (5.27) have been obtained using $U_-(t)$. The principal value of $U(t)^{1/3}$ is defined according to [39, 40]:

$$U^{1/3}(t) = |U(t)|^{1/3} \exp\left[i\frac{\arg(U(t))}{3}\right],$$
(5.31)

where $\arg(U(t))$ ranges from $[-\pi, \pi)$. Let $d\Phi_U > 0$ be a small variation in the argument of function $U(t)$. Suppose that at $t = t_{0_-}$ the argument of $U(t_{0_-})$ is given by $-(180^o - d\Phi_U)$ and the modulation applied to the sensors adds $2d\Phi_U$ to $\arg(U(t))$ at $t = t_{0_+}$. Thus, the term $\arg(U(t))/3$ in Eq. (5.31) induces a discontinuity according to:

$$\frac{\arg(U(t_{0_-}))}{3} = \frac{(-\pi - d\Phi_U)}{3} \rightarrow \frac{\arg(U(t_{0_+}))}{3} = \frac{+\pi - d\Phi_U}{3},$$
(5.32)

due to the fact that $\arg(U(t))$ is always limited by the range $[-\pi, \pi)$. As a result, the paths $W_j(t)$ (for $j = 1, 2, 3$) swap according to:

$$\begin{aligned}
W_1(t_{0_-}) &\rightarrow W_3(t_{0_+}), & Z_1(t_{0_-}) &\rightarrow Z_3(t_{0_+}) \\
W_2(t_{0_-}) &\rightarrow W_1(t_{0_+}), & Z_2(t_{0_-}) &\rightarrow Z_1(t_{0_+}) \\
W_3(t_{0_-}) &\rightarrow W_2(t_{0_+}), & Z_3(t_{0_-}) &\rightarrow Z_2(t_{0_+}).
\end{aligned}$$
(5.33)

This situation can be observed in the Riemann surfaces shown in Figs. 5.4(e) and 5.4(f). The figures show the real and imaginary part of the paths $W_1(t)$, $W_2(t)$ and $W_3(t)$ obtained from the measured complex voltages for $0.3 < t < 0.5$ s, which corresponds to the first swap of complex variables of Fig. 5.5(a). The figure also depicts three sheets (in blue, red and green) corresponding to the three branches of the complex cubic root, on which the paths $W_1(t)$, $W_2(t)$ and $W_3(t)$ travel along. The three branches of the complex cubic roots are discontinuous at the semi-plane $\arg(U) = 180°$, causing $W_1(t)$, $W_2(t)$ and $W_3(t)$, calculated from Eq. (5.30) and Eq. (5.31), to be discontinuous. However, by joining the three discontinuous branches, Figs. 5.4(e) and 5.4(f) show that the three cubic roots of $U(t)$ are continuous everywhere. This assures the continuity of the retrieved values of the resonance wavelength modulation of the sensors, encoded in the complex variables' arguments.

For the symmetric system of equations, solutions are given as permutations of the variables $(Z_1(t), Z_2(t), Z_3(t))$. Hence, the swapping of the complex variables indeed represents a swapping of the solutions. Solutions also swap in the original system of equations, in which only one of the solutions is valid. The cross markers in Fig. 5.5(a) indicate the points at which the solutions obtained from *Method 1* swap. Those points are identified by function $\Delta(t)$, which senses when a different solution has the modulus of its complex variables closer to unity. The swapping of the solutions in Fig. 5.5(a) occurs close to the points where functions $W_1(t)$, $W_2(t)$, and $W_3(t)$ swap. Such difference occurs due to the small difference of coefficients b_1, b_2 and b_3 of the original and the symmetric system of equations.

Figs. 5.6(a) and (b) show zoomed-in graphs of the resonance wavelength modulation of sensor 3, obtained by solving the symmetric, and the original system of
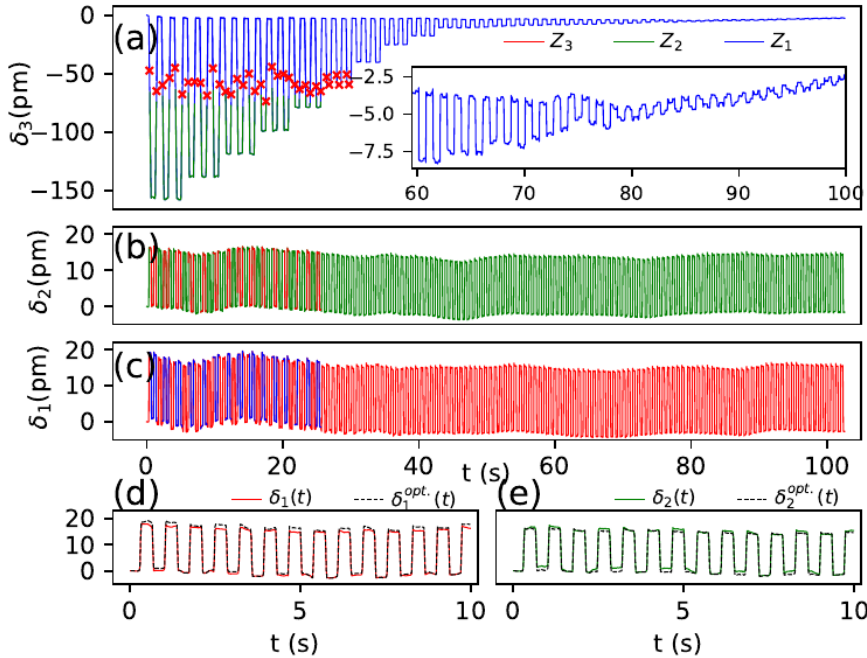
Figure 5.5: (a) Resonance wavelength modulation of sensor 3. The inset shows that the modulation of FBG 3 slowly drifts along the time. This occurs since the sensors also respond to local fluctuations of the temperature. (b) Resonance wavelength modulation of sensor 2. (c) Resonance wavelength modulation of sensor 1. Colors indicate the complex variable from which the resonance wavelength has been obtained, where $Z_1(t)$, $Z_2(t)$ and $Z_3(t)$ are defined in Eq. (5.30). The crosses indicate the time instants at which the solutions obtained from *Method 1* swap. (d), (e) Zoomed resonance wavelengths $\delta_1(t)$ and $\delta_2(t)$ for $t < 10$.

equations, respectively. The distortion of function $\delta_3(t)$ observed in both figures is caused by cross-talk: although not visible in Figs. 5.6(a) and (b), the disturbances of the function $\delta_3(t)$ follow the modulation of $\delta_1(t)$ and $\delta_2(t)$. Comparing the resonance obtained by solving the symmetric and the original system of equations, shown in Figs. 5.6, the cross-talk is much less present in the solution of the original system. This indicates that the accuracy of coefficients b_1 and b_2 impact the cross-talk, although some cross-talk is still visible in Fig. 5.6(b). In the next section, spurious solutions obtained using *Method 1* are used to reduce the cross-talk.

5.5.2. Optimization of the solutions

Despite the higher cross-talk, the resonance wavelength modulations calculated from the spurious solutions are of similar value to the values shown in Figs. 5.5(a), (b) and (c). The similarity can be explained by the fact that the algebraic system is quasi-symmetric. If $b_1 \cong ... \cong b_M \cong 1$, it follows from the Proposition of Section 5.3.2 that the locus in the complex plane of spurious solutions lies close to the actual solution. Fig. 5.4(c) experimentally demonstrates this phenomenon, as discussed in the previous section. The closer the coefficients $b_1, ..., b_m$ are to a value of one, the closer the non-physical solutions are to the actual solution, and the less cross-talk they feature. One of the spurious solutions, however, showed an unusual behaviour. As expected, for $t < 40s$, when larger stresses are applied to FBG 3, its cross-talk was higher compared to the actual solution. For $t > 40s$, on the other hand, the cross-talk diminishes significantly, becoming smaller compared to the actual solution. A possible explanation for this is inaccuracies of the parameters b_1, b_2 and $a_{m,ref}$ (for $m = 1, 2, 3$) retrieved in the calibration procedure. Eqs. (5.22) gives the relationship between the radius of the circle arc fitted and the modulus of the variables a_{mk}. Hence, inaccuracies in the fitting lead to inaccuracies of variables a_{mk} and b_k. As a result, the modulus of complex variables must change to keep the equality in Eqs. (5.25). Moreover, with the presence of some noise level, circle centres obtained from the fitting can also be inaccurate, resulting in $|z_m| \neq 1$ for $|z_m| \neq 1$ for $m = 1, 2, 3$.

In order to improve the current solution, the following optimization procedure has been implemented:

$$\text{Minimize } F_{opt}(\Delta b_1, \Delta b_2, G_{v1}, G_{v2}, G_{v3}, \Delta\hat{v}_1, \Delta\hat{v}_2, \Delta\hat{v}_3, \Delta a_3) =$$

$$\sum_{i=0}^{2} w_{ti} \int_{t_{opt,i}} \sum_m \left| -\left(g_{vm} \frac{\hat{V}_m(t)}{a_{m,3}} + \Delta V_m \right) + (b_1 + \Delta b_1) \exp\left[im \; argz_1(t) \right] + \right.$$

$$\left. (b_2 + \Delta b_2) \exp\left[im \; argz_2(t) \right] + \exp\left[im \; argz_3(t) \right] \right|, \quad (5.34)$$

where $w_{t_1} = 1$ and $w_{t_2} = 25$ are the weights of the intervals considered in the optimization procedure: $0 < t_{opt,1} < 6s$ and $62s < t_{opt,2} < 72s$. The complex exponentials in Eq. (5.34) impose the condition $|z_1| = ... = |z_M| = 1$, according to Eq. (5.10). Parameters $\Delta b_1, \Delta b_2, g_{v1}, g_{v1}, g_{v3}$, compensate for inaccuracies in the radius of the circle arcs, while parameters $\Delta\hat{v}_1, \Delta\hat{v}_2$ and $\Delta\hat{v}_3$ compensate for voltage

offsets introduced by inaccuracies in the centers of the circle arcs. During the optimization, the values of the complex variables $z_1(t)$, $z_1(t)$ and $z_3(t)$ depend on the reference chosen. The first optimization interval uses the current solution from *Method 1* as a reference in order to avoid an increase in the cross talk for large stresses applied to FBG 3. The second interval, in contrast, as reference, uses the spurious solution found in *Method 1* whose resonance modulation for sensor 3 is shown in Figs. 5.6(b). The results of the optimization are shown in Table 5.3.
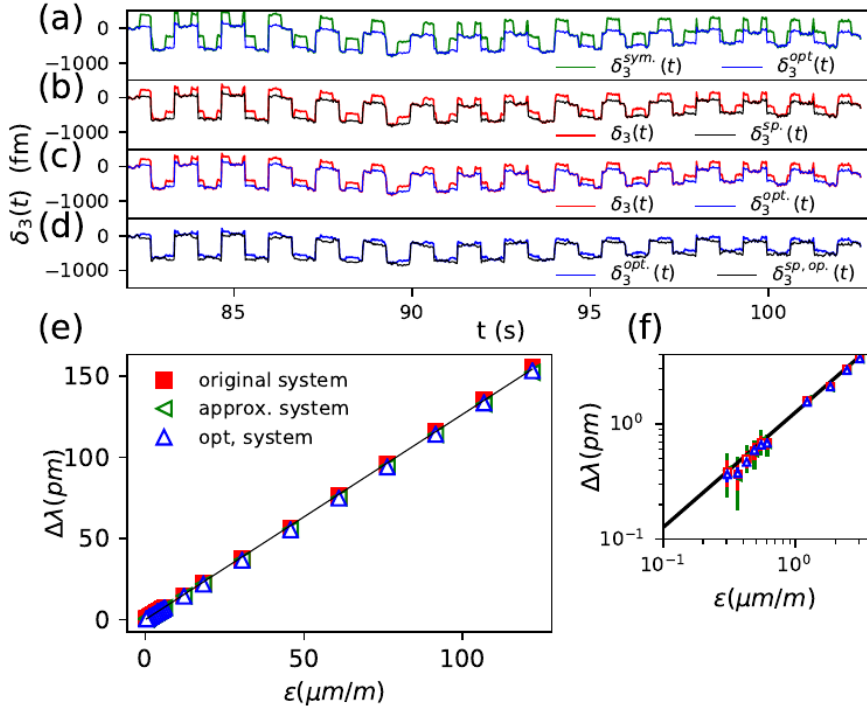

Figure 5.6: (a)-(d) Zoomed resonance wavelengths obtained for sensor 3. The thermal background, shown in the inset of Fig. 5.5(a), has been subtracted for a better visualization. (a) Compares the optimized and symmetric solution; (b) compares the spurious and original solution; (c) compares the original and the optimized solution and (d) compares the optimized solution and one of the spurious solutions of the optimized system of equations. (e) Amplitude of the resonance wavelength modulation as a function of the strain. (f) Zoom of the amplitude of the resonance wavelength modulation as a function of the strain.

After the optimization, the parameters of the equations have been adjusted using the corrections shown in Table 5.3. The algebraic system of Eqs. (5.25) has been solved using Methods 1 and 2 and the resonance wavelength modulations $\delta_1^{opt.}(t)$ and $\delta_2^{opt.}(t)$ and $\delta_3^{opt.}(t)$ have been computed according to the procedure

Table 5.3: Parameters obtained from the optimization

Δb_1	Δb_2	G_{v1}	G_{v2}
3.327 10^{-3}	-11.14 10^{-3}	0.983	1.004

G_{v3}	Δv_1 (μV)	Δv_2 (μV)	Δv_3 (μV)
0.974	(-2.848 + 8.991 i)	(15.61 -22.52 i)	(72.49 + 28.10 i)

described in Section 5.3.2. A meaningful overall reduction of the cross-talk can be observed, especially for small stresses applied to FBG3, as seen in Figs. 5.6(a) and (c). The figures show a maximum cross-talk of approx. 100 fm observed for $\delta_3^{opt}(t)$, which is around three times smaller than for $\delta_3(t)$. For the other time instants, the values of $\delta_m^{opt.1}(t)$ and $\delta_m(t)$ (for $m = 1, 2, 3$) are very similar. Some differences can be observed in sensors 1 and 2 for $t < 10$s, as shown in Figs. 5.5(d) and (e). The maximum cross-talk increases to about 1% (resonance wavelength pertubation of about 1.5 pm), observed in resonance wavelengths obtained from the original system of equations, to about 2.0 pm for the optimized resonance wavelength modulations. Cross-talk also affects the moduli of complex variables. Fig. 5.4(d) compares the function $\Delta(t)$, calculated for the solutions of the optimized and of the original system of equations. For $t < 20$ s, the complex variable moduli of the optimized solution feature a larger deviation from unity compared to the solution of the original system of equations. For $t > 60$ s, however, function $\Delta(t)$ is around four times smaller for the optimized solution.

Although the optimization significantly reduces cross-talk, some cross-talk remains present. Fig. 5.6(d) compares the resonance wavelength modulation obtained from one of the spurious solutions from the optimised system of equations and function $\delta_3^{opt}(t)$. The spurious solution shown in Fig. 5.6(d) is very similar to the one used as a reference in the optimization procedure: for small stresses of FBG3, the cross-talk is slightly smaller than for the one observed in $\delta_3^{opt}(t)$. In Eq. (5.9), it has been assumed that the lineshapes $s_k(\lambda)$ are identical except by a constant which specifies the peak height of the spectrum. However, this is not the case: the FWHM of $s_1(\lambda)$, $s_2(\lambda)$ and $s_3(\lambda)$ are 100 pm, 125 pm, and 110 pm, respectively, making this assumption inaccurate. This results in some cross-talk for either large or small stresses applied to the fibers. By increasing the ratio of the optimization weights w_{t_2}/w_{t_1}, it is possible to achieve a similar cross-talk level, compared to the spurious solution, at the cost of a cross-talk enhancement for $t < 10$ s.

Figs. 5.6(e) and (f) show the modulation amplitude of FBG 3 as a function of the strain in the fiber. The modulation amplitude is defined as:

$$\Delta\lambda_j^{(1)} = \left| \overline{\delta_{1,j}^{dip}} - \overline{\delta_{1,3j}^{max}} \right|, \tag{5.35}$$

where $\delta_{1,j}^{dip}$ is the average of the function $\delta_1(t)$ when the stepper motor rests at the position $x = \Delta x_j$; $\delta_{1,j}^{max}$ is the average of the function $\delta_1(t)$ when the stepper motor is at the position $x = 0$, immediately after the stepper motor has returned from $x = \Delta x_j$. The stress applied by the stepper motor is always negative, keeping

the function $\delta_3(t)$ at a minimum while it rests at $x = \Delta x_j$. In contrast, a local maximum is observed in function $\delta_3(t)$ when the stepper motor returns to $x = 0$ and stresses the fiber. Since the stepper motor travels 3 times to $x = \Delta x_j$, as indicated in Fig. 5.3(b), the three dips in function $\delta_3(t)$(for $x = \Delta x_j$) are considered in the j-th value of $\delta_{1,j}^{dip}$. Similarly, the data-points of three consecutive maxima of function $\delta_3(t)$ are considered in the calculation of $\delta_{1,j}^{max}$. The strain of the fiber is given by:

$$\varepsilon_j = \frac{\Delta x_j}{\ell_3},\qquad(5.36)$$

where ℓ_3 = 1.65 m is the fiber length. The strain in the fiber is assumed to be uniform so that the strain in the FBGs is given by Eq. (5.36). The angular co-efficients of the curves shown in Fig. 5.6(e) are 1.245 $\pm$ 0.001 pm/$\mu\epsilon$, 1.266 $\pm$ 0.002 pm/$\mu\epsilon$ and 1.242 $\pm$0.002 pm/$\mu\epsilon$ for the symmetric, original and optimized system of equations respectively. These values match the nominal slope provided by the manufacturer (1.2 pm//$\mu\epsilon$) and are consistent with the values presented in our previous article. The minimum scattering of the data points around the straight line shown in Figs. 5.6(e) and (f) occur for the optimized solution, which features the smallest cross-talk. The minimum resonance amplitude experimentally resolved was 365 fm. The signal to noise ratio is given by:

$$SNR = 20\log_{10}\frac{R}{\sigma},\qquad(5.37)$$

where σ is the noise standard deviation of $\hat{V}_1(t)$ and R = 283 mV is the radius of sensor 3 traced in the Lissajous curve $(\Re\hat{V}_1(t), \Im\hat{V}_1(t))$ shown in Fig. 5.4 (b). The SNR is 58 dB.

Limitations of FT interrogator can be enumerated as:

- Cross-talk caused by errors during calibration. This effect has been mitigated by the optimization procedure.

- Cross-talk due to the assumption the FWHM of the sensors is identical. This is a minor cause of the noise, which can also be compensated using Newton's method. However, in the context of interrogating high-speed sensors, integrated photonics allows the design of sensors with very similar Quality factor values, so that this effect can be neglected.

- Noise. The primary source of noise is electronic.

The noise RMS value of the demodulated signal is given by:

$$\sigma_{RMSE} = \sqrt{\frac{\sum_i^{N_{pts.}}\left(\delta_3^{opt.} - \overline{\delta_3^{opt.}}\right)^2}{N_{pts.}}},\qquad(5.38)$$

$N_{pts.}$ is the number of data points and $\overline{\delta_3^{opt.}}$ is the average value of $\delta_3^{opt.}$ for the stepper motor is at rest. Thus, σ_{RMSE} is the standard deviation of the noise and its value is 65 fm.

5.5.3. Comparison with other Interrogators

Table 5.4: Limit of detection of the FT Interrogator compared to other common interrogation methods. Focus is given to integrated interrogators, but some fiber interrogators are also presented. MRW is the minimum resonance wavelength experimentally resolved.

Author/Reference	Interrogation method	Limit of Detection
This work	Fourier Transform interrogator, algebraic formulation	σ_{RMSE} = 218 fm, $S_0 = 1.66\ n\varepsilon/\sqrt{Hz}$, MRW= 700 fm
D. Tosi[41]	Spectrometer, KLT	σ_{RMSE} = 0.003 C σ_{RMSE} ~30 fm
D. Tosi[42]	Spectrometer, KLT	σ_{RMSE} = 4.9 fm
Pustakhod et. el [43]	Integrated Spectrometer	MRW = 320 fm
Li et. al [44]	Integrated Spectrometer	MRW = 1 pm
Guo et. al [45]	Integrated Spectrometer	MRW < 1 pm
Orr et. al.[11]	MZI + Spectrometer + Optical Switch	$S_0 = 10\ n\varepsilon/\sqrt{Hz}$
Perry et. al.[12]	MZI + Spectrometer + Optical Switch	$S_0 = 10\ n\varepsilon/\sqrt{Hz}$
Merlin et. al. [46]	MZI, active modulation + Integrated spectrometer	$S_0 = 4.56\ n\varepsilon/\sqrt{Hz}$
Merlin et. al. [47]	MZI, active modulation + External spectrometer	$S_0 = 73\ n\varepsilon/\sqrt{Hz}$
He et. al [48]	Tunneable laser	$S_0 < 10\ n\varepsilon$
I4g FAZ Optics 11[49]	Tunneable laser	$S_0 < 0.83\ n\varepsilon/\sqrt{Hz}$@ 1kHz

Results presented in Sections 5.5.1 and 5.5.2 have been obtained after applying a low pass filter to the complex voltages $\hat{V}_1(t)$, $\hat{V}_2(t)$ and $\hat{V}_3(t)$. Indeed, effects such as the signals' cross-talk and the optimization performed in Section 5.5.2 are only visible for a reduced noise. Hence, the bandwidth has been limited. To properly compare the FT interrogator with others available in the literature, the algebraic systems of equations have been solved without applying any filter to the input complex voltages. In this section, we use the notation $\delta_3(t) = \delta_3^{opt.}(t)$, as the analysis has been done using the optimized parameters (see table 5.3). Fig. 5.7(a) shows $\delta_3(t)$ as a function of time: the SNR reduces to about 42 dB, while the bandwidth increases to about 1 kHz (Nyquist frequency is 5 kHz, but electronic PCBs provide a nearly flat response up to 1 kHz). For a moderate values of SNR = 40 dB, FT-interrogator is limited by the noise. The σ_{RMSE} increases to 218 fm, giving a 3 σ_{RMSE} = 654 fm. The minimum resonance wavelength resolved is about 700 fm, as shown in the inset of Fig. 5.7(a).

Fig. 5.7 shows the power spectral density (PSD) of $\delta_3(t)$. The multiple peaks, shown in the range $f < 100$ Hz, originate from the fact that the applied stress to FBG3 consists of an array of trapezoidal signals (see Fig. 5.3(b)) with different amplitudes, causing multiple harmonics to be present in the PSD of $\delta_3(t)$. The PSD also shows high peaks at multiples of the frequency $f_{el.}$ =50 Hz, corresponding to
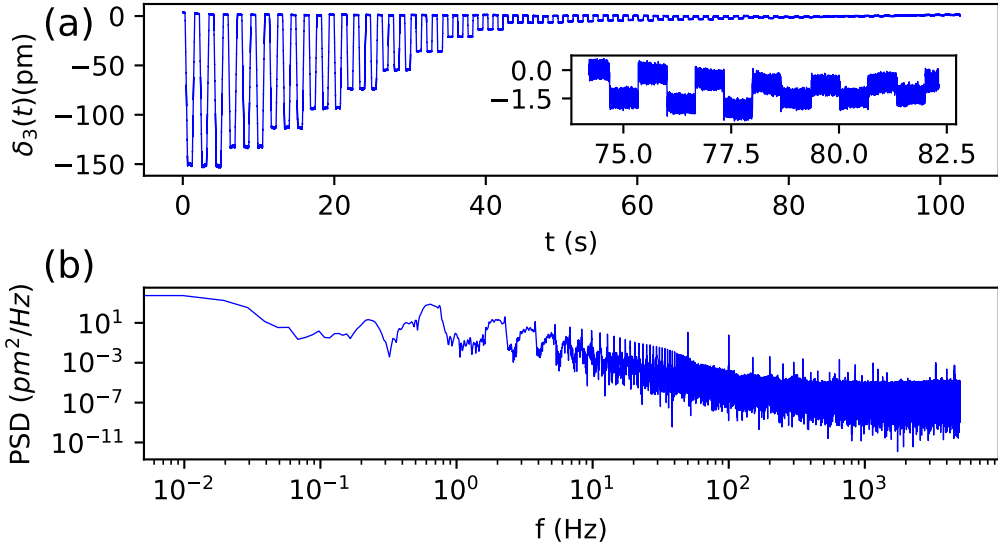
Figure 5.7: (a) Demodulated $\delta_3(t)$ for no applied low pass filter. (b) Power spectral density of $\delta_3(t)$.

the harmonics of the electric signal (50 Hz in Europe). They represent a major contribution to σ_{RMSE}: filtering these frequencies reduces σ_{RMSE} to 140 fm (112 nε, in units of strain) and 3 σ_{RMSE} to 420 fm (338 nε, in units of strain). PSD reaches its noise floor at approximately 300 Hz, and its value is $N_0^2 = 4.23 fm^2/Hz$ and $N_0 = 2.05 fm/\sqrt{Hz}$, where N_0 is the noise amplitude spectral density. The dynamic strain resolution is given by:

$$S_0 = N_0 \left(\frac{d\Delta\lambda}{d\varepsilon} \right)^{-1}, \tag{5.39}$$

where $d\Delta\lambda/d\varepsilon = 1.242\ pm/\mu\varepsilon$ is the slope of the curve wavelength shift per strain shown in Fig. (5.6) (e). The dynamic strain is given by $S_0 = 1.66\ n\varepsilon/\sqrt{Hz}$.

Table 5.4 compares the performance of FT spectrometer with other common interrogation methods described in the literature. Different authors characterize the interrogator limit of detection(LOD) using different parameters. These parameters, such as the minimum resonance wavelength demodulated and the noise rms value, depend on the SNR and the bandwidth at which measurements have been taken. Unfortunately, this information is not available for all the references listed in Table 5.4. Thus, the table gives only an idea of the performance of the various interrogation methods but is sufficient to demonstrate the high resolution of the FT-interrogator compared to other interrogators.

Tosi et al. [41, 42] use Karhunen Loeve Transform(KLT) algorithm to interrogate an array of FBG sensors. The noise RMS of the FT spectrometer is 218 fm, to be compared with 30 fm, reported in [41] and 4.9 fm in [42]. *Tosi et. al*[41, 42] applies

the KLT algorithm using commercial spectrometers, whose sampling frequencies are usually limited up to kHz range. The design of broadband, high-resolution integrated and high-speed spectrometers, although possible, is challenging. In terms of computational complexity, KLT requires the eigenvalue evaluation of a large matrix: matrices should be larger than 30×30 (typically 50×50) for about 10 FBG sensors [42]. The algebraic approach for the FT interrogator, on the other hand, requires evaluating roots of polynomial, which is equivalent to finding eigenvalues of M×M matrix, for M sensors. Efficient eigenvalue algorithms are available to compute roots of polynomials given the sparsity of the companion matrix [37]. For non-symmetric systems, corrections using Newton's method are also required. Alternatively, it is possible to implement the approach of [38], which consists of solving an M×M linear system + computing the roots of an M order polynomial.

Marin et. al. [46, 47] interrogates FBG sensors using an integrated MZI and an AWG spectrometer. The method offers high strain resolution (4.56 $n\varepsilon/\sqrt{Hz}$) and could be applied to fast sensors. The modulator employed in the design, however, is thermal-based, whose time constant is 7 μs[46], limiting the sensors' speed. A redesign of the chip using faster modulators would extend the interrogation method for higher speeds sensors. Refs. [11, 12] use a similar approach (using a passive MZI instead). A spectrometer separates the spectrum from the sensors and an optical switch selects one of the channels to be interrogated and guides it to an MZI. The noise floor reported is S_0 = 10$n\varepsilon/\sqrt{Hz}$. The demodulation approach of MZI+spectrometer [11, 12, 46, 47] requires the alignment of the wavelength of the center of the sensor's spectrum of one of the spectrometer channels. The FT interrogator's key benefit is the flexibility, being tolerant to variations in the resonance wavelength of the sensors.

The interrogators based on integrated spectrometers proposed by *Pustakhod et. al* [43] and others [44, 45] use a different demodulation strategy compared to the demodulation methods described by *D. Tosi* in [50]. Although the spectral resolution of these integrated spectrometers is much limited (a few nm), the minimum value of resonance wavelength obtained is about 320 fm in [43], in the same order of magnitude as the one presented in this work (700 fm, for no low pass filter applied). The approach is suitable for demodulating high-speed sensors and provides a high interrogation resolution. It consists of placing the sensor's resonance wavelengths close to the AWG channels' border, where the lineshape of the AWG channels can be linearized. As previously explained, this is an issue for integrated sensors, given the fact that the resonance wavelengths cannot be predicted during the sensor design.

High interrogation resolution is achieved for interrogators based on tunnelable lasers. *He et. al* [48] reports a minimum strain of 10 $n\varepsilon$, to be compared with 868 $n\varepsilon$ (for no digital filter applied) obtained for the FT interrogator. The dynamic strain resolution of I4g FAZ/Optics 11 [49] interrogator is better than 0.83 $n\varepsilon/\sqrt{Hz}$ for a wavelength sweep of 1 kHz, being able to resolve wavelength modulations of about 20 pm. The method is also tolerant for variation of resonance wavelength of sensors, but different strategies are needed for sensors operating in tens of kHz to MHz range.

In summary, the FT features a high interrogation resolution, being tolerant to

variation of resonance wavelength modulations. Here the bandwidth has been limited up to 1 kHz, but the method is suitable for a much higher speeds. Integrated photodetectors in this chip can reach hundreds of MHz, although a redesign of the electronic PCBs would be needed for such speeds. InP platform offers RF photodetectors at speeds up to tens of GHz. However, for a larger number of sensors, a higher optical power is needed, given that optical power is shared among the MZIs. *Kita et. al* [51] handles this issue using integrated optical switches so that no power splitting occurs. In this case, for applications at sensors that operate at MHz range, the design of high-speed optical switches is needed. Electro-optic phase modulators, available in InP platform, can reach speeds up to GHz range.

5.6. Conclusion

In this paper, we have interrogated an array of photonic sensors by solving an algebraic system of equations derived from an integrated Fourier transform interrogator. It has been shown that the modulus of the complex variables of the system of equations is theoretically one, while their argument is proportional to the resonance wavelength of the sensors. The experiments confirmed the theoretical prediction: the modulus of the complex variables deviates no more than 2% from unity; moreover, the plot amplitude modulation, derived from the argument of the complex variables, as a function of the strain, results in a straight line. The slope, for the optimal case, is 1.242 pm/μm in agreement with the results presented in our previous article and the specification provided by the FBG manufacturer.

The coupled equations have been solved using two semi-analytical approaches. The first one consists of solving the system of equations by computing the Gröbner basis of the polynomial ideal using lexicographical monomial order. The retrieved system of equations has been solved using a semi-analytical method since the polynomials' degree is higher than 4. For three sensors, six retrieved solutions have been obtained per time step where 5 of these are non-physical. The spurious solutions have been used to improve the actual solution, reducing both the cross-talk among the sensors and also the minimum amplitude modulation to 365 fm (for a bandwidth of 45 Hz). The dynamic strain resolution, obtained for no digital filter applied, is 1.66 n$\varepsilon/sqrtHz$.

If the spectra of all photonic sensors are equal, the derived algebraic system of equations is symmetric. The second approach exploits this symmetry. Then, the algebraic system can be reduced to a single univariate polynomial whose roots give the solution of the algebraic system. The results of the calibration procedure are that the coefficients b_1 and b_2 of the equation terms deviate around 4% from unity, breaking the symmetry of the algebraic system. For that reason, the solution of the symmetric system is taken as an initial guess and updated using Newton's method. Convergence has been achieved with 3 iterations. By processing with a GPU, it was possible to solve a system of 1 026 000 equations in 9 ms. The processing time per equation is 9 ns, allowing for real time interrogation of high-speed sensors.

The FT interrogator is a promising candidate for interrogating arrays of integrated arrays of photonic ultrasound sensors. If the lineshapes of the sensor spectra are the same, but they have varying peak values, the algebraic system of equations

can be solved using the approach described in [38]. That requires a redesigning of the chip so that the attenuation caused by the finite coherence length of the sensors can be neglected in larger MZIs.

Acknowledgement

Appendix A: Mathematical analysis of the Proposition of Section 5.3.2

In this Section, the mathematical details of the Preposition in Section 5.3.2 are presented. Although some steps required for a formal mathematical proof are not shown, we present valid reasoning for the Preposition's items.

Proposition. Let $(\delta_1(t),...,\delta_M(t))$ be the resonance wavelength modulation of M sensors, encoded in the argument of the complex variables $z_1(t), z_2(t), ..., z_M(t)$ defined by Eq. (5.10). The spectrum of the sensors is finite and their lineshapes are all equal, except each having a slightly different peak height. The combined spectrum of the sensors interfere in M interferometers according to the FT interrogator description presented in Section 5.2. Eq. (5.11), given by:

$$\sum_k b_k z_k^m = \hat{V}_m/a_{m,ref}, \qquad (5.40)$$

satisfy the following properties:

1. The polynomials in Eq. (5.40) intersect in $M!$ points;

2. If $Z_{sol} = (z_1,...,z_M)$ is a solution of Eq. (5.40) and the coefficients $b_1,...,b_M$ are all equal, the other solutions are given by all possible permutations of the coordinates of Z_{sol}. Moreover, $|z_m| = 1$, for $m = 1,...,M$;

3. If the coefficients $b_1 \neq b_2 \neq ... \neq b_M$ are all different, there is only one solution whose complex variables satisfy $|z_1| = ... = |z_M| = 1$. For all the other solutions, there is at least one complex variable whose modulus is different from one.

Assumptions

- If the coefficients $b_1 \neq b_2 \neq ... \neq b_M$ are all different, their values are assumed to be sufficiently close to one so that the solutions can be obtained by linear correction of Eq. (5.40), where the starting point is the solution for the system where $b_1 = ... = b_M = 1$

- For any value of t, the arguments of complex variables are sufficiently different from each other so that matrix $\mathbf{Q}_H$, defined by Eq. (5.57) is positive-definite and the jacobian of Eq. (5.40) is well-conditioned.

- The interrogator is noiseless.

Mathematical Analysis / Justification

Item (1). It can be shown that the solution of Eq. (5.40) always exits and the number of solutions is finite. Since polynomials in Eq. (5.40) intersect in a finite number of points, Bezout's theorem for M variables [25, 26] states that the maximum number of solutions is given by the product of the degrees of the polynomial equations. Hence, for Eqs. (5.40), the maximum number of solutions is given by $M!$. If the coefficients $b_1, ..., b_M = 1$ the polynomial in the left-hand side of Eqs. (5.40) is said to be symmetric: any transformation given by

$$z_k \to z_j$$
$$z_j \to z_k \tag{5.41}$$

for $(j \neq k)$ does not change the left-hand side of Eqs. (5.40). Therefore if $Z_{sol} = (z_1, ..., z_M)$ is a solution, any permutations of Z_{sol} coordinates also satisfies Eqs. (5.40). Since there exists $M!$ permutations of $(z_1, ..., z_M)$, there are $M!$ solutions. If the coefficients $b_1, ..., b_m$ are slightly different from one, each solution of the symmetric system is corrected using a linear approximation of Eq. (5.40) and the number of solutions remains the same.

Item (2). The algebraic system (Eqs. (5.11)) is equivalent to Eqs. (5.8), given by:

$$\frac{\hat{V}_m(t)}{a_{ref,m}} = \sum_{k=1}^{K} \frac{\int_{-\infty}^{\infty} s_k(\lambda') \exp\left(i2\pi \frac{m}{F_1}\lambda'\right) d\lambda'}{\int_{-\infty}^{\infty} s_{ref}(\lambda') \exp\left(i2\pi \frac{m}{F_1}\lambda'\right) d\lambda'} \exp\left[i2\pi \frac{m}{F_1}\left(\lambda_{0k} - \lambda_{0ref} + \delta_k(t)\right)\right]. \tag{5.42}$$

The complex variables have been defined according to Eq. (5.10), are here repeated:

$$z_k(t) = \exp\left[i\frac{2\pi}{F_1}\left(\lambda_{0k} - \lambda_{0ref} + \delta_k(t)\right)\right], \tag{5.43}$$

where $k = 1, ..., M$. Replacing the definition of Eq. (5.43) into Eq. (5.42), we see that $(z_1, ..., z_M)$ satisfies Eqs. (5.11) and $|z_1(t)| = ... = |z_M(t)| = 1$. Hence, at least one of the solutions of Eqs. (5.11) has all its variables with unitary modulus. From Item (1), it is known that there are, in total, $M!$ solutions, each given by the $M!$ possible permutations of the coordinates of $Z_{sol} = (z_1(t), ..., z_M(t))$, where $z_1(t), ..., z_M(t)$ are defined in Eq. (5.43).

Item (3). Let $(z_1, ..., z_M)$ and $(w_1, ..., w_M)$ be two of the solutions of Eq. (5.40). Eq. (5.40) can be rewritten according to:

$$\hat{V}_m(t) = \sum_{k=1}^{M} b_k z_k^m = \sum_{k=1}^{M} b_k w_k^m. \tag{5.44}$$

As explained in Item (3), one of the solutions of Eq. (5.40) has all the complex variables with unitary modulus. Let $|z_1| = ... = |z_M| = 1$. We want to show that the

modulus of at least one of complex variables in the solution $(w_1, ..., w_M)$ is different from one. Although the permutations of $(z_1, ..., z_M)$ no longer satisfy Eqs. (5.11), since $b_1 \cong ... \cong b_M \cong 1$, the solution $(w_1, ..., w_M)$ is in the neighbourhood of one of the permutations of complex variables $(z_1, ..., z_M)$. Let $R(k)$ be an operator that re-arrange the summation indexes according to the permutation of complex variables. For instance, if solution $(z_1, z_2, ..., z_M)$ is in the solution $(w_2, w_1, ..., w_M)$ neighbour-hood, then $(R(1), R(2), ..., R(M)) = (2, 1, ..., M)$. By manipulating Eq. (5.44), we obtain:

$$\sum_{k=1}^{M} \left[b_{R[k]} z_{R[k]}^m - b_k w_k^m \right] =$$

$$\sum_{k=1}^{M} z_{R[k]}^m \left[b_{R[k]} - b_k \frac{w_k^m}{z_{R[k]}^m} \right] =$$

$$\sum_{k=1}^{M} e^{im\phi_{R[k]}} \left[b_{R[k]} - b_k \left(|w_k|^m e^{im(\theta_k - \phi_{R[k]})} \right) \right] = 0. \qquad (5.45)$$

In the last step, we wrote the complex variables as $z_k = \exp(i\phi_k)$ and $w_k = |w_k| \exp(i\theta_k)$ (for $k = 1, ..., M$), where $(\phi_1, ..., \phi_M)$ and $(\theta_1, ..., \theta_M)$ are the arguments of complex variables $(z_1, ..., z_M)$ and $(w_1, ..., w_M)$, respectively. Let

$$\Delta A_k \equiv |w_k| - |z_{R[k]}| = |w_k| - 1$$
$$\Delta \theta_k \equiv \theta_k - \phi_{R[k]}, \qquad (5.46)$$

for $k = 1, ..., M$. ΔA_k and $\Delta \theta_k$ represents the corrections of the modulus and phase of complex variable w_k, respectively. Given that coefficients $b_1 \cong ... \cong b_M \cong 1$, $|\Delta A_k| << 1$ and $\Delta \theta_k \cong 0$. As a result

$$\exp(im\Delta\theta_k) = 1 + im\Delta\theta_k + O(\Delta\theta_k^2)$$
$$|w_k|^m = (1 + \Delta A_k)^m = 1 + m\Delta A_k + O(A_k^2), \qquad (5.47)$$

according to Taylor series expansion. By substituting Eqs. (5.47) into Eq. (5.45) and neglecting the second order terms, we obtain:

$$\sum_{k=1}^{M} e^{im\phi_{R[k]}} \left[(b_{R[k]} - b_k) - mb_k (\Delta A_k + i\Delta\theta_k) \right] = 0$$

$$\frac{1}{\sqrt{M}} \sum_{k=1}^{M} e^{im\phi_{R[k]}} (b_k m \Delta\zeta_k) = \frac{1}{\sqrt{M}} \sum_{k=1}^{M} e^{im\phi_{R[k]}} (b_{R[k]} - b_k), \qquad (5.48)$$

where $\Delta\zeta_k = \Delta A_k + i\Delta\theta_k$. Both sides of Eq. (5.48) have been multiplied by the factor $1/\sqrt{M}$ so that the columns of matrix $\mathbf{V}$, defined later in Eq. (5.52), are normalized.

Eq. (5.48) represents a linear system of equations, which can be written using matrices, according to:

$$\mathbf{CVB}\Delta\zeta = \mathbf{V}\Delta\mathbf{b} \tag{5.49}$$

where B and C are diagonal matrices:

$$\mathbf{C} = diag(1, 2, ..., M),$$
$$\mathbf{B} = diag(b_1, b_2, ..., b_M); \tag{5.50}$$

$\Delta\mathbf{b}$ and $\Delta\zeta$ are column vectors:

$$\Delta\mathbf{b} = [b_{R[1]} - b_1, ..., b_{R[M]} - b_M]^T$$
$$\Delta\zeta = [\Delta\zeta_1, \Delta\zeta_2, ..., \Delta\zeta_M]^T \tag{5.51}$$

and V is the modified Vandemonde matrix:

$$\mathbf{V} = \frac{1}{\sqrt{M}} \begin{pmatrix} z_{R(1)} & z_{R(2)} & ... & z_{R(M)} \\ z_{R(1)}^2 & z_{R(2)}^2 & ... & z_{R(M)}^2 \\ ... & & & \\ z_{R(1)}^M & z_{R(2)}^M & ... & z_{R(M)}^M \end{pmatrix}, \tag{5.52}$$

where the factor $\frac{1}{\sqrt{M}}$ normalizes the columns of matrix $\mathbf{V}$. The determinants of matrices $\mathbf{B}$ and $\mathbf{C}$ are real and non-zero, implying that $\mathbf{B}^{-1}$ and $\mathbf{C}^{-1}$ exist. Matrix $\mathbf{V}$ determinant can be shown to be zero only, and if only, the modulus of one of the complex variables in the solution $(z_1, ..., z_M)$ is zero or if two or more complex variables are equal [52]. Since the arguments $\phi_1, ..., \phi_M$ are by assumption different from each other and $|z_1| = ... = |z_M| = 1 \neq 0$, the determinant of V is non-zero. Hence, the linear system has always a solution for an arbitrary value of $\Delta\mathbf{b}$. Also, we assumed that coefficients $b_1, ..., b_M$ are different from each other, implying that $\Delta\mathbf{b} = 0$ if only no permutation of complex variables $(z_1, ..., z_M)$ is considered in Eq. (5.45). In this case, $\Delta\zeta = 0$ and solutions $(w_1, ..., w_M) = (z_1, ..., z_M)$ are the same. The analysis below is done for the case where $\Box\mathbf{b} \neq 0$. The linear system can be rewritten as:

$$\mathbf{B}\Delta\mathbf{z} = \mathbf{V}^{-1}\mathbf{C}^{-1}\mathbf{V}\Delta\mathbf{b} = \mathbf{Q}\Delta\mathbf{b}, \tag{5.53}$$

where $\mathbf{Q} \equiv \mathbf{V}^{-1}\mathbf{C}^{-1}\mathbf{V}$. Matrices $\mathbf{Q}$ and $\mathbf{C}^{-1}$ are similar, and their eigenvalues are $1, 1/2, 1/3, ..., 1/M$. The columns of the matrix $\mathbf{V}^{-1}$ give eigenvectors of matrix $\mathbf{Q}$.

The goal is to show that at least one of the elements of the vector $\Re\{\Delta\zeta\} = \Delta\mathbf{A}$ is non-zero, causing the modulus of one of the complex variables $(w_1, ..., w_M)$ to be different from one. By multiplying both sides of Eq. (5.53) by $\Delta\mathbf{b}^T$, we obtain:

$$\Delta\mathbf{b}^T\mathbf{B}\Delta\zeta = \Delta\mathbf{b}^T\mathbf{Q}\Delta\mathbf{b} \tag{5.54}$$

We start by analysing the case where the arguments of the complex variables $(z_1, ..., z_M)$ are equally distributed along the unit circle, i. e, the complex variables are given by $z_k = \exp(i2\pi k/M + i\phi_0)$ (for $k = 0, .., M-1$ and $\phi_0 \in [0, 2\pi)$). For this case, it can be shown that $\mathbf{V}^H = \mathbf{V}^{-1}$, so that Matrix $\mathbf{Q}$ becomes Hermitian. Eigenvalues of $\mathbf{Q}$ are given by $1, 1/2, ..., 1/M$, i. e., they are real and positive. Therefore,

Q is definite positive, making the right-hand side of Eq. (5.54) real and positive for any non-zero vector $\Delta\mathbf{b}$. As a result, the real and imaginary parts of the left side of Eq. (5.54) are given by:

$$\Im\{\Delta\mathbf{b}^T\mathbf{B}\Delta\zeta\} = 0$$

$$\Re\{\Delta\mathbf{b}^T\mathbf{B}\Delta\zeta\} = \Delta\mathbf{b}^T\mathbf{B}\Re\{\Delta\zeta\} = \sum_k \Delta b_k\, b_k\, \Re\{\Delta\zeta_k\} > 0. \tag{5.55}$$

Hence, at least one of the vector $\Re\{\Delta\zeta\}$ elements must be different from zero, so that the sum in Eq. (5.55) is real and positive. As a result, the modulus of at least one of the complex variables in the solutin $(w_1, ..., w_M)$ must be different from one.
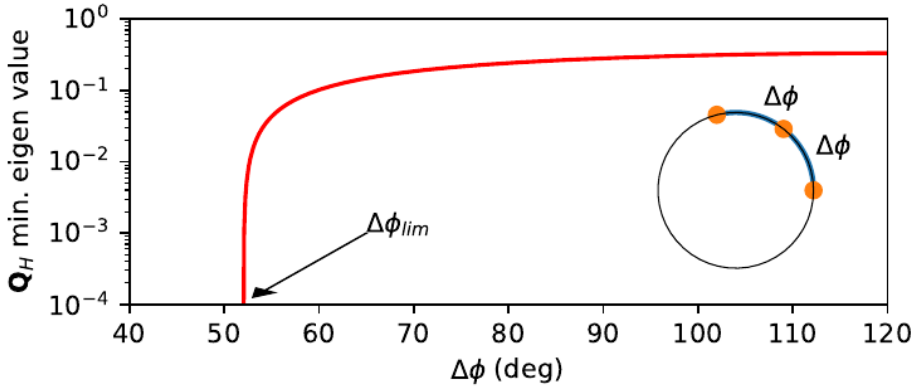

Figure 5.8: Minimum eigenvalue of matrix $\mathbf{Q}_H$ as a function of distance among the arguments $(\Delta\phi)$, defined in the inset.

The analysis made for the case where $z_k = \exp(i2\pi k/M + i\phi_0)$ (for $k = 0, .., M-1$ and $\phi_0 \in [0, 2\pi)$) can be extended. As long as $\phi_1 \neq ... \neq \phi_M$, the expression $\Re\{\Delta\mathbf{b}^T\mathbf{B}\square\square\}$ can be shown to be a continuous function of the arguments $\phi_1, ..., \phi_M$. For an arbitrary distribution of the arguments $\phi_1, ..., \phi_M$ (where $\phi_1 \neq ... \neq \phi_M$) along the unit circle, the real part of Eq. (5.54) is given by:

$$\Re\left\{\Delta\mathbf{b}^T\mathbf{B}\Delta\zeta\right\} = \Re\left\{\Delta\mathbf{b}^T\mathbf{Q}\Delta\mathbf{b}\right\} = \Delta\mathbf{b}^T\mathbf{Q}_H\Delta\mathbf{b}, \tag{5.56}$$

where $\mathbf{Q}_H$ is the Hermitian component of matrix $\mathbf{Q}$, given by:

$$\mathbf{Q}_H = \frac{1}{2}\left[\mathbf{V}^{-1}\mathbf{C}^{-1}\mathbf{V} + \left(\mathbf{V}^{-1}\mathbf{C}^{-1}\mathbf{V}\right)^H\right]. \tag{5.57}$$

$\mathbf{Q}_H = \mathbf{Q}$ for $z_k = \exp(i2\pi k/M + i\phi_0)$. Eigenvalues of $\mathbf{Q}_H$ are real since the matrix is Hermitian. $\Delta\mathbf{A} = \Re\{\Delta\zeta\}$ is guaranteed to be non-zero and positive if $\mathbf{Q}_H$ is positive definite.

Although analytical expressions for eigenvalues of matrix $\mathbf{Q}_H$ are difficult to be obtained for a larger number of sensors, eigenvalues of $\mathbf{Q}_H$ can be evaluated

numerically. Fig. 5.8 shows the minimum eigenvalue of matrix $\mathbf{Q}_H$ as a function of the relative phase distance of the arguments ($\Delta\phi$), as indicated in the inset. As long as $\Delta\phi$ is larger than $\Delta\phi_{lim} = 52.02^o$, $\mathbf{Q}_H$ is definite positive, and $\Delta\mathbf{A}$ is non-zero. For $\Delta\phi$ smaller than $\Delta\phi_{lim}$, matrix $\mathbf{Q}_H$ is indefinite, and $\Delta\mathbf{b}^T\mathbf{Q}_H\Delta\mathbf{b}$ can be either zero, positive or negative. However, even for $\Delta\phi < 52.02^o$ no values of $\Delta\mathbf{b}$ have been found so that $\Delta\mathbf{A} = 0$. For $\Delta\phi < \Delta\phi_{lim}$ and in the unlikely situation when $\Delta\mathbf{A} = 0$, so that two or more solutions cannot be distinguished, *Method 2* described in the main text could be used to make such distinction. A similar analysis can be performed for $M > 3$ sensors.

Appendix B: Analytical solutions for the symmetric system of equations

The goal of this appendix is to derive an analytical solution for Eq. (5.11) for $b_1 = \dots = b_M = 1$. For this case, Eq. (5.11) can be rewritten as:

$$\hat{v}_m(z_1, \dots, z_M) = \sum_{k=1}^{M} z_k^m, \tag{5.58}$$

where $\hat{v}_m = \hat{V}_m/a_{m,ref}$. The time dependence has been withheld for simplifying the notation. According to Eq. (5.9) in Section 5.3.1, the b_k coefficients are equal to unity only if the lineshapes of the photonic sensors $s_k(\lambda)$ (for $k = 1...M$) are equal. In this case, the polynomial in the right-hand side of Eqs. (5.58) is said to be symmetric: any transformation given by

$$\begin{aligned} z_k &\rightarrow z_j \\ z_j &\rightarrow z_k \end{aligned} \tag{5.59}$$

for ($j \neq k$) does not change the left-hand side of Eqs. (5.58). Therefore, if $\{z_1, \dots, z_K\}$ is a solution set, any permutation of the complex variables within this solution also satisfies Eqs. (5.58).

According to Newton's theorem (see chapter 7 of [26]), symmetric polynomials can be expressed as linear combinations of elementary symmetric polynomials, defined as:

$$e_m(z_1, \dots, z_M) = \sum_{1 < j_1 < j_2 < \dots < j_M} z_{j1} \times z_{j_2} \times \dots \times z_{j_M}, \tag{5.60}$$

where e_m is the m-th symmetric polynomial for M complex variables. The symmetric polynomials for 3 variables are given by:

$$\begin{aligned} e_0(z_1, z_2, z_3) &= 1 \\ e_1(z_1, z_2, z_3) &= z_1 + z_2 + z_3 \\ e_2(z_1, z_2, z_3) &= z_1 z_2 + z_1 z_3 + z_2 z_3 \\ e_3(z_1, z_2, z_3) &= z_1 z_2 z_3. \end{aligned} \tag{5.61}$$

The relation between the elementary symmetric polynomials $(e_0,...,e_M)$ and the sum of power monomials $(\hat{v}_1,...,\hat{v}_M)$ is given by [34]:

$$m e_m(z_1, ..., z_M) = \sum_{j=1}^{M} (-1)^{j-1} \hat{v}_j e_{m-j}. \tag{5.62}$$

Eq. (5.62) represents a triangular system of M equations ($m = 1...M$) with variables $\{e_1, ..., e_M\}$. The system is non-homogeneous since the last term of the summation is proportional to $e_0 = 1$. Thus, it is always possible to write the complex voltages as a function of the symmetric polynomials. The inverse relation for three complex voltages is given by:

$$e_1(z_1, z_2, z_3) = \hat{v}_1$$

$$e_2(z_1, z_2, z_3) = \frac{\hat{v}_1^2}{2} - \frac{\hat{v}_2}{2}$$

$$e_3(z_1, z_2, z_3) = \frac{\hat{v}_3^3}{6} - \frac{\hat{v}_1 \hat{v}_2}{2} + \frac{\hat{v}_3}{3}. \tag{5.63}$$

In order to solve the algebraic system in Eqs (5.58), we build a polynomial whose roots are $\{z_1, z_2, z_3\}$, i. e., the roots are equal to one of the solution sets of Eq. (5.58). In this case, the polynomial is given by

$$F(Z) = (Z - z_1)(Z - z_2)(Z - z_3). \tag{5.64}$$

The roots of $F(Z)$ give the solution set $\{z_1, z_2, z_3\}$. Expanding the right-hand side of Eq. (5.64), we obtain:

$$F(Z) = Z^3 - (z_1 + z_2 + z_3)Z^2 + (z_1 z_3 + z_1 z_3 + z_2 z_3)Z - (z_1 z_2 z_3). \tag{5.65}$$

The coefficients of Z^m (for $m = 0, 1, 2$) in the right-hand side of Eq. (5.65) can be recognized as the fundamental symmetric polynomials. Eq. (5.65) can be generalized for M complex variables using the Newton-Gerard identities:

$$F(Z) = \sum_{m=0}^{M} (-1)^m e_m Z^{M-m}. \tag{5.66}$$

The solution sets $\{z_1, ..., z_M\}$ are then obtained by substituting the relations $e_m = e_m(\hat{v}_1, ..., \hat{v}_M)$ into Eq. (5.66) and by calculating the roots of the polynomial $F(Z)$. For the case of 3 variables, $F(Z)$ is given by:

$$F(Z) = Z^3 - v_1 Z^2 + \left(\frac{\hat{v}_1^2}{2} - \frac{\hat{v}_2}{2} \right) Z - \left(\frac{\hat{v}_3^3}{6} - \frac{\hat{v}_1 \hat{v}_2}{2} + \frac{\hat{v}_3}{3} \right) \tag{5.67}$$

Eq. (5.67), except for a constant factor of 6, is identical to the univariate polynomial of the Gröbner basis shown in Section 5.5. By obtaining the roots of Eq. (5.67), we obtain the solution set $\{z_1, z_2, z_3\}$.

In Section 5, we demonstrate that the solution sets swap their values over time. Since the swapping depends on how the cubic roots are evaluated, the cubic root derivation is detailed here. A similar derivation is presented in [53]. Eq. (5.67) is first written as a general cubic polynomial, according to:

$$c_1 Z^3 + c_2 Z^3 + c_3 Z + c_4 = 0, \tag{5.68}$$

where the coefficients are defined by Eq. (5.67). Eq. (5.68) can be simplified by substituting $Z = y - c_2/(3c_1)$:

$$y^3 + Py + Q = 0, \tag{5.69}$$

Eq. (5.69) is known as a depressed cubic equation where P and Q are depressed cubic coefficients, given by:

$$P = \frac{c_3}{c_1} - \frac{c_2^2}{3c_1^2}$$

$$Q = \frac{d}{c_1} - \frac{c_2 c}{3c_1^2} + \frac{2c_2^3}{27c_1^3}. \tag{5.70}$$

In order to obtain the roots of Eq. (5.69), the following transformation is applied:

$$y = W - \frac{P}{3W}. \tag{5.71}$$

Substituting Eq. (5.71) into Eq. (5.69), we obtain:

$$W^3 + Q - \frac{P^3}{27W^3} = 0. \tag{5.72}$$

Assuming W is non-zero, both sizes of Eq. (5.72) are multiplied by W^3. Next, we substitute $U = W^3$:

$$U^2 + QU - \frac{P^3}{27} = 0. \tag{5.73}$$

Solving the second degree equation, we obtain:

$$U_\pm = \frac{-Q}{2} \pm \sqrt{\frac{P^3}{27} + \frac{Q^2}{4}}. \tag{5.74}$$

W is obtained by taking the cubic root of Eq. (5.74):

$$W_{j+} = \xi_j U_+^{1/3}$$
$$W_{j-} = \xi_j U_-^{1/3}, \tag{5.75}$$

where $\xi_j = (1, \exp(-i2\pi/3), \exp(i2\pi/3)$ are the cubic roots of 1. By substituting the values of W into Eq. (5.71) and substituting the value of y in its definition $Z_j = y_j - c_2/(3c_1)$, we obtain:

$$Z_j(t) = W_j(t) - \frac{P(t)}{3\xi_j W_j(t)} - \frac{c_2}{3c_1}. \tag{5.76}$$

It can be shown that both sets $\{W_{1+}, W_{2+}, W_{3+}\}$ and $\{W_{1-}, W_{2-}, W_{3-}\}$ of Eq. (5.75) result in the same solution set $\{Z_1, Z_2, Z_3\}$.

References

[1] N. A. Yebo, D. Taillaert, J. Roels, D. Lahem, M. Debliquy, D. Van Thourhout, and R. Baets, *Silicon-on-insulator (SOI) ring resonator-based integrated optical hydrogen sensor,* IEEE Photonics Technology Letters **21**, 960 (2009).

[2] N. A. Yebo, W. Bogaerts, Z. Hens, and R. Baets, *On-chip arrayed waveguide grating interrogated silicon-on-insulator microring resonator-based gas sensor,* IEEE Photonics Technology Letters **23**, 1505 (2011).

[3] K. De Vos, J. Gironès Molera, S. Popelka, E. Schacht, R. Baets, and P. Bienstman, *Soi optical microring resonator with poly(ethylene glycol) polymer brush for label-free biosensor applications,* Biosensors & Bioelectronics **24**, 2528 (2009).

[4] K. de Vos, Girones, J. Girones, T. Claes, Y. D. Koninck, S. Popelka, E. Schacht, R. Baets, and P. Bienstman, *Multiplexed antibody detection with an array of silicon-on-insulator microring resonators,* IEEE Photonics Journal **1**, 225 (2009).

[5] G. G. Daaboul, C. A. Lopez, A. Yurt, S. Member, and B. B. Goldberg, *Label-Free Optical Biosensors for Virus Detection and Characterization,* IEEE Journal of selected topics in quantum electronics **18**, 1422 (2012).

[6] A. D. Kersey, *Optical fiber sensors for downwell monitoring applications in the oil and gas industry,* IEICE Transactions on Electronics , 400 (2000).

[7] X.-W. Ye, Y.-H. Su, and P.-S. Xi, *Statistical analysis of stress signals from bridge monitoring by fbg system,* Sensors **18**, 1 (2007).

[8] S. M. Leinders, W. J. Westerveld, J. Pozo, P. L. M. J. van Neer, B. Snyder, P. O'Brien, H. P. Urbach, N. de Jong, and M. D. Verweij, *A sensitive optical micro-machined ultrasound sensor (OMUS) based on a silicon photonic ring resonator on an acoustical membrane.* Scientific reports **5**, 14328 (2015).

[9] F. G. Peternella, B. Ouyang, R. Horsten, M. Haverdings, P. Kat, and J. Caro, *Interrogation of a ring-resonator ultrasound sensor using a fiber mach-zehnder interferometer,* Opt. Express **25**, 31622 (2017).

[10] B.-Y. Hsieh, S.-L. Chen, T. Ling, L. J. Guo, and P.-C. Li, *Integrated intravascular ultrasound and photoacoustic imaging scan head,* Opt. Lett. **35**, 2892 (2010).

[11] P. Orr and P. Niewczas, *High-speed, solid state, interferometric interrogator and multiplexer for fiber Bragg grating sensors,* Journal of Lightwave Technology **29**, 3387 (2011).

[12] M. Perry, P. Orr, P. Niewczas, and M. Johnston, *High-speed interferometric fbg interrogator with dynamic and absolute wavelength measurement capability,* Journal of Lightwave Technology **31**, 2897 (2013).

[13] F. G. Peternella, T. Esselink, B. Dorsman, P. Harmsma, R. C. Horsten, T. Zuidwijk, H. P. Urbach, and A. L. C. Adam, *On-chip interrogator based on fourier transform spectroscopy,* Opt. Express **27**, 15456 (2019).

[14] M. Florjańczyk, P. Cheben, S. Janz, A. Scott, B. Solheim, and D. X. Xu, *Multiaperture planar waveguide spectrometer formed by arrayed Mach-zehnder interferometers,* Optics express **15**, 18176 (2007).

[15] A. V. Velasco, P. Cheben, P. J. Bock, A. Delâge, J. H. Schmid, J. Lapointe, S. Janz, M. L. Calvo, D. X. Xu, M. Florjańczyk, and M. Vachon, *High-resolution fourier-transform spectrometer chip with microphotonic silicon spiral waveguides,* Optics letters **38**, 706 (2013).

[16] H. Podmore, A. Scott, P. Cheben, A. V. Velasco, J. H. Schmid, M. Vachon, and R. Lee, *Demonstration of a compressive-sensing fourier-transform on-chip spectrometer,* Optics letters **42**, 1440 (2017).

[17] A. Herrero-Bermello, A. V. Velasco, H. Podmore, P. Cheben, J. H. Schmid, S. Jans, M. L. Calvo, D.-X. Xu, A. Scott, and P. Corredera, *Temperature dependence mitigation in stationary Fourier-transform on-chip spectrometers,* Optics letters **42**, 2239 (2017).

[18] D. M. Kita, B. Miranda, D. Favela, D. Bono, J. Michon, H. Lin, T. Gu, and J. Hu, *High-performance and scalable on-chip digital fourier transform spectroscopy,* Nature Communications **9**, 4405 (2018).

[19] R. Uda, K. Yamaguchi, K. Takada, and K. Okamoto, *Fabrication of a silica-based complex fourier- transform integrated-optic spatial heterodyne spectrometer incorporating 120o optical hybrid couplers,* Applied Optics **57**, 3781 (2018).

[20] B. I. Akca, *Design of a compact and ultrahigh-resolution fourier-transform spectrometer,* Opt. Express **25**, 1487 (2017).

[21] A. Herrero-Bermello, J. Li, M. Khazaei, Y. Grinberg, A. V. Velasco, M. Vachon, P. Cheben, L. Stankovic, V. Stankovic, D.-X. Xu, J. H. Schmid, and C. Alonso-Ramos, *On-chip fourier-transform spectrometers and machine learning: a new route to smart photonic sensors,* Opt. Lett. **44**, 5840 (2019).

[22] K. Takada, H. Aoyagi, and K. Okamoto, *Correction for phase-shift deviation in a complex fourier-transform integrated-optic spatial heterodyne spectrometer with an active phase-shift scheme,* Opt. Lett. **36**, 1044 (2011).

[23] K. Okamoto, *Fourier-transform, integrated-optic spatial heterodyne (fish) spectrometers on planar lightwave circuits,* in *International Conference on Fibre Optics and Photonics* (Optical Society of America, 2012) p. M2A.1.

[24] A. Herrero-Bermello, A. V. Velasco, H. Podmore, P. Cheben, J. H. Schmid, S. Janz, M. L. Calvo, D.-X. Xu, A. Scott, and P. Corredera, *Temperature dependence mitigation in stationary fourier-transform on-chip spectrometers,* Opt. Lett. **42**, 2239 (2017).

5

[25] D. Cox, J. Little, and D. O. Shea, *Using Algebraic Geometry*, 2nd ed. (Springer, 2005).

[26] D. Cox, J. Little, and D. O. Shea, *Ideals, varieties, and algorithms*, 3rd ed. (Springer, 2006).

[27] M. Mencinger, *On groebner bases and their use in solving some practical problems,* Universal Journal of Computational Mathematics **1**, 5 (2013).

[28] M. Kalkbrener, *Solving systems of algebraic equations by using gröbner bases,* in *Eurocal '87*, edited by J. H. Davenport (Springer Berlin Heidelberg, Berlin, Heidelberg, 1989) pp. 282–292.

[29] Y. Sun and D. Wang, *The f5 algorithm in buchberger's style,* Journal of Systems Science and Complexity **26**, 1218 (2011).

[30] Maplesoft, *Maple user manual. toronto: Maplesoft, a division of waterloo maple inc., 2005-2019.* https://www.maplesoft.com/documentation_center/maple18/usermanual.pdf, accessed: 2020-07-07.

[31] D. Lazard, *Solving zero-dimensional algebraic systems,* J. Symbolic Computation **13**, 117 (1992).

[32] A. Dickenstein and I. Z. Emiris", eds., *"Solving Polynomial Equations Foundations, Algorithms, and Applications"* ("Springer", "2005").

[33] D. Cox, *Galois Theory*, 2nd ed. (John Wiley and Sons, 2012).

[34] I. G. Macdonald, *Symmetric Functions and Hall Polynomials* (Oxford University Press, 2008).

[35] A. Maxwell, S.-W. Huang, T. Ling, J.-S. Kim, S. Ashkenazi, and L. Jay Guo, *Polymer microring resonators for high-frequency ultrasound detection and imaging,* IEEE Journal of Selected Topics in Quantum Electronics **14**, 191 (2008).

[36] C. Zhang, S.-L. Chen, T. Ling, and L. J. Guo, *Review of imprinted polymer microrings as ultrasound detectors: Design, fabrication, and characterization,* IEEE Sensors Journal **15**, 3241 (2015).

[37] V. Y. Pan and A.-L. Zheng, *New progress in real and complex polynomial root-finding,* Computers Mathematics with Applications **61**, 1305 (2011).

[38] C. Connell, *A solution to certain polynomial equations with applications to nonlinear fitting,* Mathematics of Computation **74**, 303 (2004).

[39] H. Cohen, *Complex Analysis with Applications in Science and Engineering*, 2nd ed. (Springer, 2007).

[40] E. Wegert, *Visual Complex Functions*, 1st ed. (Springer, 2012).

[41] D. Tosi, *Advanced Interrogation of Fiber-Optic Bragg Grating and Fabry-Perot Sensors with KLT Analysis,* Sensors **15** (2015), doi: 10.3390/s151127470.

[42] D. Tosi, *KLT-Based Algorithm for Sub-Picometer Accurate FBG Tracking With Coarse Wavelength Sampling,* IEEE Photonics Technology Letters **27** (2015), 10.3390/s17102368.

[43] D. Pustakhod, E. Kleijn, K. Williams, and X. Leijtens, *High-resolution awg-based fiber bragg grating interrogator,* IEEE Sensors Journal **28**, 2203 (2016).

[44] H. Li, X. Ma, B. Cui, Y. Wang, C. Zhang, J. Zhao, Z. Zhang, C. Tang, and E. Li, *Chip-scale demonstration of hybrid III - V / silicon photonic integration for an FBG interrogator,* Optica **4**, 692 (2017).

[45] H. Guo, G. Xiao, N. Mrad, and J. Yao, *Echelle diffractive grating based wavelength interrogator for potential aerospace applications,* Journal of Lightwave Technology **31**, 2099 (2013).

[46] Y. E. Marin, A. Celik, S. Faralli, L. Adelmini, C. Kopp, F. D. Pasquale, and C. J. Oton, *Integrated dynamic wavelength division multiplexed fbg sensor interrogator on a silicon photonic chip,* J. Lightwave Technol. **37**, 4770 (2019).

[47] Y. E. Marin, T. Nannipieri, C. J. Oton, and F. D. Pasquale, *Integrated FBG Sensors Interrogation Using Active Phase Demodulation on a Silicon Photonic Platform,* Journal of Lightwave Technology **35**, 3374 (2017).

[48] Z. He, Q. Liu, and T. Tokunaga, *Development of nano-strain-resolution fiber optic static strain sensor for crustal deformation monitoring,* in *Asia Communications and Photonics Conference* (Optical Society of America, 2012) p. AS1E.2.

[49] S. K. Ibrahim, M. Farnan, and D. M. Karabacak, *Design of a photonic integrated based optical interrogator,* in *Photonic Instrumentation Engineering IV*, Vol. 10110, edited by Y. G. Soskind and C. Olson, International Society for Optics and Photonics (SPIE, 2017) pp. 241 – 249.

[50] D. Tosi, *Review and analysis of peak tracking techniques for fiber bragg grating sensors,* Sensors (Switzerland) **17** (2017), 10.3390/s17102368.

[51] D. M. Kita, B. Miranda, D. Favela, D. Bono, J. Michon, H. Lin, T. Gu, and J. Hu, *High-performance and scalable on-chip digital fourier transform spectroscopy,* Nature Communications **9**, 4405 (2018).

[52] F. Soto-Eguibar and H. Moya-Cessa, *Inverse of the Vandermonde and Vandermonde confluent matrices,* Applied Mathematics and Information Sciences **5**, 361 (2011).

[53] A. T. Tiruneh, *A simplified expression for the solution of cubic polynomial equations using function evaluation,* arXiv e-prints , arXiv:2002.06976 (2020), arXiv:2002.06976 [math.GM] .

5

6

Conclusion

In this thesis, two types of interferometric interrogators for photonic sensors have been designed and characterized. In the first part of the thesis, an ultrasound sensor based on an integrated ring-resonator (RR) in the MHz range was interrogated. In this case, a single fiber Mach Zehnder interferometer(MZI) was employed, and no demultiplexing is needed. The results from the fiber interrogator, presented in Chapter 3, have been used to develop a novel interrogator method, presented in Chapters 4 and 5. The novel interrogator is based on an integrated Fourier transform (FT) spectrometer where many interferometers are employed to demultiplex and demodulate an array of sensors. The experiments presented in Chapters 4 and 5 were conducted using an array of FBGs strain sensors, but the novel interrogator is suitable to interrogate RR arrays.

The work on the fiber interrogator represents an important step towards the interrogation in real-time. The long term goal of this project is for medical applications and IVUS imaging. The ring resonators presented in Chapter 3 are much smaller than the conventional piezo-electric devices used for different types of medical imaging, and it is possible to integrate large arrays of RRs in a single die featuring a small cross talk. Results shown in Chapter 3 indicate that the minimum amplitude modulation detected by the interrogator is comparable to the state of art ultrasound sensors based on piezo-electric devices. However, the realization of a commercial device requires an enhancement of the acoustic bandwidth. This is possible by reducing the membrane diameter and its thickness[1], which increases the membrane acoustic resonance frequency.

The mathematical model of the interrogator presented in Chapter 3 allows a geometrical interpretation of the interrogation parameters. The interferometric interrogator converts the resonance wavelength modulation into a phase modulation: by combining the output voltages of the interrogator, two 90 ° phase shifted volt-

131

ages were calculated, whose Lissajous curve describes an arc of a circle:

$$V_x(t) = R \cos(\Phi(t) + \psi_e) + x_0$$
$$V_y(t) = R \sin(\Phi(t) + \psi_e) + y_0, \tag{6.1}$$

where R is the circle radius, (x_0, y_0) is its centre, ψ_e is a phase which is accord-ing to local variations of temperature within the MZI and $\Phi(t)$ is a phase which is proportional to the resonance wavelength. The external excitation (ultrasound, in this case) causes the resonance wavelength to shift, inducing a modulation of the phase $\Phi(t)$. Since the coherence lengths of the transmission spectrum of the RR pass port and of the FBG reflection spectrum have comparable values, both signals undergo interference within the fiber MZI. While the resonance wavelength modulation induces a modulation of the angle $\Phi(t)$, the interference of the FBG reflection spectrum causes the circle arc centre to shift from the origin and causes a deformation of the circle arc. Also, as a result of the interference of the FBG spectrum, this centre depends on the drift of the phase ψ_e. These phenomena have been taken into account in one hand, by fitting a circle to the Lissajous curve of the experimental curve $(V_x(t), V_y(t))$ in order to retrieve the radius and the cir-cle centre; on the other hand, by introducing a correction factor, which accounts for the deformation of the circle arc. A novel version of this interrogator, already demonstrated by [5], uses the FWHM of the FBG reflection is much larger than that of the RR transmission spectrum. As a result, the interference of the FBG curve to vanish. The new version, however, does not perform demultiplexing and still only interrogates a single photonic sensor.

The theoretical model presented in the appendix of Chapter 3 has been used as the basis for the development of the Fourier transform interrogator of Chapter 4. In this case, a large list of applications is possible, as discussed in Chapters 1 and 2. In special, FT-interrogator has been designed to monitor the ultrasound sensors based on RR: this novel interrogator can be applied to demultiplex and demodulate arrays of integrated sensors whose resonance wavelengths cannot be predicted during their design stage. The same flexibility could not be achieved using conventional interferometric interrogators, which typically use a combination of a dispersive spectrometer (such as an AWG) and an array of MZIs, as discussed in Chapter 2.

The demultiplexing and demodulation of the resonance wavelengths are per-formed simultaneously for the FT-interrogator. Given M interferometers and K pho-tonic sensors, the complex output voltages of the FT interrogator can be written as:

$$\hat{V}_m(t) = \sum_{k=1}^{K} R_m \exp(m\Phi_k(t)) \tag{6.2}$$

where $\Phi_k(t)$ is the induced phase modulation of the k-th sensor and the equa-tion sub-index $m = 1, ..., M$. The method consists of solving a non-linear system of equations, described by Eq. (6.2), for each instant of time. Eq. (6.2) reduces to

Eq. (6.1), for $K = 1$ (one sensor) and $M = 1$ (one interferometer) and by taking $V_x = \Re(V_1)$ and $V_y = \Im(V_1)$ indicating that the method presented in Chapter 4 generalizes the method presented in Chapter 3. Another benefit of the FT interrogator is its high measurement resolution. The experiments presented in Chapter 4 show that the measurement resolution experimentally retrieved was about two orders of magnitude smaller than the FT spectrometer resolution.

One of the main drawbacks of the FT interrogator is its high computational cost. In Chapter 4, Eq. (6.2) has been solved numerically using Newton's method. In Chapter 5, Eq. (6.3) is solved using semi-analytical methods. Eq. (6.2) is rewritten as a coupled system of polynomial equations and solved using semi-analytical methods. In the case of 3 sensors, Eq. (6.2) can be written as:

$$f_1(z_1, z_2, z_3) = b_1 z_1 + b_2 z_2 + b_3 z_3 = \hat{V}_1/a_{1,3}$$
$$f_2(z_1, z_2, z_3) = b_1 z_1^2 + b_2 z_2^2 + b_3 z_3^2 = \hat{V}_2/a_{2,3}$$
$$f_3(z_1, z_2, z_3) = b_1 z_1^3 + b_2 z_2^3 + b_3 z_3^3 = \hat{V}_3/a_{3,3},$$

$$(6.3)$$

where b_1, b_2, b_3, $a_{1,3}$, $a_{2,3}$ and $a_{3,3}$ are coefficients determined by the calibration procedure (see Sections 4.3.2 and 5.4.2). Suppose the lineshapes of the sensors are equal. In that case, $b_1 = b_2 = b_3 = 1$ and the polynomials $f_1(z_1, z_2, z_3)$, $f_2(z_1, z_2, z_3)$ and $f_3(z_1, z_2, z_3)$ are said to be symmetric. As shown in Appendix B of Chapter 5, the system can be reduced to a single polynomial equation, whose roots give this system's solution. In case coefficients b_1, b_2 and b_3 are different from each other, the Gröbner basis[7, 8] of the polynomial ideal $I =< p_1, p_2, p_3 >$ is calculated for a lex monomial order, where $p_1 = f_1 - \hat{V}_1/a_{1,3}$, $p_2 = f_2 - \hat{V}_1/a_{2,3}$ and $p_3 = f_3 - \hat{V}_3/a_{1,3}$. $\hat{V}_1, \hat{V}_2$, and $\hat{V}_3$ are kept as are parameters. The polynomials of the basis satisfy:

$$g_1(z_1, z_2, z_3) = 0$$
$$g_2(z_2, z_3) = 0$$
$$g_3(z_3) = 0, \qquad\qquad (6.4)$$

where g_j ($j = 1, 2, 3$) are the polynomials of the Gröbner basis. Eq. (6.4) can be solved analytically, enhancing the processing speed. Two main issues have been identified with this approach: for M sensors, the number of solutions is $M!$, and in general, only one of these solutions is valid. Moreover, computation of Gröbner basis using lex monomial order of Eq. (6.3) is not feasible for a larger number of sensors. Thus, Eq.(6.4) is solved using two steps: we first compute the solution of Eq. (6.4) by approximating coefficients $b_1 = ... = b_M = 1$; subsequently, we correct the solutions using the Newton method. The algebraic system has been solved in a GPU, resulting in a 9.0 ns/equation performance, allowing the real-time interrogation of high-speed sensors.

Improvements in the calibration procedure are required for the interrogation of a large array of sensors. In Chapters 4 and 5, each sensor is individually excited, and coefficients of the non-linear equations are retrieved from the properties of the

ellipses fitted against the Lissajous Curves $(V_{x,m}(t_{cal,k}), Vy_{x,m}(t_{cal,k}))$ for $m = 1...M$, where M are the number of interferometers and t_{cal} the calibration time of k-th sensor. The algebraic formulation presented in Chapter 5 simplifies the procedure, and the excitation of the reference sensor is needed. Coefficients b_k (for $k = 1...M$), which are real-valued, are given by the ratio of the peaks of the sensor spectrum. Excitation of other sensors is only needed in order to retrieve the voltage offsets. As an alternative to individual excitation of the sensors (to be explored in the future), offsets can also be obtained by exciting all sensors simultaneously and using an optimization procedure similar presented in Section 5.5.2 of Chapter 5.

Chapter 5 exploits the fact that coefficients $b_1, ..., b_M$ are close to one, so that polynomials $f_1(z_1, z_2, z_3)$, $f_2(z_1, z_2, z_3)$ and $f_3(z_1, z_2, z_3)$ in Eq. (6.3) are nearly symmetric. This is obtained if the sensors' spectra lineshapes are all similar. For FBG sensors, the fabrication technology is sufficiently mature to meet such condition [9, 10]. For arrays of ring resonator sensors integrated into the same chip, this can be achieved by designing an array of identical rings except for a small difference in the ring's length. As explained in Section 1.2.1, ring resonators may present multiple resonances along the C-band, and an optical filter needs to be applied at the output of each ring to isolate one of the resonances. Such filters could differently affect the height of the curves $s_k(\lambda)$, resulting in $b_1 \neq ... \neq b_M$. Hence, the spectra of the optical filters have to be considered. If coefficients $b_1, ..., b_M$ are much different from the unity, other methods can be applied to solve equations' algebraic system. For instance, the method proposed by *Connell et al.* [11] is quite advantageous. On the one hand, the method uses nearly twice the number of complex voltages, increasing the device footprint and the number of Mach-Zehnder interferometers. On the other hand, the method requires no calibration procedure. However, applying such an approach may require the chip redesign since the complex voltages obtained from larger MZI are much attenuated due to the coherence length of the FBG reflection spectrum (typically given by hundreds of pm).

Finally, another application of the FT-interrogator, not explored in the thesis, is the interrogation of arrays of sensors based on low Q Fabry-Perot interferometers (FPI). The manufacturing costs of such sensors is quite low since they typically use a cleaved fiber and a moving mirror. The external excitation modulates the mirror position and the cavity length as a function of time. Assuming that the optical path(OP) of the k-th FPI sensor matches the OPD of the m-th interferometer within the chip, it can be shown that the m-th complex voltage encodes in its argument the modulation of the FPI sensor. The demodulation is much simplified for an array of FPI sensors, as no algebraic system of equations needs to be solved. A key benefit of our technique would be the speed, being possible the demodulation of sensors that operate at hundreds of MHz or even a few GHz, depending on the electronics.

References

[1] W. Westerveld, *Silicon photonic micro-ring resonators to sense strain and ultrasound*, Ph.D. thesis, Delft University of Technology (2014).

[2] D. Soulioti, N. Barkoula, A. Paipetis, T. Matikas, T. Shiotani, and D. Aggelis,

Acoustic emission behavior of steel fibre reinforced concrete under bending, Construction and Building Materials **23**, 3532–3536 (2009).

[3] K. S. C. K. Dan Li and C. G. Koh, *Fatigue crack sizing in rail steel using crack closure-induced acoustic emission waves,* Measurement Science and Technology **28**, 065061 (2017).

[4] S. Liang, C. Zhang, W. Lin, L. Li, C. Li, X. Feng, and B. Lin, *Highly sensitive spectroscopic detection of heme-protein submonolayer films by channel integrated optical waveguide,* Opt. Letters **34**, 1858 (2009).

[5] B. Ouyang, M. Haverdings, R. Horsten, M. Kruidhof, P. Kat, and J. Caro, *Integrated photonics interferometric interrogator for a ring-resonator ultrasound sensor,* Opt. Express **27**, 23408 (2019).

[6] P. Orr and P. Niewczas, *High-speed, solid state, interferometric interrogator and multiplexer for fiber Bragg grating sensors,* Journal of Lightwave Technology **29**, 3387 (2011).

[7] B. Buchberger, *A theoretical basis for the reduction of polynomials to canonical forms,* ACM SIGSAM Bulletin **10**, 3374 (1973).

[8] D. Cox, J. Little, and D. O'Shea, *Ideals, Varieties, and Algorithms*, 3rd ed. (Springer, 2007).

[9] J. Habel, T. Boilard, J.-S. Freniere, F. Trepanier, and M. Bernier, *Femtosecond fbg written through the coating for sensing applications,* Sensors **17**, 2519 (2017).

[10] R. "Falciai, R. Fontana, and A. Schena, *"the stretch-and-write technique for fabrication of fiber bragg-grating arrays",* pp. "129–135".

[11] C. Connell, *A solution to certain polynomial equations with applications to nonlinear fitting,* Mathematics of Computation **74**, 303 (2004).

6

Curriculum Vitæ

Fellipe GRILLO PETERNELLA

15-12-1983   Born in Campinas, Brazil.

Education

1999–2002   Technical school in programming
                     Technical High School of Campinas
2003–2008   Undergraduate in Electrical Engineering
                     Campinas State University
2010–2012   Master in Electrical Engineering
                     Campinas State University
Thesis: Revisão dos modos espúrios na análise modal de guias de
                     onda por elementos finitos
Promotor: Prof. dr. Hugo Hernandez Figueroa

List of Publications

Journal Papers

1. **Fellipe Grillo Peternella, Peter Harmsma, Roland C. Horsten, Thim Zuidwijk, H. Paul Urbach, and Aurèle J. L. Adam**, *Algebraic solutions for the Fourier transform interrogator*, Opt. Express 29, 25632-25662 (2021).

2. **Fellipe Grillo Peternella, Thomas Esselink, Bas Dorsman, Peter Harmsma, Roland C. Horsten, Thim Zuidwijk, H. Paul Urbach, and Aurèle J. L. Adam** , *On-chip interrogator based on Fourier transform spectroscopy* Optics Express, Vol. 27, Issue 11, pp. 15456-15473 (2019) .

3. **Fellipe Grillo Peternella, Boling Ouyang, Roland Horsten, Michael Haverdings, Pim Kat, and Jacob Caro** , *Interrogation of a ring-resonator ultrasound sensor using a fiber Mach-Zehnder interferometer* Optics Express, Vol. 25, Issue 25, pp. 31622-31639 (2017).

4. **Luciano A. Montoro,Marina S. Leite, Daniel Biggeman, Joost K. Batenburg, G. Medeiros-Riberio, Fellipe G. Peternella, Antonio J. Ramirez**, *Revealing Quantitative 3D Chemical Arrangement on Ge−Si Nanostructures.* Journal of Physical Chemistry. C, v. 113, p. 9018-9022, 2009.

Conference Papers

1. **F. G. Peternella, B. Ouyang, R. Horsten, M. Haverdings, P. Kat, J. Caro** , *MZI based interrogation of a ring-resonator ultrasound sensor* IEEE Photonics Benelux, 2017 Delft, The Netherlands .

2. **Atul K. Srivastava, Julio C. R. F. de Oliveira, Alexandre p. Freitas; Fellipe G. Peternella, Leandro Matiolli, Valentino Corso, Flavio Borin, Bernardo Kyotoku, Neil Guerrero-Gonzalez**, *112 Gb/s compact silicon-on-insulator coherent receiver.* SPIE OPTO, 2015, San Francisco. p. 93900D. .

3. **Atul K. Srivastava, Julio C. R. F. de Oliveira, Alexandre p. Freitas; Fellipe G. Peternella, Leandro Matiolli, Valentino Corso, Flavio Borin, Bernardo Kyotoku, Neil Guerrero-Gonzalez**, *The first brazilian integrated 100G DPQPSK transmitter on a 4 3 mm silicon photonic chip* SPIE OPTO, 2014, San Francisco. p. 90100D. .

4. **Fellipe Grillo Peternella; Luciano Oliveira, Hugo Hernandez Figueroa .** , *Novel FEM modal simulator for photonic structures completely free of spurious modes* 2011, Ottawa. 2011 ICO International Conference on Information Photonics. p. 1. .

Book Chapters

1. **E. A. T. Lopez, Fellipe Grillo Peternella, Antonio J. Ramirez** , *In Situ Scanning Electron Microscopy high Temperature Deformation Experiments to Study Ductility Dip Cracking of Ni-Cr-Fe Alloys.* In-situ Studies with Photons, Neutrons and Electrons Scattering. 1ed.: Berlin, Heidelberg, 2010, v. 1, p. 27-39..

Patent depositions

1. **Fellipe Grillo Peternella, Aurèle J. L. Adam, H. Paul Urbach** , *Interrogation of an optical sensor array* NL2021771B1, 2020-05-12, UNIV DELFT TECH [NL] .

2. **Alexandre Passos Freitas, Bernardo de Barros Correia Kyotoku, Fellipe Grillo Peternella** , *Indium phosphide integrated gain equalizer filter* BR102014011997A2, 2016-02-10, FUNDACAO CPQD CT PESQUISA E DESENVOLVIMENTO EM TEL [BR] .

3. **Alexandre Passos Freitas, Bernardo de Barros Correia Kyotoku, Fellipe Grillo Peternella, Julio Cesar Rodrigues Fernandes de Oliveira** *Integrated polarization rotator and divider compatible with integrated photonics fabrication* BR102014016435A2, 2016-06-07, FUNDACAO CPQD CT PESQUISA E DESENVOLVIMENTO EM TEL [BR] .

4. **Alexandre Passos Freitas, Fellipe Grillo Peternella** *Configurable rf filter implemented in integrated photonics* BR102014014659A2, 2016-04-19, FUNDACAO CPQD CT PESQUISA E DESENVOLVIMENTO EM TEL [BR] .